Burns, Max William (2017) ***Kinetic investigations of struvite crystallisation in Poiseuille flow using discretised population balance methods*****. PhD thesis, James Cook University.**

KINETIC INVESTIGATIONS OF STRUVITE CRYSTALLISATION IN POISEUILLE FLOW USING DISCRETISED POPULATION BALANCE METHODS

Thesis submitted by:

Max William Burns

Bachelor of Engineering (Chemical) (Hons 1st), *James Cook University*

July 2017

This thesis is submitted for the degree of Doctor of Philosophy in the School of Engineering and Physical Sciences at James Cook University

ACKNOWLEDGEMENTS

Primarily I would like to acknowledge the support provided by my supervisory team. My primary supervisor AProf. Philip A. Schneider gave invaluable insight into various aspects of this work and enabled me to become an independent researcher. My secondary supervisor Dr. Madoc Sheehan offered excellent feedback on my writing and thesis structure. Finally, Prof. Peter Ridd helped me make valuable insight into the mechanics of fluid mixing. I am grateful to all of these contributions.

I would also like to thank all of the JCU support staff who contributed many hours to helping me. Melissa Norton helped to solve every logistical and administrative problem which arose during my candidature – I really do appreciate her efforts. Thanks also go to the workshop staff Curt Arrowsmith, Ross Barret and Dean Frendon, who helped with construction of various iterations of experimental systems. Acknowledgements are also due to the funding bodies who supported my work – the CSIRO and Commonwealth Government.

Most importantly, I'd like to acknowledge all of the friends and family who offered the love and support necessary for me to endure this process. The various distractions, kind words and occasional indifference kept me grounded. Specifically I want to acknowledge my partner Tanya, my siblings James and Eleanor and my parents Cindy and Ian for all of your support.

STATEMENT ON THE CONTRIBUTION OF OTHERS

The direction of this research was contributed to significantly by the primary supervisor, Dr. Philip A. Schneider. Minor feedback on experimental techniques and discussion were also made by both co-supervisors; Dr. Madoc Sheehan and Prof. Peter Ridd. Leynard Natividad-Marin, a fellow PhD student provided assistance with laboratory data collection and analysis and thermodynamic modelling.

Financial support for my scholarship was provided by CSIRO and the Commonwealth Government. Financial support for lab equipment, software and conference travel was provided by CSIRO and the James Cook University School of Engineering and Physical Sciences.

ABSTRACT

Phosphorus is a non-renewable resource, essential for agriculture. Struvite crystallisation from wastewater offers an easy method of recovering up to 17% of global phosphorus losses. Reported struvite crystallisation kinetics vary significantly, resulting in large uncertainties in crystalliser design. Additionally, crystallisation models are rarely capable of describing particle size distribution, which is a key property of crystallisation kinetics, crystal packing and crystal dissolution rates.

This thesis consisted of three major components: model development, experimental investigations and parameter estimation. As a precursor to model development, a review was conducted on struvite crystallization modelling and data from multiple kinetic investigations was analysed to identify trends and areas for targeted improvement. The large range in kinetic modelling techniques and results suggested the need for more detailed modelling, incorporating aggregation. On this basis, further investigations were conducted on population balances used to model aggregation processes. The volume average technique and a modified Hounslow technique were adopted for this work. Model testing showed that implementation of the cell average technique produced more accurate results but longer simulation times. The final approach used to analyse data in this work combined both models – using the cell average technique for nucleation and crystal growth analysis and the Galbraith modified Hounslow technique for the more computationally intensive aggregation investigations. A non-ideal thermodynamic model was used to describe the kinetic driving force for crystallization in the population balance model, which was then integrated into a continuum Poiseuille flow reactor model. Model tuning resulted in an acceptable level of output uncertainty. The key output of the modelling work was the development of a framework for nucleation, growth and aggregation investigation occurring in Poiseuille flow.

In the experimental phase of this work, a lab-scale Poiseuille flow reactor was developed and used to investigate the impacts of feed mixing and supersaturation level on phosphorus recovery and particle size distribution. Sonication was successfully used to disrupt weakly bound aggregates providing insight into the aggregation process. Disrupted particles were relatively independent of operational conditions, showing that they continue to grow during the aggregation process. Vortex mixing was shown to have a significant influence on PSD and phosphorus recovery. A major output of the experimental work was the development of techniques for investigating aggregation, with potential for further application.

The final major component of this work was to combine experimental results and the reactor model to regress kinetic parameters for nucleation growth and aggregation. The parameter estimation process was preceded by model sensitivity analysis. This allowed identification of (1) the most sensitive kinetic parameters, (2) how parameters affect outputs, (3) which parameters are correlated, and (4) how input variable uncertainty affected output variable uncertainty. Point 4 was used to inform uncertainty in the parameter regression process. Finally, parameter optimisation was conducted using a global, normalised, weighted objective function. Sonicated data provided nucleation and growth parameters which were then fixed to separately analyse non-sonicated data, providing aggregation parameters. The regressed parameters were close to those found by other population balance work on struvite – a significant result considering the large variation seen in the literature.

TABLE OF CONTENTS

LIST OF FIGURES

LIST OF TABLES

NOMENCLATURE

Note: the nomenclature given below refers only to variables used in this work and excludes those from some equations discussed in the literature review but not used here.

Abbreviations:

Symbol	Variable
IAP	Ion activity product
CA	Cell average
AGG_INDEX_i	Index determining whether aggregation related birth event will occur in cell i
$MM_{struvite}$	Molecular mass of struvite $[g\ mole^{-1}]$

Latin Symbols:

Symbol	Variable
a	DeBye-Hückel equation constant
a_i	Activity of Species i
A	DeBye-Hückel equation constant
A''	Growth rate constant in the 'birth and spread' model $[\mu m\ min^{-1}]$
A_n	Nucleation pre-exponential factor/ collision factor $[cm^{-3}s^{-1}]$
A_y	Generalisation of ionic compound with charge y
b	DeBye-Hückel equation constant
b_i	Birth rate of particles distributed into cell i
B	Total birth rate of particles from all mechanisms (continuous) $[\#\ min^{-1}]$
B'	Supersaturation constant in the 'birth and spread' model
$B_{agg,i}$	Total birth rate of particles in cell i via aggregation $[\#\ min^{-1}]$
$B_{growth,i}$	Total birth rate of particles in cell i via growth $[\#\ min^{-1}]$
B_i	Total birth rate of particles from all mechanisms in cell i (discrete) $[\#\ min^{-1}]$
$B_{i,p}$	Total birth rate of particles from all mechanisms in cell i as a result of event p (discrete) $[\#\ min^{-1}]$
B_{ind}	Induction time model constant
$B_{ind}{}'$	Induction time model constant
$B_{nuc,i}$	Total birth rate of particles in cell i via nucleation $[\#\ min^{-1}]$
B_0	Nucleation rate $[\#\ min^{-1}]$
C_D	Particle drag coefficient
C_i	Concentration of species i
D	Total particle death rate from all mechanisms (continuous) $[\#\ min^{-1}]$
$\boldsymbol{\mathcal{D}}$	Diffusivity $[m^2\ min^{-1}]$
$D_{agg,i}$	Total death rate of particles in cell i via aggregation $[\#\ min^{-1}]$
$D_{growth,i}$	Total death rate of particles in cell i via growth $[\#\ min^{-1}]$
D_i	Total particle death rate from all mechanisms in cell i (discrete) $[\#\ min^{-1}]$
$D_{nuc,i}$	Total death rate of particles in cell i via nucleation $[\#\ min^{-1}]$
$D_{reactor}$	Reactor diameter $[m]$

E_f	Absolute error in a predicted variable f
$\widehat{E_f}$	Normalised absolute error in a predicted variable f
$E(t)$	Exit age distribution $[s^{-1}]$
g	Acceleration due to gravity $[m\ s^{-2}]$
G	Growth rate $[\mu m^3\ min^{-1}]$
G_L	Length based particle growth rate e $[\mu m\ min^{-1}]$
$H(x)$	Heaviside step/ unit step function
i	Index/ iterator
I	Ionic strength
j	Index/ iterator
k	Index/ iterator
k_{agg}	Aggregation rate constant $[L\ min^{-1}]$
k_g	Growth rate constant $[\mu m\ min^{-1}]$
k_{nuc}	Nucleation rate constant $[\#\ L^{-1}\ min^{-1}]$
K_{eq}	Speciation equilibrium constant
K_{sp}	Solubility product
L	Spherical equivalent particle diameter $[\mu m]$
L_e	Entry length $[m]$
n	Number density $[\#\ \mu m^{-1} L^{-1}]$
n_{agg}	Aggregation rate order
n_g	Growth rate order
n_{nuc}	Nucleation rate order
N	Particle number $[\#\ L^{-1}]$
p	Index/ iterator
P	Total number of events resulting in a birth in a cell
Q	Reactor flow rate $[m^3\ min^{-1}]$
r	Reactor radius domain $[m]$
$r_{struvite}$	Rate of struvite crystallisation $[mol\ min^{-1}]$
R	Reactor radius $[m]$
Re	Reynolds number of reactor
Re_{jet}	Reynolds number of mixer jet
Re_{mix}	Reynolds number of mixer
S_r	Supersaturation ratio of multi-component system
SI	Saturation index of multi-component system
t	Time $[min]$
$\bar{t}$	Mean residence time $[min]$
t_{ind}	Induction time $[min]$
T	Temperature $[K]$
v	Particle volume $[\mu m^3]$
$\bar{v}$	Average particle volume $[\mu m^3]$
$v_{settling}$	Particle settling velocity $[m\ min^{-1}]$
v_z	Fluid velocity along the reactor length $[m\ min^{-1}]$
$\overline{v_z}$	Average fluid velocity along the reactor length $[m\ min^{-1}]$
v_m	Molecular volume $[cm^3]$
v_{MAP}	Particle velocity along the reactor length $[m\ min^{-1}]$
V	Reactor volume $[m^3]$
$V_{agg,i}$	Total volume of particles born into cell i via aggregation $[\mu m^3\ min^{-1}]$
$V_{growth,i}$	Total volume of particles born into cell i via growth $[\mu m^3\ min^{-1}]$
$V_{nuc,i}$	Total volume of particles born into cell i via nucleation $[\mu m^3\ min^{-1}]$
x	Generalised distribution domain/internal physical property/coordinate

z	Reactor length domain $[m]$
Z	Reaction length $[m]$
Z_i	Charge of species i

Symbols:

Symbol	Variable
β	Aggregation kernel
β_0	Size independent aggregation kernel
δ	Dirac delta function
ϵ_f	Absolute measurement tolerance of variable f
γ	interfacial tension $[mJ.m^{-2}]$
γ_i	Activity coefficient of species i
γ_s	Interfacial tension $[N/m]$
μ_i	i^{th} moment of a particle size distribution
$\lambda_i^{\pm}(v)$	Weighting factor determining the fraction of births in a cell assigned to higher or lower cells
Ω	Saturation ratio
ρ_p	Particle density $[kg\ m^{-3}]$
ρ_f	Fluid density $[kg\ m^{-3}]$
σ^2	Residence time distribution variance
τ_{ind}	Induction time $[min]$
ν	Number of ions making up a salt

Chapter 1 Introduction

This chapter gives a background to the motivations for the investigations documented in this thesis. The importance of phosphorus is discussed, followed by a summary of existing supplies and consumption at various locations around the world. Focus is then narrowed to the role of struvite crystallisation in phosphorus recycling, highlighting research areas addressed in this thesis.

1.1 Nutrient stewardship

Phosphorus is critical for all life on the planet; it is a key element in DNA and the ATP energy cycle. Humans and animals obtain phosphate via the food they consume. Like oil, phosphorus is a finite resource, but unlike oil it has no alternative. The motivations for this research are concerned with the stewardship of phosphorus. That is, taking action to control the destination of phosphorus after its use so that it may be reused in the future.

Resource reuse is coupled with ideas of sustainability and resilience. In a truly sustainable system, resource reuse is complete and ideally the only resource allowed to exit a system is that which continuously enters – energy from sunlight. Resilience of a system is the capacity of a system to adapt to change while continuing to develop.[1] Ensuring system resilience requires an understanding of the self-organizing capacity of a system and the feedbacks within it. A continuously evolving system will increase its resilience when it is faced with disturbances or increase its efficiency when it is not. When a system is not faced with disturbances, its resilience may decrease. On a global scale disturbances caused by resource depletion are yet to be seen.

---

[1] http://www.stockholmresilience.org/research/resilience-dictionary.html

Since the industrial revolution, oil, water and fertilisers have been in constant supply, allowing humans to develop highly efficient and networked food production systems. Market forces are the primary mechanisms used to manage production, and while they can allow the food production system to adapt to find the most cost effective solution, they are reactionary and do not attribute value to environmental or social degradation. Environmental degradation may not be immediately costly, but recent estimates suggest that the value of services provided by natural ecosystems is nearly double that of global GDP (Costanza et al., 2014). Socially, short term fertiliser price spikes can cause civil unrest due to unaffordable food as seen in 2008 (Berazneva & Lee, 2013; Mittal, 2009) and long term resource shortages often contribute to conflicts (Klare, 2012; Nillesen & Bulte, 2014). Perhaps it would be wise to nurture a smooth revolution to sustainable and resilient food supply systems, after all "there are only nine meals between mankind and anarchy" (Lewis, 1906).

Impacts of geographical distributions of resources and increasing transport costs can be attenuated by localising food supply. External cost fluctuations can be buffered by minimising resource consumption and improving local supply. For the case of phosphorus fertilisers, this can be achieved by reducing the demand for phosphorus intensive agriculture, increasing efficiency of phosphorus use and increasing phosphorus recycling from points of losses within the system. This research focuses on developing an improved understanding of phosphorus recycling technology.

1.2 Phosphorus reserves and fluxes

Nitrogen, phosphorus and potassium, commonly known as NPK in the fertiliser industry, are macro-nutrients essential for all plant growth and therefore a vital part of global food production. Each of these nutrients undergoes biological and geological cycles. An understanding of the phosphorus cycle provides a basis for the need for phosphorus recycling.

On average, 90.73% of phosphorus resides as deep ocean sediment and 8.54% in ocean surface waters (<300m deep), leaving only 0.73% available on land. Of the phosphorus on land, 76.6% occurs in plant matter, 10.6% in marine plant matter, 5.8% in animal matter, 6.6% in soil and 0.4% in humans (Smil, 2000). This leaves a small fraction of phosphorus available for use as a mineral fertiliser. Within the soil, 83% of phosphorus occurs in its inorganic form, which is quickly fixed into a highly insoluble form (*e.g.* $AlPO_4$, $FePO_4$, $Ca_5(PO_4)_3OH$ and $Ca_5(PO_4)_3F$) making much of the phosphorus in soil unavailable to plants at a given point in time (Smil, 2000). Increased phosphorus concentrations in agricultural land may reduce future demand (Van Vuuren, Bouwman, & Beusen, 2010), but a better understanding of the interactions between phosphorus and soil is required to properly model these fluxes (Dumas, Frossard, & Scholz, 2011).

The geological processes which transport phosphorus mineral deposits from ocean sediment to the earth's surface operate on a timescale of tens to hundreds of millions of years (Neset & Cordell, 2012). On a 1000-year timescale, phosphorus is currently a one way transition from mineral deposits to the ocean by mineralization, weathering, erosion and runoff. Modelling has suggested that 25% of phosphate rock mined flows to waterways (Van Vuuren et al., 2010), although losses to waterways are difficult to account for as very little data is available (Dumas et al., 2011). The increased flow of phosphorus (and nitrogen) into waterways as a result of various human activities is the subject of significant concern as they cause freshwater eutrophication and ocean dead zones (Ashley, Cordell, & Mavinic, 2011).[2]

Terrestrial phosphorus flows are relatively fast, occurring on a timescale of less than one year, and account for 10% of global phosphorus fluxes (Smil, 2000). Organic phosphorus fluxes account for 73% of terrestrial phosphorus movement while the remainder is due to erosion. Biological reuse is naturally

---

[2] Increased nutrient loads accelerate algal growth, stripping water bodies of oxygen, killing larger aquatic animals – in 2011, 530 dead zones had been identified with 228 additional sites exhibiting signs of eutrophication (http://www.wri.org/our-work/project/eutrophication-and-hypoxia). On release to land, nutrient bearing wastewater also causes soil acidification, leading to the death of plants and trees (R. Kumar & Pal, 2015). Recent estimates suggest that global nitrogen and phosphorus loads on the environment significantly exceed planetary boundaries and pose a high risk of a large scale ocean anoxic event and widespread eutrophication of localised freshwater systems (Steffen et al., 2015).

very efficient as phosphorus is recycled hundreds of times before leaving the system, although industrialized agriculture, where most mined phosphorus is used, is far less efficient.(Smil, 2000).

Global food production obtains 60% of its phosphorus requirements from rock phosphate (Cooper, Lombardi, Boardman, & Carliell-Marquet, 2011), which accounts for at least 80% - 90% of mined phosphorus (Neset & Cordell, 2012; Shu, Schneider, Jegatheesan, & Johnson, 2006). While the finite nature of phosphate rock has been of concern since as early as 1798 (Ashley et al., 2011), modern estimates of phosphorus reserves have been made since 1972 (Ashley et al., 2011; Van Vuuren et al., 2010). Peak in phosphate production has been predicted to occur between 2030 and 2040 and estimates of phosphate rock exhaustion vary from approximately 2100 to 2400 (Ashley et al., 2011; Van Kauwenbergh, 2010; Van Vuuren et al., 2010). Inconsistent estimates of viable reserves are due to various factors including inconsistent definition of the term 'reserves', non-disclosure of reserve estimates because of corporate secrecy and lack of independent assessments, decline in product quality, and uncertain production rates. Because of declining availability of high quality phosphate rock, it is estimated that phosphate production costs will increase by a factor of 3 – 5 fold in the coming century (Van Vuuren et al., 2010). These cost increases will inevitably result in increases in food costs globally, but localised price spikes can occur long before global reserve depletion due to disproportionate geographical distribution.

It is estimated that 70% of global phosphate production relies on reserves which will be depleted by 2100, increasing costs for countries like the US which will then rely solely on importation (Van Vuuren et al., 2010). China already takes steps to control domestic reserves – they hold the second largest phosphorus reserve, but control exports and were a net importer until 2006 (Persona, 2014). Approximately 77% of known global reserves are found in Moroccan occupied Western Sahara, a region historically contested for ownership.[3] By 2100, Morocco will need to increase production by

---

[3] Morocco currently. It had been under Spanish control since 1884 and was declared a province of Spain in 1934. After guerrilla insurgencies in the early 1970's by the native Sahawari's, the Polisario front, representing the Saharan people, was established on 10 May 1973. The Spanish relinquished control of the region due to pressure

700% to meet global demands, accruing an 80% market share of global production and an 89% share of global reserves (Cooper et al., 2011).

Considering declining phosphate rock quality, geographical imbalances, an emerging monopoly, and eutrophication risks, phosphorus is evidently a strategic element for the security of food supply and aquatic environments of many countries. Consequently, is broadly agreed that there should be a concerted effort to increase efficiency in phosphorus mining and use (Cooper et al., 2011; Van Kauwenbergh, 2010; Van Vuuren et al., 2010). This can be addressed by taking a number of steps including reducing fertiliser use, reducing losses from agricultural and food systems, reduction of livestock as a food source, and increased phosphorus recycling from human and livestock wastewater. This work focusses on the latter.

Currently phosphorus is not recycled significantly within the use chain - 90% of phosphorus mined is used for food production and only 17% of that makes it to human consumption. Human and livestock effluents account for 15% and 40% of mined phosphorus, respectively (Cordell, Drangert, & White, 2009). Point losses of interest include food processing, digested sewerage sludge, landfill leachate, semi-conductor wastewater, human urine, dairy and piggery wastewater, feedlot run-off, coal power plants, leather industries, paper pulp industries, construction sites and mines (Cordell, Neset, & Prior, 2012; R. Kumar & Pal, 2015).

Phosphorus removal options include biological accumulation (bacteria or algae), chemical coagulation and flocculation (usually iron or aluminium based), ion adsorption, solvent extraction, plant extraction, membrane filtration, and magnetic separation (Mehta, Khunjar, Nguyen, Tait, & Batstone, 2014). Further processing is often required to release phosphorus before it can be recovered. Struvite

---

from Morocco and Mauritania. Territorial claims by both. Morocco and Mauritania were rejected by the international court of justice (October 16 1975) and later the UN (Corell, 2002). Violent conflict continued between Morocco and the Polisario front, resulting in 10,000 – 20,000 deaths. A cease fire was signed on 6 Sep 1991. Since then various UN brokered attempts at resolutions have been successful (BBC News Africa, 2014; New Internationalist Magazine, 1997).

($MgNH_4PO_4 \cdot 6H_2O$) precipitation is a common method of phosphorus recovery because waste streams often contain an excess of NH_4^+ and only require the addition of Mg^{2+} and minor pH adjustment to alkaline conditions to achieve crystallisation.

1.3 Struvite crystallisation

This section gives an overview of struvite crystallisation motivations, economics, and areas for improvement. For the interested reader, more detailed struvite crystallisation reviews are available on modelling techniques (Le Corre, Valsami-Jones, Hobbs, & Parsons, 2009), nucleation kinetics (Galbraith & Schneider, 2009b), and industrial scale implementation (R. Kumar & Pal, 2015; Le Corre et al., 2009; Md. Mukhlesur Rahman et al., 2014; Tao, Fattah, & Huchzermeier, 2016).

1.3.1 Why struvite?

Struvite crystallisation ranks higher than other technologies because of its simplicity, cost effectiveness, and safety (Mehta et al., 2014). Additionally, struvite crystallisation leaves contaminants like hormones, pharmaceuticals and heavy metals remain in solution, allowing it to be applied directly as a fertiliser (Kataki, West, Clarke, & Baruah, 2016b; Ronteltap, Maurer, & Gujer, 2007b).

Struvite was identified as a leading alternative to fossil-based mineral fertilisers when compared to other waste streams (Sigurnjak, Crappé, Michels, & Meers, 2015), although it cannot be used alone as it does not deliver the correct nutrient ratios and may affect availability of other nutrients (Kataki, West, Clarke, & Baruah, 2016a; Md M Rahman, Liu, Kwag, & Ra, 2011). It is sparingly soluble (≈0.02g/100mL H_2O (Kataki et al., 2016a)) and has a high specific gravity (≈1.7), making it ideal as a slow release fertiliser as it is unlikely to be solubilized or washed away during rain events. Low solubility also results in lower nitrogen leaching rates (1.99%) than conventional superphosphate/urea mixes (7.14%), resulting in greater efficiency and sustained nitrogen supply (Md M Rahman et al., 2011). A recent study has also shown that plants are able to solubilize struvite as a nutrient source (Ahmed et al., 2015). In comparison to traditional phosphorus fertilisers, di-ammonium phosphate

(DAP) and triple super phosphate (TSP), struvite provides lower initial phosphorus supply, but equivalent rates of P uptake, yield and apparent fertiliser recovery at harvest (Talboys et al., 2015).

1.3.2 Economic potential

Struvite costs vary between locations but its recovery is generally economically viable, with production costs ranging from 140 – 460 USD/t (Forrest, Fattah, Mavinic, & Koch, 2008) and market values in the range of 198–1885 USD/t (Jaffer, Clark, Pearce, & Parsons, 2002; Ueno & Fujii, 2001). Some research has indicated that operational costs of struvite recovery marginally outweigh returns on sale but that reduced chemical consumption and sludge disposal costs compensate for this (Shu et al., 2006). Fluidisation energy (Paolo Battistoni, Paci, Fatone, & Pavan, 2005) and sale price (Shepherd, Burns, Raman, Moody, & Stalder, 2009) have been identified as economically limiting factors. Additionally, it has been asserted that the full potential of struvite as a fertiliser product can only be realised when particles are produced in a 3 – 5 mm size range, with sufficient hardness to be spread by a commercial fertiliser spreader (Adnan, Mavinic, & Koch, 2003; Forrest et al., 2008). The shape and size of a crystal particulate has a significant impact on the quality of the final product. Size enlargement is used to improve flowability, dispersibility, bulk density and dusting behaviour of a particulate (Wauters, Liu, & Meesters, 2001). Apart from chemical composition, flowability is the most important parameter of particulate fertilisers (Kohonen, Reinikainen, & Höskuldsson, 2009). As such, the ability to control the crystal size distribution (CSD) is of great value (A. Randolph & Larson, 1988). Although struvite crystallisation is economically feasible in some scenarios, efficiency and product quality improvements are necessary for it to become a default technology in wastewater treatment.

1.3.3 Industrial applications

Large-scale struvite recovery has been implemented in various locations around the world, with the fluidised bed reactor (FBR) being the most common method of recovery (P Battistoni, Paci, Fatone, & Pavan, 2006; Britton et al., 2005; Kazuaki Shimamura, Ishikawa, Tanaka, & Hirasawa, 2007). In these FBRs, fluid streams are mixed by submerged impinging jets, after which they flow upward through a fluidised crystal bed. Many struvite crystallisers operate in a semi-batch mode where crystals are intermittently harvested, while a stock of crystals is retained. Building the crystal stock to obtain an effective steady state operation, can take weeks to months to achieve (P Battistoni et al., 2006; Britton et al., 2005). Continuous seeding offers a means of reducing this time and improving reactor operation and control.

1.3.4 Effects of crystalliser seeding

Struvite seeding has been experimentally shown to improve recovery by 12% (Kim, Ryu, Kim, Kim, & Lee, 2007) and a semi batch seeding crystalliser has been utilised to smooth struvite FBR crystalliser operation and obtain better control over crystal size (Kazuaki Shimamura et al., 2007). The effects of seeding depend on seed loading and seed Particle Size Distribution (PSD), since these properties affect the surface area available for mass transfer For example, when seeds are initially added to a system, crystal mass deposition increases with increasing seed load (surface area). Then, at a certain seed loading, the rate of mass deposition becomes less dependent on crystal surface area and more dependent on the rate of change of reagents from liquid to crystal (Schneider, Wallace, & Tickle, 2013). At this point the system is reaction limited and able to accommodate increases in feed concentration at the highest rate possible. Therefore, introducing seeds reduces the time taken for an effective steady state to be achieved. Reactor simulations have also shown that increased struvite seed loading rate increases supersaturation buffering and decreases final particle size (Schneider et al., 2013). Struvite seed crystal sizes have varied from 30 to 500 µm, however further experimental investigations are necessary to determine optimum seed size and loading (Kataki et al., 2016a). No work to date has been published investigating continuous struvite seed production.

Systematic seed crystal design may enable tailoring of the final product PSD to achieve desired handling, packaging and dissolution properties. PSD can also be used as a process actuator[4] in system control (Nagy & Aamir, 2012). A common method of tailoring seeds to control PSD is to classify seeds

---

[4] A manipulated variable in a feedback loop

based on standard sieve sizes (Aamir, Nagy, & Rielly, 2010). Recently however, continuous seeding of a FBR has been shown to significantly influence output PSD (Binev, Seidel-Morgenstern, & Lorenz, 2015) and continuous seeding of a fed batch crystalliser has been shown to produce a controlled PSD (Jiang et al., 2012; Woo, Tan, & Braatz, 2011). As such, this research investigated the controlled production of struvite seeds.

1.3.5 Seed production methods

One method of continuous seed production that has become prominent in pharmaceutical production over the last two decades is rapid mixing and nucleation followed by a particle growth reactor. Rapid mixing creates uniform *SI*, causing more uniform nucleation rates and a narrower PSD than could be achieved in a well-mixed volume (Ferguson, Morris, Hao, Barrett, & Glennon, 2012). Confined impinging jets are most commonly used, while vortex mixers, shown in Figure 1.1, offer an alternative. Vortex mixers with two tangential feed streams at 180° are known as Roughton mixers. They can achieve five times shorter mixing times than Y-mixers for the same Reynolds number and are able to operate efficiently in situations where feed stream ratios and viscosities differ (Lindenberg & Mazzotti, 2009).

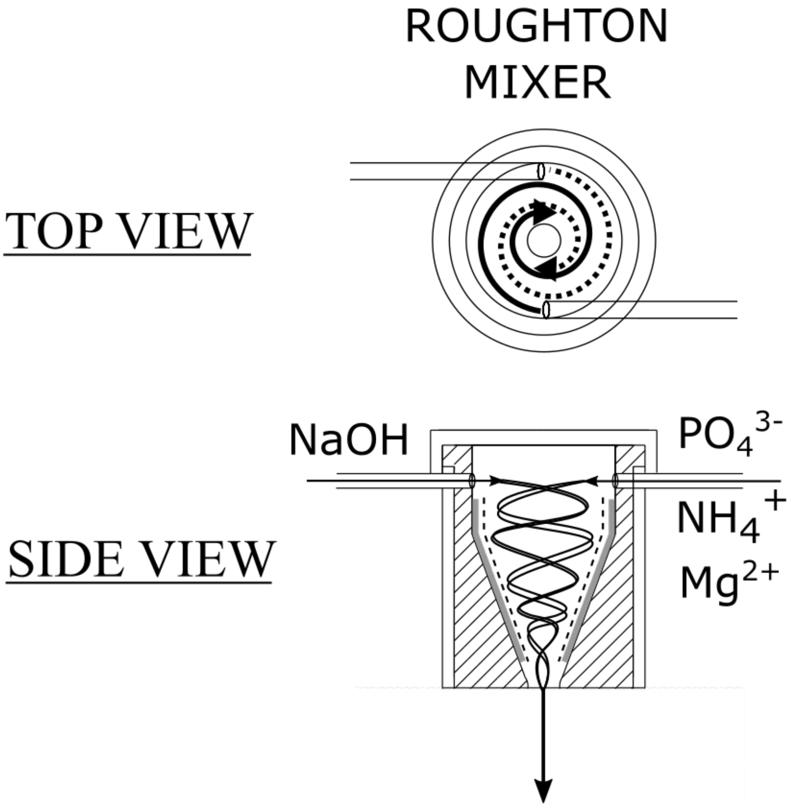

Figure 1.1 – Roughton mixer schematic

A plug flow (fully turbulent) section often follows the rapid mixing in order to sustain higher *SI* levels than could be achieved in back-mixed volumes. Plug flow crystalliser hydraulic residence times (HRT) reported in the literature vary significantly and depend on turbulence levels and crystallisation kinetics, each of which affects PSD output. Rigorous design of plug flow crystallisers is rarely described in detail, although reactor geometry is usually constrained by available supply pressures (Ferguson et al., 2012). Some work has utilised a short plug flow section after rapid mixing, followed by a continuously stirred tank reactor (CSTR) for subsequent crystal growth (Hacherl, Paul, & Buettner, 2003). Poiseuille flow, which describes fully developed laminar flow (Re<2000) in a cylindrical pipe, is a compromise between the two mixing regimes, offering a lower variance in HRT than a CSTR, while achieving pressure losses >10 times less than a plug flow system of the same residence time. Struvite crystallisation in Poiseuille flow has only been theoretically investigated for application to catheter encrustation (Band, Cummings, Waters, & Wattis, 2009). This work investigates a Poiseuille Flow

Reactor (PFR) as a novel means of continuously producing seeds for the struvite system, although results are applicable to any crystallisation system.

1.3.6 Modelling

Accurate struvite process model development is necessary for reactor design and optimisation. It facilitates sensitivity analysis on experimental variables (Schneider et al., 2013) and kinetic models (Galbraith, Schneider, & Flood, 2014). In recent years a focus has developed in the wastewater treatment industry for plant-wide modelling, with an increased focus on improved physico-chemical and chemical processes (Lizarralde et al., 2015). Development of accurate struvite crystallisation models contributes to this goal.

Model confidence relies on adequate model complexity and knowledge of kinetic and thermodynamic parameters. This sub-section provides an introduction to struvite modelling and associated gaps in the literature, while a detailed review of struvite modelling is provided in Chapter 2. Reaction equation 1.1 shows that three ions take place in struvite formation.

$$Mg^{2+}\,(aq) + NH_4^+(aq) + PO_4^{3-}\,(aq) + 6H_2O(l) \leftrightarrow MgNH_4PO_4 \cdot 6H_2O(s) \qquad 1.1$$

Key properties which must be described by a model are total recovery, PSD and rate of recovery. To describe these properties the model requires ‘hardware’ describing mass conservation and ‘software’ describing phenomenological relations like thermodynamics and kinetics. Thermodynamics describe the achievable recovery and the driving force for crystallisation, while kinetics describe the rate of crystallisation. Thermodynamics and kinetics are related by the supersaturation, which is a function of ion concentrations, described in this work by the saturation index, termed *SI* (equation 1.2).

$$SI = f\left(C_{Mg^{2+}}, C_{NH_4^+}, C_{PO_4^{3-}}\right) \qquad 1.2$$

The *SI* describes both the total recovery achievable and the driving force for crystallisation, which influences the rate of crystal formation via three concurrent mechanisms:

1. Nucleation – appearance of new particles

2. Growth – enlargement of existing particles
3. Aggregation – sticking together of particles

Each crystallisation mechanism influences the PSD, as shown by Figure 1.2.

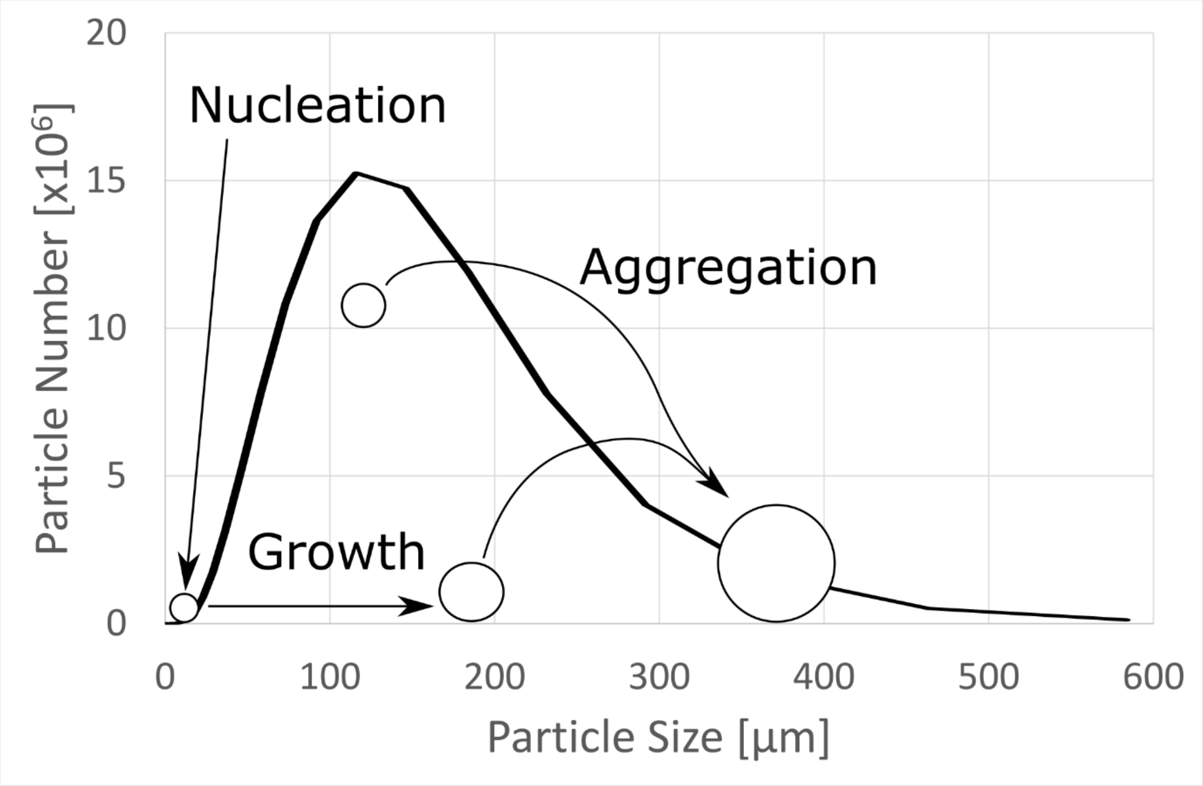

Figure 1.2 – PSD and crystallisation mechanisms

Struvite thermodynamic modelling, while complex, is well understood. Authors have applied various water chemistry software packages including PhreeqC (Ariyanto, Sen, & Ang, 2014; Bhuiyan & Mavinic, 2008; Ronteltap, Maurer, Hausherr, & Gujer, 2010; Sakthivel, Tilley, & Udert, 2012; Warmadewanthi & Liu, 2009), MinteqA2 (Golubev, Pokrovsky, & Savenko, 2001; Hanhoun et al., 2011; Nelson, Mikkelsen, & Hesterberg, 2003; Pastor, Mangin, Barat, & Seco, 2008), Minteql + (Bhuiyan, Mavinic, & Beckie, 2007; A. N. Kofina & Koutsoukos, 2005), ChemEQ L v 2.0 (Bouropoulos & Koutsoukos, 2000), and Aquasim 2.0 (Morales, Boehler, Buettner, Liebi, & Siegrist, 2013; Udert, Larsen, Biebow, & Gujer, 2003). Alternatively, others have developed their own water chemistry models, using the same thermodynamic relationships, to allow easy integration into larger process models (Ali & Schneider, 2008b; Galbraith & Schneider, 2014; Harada et al., 2006; Rahaman, Mavinic, Meikleham, & Ellis, 2014). Thermodynamic modelling has been carried out on various wastewater systems including swine and dairy wastewater (Celen, Buchanan, Burns, Bruce Robinson, & Raj Raman, 2007; Nelson et al., 2003), urine (Ronteltap, Maurer, & Gujer, 2007a; Sakthivel et al., 2012), anaerobic supernatant (Mehta & Batstone, 2013; B. N. Ohlinger, Young, & Schroeder, 2000), and synthetic solutions (Abbona & Boistelle, 1985; Ali & Schneider, 2008a; Bouropoulos & Koutsoukos, 2000; Buchanan, Mote, & Robinson, 1994; K. N. Ohlinger, Young, & Schroeder, 1998).

While thermodynamics are relatively well understood, struvite kinetic models vary widely in the literature, both in rate equation form and rate coefficient values (section 2.2). Assuming accurate measurement techniques, the causes of this variation are inaccurate model assumptions and/or oversimplifications. Some assumptions which have been made are:

- Model crystallisation is dependent only on liquid phase concentrations (neglecting particle surface area) (Bhuiyan, Mavinic, & Beckie, 2008; Bouropoulos & Koutsoukos, 2000; Le Corre, Hobbs, & Parsons, 2007a; Nelson et al., 2003; B. K. N. Ohlinger, Young, & Schroeder, 2000; Quintana, Sánchez, et al., 2005; Rahaman, Ellis, & Mavinic, 2008; Türker & Celen, 2007).
- A point distribution of particles exists, which does not change in number because
    - The reactor was seeded and nucleation and aggregation are assumed negligible (Ali & Schneider, 2008a; Mehta & Batstone, 2013; Rahaman, Mavinic, & Ellis, 2008)
    - Rapid nucleation occurs, followed by growth, assuming no aggregation (P. Battistoni, De Angelis, Prisciandaro, Boccadoro, & Bolzonella, 2002)
- Variables which affect crystallisation rate are not included in the model, most notably hydrodynamics (Koralewska, Piotrowski, Wierzbowska, & Matynia, 2009; Qu, 2003; Rahaman & Mavinic, 2009; Rahaman et al., 2014).

These assumptions make the problem easier to solve but introduce potentially significant uncertainty. It is evident throughout the literature that aggregation plays a key role in struvite formation, as detailed in section 2.2.5. Nucleation and growth have also been observed simultaneously, even at low supersaturation levels, where secondary nucleation is dominant (Galbraith et al., 2014; Mehta & Batstone, 2013).

To model any combination of nucleation, growth and aggregation simultaneously, a population balance model (PBM) is required. PBMs describe the total rate of change of particle number of a given size - they are described in detail in Chapter 3. Some struvite kinetic investigations have used PBM methods (Galbraith & Schneider, 2014; Hanhoun et al., 2013; Koralewska et al., 2009; Triger, Pic, & Cabassud, 2012). Of these works, only Galbraith's incorporated aggregation, however it made PSD assumptions for particles <2µm and applied a novel modelling approach which had not been analytically validated. He also found that kinetic parameters regressed simultaneously resulted in parameter correlation.

1.4 Research objectives

The following core objectives were addressed in this work:

1. Develop a dynamic reactor model capable of accurately predicting Poiseuille flow seed reactor operation
2. Perform sensitivity analysis to determine key input variables and kinetic parameters
3. Investigate continuous struvite seed production in a lab-scale novel Poiseuille flow crystalliser
4. Regress nucleation, growth and aggregation kinetic parameters using experimental and modelling work

The effects of supersaturation on PSD were a key focus of experiments. Supersaturation was selected as an independent variable, since this is the primary driving force for crystallisation and can therefore be used to drive kinetic models. PSD was measured because it is considered a key seed crystal property and is integral for mechanistic kinetic parameter regression. Particles down to 0.01µm were measured, overcoming the shortfall of Galbraith's work, which measured particles down to 2µm. This work examined a novel technique of decoupling the aggregation mechanism within experimental data, allowing its investigation separately, therefore improving confidence in the estimation techniques. The impact of vortex mixing on PSD was also investigated for comparison with traditional techniques.

Previous studies have reported struvite crystal growth rates ranging five orders of magnitude as a result of varying assumptions discussed in detail in section 2.2.4. To address this issue, this work placed great emphasis on accurate reactor modelling and struvite parameter estimation. This was achieved by integrating a new, high accuracy PBM technique with detailed hydrodynamic and thermodynamic models, and conducting model validation and sensitivity analysis to an extent not seen in struvite literature.

1.5 Thesis structure

In this thesis, the first three chapters detail varying levels of model development to create a reactor model, then the fourth chapter uses the model to examine reactor operation. Next, experimental investigations are presented, followed by sensitivity analysis, which combine to inform a chapter detailing parameter regression. Finally results and conclusions are presented. A summary of each chapter is presented below:

Chapter 2 – Review of struvite thermodynamic and kinetic modelling techniques – provides in-depth detail on how crystallisation thermodynamic and kinetic modelling techniques, of varying complexity, have been applied to struvite crystallisation. Struvite kinetic models are analysed on a common basis, enabling comparisons not previously presented in the literature. The insight gained is used to inform experimental and modelling design in the remainder of this thesis.

Chapter 3 – Population balance model development and validation – outlines a PBM technique not previously applied to struvite. Validations are then presented, ensuring model accuracy and confidence in subsequent analysis and parameter regressions.

Chapter 4 - Poiseuille flow crystalliser model development – presents the fluid flow model which was developed to achieve an acceptable level of accuracy in a minimal solution time. Model validation presented includes solution methods, scaling techniques and a grid convergence.

Chapter 5 – Poiseuille flow reactor simulations – combines mass balance, fluid flow, population balance and thermodynamic models to examine predicted reactor operation. This includes startup transients at the outlet and along the reactor length, steady kinetic parameters, PSDs, the velocity profile and expected residence time distributions

Chapter 6 – Poiseuille flow reactor design and testing – details the design and testing of the Poiseuille flow reactor. Design details include information on: supersaturation; reactor orientation, length and diameter; residence time and flow regime; and mixing characteristics. Experimental examinations include supersaturation and mixing regime. Information is presented on how sonication techniques were used to elucidate aggregation effects.

Chapter 7 – Poiseuille flow crystalliser sensitivity analysis – sensitivity of model outputs to known parameters is examined to remove unnecessary model complexity and improve model solution time. Sensitivity analysis is then used to show which input variables and yet to be estimated kinetic parameters have the greatest influence on output variables. This information is used to inform accurate parameter regression methods and can be used in future experimental designs.

Chapter 8 – Struvite kinetic parameter regression – Experimental results are used to regress nucleation, growth and aggregation kinetic parameters in the process model. Detailed discussion is presented on the parameter regression process including numerical methods, uncertainty, stability and parameter selection. Parameter regression results are then used to investigate the applicability of an alternative kinetic model.

Chapter 9 – Conclusions and recommendations – Summarises conclusions of the work performed in this thesis in the context of the existing literature. Recommendations are made based on these conclusions and ideas are presented for potential future investigations.

Appendix A. – Photomicrographs

Appendix B. – DPB formulations

Appendix C. – Population balance analytic solutions

Appendix D. – Derivation of advection, diffusion & reaction model and key process parameters

Appendix E. – gPROMS model code

Appendix F. – Grid convergence methods

Appendix G. – Supplementary batch experiments

Chapter 2 Review of struvite crystallisation

This chapter provides a background on solution chemistry and crystallisation kinetic modelling techniques, with a focus on identifying best practices for struvite. Differences in the literature are highlighted to eliminate the possibility of false comparisons. Significant uncertainties are evident in struvite nucleation models, suggesting that a power law model may be as effective as any other model form. Comparisons of nucleation and growth rates show large variations across the literature, which are suspected to be due to oversimplified model formulations. Additionally, struvite agglomeration is identified as an area which has not yet been thoroughly investigated. A detailed summary of key findings is presented at the conclusion of this chapter.

2.1 Solution chemistry modelling

Thermodynamics of a chemical system refers to the interrelation of heat and work to the reactions occurring in the system. This includes the effects of temperature, pressure, concentration, ionic dissociation and ion interactions. It is the sum of all of these factors which determines whether it is energetically favourable for a phase change from aqueous to solid to occur *i.e.* crystallisation. By properly understanding and modelling thermodynamic interactions, it is possible to predict the driving force for crystallisation. This can then influence predictions of the rate at which crystallisation occurs.

2.1.1 Real solution effects

The activity (a_i) of a species i in solution represents its effective concentration as a result of molecular and/or ionic interactions. Activity coefficients (γ_i) are used to relate the activity and concentration (C_i) of species i, as shown in equation 2.1:

$$a_i = \gamma_i C_i \tag{2.1}$$

For sparingly soluble salts, average activity coefficients are used for all species of a particular valency. The DeBye-Hückel relationship with Davies approximation (equation 2.2) can be used to determine average activity coefficients for any ion of a particular charge. In this equation, A is the Debye-Hückel constant (0.59 at 25˚C), z_i is the valency of the species, a and b are constants, and I is the ionic strength [mol/L], which describes the total concentration of ions in solution and is defined by equation 2.3.

$$-log(\gamma_i) = A{z_i}^2\left(\left[\frac{\sqrt{I}}{1 + a\sqrt{I}}\right] - bI\right) \tag{2.2}$$

$$I = \frac{1}{2}\sum_i C_i {Z_i}^2 \tag{2.3}$$

The upper limit of ionic strength for equation varies depending on the source. Davies originally proposes that $a = 1$ and $b = 0.2$ and that the relationship is valid up to $I < 0.1$ (Davies, 1932). Later Davies proposed the more commonly used coefficient values of $a = 1$ and $b = 0.3$. For the latter version, Mullin suggests that the equation holds up to $I < 0.2M$ (Mullin, 2001), Stumm & Morgan suggest a limit of $I < 0.5$ (Stumm & Morgan, 1996), and Sohnel and Garside suggest an upper limit as high as $I < 1.0M$ (Sohnel & Garside, 1992). Research on struvite thermodynamics in urine claims that the DeBye-Hückel equation with Davies approximation is accurate up to $I < 0.5$ M (Ronteltap, Maurer, & Gujer, 2007). On this basis, this work assumes an ionic strength upper limit of 0.5 M.

2.1.2 Equilibrium

In any crystal system, the compounds in the crystalline lattice are continually moving into and out of solution. When the rate of these processes are equal, the system is at equilibrium. The driving force for this process depends only on the concentration of ion in solution and not on the solid crystal mass.

This means that crystal equilibrium is modelled differently to chemical equilibrium involving multiple liquid or gas phases – the solid concentration is omitted from the description, as a pure solid has an activity of 1 (equation 2.5).

2.1.3 Solubility and supersaturation

Solubility describes the amount of a solid that can be dissolved into a liquid at equilibrium, at a fixed set of conditions (*e.g.* temperature, pressure and pH), while supersaturationdescribes the amount of a compound dissolved in solution relative to saturation. A solution in contact with a crystal can be over or under-saturated but will tend towards equilibrium with time. The difference between the supersaturation and saturation (described by the solubility) is the driving force for precipitation (supersaturation) or dissolution (undersaturation). A greater driving force results in faster precipitation processes. Describing this driving force is the focus of thermodynamic modelling detailed here. All of the factors discussed below are important because they allow the accurate description of saturation.

In order to describe the degree of supersaturation, a description of solubility is necessary. In the simplest case, where a single ionic solute is being dissolved in a solvent with no other compounds present, solubility can be described using the concentration of the species resulting from the dissolution of the solid phase, at equilibrium. This is known as the concentration solubility product (K_{sp}) (Mullin, 2001). Given the following general reaction:

$$M_xA_y \rightleftharpoons xM^{y+} + yA^{x-} \tag{2.4}$$

Where x and y are the stoichiometric numbers and correspond to the ion valencies, then for a saturated solution:

$${C_M}^x {C_A}^y = K_{sp} = constant \tag{2.5}$$

The expression involving concentration is only applicable for solutions of total ion concentration less than 0.001M (Mullin, 2001). In scenarios where ionic strength is greater than this value, concentrations are replaced with activity coefficients. This is the case even if, as in the case of this research, the precipitate in question is sparingly soluble. This is because foreign ion concentration can create higher ion concentration (*i.e.* ionic strength, given by equation 2.3) than if only the solute were dissolved in the solvent. In the scenario where activities are used in place of concentration, the solubility is designated K_a, where a indicates activity. This value can deviate significantly from the actual solubility as a result of changes in solution phase species concentrations.

Supersaturation can be described in many ways depending on the derivation and application. Various descriptions are provided below to help the reader understand the importance of clarity when describing precipitation. It should be noted that there is little consistency in symbol use and terminology in crystallisation texts and research papers, making it an imperative that the reader is always aware of the description being used (Jones, 2002; Mullin, 2001; Sohnel & Garside, 1992). In this work, terminology and symbols for crystallisation fundamentals are adopted from work by Mullin (Mullin, 2001). In addition, this work takes other terminologies specifically relevant to recent research on struvite crystallisation. For a compound where driving force for crystallisation depends on only one species in solution, the difference between the concentration (C) and the equilibrium concentration (C_{eq}) can be used to describe supersaturation (ΔC[5]):

$$\Delta C = C - C_{eq} \qquad 2.6$$

This description is applicable when a compound is precipitating only with itself (*e.g.* sugar), or where the rate depends primarily on a single limiting reactant Various examples of this approach exist in the struvite literature (Le Corre, Hobbs, & Parsons, 2007a; B. N. Ohlinger, Young, & Schroeder, 2000; Rahaman, Ellis, & Mavinic, 2008). An alternative description uses a supersaturation ratio rather than a difference (Mullin, 2001). This has been denoted using the variable S by Mullin and S_r by Sohnel and Garside (Sohnel & Garside, 1992). Here we will use S_r^* to distinguish from later variables:

---

[5] The concentration difference ΔC is sometimes interchanged with the variable S.

$$S_r^* = \frac{C}{C_{eq}} \tag{2.7}$$

Combining equations 2.6 and 2.7 gives what is termed an absolute supersaturation, S_a^* (Mullin, 2001), or relative supersaturation, σ (Jones, 2002). The difference in terminology here highlights the inconsistencies between texts.

$$S_a^* = \sigma = \frac{C - C_{eq}}{C_{eq}} = S - 1 \tag{2.8}$$

These descriptions become slightly more complex in multi-ionic systems because the ratios of species contributing to precipitation can vary. This problem is dealt with by introducing a term similar to the concentration solubility product presented in equation 2.5, but at non-equilibrium conditions. For scenarios where non-ideal solution thermodynamics occur, concentrations are replaced with ion activities and the variable is termed an ion activity product (IAP), which as its namesake suggests, is the product of the activities of ions in the system. Supersaturation is then defined by the IAP relative to itself at saturation (K_{sp}), where the subscript sp denotes 'solubility product'. Alone, this is termed the supersaturation ratio (equation 2.9), represented by both Ω and SSR in the literature. Various researchers have utilised this description when analysing struvite precipitation (Bhuiyan, Mavinic, & Beckie, 2009; Fattah, Mavinic, Koch, & Jacob, 2008).

$$\Omega = \mathrm{SSR} = \frac{IAP}{K_{sp}} \tag{2.9}$$

Alternatively, supersaturation (termed absolute or relative) is often defined by equation 2.10 (Jones, 2002; Mullin, 2001):

$$S_a = \sigma = \Omega^{1/\nu} = \left(\frac{IAP}{K_{sp}}\right)^{1/\nu} \tag{2.10}$$

Where ν is the number of ions which make up the salt, which in the case of struvite crystallisation is 3; Mg^{2+}, NH_4^+ and PO_4^{3-}. This description was applied in the struvite crystallisation study which produced the most commonly used K_{sp} value (K. N. Ohlinger, Young, & Schroeder, 1999). The relative supersaturation for struvite has also been presented using equation 2.11 (Bhuiyan, Mavinic, & Beckie, 2008), which combines supersaturation descriptions given in equations 2.10 and 2.8. This formulation is only presented here for the reader's awareness while assessing the literature and will not be used in this work. It is interesting to note though that descriptions of struvite saturation vary even within individual research groups.

$$S_r = \Omega^{1/3} - 1 \tag{2.11}$$

Another alternative description, which is only listed here due to its specific use in some struvite investigations (Hanhoun et al., 2013), defines saturation as the difference between IAP and K_{sp} including the inverse power of the number of ions (equation 2.12). This has been termed S_h here for distinction between other saturation definitions.

$$S_h = IAP^{1/3} - K_{sp}^{1/3} \tag{2.12}$$

The description of supersaturation used in this work is the saturation index (SI), which has been adopted by many struvite research groups (Ariyanto, Sen, & Ang, 2014; Bhuiyan & Mavinic, 2008; Galbraith & Schneider, 2014; Tilley, Gantenbein, Khadka, Zurbrügg, & Udert, 2009; Jiansen Wang, Song, Yuan, Peng, & Fan, 2006; Warmadewanthi & Liu, 2009), is given by equation 2.13.

$$SI = \log_{10}\left(\frac{IAP}{K_{sp}}\right) \tag{2.13}$$

An alternative formulation, given by equation 2.14 has also been used by some authors (Ali & Schneider, 2008; Triger, Pic, & Cabassud, 2012). Expression of the saturation on a log scale overcomes many numerical issues associated with calculating species concentrations with differences of many orders of magnitude between them. This description is also beneficial in that it describes the interactions of all ions driving crystallisation by using the IAP and K_{sp}, and has the property that (like equation 2.11) it is equal to zero when saturation is reached. This is important when incorporating the description of supersaturation into crystal growth mechanism rate functions. Ultimately, it is only important to ensure that differences in saturation descriptions are accounted for when making comparisons and that rate coefficients are adjusted accordingly.

$$SI = \log_{10}\left(\frac{IAP}{K_{sp}}\right)^{1/3} \qquad 2.14$$

2.1.4 Ion speciation

Ions in solution interact to create many different species, each of which is in equilibrium with all other species. The degree to which each species forms is determined by the equilibrium reaction for its formation. The equilibrium constants for each reaction associated with struvite formation are given in Table 2.1.

Table 2.1 – Species expected to form in a system containing water, magnesium, ammonium and phosphate ions

Species	Equilibrium Equation and Constant ($\boldsymbol{K_{eq}}$)	Reference
$\boldsymbol{HPO_4^{2-}}$	$\frac{a_{H^+} \times a_{PO_4^{3-}}}{a_{HPO_4^{2-}}} = 10^{-12.35}$	(Morel and Hering 1993)
$\boldsymbol{H_2PO_4^-}$	$\frac{a_{H^+} \times a_{HPO_4^{2-}}}{a_{H_2PO_4^-}} = 10^{-7.20}$	(Morel and Hering 1993)
$\boldsymbol{H_3PO_4}$	$\frac{a_{H^+} \times a_{H_2PO_4^-}}{a_{H_3PO_4}} = 10^{-2.15}$	(Martel and Smith 1989)
$\boldsymbol{MgPO_4^-}$	$\frac{a_{Mg^{2+}} \times a_{PO_4^{3-}}}{a_{MgPO_4^-}} = 10^{-4.80}$	(Martel and Smith 1989)
$\boldsymbol{MgHPO_4}$	$\frac{a_{Mg^{2+}} \times a_{HPO_4^{2-}}}{MgHPO_4} = 10^{-2.91}$	(Martel and Smith 1989)
$\boldsymbol{MgH_2PO_4}$	$\frac{a_{Mg^{2+}} \times a_{H_2PO_4^{2-}}}{a_{MgH_2PO_4}} = 10^{-0.45}$	(Martel and Smith 1989)
$\boldsymbol{MgOH^+}$	$\frac{a_{Mg^{2+}} \times a_{OH^-}}{a_{MgOH^+}} = 10^{-2.56}$	(Childs 1970)
$\boldsymbol{NH_4^+}$	$\frac{a_{NH_3} \times a_{H^+}}{a_{NH_4^+}} = 10^{-9.25}$	(Taylor, Frazier et al. 1963)

$\boldsymbol{H_2O}$	$\frac{a_{OH^-} \times a_{H^+}}{a_{H_2O}} = 10^{-14}$	(Harris 2003)

The system of equations was solved using logarithmic scaling, for example:

$$\log_{10}(a_{H^+}) + \log_{10}(a_{PO_4^{3-}}) - \log_{10}(a_{HPO_4^{2-}}) = -12.35 \qquad 2.15$$

It should be noted that during simulations performed in this work, numerical solutions were more difficult to find (*i.e.* long initialisation times) when H_3PO_4 was included since its concentration is very low at high pH. Concentrations very close to zero can be rounded to zero, causing the Davies approximation to raise zero to a negative power. This problem was resolved by removing this species as it did not affect the mass balance to any discernible extent.[6]

2.1.5 Temperature

Changes in temperature affect struvite solubility and ion species equilibria. For each equilibrium constant (from Table 2.1), the temperature change effects can be modelled using the Van't Hoff equation:

$$\ln(K_{eq}) = -\frac{\Delta H}{RT} + \frac{\Delta S}{R} \qquad 2.16$$

Where ΔH is the enthalpy of reaction, ΔS is the change in entropy, $R = 8.234\ [J\ mol^{-1}\ K^{-1}]$ is the ideal gas constant, and $T\ [K]$ is temperature.

Various investigations have been conducted on the effects of temperature on struvite solubility product (Aage, Andersen, Blom, & Jensen, 1997; Bhuiyan, Mavinic, & Beckie, 2007; Burns & Finlayson, 1982; Hanhoun et al., 2011), although they each involve the use of different sets of ionic species and equilibrium coefficients, making comparisons difficult. Recent investigations, involving more detailed thermodynamic modelling techniques are in agreement that a minimum solubility is reached at approximately 30˚C (Bhuiyan et al., 2007; Hanhoun et al., 2011). Bhuiyan *et al.* determined that the

---

[6] Initialising with guess values very close to the solution also improves the likelihood of obtaining a solution

minimum solubility product to be $pK_{sp} = 13.17 \pm 0.05$ by dissolving it into water, while Hanhoun *et al.* used an optimisation simulation based on the temperature dependent expression for free energy, which predicted the minimum solubility product to be $pK_{sp} = 13.00 \pm 0.04$. These figures are very close, making them effectively the same.

Since a non-linear relationship exists between $\ln(K_{sp})$ and $1/T$, equation 2.14 is not suitable for modelling struvite K_{sp}. This is because enthalpy and entropy of struvite crystallisation are also a function of temperature. Struvite K_{sp} must therefore be modelled as a higher order function of temperature, for example:

$$\ln(K_{sp}) = a' + \frac{b'}{T} + \frac{c'}{T^2} \qquad 2.17$$

Where a, b and c absorb the enthalpy, entropy and gas constant terms.

In this work, the solubility of struvite is assumed to be $\log_{10}(K_{sp}) = -13.26$ at 25° (corresponding to all experimental conditions. This avoids any uncertainties associated with temperature variations.

2.1.6 Electroneutrality and pH

Although gradients of electrical charge may exist within a system, as a whole, any solution is electrically neutral. By knowing the concentration and valency of each ion in solution, a charge balance can be written:

$$0 = \sum C_i Z_i \qquad 2.18$$

Where Z_i is the valency of component i. The electro-neutrality condition completes the thermodynamic model, allowing for supersaturation and pH predictions to be made with only the knowledge of ion concentrations. Converting pH from a model input variable to a predicted variable is very important as it and enables kinetic parameter regression based on pH. However, it is important to distinguish between speciation based pH prediction and reaction equation based pH prediction, which includes hydrogen in the crystallisation reaction equation as shown in equations 2.19 and 2.20, which have been asserted by some researchers with the aid of a thermodynamic model (Bouropoulos & Koutsoukos, 2000; Jun Wang, Burken, & Zhang, 2006) and by various other without a thermodynamic model (Koralewska, Piotrowski, Wierzbowska, & Matynia, 2007; Le Corre, Hobbs, & Parsons, 2007b; Matynia, Koralewska, & Wierzbowska, 2006; Stratful, Scrimshaw, & Lester, 2001; Zeng & Li, 2006).

$$Mg^{2+} + NH_4^+ + HPO_4^{2-} + 6H_2O \rightleftharpoons MgNH_4PO_4 \cdot 6H_2O + H^+ \qquad 2.19$$

OR

$$Mg^{2+} + NH_4^+ + H_2PO_4^- + 6H_2O \rightleftharpoons MgNH_4PO_4 \cdot 6H_2O + 2H^+ \qquad 2.20$$

Applying this approach without a thermodynamic model is erroneous because changes in pH occur when ion concentrations change and thermodynamic equilibriums adjust to maintain electroneutrality. As a result, pH sensitivity to crystal formation can vary drastically between systems with different ionic concentrations and ionic ratios. This does not mean that pH can’t be used, but that non-ideal thermodynamic modelling must be applied to describe its effect correctly. This method was applied in this work.

2.2 Crystallisation kinetics

In a supersaturated system, crystallisation occurs and the solution equilibria change. The rate of solution equilibria formation is much higher than that of crystallization. As a result, they can be accurately represented by the algebraic equations presented earlier in this chapter. The rate at which crystalline lattice forms is proportional to the level of supersaturation (the driving force for crystallisation). As discussed earlier, the level of supersaturation is determined by the equilibria formed in solution and the solubility of struvite. The subject of this section is to examine how the crystallisation rate is influenced by supersaturation and how this relationship has been modelled.

Interestingly, a positive driving force for crystallisation (supersaturation) does not necessarily imply that crystal formation will occur within any immediate time interval. As supersaturation is increased, there first exists what is termed a meta-stable range, in which the driving force is too low to initiate spontaneous crystal formation. Often crystallisers are operated in this range to achieve growth of existing crystals without introducing new smaller crystals to the system. As supersaturation is further increased there is a gradual transition into what is known as the labile range, where spontaneous crystallisation occurs. Interpretation of what is ‘spontaneous’ remains open, leaving any specific transition indistinct. Instead, the transition from metastable to labile is described by a logarithmically reducing time interval between when a given supersaturation is reached and spontaneous crystal nucleation begins. This interval is known as the induction time and is the subject of the next section.

2.2.1 Induction time

Theoretically, induction time can be defined as the time taken from the creation of supersaturation to the onset of nucleation. The molecular process of crystal nuclei formation is not known with any degree of certainty, making the exact definition of induction time difficult. Ions must coagulate, resist the tendency to re-dissolve, and become oriented into a fixed crystalline lattice (Mullin, 2001). Practically, the definition of the appearance of nuclei is dependent on the method of particle detection. Jones defines induction time to consist of the time taken for nuclei formation plus the time taken for nuclei to grow to a detectable size (Jones, 2002), while Mullin also includes a relaxation time for ions to evenly diffuse through the system and describes an extra ‘latent period’ between the induction time and the time of detectable de-supersaturation (Mullin, 2001). Induction time models are widely based on the concept that induction time is inversely proportional to nucleation rate:

$$t_{ind} \propto B_0^{-1} \qquad 2.21$$

Where t_{ind} is the induction time and B_0 is the nucleation rate. All struvite induction time studies assume that nucleation time is much greater than subsequent growth time, causing induction time to be defined as the time needed for the formation of a critical nucleus. In reality, this time cannot be measured and the induction time should be modelled as the time taken for a particle to grow to a detectable size. Jones gives various models for this scenario based on different crystal growth mechanisms (Jones, 2002).

Two forms of the induction time model have been applied to struvite by various research groups. They differ by their representation of saturation but are otherwise equivalent. Bouropoulos & Koutsoukos (Bouropoulos & Koutsoukos, 2000) and Bhuiyan (Bhuiyan & Mavinic, 2008) both used equation 2.22, which was given by Mullin (Mullin, 2001). This form of the equation uses Ω, given by equation 2.9, as the measure of supersaturation.

$$\log \tau_{ind} = \log A_{ind} + \frac{B_{ind}}{(\log \Omega)^2} \qquad 2.22$$

Where A is constant and B is given by:

$$B_{ind} = \frac{\beta v_m^2 \gamma_s^2}{(2.303 k_B T)^3} \qquad 2.23$$

Where β is a nucleus shape factor (32 for cubes and $16\pi/3$ for spheres), v_m is the molecular volume of struvite (=molecular weight/(Avogadro's number × density × number of ions in a formula unit) = 7.95×10^{-23}cm^3 for struvite), γ_s is the interfacial tension (*i.e.* surface energy) of the solid which is forming, k_B is the Boltzmann constant and T is the absolute temperature. Other groups have also used equation 2.24 which uses S_a, described by equation 2.10, as the measure of saturation (Galbraith & Schneider, 2009; Mehta & Batstone, 2013; K. N. Ohlinger et al., 1999).

$$\log \tau_{ind} = \log A_{ind} + \frac{B_{ind}'}{(\log \mathrm{S_a})^2} \qquad 2.24$$

Where again A is constant and B is identical, accept in this instance includes the number of ions into which a molecule of the crystal dissociates, ν, which accounts for the different measure of saturation:

$$B_{ind}' = \frac{\beta v_m^2 \gamma_S^3 f(\theta)}{(2.303 k_B\, T)^3 \nu^2} \qquad 2.25$$

In equation 2.25, $f(\theta)$ is a correction factor to account for heterogeneous nucleation. θ is the wetting angle of the solid phase by the liquid, where $f(\theta) = 1$ for homogeneous nucleation. This model has been applied successfully to heterogeneous nucleation (K. N. Ohlinger et al., 1999; A. Randolph & Larson, 1988).

Although homogeneous nucleation is asserted during measurements of induction time, heterogeneous primary nucleation (induced by suspended particles) is much more likely, both in lab environments and in real solutions. This is especially true at low supersaturation levels. Many authors have identified a supersaturation level where homogeneous nucleation ceases to occur (summarised in Table 2.2). The transition between homogeneous and heterogeneous nucleation is commonly defined as the intersection of two linear regressions made on a $(\log(\Omega))^{-2}$ vs. $\log(t_{ind})$ plot. Views of the accuracy of this technique are undecided; Mullin suggests that applying the homogeneous induction time model at low supersaturations is a questionable technique, while Randolph & Larson and Ohlinger assert that it is acceptable.

Many investigations have been made into struvite induction time, the results of which vary depending on experimental methods and analysis techniques. Table 2.2 provides a consolidation of induction time models, which shows that the lower saturation bound for homogeneous nucleation has been predicted to occur anywhere in the range of $SI = 0.237 - 0.69$ (Table 2.2). Figure 2.1 then provides a comparison of model predictions of induction times over a range of SI values. This was done using methods described by Galbraith (Galbraith & Schneider, 2009) and incorporating more recent data (Le Corre, Hobbs, et al., 2007b; Mehta & Batstone, 2013). Results from Mehta 2013 were calculated using induction time model parameters rather than thermodynamic modelling, as raw data were not provided. The model from Bhuiyan *et al.* was not considered accurate as pH change was used to identify the end of induction time in a solution which likely had significant ammonia buffering (N:P ratio of 17:1).

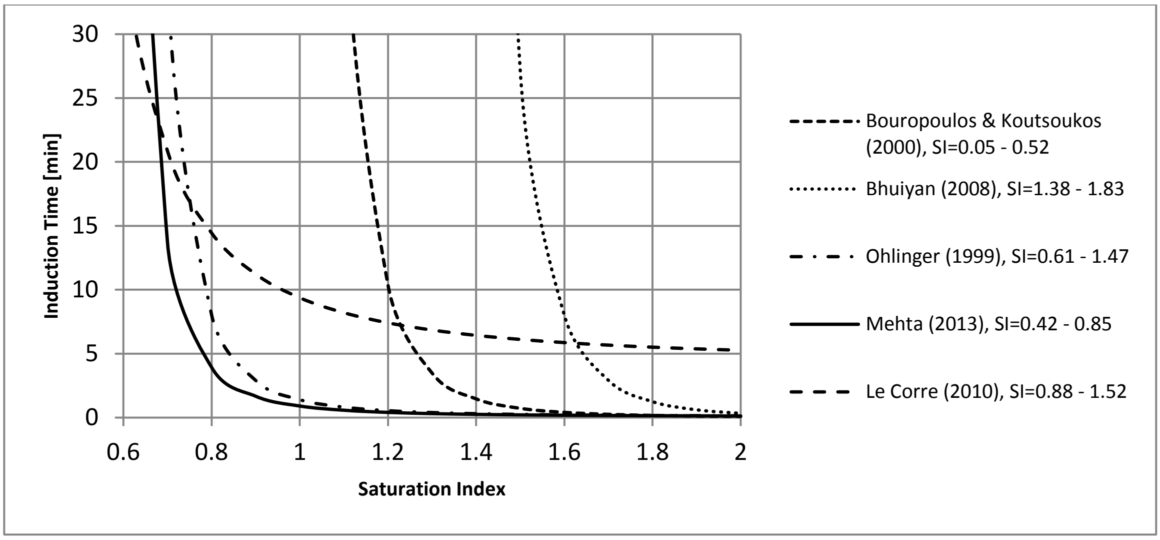

Figure 2.1 – Induction time model comparison

Figure 2.1 shows that induction time increases exponentially below *SI* = 0.8, irrespective of the model parameters adopted. Variations in induction time parameters within the literature have been attributed to many effects, including variations in detection methods, mixing speeds and reagent ion ratios (Galbraith & Schneider, 2009).

Table 2.2 – Reported induction time model conditions and homogeneous nucleation saturation level

Author	pH range	Experimental saturation range (SI)	Phosphate conc. [mM]	Molar ratio Mg:N:P	Reactor type	Mixing speed [rpm]	Method of nucleation detection	Reported Induction time range [min]	Lowest saturation for homogeneous nucleation (SI)
Mehta (Mehta & Batstone, 2013)	N/A	~0.42 – ~0.85	100	1:1:1	200mL glass bottles	300	pH change (0.05)	0.17 – 16.67	0.69
Galbraith (Galbraith & Schneider, 2009)	7.8 – 9.2	0.04 – 0.31	1.0 – 2.5	1:1:1	250mL beaker	Quiescent	Light scintillations	16.65 – 438.15	0.237
Saido (Saidou, Ben Moussa, & Ben Amor, 2009)	8.2	0.9	3.8	1:1:1	1L aerated FBR	N/A	P & Mg concentration	5 – 17	N/A
Bhuiyan et al (2008) (Bhuiyan & Mavinic, 2008)	8.2 – 8.51	1.38 – 1.83	1.81 – 3.39	1:22.1:1.3	2L square beaker	120	pH change	0.2 – 8.33	N/A
Le Corre (Le Corre, Hobbs, et al., 2007b)	9	0.88 – 1.52	2.4 – 4.6	1:2:2	250mL beaker & 10L FBR	Quiescent	pH change	0.5 – 12	N/A
Kabdasli (Kabdasli, Parsons, & Tunay, 2006)	8.44 - 9.23	0.371 - 1.135	2.45	1:1:1	1.5L cylinder, 0.2m dia.	300	Absorbance	0.83 – 42	N/A
Kofina & Koutsokous 2005	8.5	0.318 – 0.633	2.2 – 3.0	1:1:1	250mL beaker		pH change (0.005)	3.92 – 69.17	0.502 – 0.643
(Bouropoulos & Koutsoukos, 2000)	8.5	0.05 – 0.52	2.75 – 4.00	1:1:1	250mL beaker	N/A	pH change (0.005)	6 - 125	0.30
Ohlinger (1999) (K. N. Ohlinger et al., 1999)	6.3 – 7.9	0.61 – 1.47	4 – 20	1:1:1	beaker	570	Light scintillations	0.22 – 38	N/A

When induction time is reached and crystal formation begins, the formation rate can be represented with various mathematical descriptions, each with its benefits and trade-offs. Generally, struvite mass formation rate is calculated using two different kinetic models: rates of liquid phase species depletion and rates of individual crystal formation mechanisms. These categories are discussed in more detail in the following sections.

2.2.2 Liquid phase species desupersaturation rate

The simplest and most commonly implemented method of modelling struvite formation rate is by measuring the rate of change of one species in the solution phase and inferring the struvite formation rate using stoichiometry. Usually the limiting reagent is selected as the driver for de-supersaturation, which in most struvite applications is phosphate. Species concentration or supersaturation (given by any of equations 2.6 to 2.8) is used as the driving force in a rate equation. A power law kinetic model (equation 2.26) is most commonly implemented.

$$\frac{dC}{dt} = kC^n \tag{2.26}$$

Where C is the concentration of the species in question, t is some measure of time and k and n are the rate constant and order.

Various researchers have modelled struvite by applying a first order kinetic model ($n = 1$), which when integrated gives equation 2.27 (Ariyanto et al., 2014; Le Corre, Hobbs, et al., 2007a; Nelson, Mikkelsen, & Hesterberg, 2003; B. K. N. Ohlinger, Young, & Schroeder, 2000; Quintana et al., 2005; Rahaman et al., 2008).

$$\ln\left(C - C_{eq}\right) = -kt + \ln(C - C_0) \tag{2.27}$$

Where C, C_{eq} and C_0 are the concentrations of the reactant at time t, at equilibrium and at time 0, respectively. Le Corre *et al.* used magnesium as the ion of interest as it was the limiting reagent, inferring its concentration change in Mg concentration by pH measurement and the stoichiometry given by equation 2.20 (Le Corre, Valsami-Jones, Hobbs, & Parsons, 2007b). Le Corre *et al.* noted that at a given initial pH, as ion concentration increased, the rate of pH drop decreased. Two other studies, utilising a first order model based on phosphate concentration, observed variations in first order rate constant with changes in Mg:P ratio (Quintana et al., 2005; Rahaman et al., 2008). Nelson used $PO_4 - P$ as the limiting reagent and observed a three-fold increase in rate constant using a constant caustic dose (although starting solution pH varied by 0.6). (Nelson et al., 2003). Ariyanto *et al.* showed that first order growth rate increased with pH, temperature, NaCl concentration and mixing speed (Ariyanto et al., 2014). Each of these studies suggests that a more detailed kinetic model is necessary to represent the struvite system over a range of conditions. The abovementioned correlation of rate with ion ratio suggests that the use of a single species in a reaction equation is flawed and that struvite kinetics are likely better described using the ion activity product.

Some struvite research, in which faster growth rates have been observed, found that a second order kinetic model provided a better fit. Substituting $n = 2$ into equation 2.26 and integrating gives equation 2.28.

$$\frac{1}{C} = \frac{1}{C_0} + kt \qquad 2.28$$

In a study focusing on the removal of ammonia from digester effluent by addition of phosphate and magnesium, a second order kinetic model with respect to magnesium concentration was found to fit best (Türker and Celen, 2007). The model suggested a much faster precipitation as a result of nucleation (presumably induced by higher supersaturation levels) rather than growth, although no supersaturation or particle size data was provided to support this claim. Another study of spontaneous precipitation regressed a second order dependence on S_r, indicating a surface controlled mechanism (Bouropoulos & Koutsoukos, 2000). An alternative approach utilised a two-step model, where diffusion to the crystal surface is followed by a surface reaction rate, finding that in the given conditions, the system was transport limited (Bhuiyan et al., 2008). In this scenario, the surface reaction was also assumed to be second order. In all the above mentioned studies, kinetic models and associated parameters varied with system conditions, indicating that a more detailed kinetic model is necessary if crystallisation is to be modelled under varying operating conditions.

A more detailed approach to species depletion was used by Mehta, who applied a power law molar deposition model (equation 2.29) based on reduced supersaturation ratio (S_r) and crystal surface area term described by the initial and final mass of crystal, assuming size independent growth (SIG) and no nucleation (Mehta & Batstone, 2013).

$$\frac{dC_{MAP}}{dt} = k_R A \left(\frac{m}{m_0}\right)^{\frac{2}{3}} S_r^{n_R} \tag{2.29}$$

Where C_{MAP} is the struvite concentration [mM], k_R is the rate constant (0.09±0.04 mM.m^{-2}.s^{-1}), A is the specific surface area of the seed crystals before growth occurs [m^2/L], m_0 and m represent the crystal mass initially and at any time and n_R is the growth rate order. Their work used a stirred seeded batch vessel and both synthetic wastewater and digester supernatant diluted 10:1. The struvite growth rate exhibited a higher dependence on *SI* in real wastewater than in synthetic wastewater, highlighting that results are not transferrable between the two systems. The growth order was regressed to be 3.52±0.1, significantly higher than first and second order models discussed above. While inferences about crystallisation mechanisms based on order are tenuous (as discussed later in section 2.2.4.5), this may suggest a dominant surface integration mechanism. By converting from molar growth rate, they estimated crystal linear growth rate to be 0.06 – 0.3 µm/min/unit of S_r in the *SI* range of 0.12 – 1.47, although PSD assumptions necessary to make this conversion were unclear. The corresponding maximum and minimum crystal growth rates, plotted in Figure 2.3 (section 2.2.4.5) for comparison to other kinetic models, span a significant range and are within the region of growth rates predicted by other research.

The alternative approach to using a liquid phase species depletion rate is to model individual crystallisation mechanisms. Crystal growth can be broken down into various phenomenon, namely, nucleation, growth and agglomeration. In all of the above examples, these mechanisms have been neglected or merged. The following sections introduce mechanisms of crystallisation and identify deficiencies in the struvite crystallisation literature.

2.2.3 Nucleation

The formation of a nuclei can be defined as the point at which the solute changes state from liquid to solid. It can be categorised into primary and secondary nucleation, which represent the formation of new particles with or without the presence of other particles, respectively. Primary nucleation can occur without the presence of any other particles (homogeneous) or on the surface of a non-crystalline solid in solution, for example suspended solids or container walls (heterogeneous). Secondary nucleation represents any nucleation in which a solute crystal in the solution played a role. Once crystallisation begins, the effects of primary nucleation relative to secondary nucleation become quite small.

Actually measuring or predicting the rate of nucleation and defining the size at which nuclei are said to enter a system is very difficult. This is because the resolution of even modern equipment is not high enough to capture an accurate picture of both the number and size of nuclei upon their formation. The appearance of a phase change has been found to be best determined by small angle X-ray scattering (SAXS) (Alison et al., 2003), although this method provides no information about the nuclei size distribution. As a result of this limitation, most nucleation studies involve measuring the rate at which crystals come into the smallest size range measurable. Various theories have been formulated to relate measurable quantities to fundamental theories about how nuclei form. These theories and relationships are presented below, accompanied by a discussion of investigations made with relevance to struvite.

2.2.3.1 Primary nucleation

Primary nucleation describes the formation of a crystal from a pure solution, free of all other crystal and particulate matter. This scenario is practically impossible, since all solutions contain some level of contamination, of both crystal and particulate matter. Although much effort has been invested into understanding and modelling primary nucleation, it has for the most part been to no avail. Many prominent figures in the field have discussed primary nucleation theory in much detail, only to conclude that it has not been successfully measured or modelled (A. Randolph & Larson, 1988). Nevertheless, what theory does exist can be used in an attempt to describe the formation of new particles during crystallisation.

The thermodynamic approach to representing primary nucleation utilises the Arrhenius reaction velocity equation used to represent thermally activated processes. The derivation, which can be found in Mullin (Mullin, 2001), assumes spherical nuclei and uses the Gibbs-Thompson relationship between particle size and solubility. The resulting expression of nucleation rate ($J\ [s^{-1}cm^{-3}]$) is given by:

$$J = A \exp\left(-\frac{16\pi\gamma^3 v^2}{3k^3T^3(\ln\Omega)^2}\right) \tag{2.30}$$

Where A is a kinetic factor (/ pre-exponential factor/ collision factor) with units $[cm^{-3}s^{-1}]$, k is the Boltzmann constant $(1.38 \times 10^{-23} J/K)$, Ω is the saturation ratio (equation 2.9), γ is the interfacial tension between the crystal and the solution $[mJ/m^2]$, v is the molecular volume $[cm^3]$ (described by equation 2.23), and T is the absolute temperature. If this expression is generalised to include particle shape factors it can be written as:

$$J = A \exp\left(-\frac{192k_V^2\gamma^3 v^2}{k_A k^3T^3(\ln\Omega)^2}\right) \tag{2.31}$$

Where k_V and k_A represent the volume and surface area shape factors, respectively, and can be written for any shaped particle as:

$$k_V = \frac{V}{L^3} \tag{2.32}$$

$$k_A = \frac{SA}{L^2} \tag{2.33}$$

Where V and SA are expressions for particle volume and surface area, respectively, and L is the particle characteristic length (diameter for a sphere). Note that the units given for these variables are those which they are commonly displayed with. When the nucleation rate is calculated, *SI* units must be used for the equations 2.30 and 2.31 to be correct.

For struvite, the kinetic factor A has been assumed to be $10^{17} nuclei/cm^3$ (Abbona & Boistelle, 1985; Bouropoulos & Koutsoukos, 2000) although according to the Gibbs-Volmer theory, sparingly soluble salts should have a kinetic factor in the range of $\sim 10^{25}$ (Mullin, 2001; Alan D Randolph & Larson, 1988). Alternatively, a study utilising a draft tube jet pump crystalliser, assuming MSMPR operation in the *SI* range of 4.53 – 6.59[7], predicted struvite nucleation rate in the range of $7.28 \times 10^{11} - 4.08 \times 10^{14}$. These values were estimated by applying the Rojkowski hyperbolic size dependent growth model (equation 2.45 in section 2.2.4.3) to a population balance model, incorporating nucleation and growth, and performing a least squares optimisation (Koralewska, Piotrowski, Wierzbowska, & Matynia, 2009). Calculation of a kinetic factor based on more recent nucleation studies is possible, but would still rely on an assumed value for interfacial tension, which would itself rely on previous kinetic factor estimates.

The interfacial tension γ has been found to be 15, 43, 50 and 50 mJ/m^2 by Kofina et al., Bhuiyan, Abbona & Boistelle and Bouropoulos & Koutsoukos, respectively (Abbona & Boistelle, 1985; Bhuiyan et al., 2008; Bouropoulos & Koutsoukos, 2000; Kofina & Koutsoukos, 2005). The variation of Kofina's result was attributed to interference by excess SO_4^{2-} ions, which is logical as γ is inversely proportional to a salt's solubility (Mullin, 2001). Results from induction time experiments conducted by Ohlinger assumed that struvite interfacial tension would be similar to that of silica ($78 mJ/m^2$), making predictions in the range of observed results (K. N. Ohlinger et al., 1999). Comparing these results to interfacial tensions calculated for struvite, and to Figure 2.1, which indicates that significant nucleation occurs above $SI = 0.8$, it appears that this assumed interfacial tension is too large. In any case, the determined surface tension is only an estimation due to variations in experimental conditions.

---

[7] Estimated using thermodynamic modelling

2.2.3.2 Secondary nucleation

Secondary nucleation is said to occur when a crystal is born via any process in which an existing crystal is involved. Many classifications can be made of physical processes leading to secondary nucleation as discussed below (A. Randolph & Larson, 1988):

1. *Fracture* - occurs when high agitation rates in high suspension density systems causes crystals to break, resulting in many small round crystals. This is not likely to be significant for struvite due to its high hardness.
2. *Attrition* - is effectively the same process as fracture, but occurs from crystal-crystal interactions.
3. *Needle breeding* - is a fracture process that specifically occurs when dendritic growth occurs on crystals. Rod-like crystals growing on the surface of a larger crystal are much more likely to break free than the crystal itself is to break. This is a likely process during struvite crystallisation as struvite has been shown to form dendritic/needle like crystals at high supersaturation levels (Abbona & Boistelle, 1985).
4. *Fluid sheer* - occurs when some of adsorbed layer is sheered away by a large velocity gradient in the bulk fluid. This process is not likely to represent large fraction as clusters must then be subjected to higher saturation levels than those they were produced in order to become nuclei.
5. *Contact nucleation* - is the most likely cause of secondary nucleation in a crystalliser. Contact nucleation occurs when some of the adsorbed layer of a crystal comes into contact with agitator or (more likely) with other crystals and is displaced. This process would be produced by energy levels far lower than those required for fracture or attrition as the adsorbed layer is not yet in a crystalline state. Various authors have shown that contact nucleation occurs and that it creates new nuclei without visible damage to the parent crystal. The contact energy and super saturation affect the number of nuclei produced. At higher supersaturation levels, a thicker adsorbed layer exists which results both in the production of more potential nuclei by contact nucleation and a smaller critical nucleus diameter for successful nuclei formation. Results that support this theory have been demonstrated by various authors (Garside, Rusli, & Larson, 1979; Youngquist &

Randolph, 1972). Larson and Bendig showed that above a certain contact rate, no increase in nucleation is seen. This is likely to be because the adsorbed layer is being disrupted faster than it can regenerate (Larson & Bendig, 1976). In the same study, it was found that small crystals <100µm do not play a significant role in contact nucleation. Contact nucleation depends on supersaturation and can be represented with a power law relationship (A. Randolph & Larson, 1988):

$$B_0 = k(T)\omega^l M^j S^i \qquad 2.34$$

Where $k(T)$ is a rate constant which varies with temperature, ω is a function of agitation, M is the suspension density and S is a measure of supersaturation. The exponents in this equation are determined experimentally, but j is usually 1 and i is usually between 1 and 3.

Little account is given to modelling secondary nucleation of struvite, which may play a significant role in crystallisation once a particle population is established. The degree to which each secondary nucleation mechanism occurs (if at all) can depend on particle size, number density, fluid shear, saturation and temperature (Mullin, 2001).

One study has measured secondary nucleation by measuring particle size distribution (PSD) in batch experiments, seeded with $35 \pm 3\mu m$ struvite particles to ensure that no primary nucleation was possible. The nucleation rate was represented using a power law model (equation 2.35), which is similar to 2.34, but does not describe influence of mixing energy, suspension density and temperature (Mehta & Batstone, 2013).

$$B = \frac{dN_T}{dt} = k_B(\sigma - \sigma_i)^{n_B} \qquad 2.35$$

Where k_B and n_B are the rate coefficient and exponent, estimated as $8.3 \pm 2.3 \times 10^6 [nuclei \cdot L^{-1} s^{-1}]$ and 1.75 ± 0.13, respectivley. σ_i is the threshold saturation for secondary nucleation, regressed as $\sigma_i = 0.55 \pm 0.1$, which is equivalent to $SI = 0.57 \pm 0.12$. De-supersaturation due to crystal growth was assumed negligible based on an observed 3% reduction in total phosphorus. However, our simulations show that this is equivalent to a 44.18% reduction in supersaturation at the lower supersaturation range, meaning growth likely influenced results. Contact nucleation was proposed as the most likely model, which suggests that particles $< 100\mu m$ do play a significant role in secondary nucleation, contrary to results from previous studies.

A similar study operated a seeded lab scale crystalliser in the supersaturation range of $SI = 0.25 - 0.79$, assuming mixed suspension mixed product removal (MSMPR) and implemented a general power law model, as shown below in equation 2.36 (Galbraith, Schneider, & Flood, 2014).

$$B_{nuc} = k_{nuc} SI^{n_{nuc}} \tag{2.36}$$

Where the nucleation rate constant $k_{nuc} = 8.5(\pm 0.076) \times 10^7$ and the nucleation rate order $n_{nuc} = 1.68(\pm 0.014)$. Kinetic parameters were regressed by applying a hybrid population balance technique, incorporating nucleation, growth and agglomeration (Galbraith et al., 2014). Note that population balance techniques are discussed in detail in section 3.1.

2.2.3.3 Struvite nucleation rates

Figure 2.2 compares the results of various nucleation models applied to struvite crystallisation. Primary nucleation rate is described as a function of SI, using multiple estimates of interfacial tension and equation 2.30. Equations 2.35 and 2.36 are used to describe secondary nucleation rate.

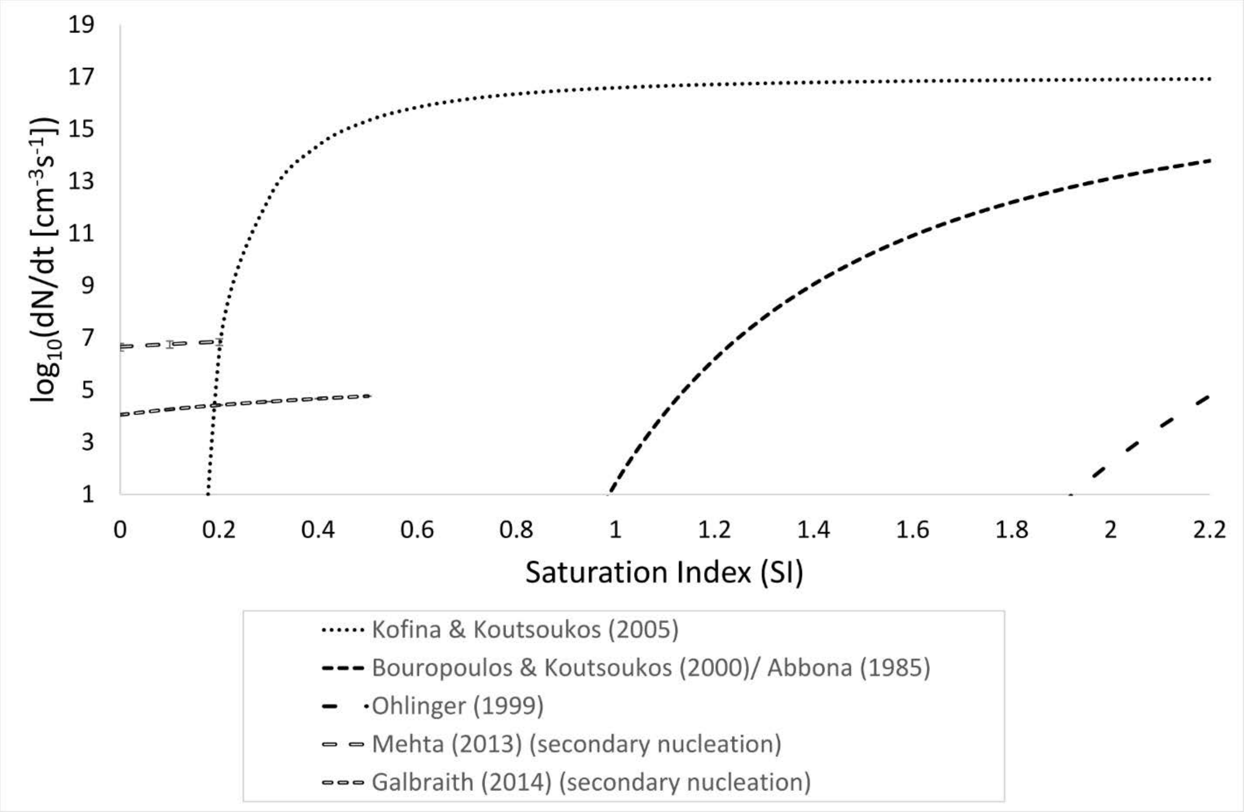

Figure 2.2 – Nucleation rate model comparison including classic primary nucleation rate models (Kofina & Koutsoukos; Bouropoulos & Koutsoukos; Abbona; Ohlinger), and power law models for primary (Galbraith et al.) and secondary (Mehta) nucleation.

The primary nucleation rate curves are described over a broad range of saturation index because the interfacial tension is a property which, so far as fundamental theory goes, does not change with supersaturation. Secondary nucleation rate relationships on the other hand are only shown for the saturation range at which their kinetic parameters were calculated, since these are empirical relationships. The significant differences in primary nucleation rates resulting from changes in the interfacial tension illustrate how sensitive the model is to this parameter, which is notoriously difficult to estimate. The asymptotic nature of equation 2.30 means that each instance of this model shown in Figure 2.2 are approaching the assumed maximum nucleation rate of $A = 1 \times 10^{17} [cm^{-3}s^{-1}]$, although, as shown above, a great deal of uncertainty is also found in this parameter.

Secondary nucleation rates are less sensitive to SI than primary nucleation rates. Compared to the large variability in primary nucleation rates, results from Mehta *et al.* and Galbraith *et al.* are reasonably close, indicating that they are likely a reasonable description of struvite secondary nucleation in that supersaturation range. These results are in the range of $10^4 - 10^7$, which align with rates suggested by Mullin (Mullin, 2001), but are significantly different to the assumed primary nucleation pre-exponential factor (10^{17}) and the maximum nucleation rate estimated by Koralewska *et al.* (in the range of $10^{12} - 10^{14}$).

Unless the transition between primary and secondary nucleation is estimated, and both key parameters in the primary nucleation model are found with a greater degree of certainty, applying a general power law model to nucleation is just as effective as any other method.

2.2.4 Particle growth

In this work, growth describes the size increase of individual particles. The following sections detail various crystal growth models, discuss the effects of impurities on crystal growth, then present a detailed review of work on struvite crystal growth rate.

2.2.4.1 Two-step growth

Particle growth is often described as a two-step process: transport of the solute to the crystal surface and integration from liquid to solid phase on the crystal surface. As these steps must operate in series, the slower of the two is always rate limiting. The dominant mechanism may change depending on the hydrodynamic properties of the system (as investigated by Tai (Tai, 1999) for sparingly soluble salts), temperature and solution composition (Sohnel & Garside, 1992). The two-step model is usually posed as a mass deposition rate, but can be converted to a particle linear growth rate with the knowledge of total particle mass, average particle diameter and solution volume (Bhuiyan et al., 2008). The diffusion rate can be written as:

$$\frac{dL}{dt} = k_d (C - C_i)^{n_d} \tag{2.37}$$

Where L is particle equivalent diameter, k_d is the diffusion rate constant, $C - C_i$ is the concentration difference between the bulk solution and the interface, and n_d is the diffusion order, which is almost always assumed to be 1, but may not necessarily be (Mullin, 2001). Struvite has been described by the diffusion model when equation 2.26 was found to be 1st order (Ariyanto et al., 2014). The surface integration rate, detailed further in the next section, is given as:

$$\frac{dL}{dt} = k_r(C_i - C_s)^{n_r} \tag{2.38}$$

Where k_r is the reaction rate constant, $C_i - C_s$ is the concentration difference between the interface and saturation and n_r is the reaction rate order. If $n_r = 1$, the diffusion and reaction steps can be combined to give:

$$\frac{dL}{dt} = K_g(C - C_s) = K_g S \tag{2.39}$$

For struvite application, the term $(C - C_s)$ should be replaced here by one of the more appropriate descriptions of supersaturation for sparingly soluble salts (generally termed S). In equation 2.39, $K_g = k_d k_r/(k_d + k_r)$. Alternatively, if $n_r = 2$, the reaction can be written as:

$$G = \frac{dL}{dt} = k_d S\left[\left(1 + \frac{k_d}{2k_r S}\right) - \sqrt{\left\{\left(1 + \frac{k_d}{2k_r S}\right)^2 - 1\right\}}\right] \tag{2.40}$$

Struvite has been modelled using equation 2.40, assuming a point distribution of particles and negligible change in seed size (Bhuiyan et al., 2008). The number of data points and fit of the model to the data were unclear, shedding some doubt on this work. Both diffusion and growth were considered and the relative orders of coefficients are used to infer diffusion as the rate controlling mechanism.

2.2.4.2 *Integration controlled crystal growth*

After the solute has diffused to the crystal surface, it must be integrated into the crystal lattice. An absorbed layer of solute exists on the surface of a growing crystal. This third phase consists of partially ordered solute in a partially de-solvated lattice. It is not yet crystalline, but it is more ordered and concentrated than the bulk solution. It is the ordering of this layer into a crystalline structure which the integration rate describes. In many struvite systems (presented later in Table 2.3), mixing is sufficient to ensure diffusion effects are negligible, transforming the growth rate to a surface integration rate controlled step. This step has been described by a number of models. A power law model can be used for parameter regression when the form of the growth rate model is unknown. Changes in the growth rate constant and order with supersaturation level are then used to infer greater model detail.

$$\frac{dL}{dt} = k_g S^{n_g} \qquad 2.41$$

Where k_g is a growth rate constant, S is some description of supersaturation and n_g is an empirical particle growth rate order. The continuous growth model (Jones, 2002), which assumes a rough surface to which ions integrate at the site of lowest energy, takes the form of equation 2.41 with $n_g = 1$.

Various works have implemented a form of equation 2.41 to describe struvite crystallisation. Hanhoun *et al.* regressed nucleation and growth kinetics with a least squares regression using supersaturation given by equation 2.12, which was predicted by pH measurements and a method of moments population balance (Hanhoun et al., 2013). Triger investigated struvite growth rate, defining supersaturation as the logarithm of supersaturation ratio using equation 2.14 (Triger et al., 2012). A least squares regression was performed using measured and predicted turbidity, which accurately predicted PSD properties but not PSD shape. Ali & Schneider also used equation 2.14 to regress struvite crystal growth rate, assuming an initial point distribution of particles and performing a least squares regression comparing measured and estimated ammonia, magnesium and phosphorus concentrations and mean crystal size (Ali & Schneider, 2008). These investigations occurred over a significant time period (36 h), making the operating *SI* lower than that achieved by the non-equilibrium state of mixing feed streams. Galbraith *et al.* investigated seeded struvite growth rate defining *SI* by equation 2.13 and using a hybrid population balance technique, incorporating nucleation, growth and agglomeration (Galbraith et al., 2014). The growth rate regressed exhibited a higher order than the 1 – 2 traditionally observed for crystallisation ($n_g = 5.062 \pm 0.005$) in the *SI* range of 0.37 – 0.54. They suggested that the high order could also be represented by a second order model with a dead-zone, where growth rate becomes insignificant below a given supersaturation, SI^*.

$$G = \frac{dL}{dt} = k_g(SI - SI^*)^2 \tag{2.42}$$

Where $SI^* = 0.3$. This outcome reinforces the null supersaturation concept used to describe secondary nucleation (Mehta & Batstone, 2013) and the surface nucleation model described below (equation 2.43).

The surface nucleation (*i.e.* birth and spread model) describes nuclei forming on a smooth crystal surface and spreading to sites of lowest energy. In this model, nucleation is the rate controlling step as spread of nuclei is much faster due to lower energy requirements (Ohara & Reid, 1973).

$$G = A''S^p \exp\left(-\frac{B'}{S}\right) \tag{2.43}$$

Where A'', B', and p are constants and $p = 1 - 2$. In this equation, B' represents a value of S at which growth becomes significant. When S is significantly larger than B', the exponential term in equation 2.43 tends to 1 reducing the equation to the same form as 2.41. When S is significantly smaller than B', the exponential term (therefore the growth rate) tends to 0. Another alternative is the continuous step growth model, which describes a self-perpetuating kink/dislocation, which forms a screw dislocation. This form of growth has been observed by crystal etching and reflective microscopy (A. Randolph & Larson, 1988). The screw dislocation model is also referred to as Burton Cabrera Frank (BCF) model (Burton, Cabrera, & Frank, 1951) and is the most widely applied model.

$$G = A'''S^2 \tanh\left(\frac{B'''}{S}\right) \tag{2.44}$$

Where A''' and B''' are constants. At low supersaturations ($S \ll B'''$), the hyperbolic term tends towards 1 and the model reduces to a power law with $n_g = 2$. At high supersaturations ($S \gg B'''$), the model can be approximated with power law model with $n_g = 1$. After the proposition of these three model types, it must still be noted that there are scenarios which cannot be explained by any of them (Alan D Randolph & Larson, 1988).

2.2.4.3 Growth rate dispersion (GRD) & size dependent growth (SDG)

GRD describes crystal growth rate variation with time and between different particles of the same size; it has been measured in many crystal systems (Ochsenbein et al., 2015; A.D. Randolph & White, 1977; Zekic, Mitrovic, Elezovic-Hadzic, & Malivuk, 2011). This phenomenon has been discussed extensively yet remains to be properly understood (Mullin, 2001; A. Randolph & Larson, 1988; Singh & Ramkrishna, 2014). An alternative theory to growth rate dispersion is size dependent growth (SDG) (Mullin, 2001; Rojkowski, 1978). Conceptually it is important to distinguish SDG from GRD. SDG asserts that a particles growth rate is a function of its size, while GRD asserts that one crystal becomes larger than another because it grew faster, rather than growing faster because it is larger. SDG has been shown to be significant only when comparing micro and macro crystals by grouping distributions of particles with different growth rate and showing little difference in growth rate within groups (Mitrovic, Zekic, & Iiic, 2002). To complicate the matter, the growth rate of an individual crystal can be random or fixed over the course of its growth (Mitrović, Žekić, & Baroš, 2008; A. Randolph & Larson, 1988), and growth rate dispersion has been observed to change over the course of a crystallisation process (Zekic et al., 2011). Feasible reasons suggested for these phenomenon include the presence of impurities; surface stage changes (which relate to a change in the dominant dislocation face as nuclei which formed quickly take on their dominant form); and lattice strain, which relates to the amount of defects on the crystal surface (Zekic et al., 2011).

A recent theory proposes that crystal growth rate dispersion is caused by randomised kink sites on crystal faces and localised fluctuations in temperature and saturation resulting from Brownian motion (Singh & Ramkrishna, 2014). The study also suggests that this effect is more noticeable at higher supersaturation ranges. It is unclear though, how significantly growth rate might vary due to temperature/supersaturation gradients, as measurable particle size exceeds the volume of fluid in which a supersaturation distribution can be observed. It should be noted that in this study, while the simulated coefficient of variation for a range of supersaturation values was 0.67, the assumed fluid volume was 22.89nm^3 and crystal growth occurs on a µm scale. As such, it would be expected that variations in growth rate at this scale would be unnoticeable when integrated through space and time for a particle system like struvite where PSDs average in the range of 10 – 1000µm. Nucleation rates on the other hand may be distributed as a result of this Brownian motion, depending on the critical nucleus size.

Struvite crystallisation has been described by the Rojkowski Hyperbolic SDG model for an MSMPR (equation 2.45), achieving the best fit out of a range of empirical and semi-empirical size dependent growth models (Koralewska et al., 2009; Lobanov, 2009; Matynia et al., 2006).

$$n(L) = n_0 \exp\left[-\left(\frac{G_\infty - G_0}{\tau a G_\infty^2}\ln\left(\frac{aG_\infty L + G_0}{G_0}\right) + \frac{L}{\tau G_\infty} + \ln\left(\frac{aG_\infty L + G_0}{(1+aL)G_0}\right)\right)\right] \quad 2.45$$

Where $n(L)$ is the population density, n_0 is the nuclei population density, a is a kinetic coefficient and G_0 and G_∞ are the growth rates of the nuclei and the largest crystals, respectively. While this model may provide a best fit to some data, it was not compared to size independent growth models and there is no physical evidence that size dependent growth is occurring, making it as good as any other that could be fit to the same data. Although there is opportunity within struvite crystallisation modelling to investigate the application of GRD SDG models, they are not investigated further in this research due to their complex and uncertain nature.

2.2.4.4 Effect of impurities on crystal growth

Impurities, in general, refer to any compounds in a system not directly taking part in the desired crystallisation reaction. The term can refer to suspended solids, dissolved metals, coagulants and flocculants and can be present in the feed, carried over from earlier parts of the process or produced as a by-product of reactions occurring. Impurities in a system are almost impossible to avoid, even under lab conditions and can both increase and decrease the rates of growth and nucleation. Impurities are often essential for nuclei formation as is the case in struvite crystallisers seeded with silica (P Battistoni, Paci, Fatone, & Pavan, 2006; B. K. N. Ohlinger et al., 2000; Regy, Mangin, Klein, & Lieto, 2001). As noted in section 2.2.3, though, silica's higher interfacial tension means that it would have a lower primary heterogeneous nucleation rate than if struvite were used as a seed. Impurities in the system can be adsorbed onto the crystal surface during growth, which can reduce the interfacial tension but also reduce the available surface area for growth (A. Randolph & Larson, 1988). Impurities may also vary the solubility of the product or cause other by-products to be formed. These effects combined can create significant differences between testing under lab conditions and testing with real solutions in which impurity levels may be quite high. The exact effect of impurities on any given system is very subjective and must be carefully studied.

2.2.4.5 Struvite growth rate discussion

In this section, struvite research is evaluated to identify common trends and assess which practices should and should not be adopted in this work. Species depletion models are not considered adequate for struvite modelling because of the relationship observed between rate constant and ion concentrations (section 2.2.2). Table 2.3 summarises investigations of struvite crystallisation investigations and Figure 2.3 provides a visual comparison of crystal growth rates on a common supersaturation scale.

Table 2.3 shows that measured struvite crystal growth rate is reported from 0.03 – 24 µm/min, while regressions based on Figure 2.3 showed growth rate 0.01 – 12.86 µm/min in the *SI* range of 0.25 – 1.4. Unfortunately such a large range in growth rate does not offer much confidence to somebody trying to find an accurate model for design purposes. To assess the impact of this uncertainty, this work will present sensitivity analysis on struvite crystallisation kinetic parameters.

Table 2.3 – Struvite particle growth rate comparison

Source	pH range*	Experimental saturation range (SI via eqn 2.13)	Phosphate conc. [mM]	Molar ratio Mg:N:P	Reactor type (seeded/continuous/ batch)	Mixing speed [rpm]	Residence time [min]	Final particle size [µm]	Model equation	saturation measure	Rate Constant(s) [µm/min]	Rate order presented	Linear growth rate [µm/min]
(Ali & Schneider, 2008)	7.22 – 7.51	0.053** 0.32 – 0.57***	6	1:1:1	Seeded fed batch recirculating (16-16.8L)	-	439.2, 480 & 2160	~170 - 195	Power law	2.14	0.784±0.14	1.64±0.19	0.011 – 0.083 (calculated)
									Power law (seed size estimated)	2.14	0.819±0.14	1.68±0.18	0.011 – 0.079 (calculated)
(Galbraith et al., 2014)	7.46 – 7.62	0.25 – 0.74	5	1:1:1	Stirred, seeded, draft tube, baffled, batch (1L)	-	120	<30	Power law	2.13	12.49±0.06	5.062±0.005	0.011 – 2.74 (calculated)
(Hanhoun et al., 2013)	8.5 – 9.6	0.26 – 0.54	3 – 4	1:1:1	Stirred batch (3L)	500	60	D[50]=70 - 89	Power law	2.12	280.64	1.34	2E-4 – 1.3E-3 (calculated)
(Ariyanto et al., 2014)	8.0 – 9.5	0.31 – 1.00	2	1:1:1	Stirred, seeded batch (1L)	50 - 120	120	24.3 – 84.8 (seed size)	Power law	2.9	0.5 – 10.0	1.05 – 1.47	0.07 – 14.39 (calculated)
(Triger et al., 2012)	9.31	~3.7** ^^	14.08 (synth)	1.3:33:1	Stirred batch (2L)	300	0.33	D[50]=54.1-52.5	Power law	2.14	1.75 - 2	1.15 – 2	2.72 – 3.56 (calculated)
	9.29	~3.7** ^^	13.95 (real)	1.3:16:1	Stirred batch (2L)	300	0.33	-	Power law	2.14	1.8	2	2.45 – 3.20 (calculated)
	9.35	~3.7** ^^	14.40 (real)	1.3:19:1	Stirred batch (2L)	150	0.33	D[50]=45.7	Power law	2.14	1.5	1.8	1.98 – 2.52 (calculated)
(Bhuiyan et al., 2008)	8.07	<1.38	~0.7 (read from plot)	-	Seeded continuous FBR (5.56L)	-	420	500 - 2000	Two-step	2.11	$k_d = 1.11E-8$ $k_r = 7.99E-5$ [m/s]	2	0.51 – 16.02 (calculated)
(Mehta & Batstone, 2013)	8.0 – 9.0	0.12 – 1.47	3.67	5.14:4.88:1	Stirred, seeded, baffled batch	-	120	D[50] ~ 100	Power law (including surface area)	2.11	-	-	0.02 – 8.55 (calculated)
(Koralewska et al., 2009)	9	4.53 – 6.59	100 - 820	1:1:1	Draft tube MSMPR (1.2L)	6.6	15	<90	SD RHG	-	-	-	0.03 – 1.99
(Mazienczuk, Matynia, Piotrowski, & Wierzbowska, 2012)	9 - 11	-	105	1:1:1	Draft tube MSMPR (1.2L)	0.25 [W/kg]	15, 30 & 60	<90 D[50]=4.1-19.1	SIG NCG	-	-	-	0.07 – 0.43
(Kozik, Hutnik, Piotrowski, & Matynia, 2014)	8.5 - 10	-	65	1.2:1:1	DT MSMPR (0.6L)	4	15, 30 & 60		SIG NCG	-	-	-	0.2 – 1.0
(Harrison, Johns, White, & Mehta, 2011)	7.5 – 8.5	-	-	-	Stirred, seeded batch (1L)	-	-	-	Power law	2.6		1.9 – 2.1	10 – 24
	8.5	-	-	-	Stirred, seeded pilot scale at abattoir (200L)	-	-	-	Power law	2.6	$k_g = 1.5E-5$ to $1.0E-4$ [µm/min/ (mg/L)^2]	2	0.45 – 0.8

*Maximum pH/SI for batch reactors and steady state *SI* for continuous; ** Calculated using thermodynamic model and conditions given. *** *SI* given in PhD thesis document. ^ Parameter regression included seed size. ^^ High ammonia concentration introduces uncertainty to *SI* prediction via thermodynamic model. N/P = not provided.

It is important to identify which assumptions may have contributed to the large variation in results. First, the assumption of negligible nucleation and agglomeration will be examined. Two examples of this include the supporting assumption of a point distribution of particles (Ali & Schneider, 2008; Bhuiyan et al., 2008). Bhuiyan *et al.* assumed a second order integration step in a two-step model and assumed that the point distribution of particles did not change in size, while Ali & Schneider regressed kinetic parameters based on total molar concentrations and mean particle size (Ali & Schneider, 2008). By operating at a very low *SI*, Ali & Schneider regressed relatively low growth rates when compared to other work (Figure 2.3). In an alternative two examples, researchers assumed constant PSD shape and calculated growth rate using PSD translation (Ariyanto et al., 2014; Harrison et al., 2011). Harrison *et al.*'s results must be taken cautiously though as they showed that PSD shape did vary and represented supersaturation using phosphorus concentration difference, neglecting ion speciation. Although Bhuiyan *et al.*, Ali & Schneider and Ariyanto *et al.* were able to produce a good fit to their individual datasets, the growth rate predictions from these 'growth only' models vary by two orders of magnitude (Figure 2.3). To eliminate some uncertainty observed in these models, this work will incorporate the nucleation mechanism, use full PSD measurements and operate within an *SI* range where kinetics can be easily observed.

Multiple works have modelled simultaneous struvite nucleation and growth using population balance techniques. Investigations by Triger incorporate nucleation and growth, but regressed parameters using only turbidity (Triger et al., 2012). Their experiments were conducted at a very high *SI*, but growth rates regressed were in the in line with other works at lower *SI*'s, indicating a diffusion limitation. The authors attribute errors to non-ideal mixing and attrition, although agglomeration and operation at a very high *SI* may also play a role. Hanhoun *et al.* also applied a nucleation and crystal growth model, but manually selected nucleation parameters, and while a least squares regression was used, it was only applied to saturation data predicted from pH rather than concentration or PSD data (Hanhoun et al., 2013). This resulted in a growth rate prediction significantly lower than those of other struvite investigations (Figure 2.3), which suggests that a single variable is insufficient for parameter regression. Koralewska *et al.*

incorporated nucleation and growth mechanisms and used a highly controlled procedure, giving reasonable confidence to the range of particle growth rates they measured, although the growth rate dispersion model they applied is theoretically unlikely, as discussed in section 2.2.4.3 (Koralewska et al., 2009). Work by Mazienczuk *et al.* regressed nucleation and growth parameters using the PSD only (Kozik et al., 2014; Mazienczuk et al., 2012). While their work was experimentally sound, the model proposed should be applied cautiously as it did not match the data in lower particle size ranges, indicating that the nucleation and growth model alone could not accurately represent the entire dataset. Improvements on these works, which can be applied to the work in this thesis include: making parameter optimisations using multiple variables, not operating at a high *SI* and examining agglomeration (discussed in section 2.2.5.5).

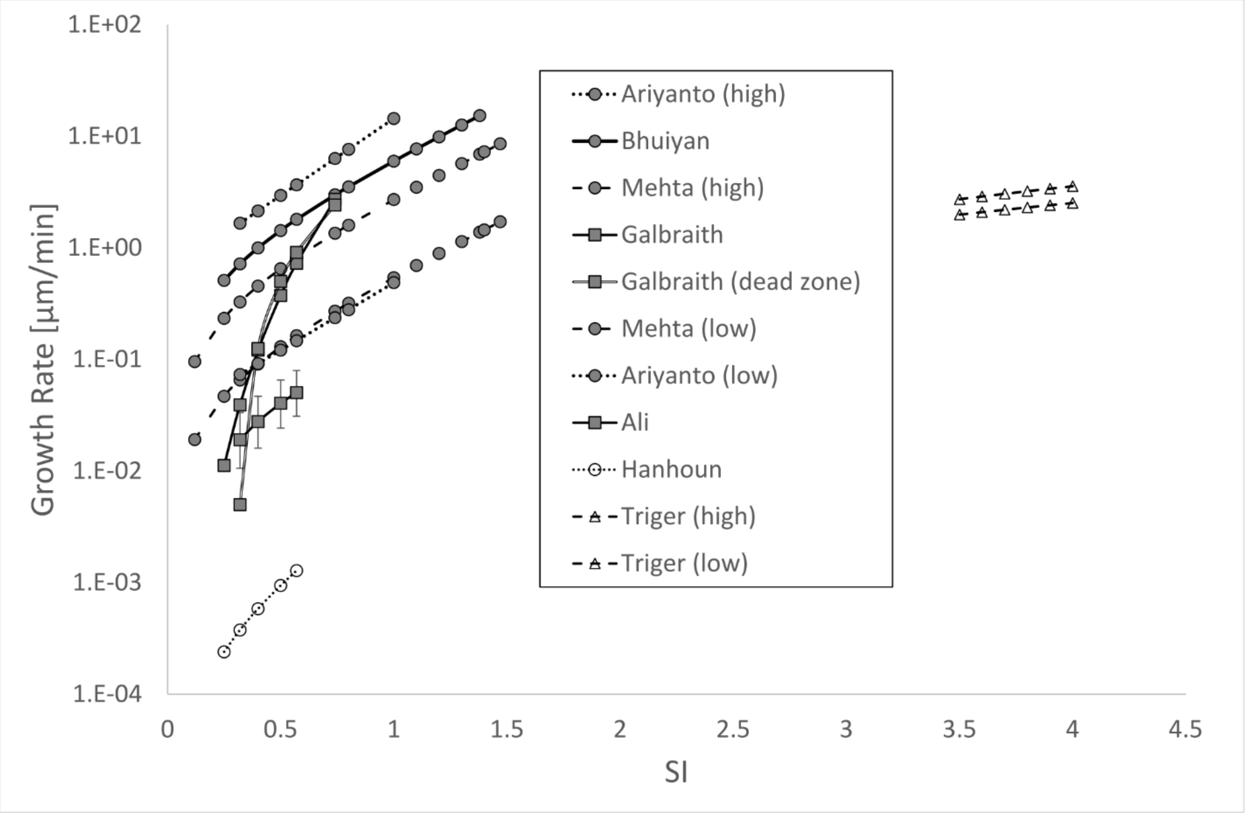

Figure 2.3 – Crystal linear growth rate comparison. Dashed and solid lines represent batch and continuous reactors, respectively. Circles indicate $C_{PO_4} < 5$ *mM, squares indicate* $5 \leq C_{PO_4} < 10$ *mM and triangles indicate* $C_{PO_4} \geq 10$ *mM. Filled and unfilled markers represent seeded and unseeded scenarios, respectively. Uncertainties in kinetic parameters were incorporated where available and significant enough to be visible.*

When comparing kinetic models based on the experimental conditions which they were obtained, Figure 2.3 shows no major trends. The growth rates predicted by these models vary over 5 orders of magnitude, although it appears that seeded growth rates are much higher than unseeded growth rates. Seeded growth rates represent the majority of the data in the 10^{-2} to 10 µm/min range. The unseeded investigation by Hanhoun *et al.* produced crystal growth rates an order of magnitude lower than all other seeded investigations in the range of *SI* = 0.25 – 0.75 (Figure 2.3 and Table 2.3). Comparisons between continuous and batch experiments also offer no insight since growth rates from continuous reactors span approximately three orders of magnitude and those from batch experiments span five. All authors reported increasing crystal growth rate with *SI* except Mazienczuk *et al.*, who observed a decrease in growth rate with increasing pH (assuming *SI* is proportional to pH within the range tested), which was attributed to a greater initial nucleation rate and associated decrease in *SI*.

Many authors suggest that since the order of reaction regressed is >1, crystallisation is likely reaction controlled. The texts often cited to justify this conclusion measure supersaturation in the diffusion-reaction model using a difference in solute concentration (Mullin, 2001; A. Randolph & Larson, 1988). Most investigations of struvite use one of various more complex descriptions of supersaturation (section 2.1.3), the selection of which will result in a variation in regressed model order. In addition to this, Mullin notes that diffusion and integration are difficult to distinguish considering that likely more steps are involved (*i.e.* boundary layer, adsorption layer and surface diffusion, ion dehydration, surface integration and counter diffusion of dehydrated water) and that diffusion term may exhibit be a higher order than 1. To examine the effect of supersaturation measure on regressed growth rate order, a power law model using *SI* was fit to each trend shown in Figure 2.3. All models gave an R^2 value >0.97 and the indices varied from 1.64 – 2 for all models accept that by Galbraith *et al.*, which has an order of 5.062. By repeating this process using reduced saturation, it was found that growth rate orders mostly fell in the range of 0.9 – 1.34, while results from Triger *et al.* and Galbraith *et al.* gave orders of 0.21 – 0.23 and 3.14, respectively. In this case all R^2 values were >0.99. This illustrates that great care must be taken to ensure consistency between selection of supersaturation measure and that conclusions about reaction or diffusion mechanisms must be taken cautiously.

2.2.5 Aggregation

In a dispersed particle system, particle collisions can result in the particles joining together to make a larger particle. As this process occurs, the PSD changes, which in turn decreases the total number of particles and potentially the specific surface area. Often terminology is interchanged within the literature. This work deals primarily with aggregation and to a lesser extent agglomeration. The following definitions are given for the readers information (Jones, 2002; A. Randolph & Larson, 1988):

- *Coagulate or flocculate* - A group of particles weakly held together by cohesive forces
- *Aggregate* - A group of particles weakly cemented together by crystalline structure
- *Agglomerate* - A group of particles cemented together by crystalline structure. Although the crystal properties remain the same, the macro-structure of the particle will determine its properties *i.e.* density, strength etc.

2.2.5.1 Primary aggregation

Aggregation can be further divided into two categories: primary and secondary. Primary aggregation is defined as mal-growth comprising of individual units within a structure *i.e.* stacking, dendrites (like snowflakes), twins etc. It is the consequence of nucleation on impurities or diffusion layer limitations at high growth rates (Jones, 2002). This process is rarely discussed as it is likely absorbed into the growth rate when modelling the system. Modelling this process as growth likely contributes to the variations in crystal growth rate models *e.g.* birth-spread and screw dislocation.

2.2.5.2 Secondary aggregation

Secondary aggregation, which is more widely investigated, is the result of particle collisions. All further references to aggregation in this thesis will refer to secondary aggregation unless otherwise stated. This process requires a number of steps to be successful. First particles must collide with sufficient energy to overcome colloidal repulsion forces (discussed in section 2.2.5.3). Particles must then spend sufficient time together to bond. Finally, saturation levels must be high enough that a bond is formed (Regy et al., 2001). These processes are discussed below in more detail.

1. Particle collisions:

A collision may result from a variety of forces depending on the particle size, particle and fluid properties, and shear rate. For smaller particles (<1um), collisions occur by Brownian motion as they travel within fluid eddies. These are referred to as perikinetic collisions. Larger particle (>1um) collisions resulting from fluid velocity gradients are referred to as orthokinetic collisions. It has been theorised that smaller particles (<100 µm) are only influenced by fluid velocity gradient, while larger particle collisions also result from particle inertia. Additionally, as aggregates grow larger, their fractal nature causes increased porosity, which increases their fluid drag, resulting in increased collision frequency (Kusters, Wijers, & Thoenes, 1997). Particle collisions can also be influenced by externally applied fields – gravitational and electrostatic.

2. Particles spend sufficient time together:

The probability that particles collide and remain together for long enough to cement depends on the colloidal forces between the particles (section 2.2.5.3 below), the rate of particle cementing (proportional to particle growth rate), and fluid shear.

3. Particles cement:

While particles are together, solute must diffuse from the bulk of solution, between them to the contact point where growth must occur. Various theories have been proposed on which variables have the most significant impact on this cementation rate.

2.2.5.3 Colloidal forces

On any phase boundary; solid, liquid or gaseous, positive and negative charges separate, creating a region of varying electrical potential. The thickness of this potential is only one or more molecular diameters but has an electrostatic potential in the range of 1V (Hunter, 2001). At the boundary between a solid and a solution, ions, electrons and dipolar constituents arrange themselves at the interface to minimise free energy levels. This results in the polarisation of neighbouring molecules. The net result of these charge interactions is a potential difference between bulk of two phases called inner of Galvani potential ($\Delta\phi$). This potential, although theoretically important, cannot be measured unequivocally unless the phases are identical (Hunter, 2001).

A crystal in solution develops a surface charge in the manner discussed above, causing some ions in solution to have a greater affinity for the crystal surface than others. As the concentration of constituent ions in the bulk solution varies, so does their affinity for adsorption onto the crystal interface. When one ion has a greater affinity for adsorption, the solid surface has an excess of that charge and then itself is charged (Hiemenz & Rajagopalan, 1997). This charge differential in the adsorbed layer is countered by an equal and opposite charge through the diffusion layer so that the system is electrically neutral (as seen in Figure 2.4). This phenomenon is referred to as the electrical double layer. These electrical double layers result in electromagnetic interactions between particles in a system. It is the properties of these layers that determine whether attractive or repulsive forces exist between particles. These forces then affect the rate of particle collisions and thus the rate of agglomeration.

The thickness of the electrical double layer is determined by fluid velocity gradients which control the diffusion layer thickness. Investigations by Melis *et al.* (Melis, Verduyn, Storti, Morbidelli, & Baldyga, 1999) show that hydrodynamics affect particle interactions when a large electrical double layer exists, but that particles with small electrical double layers seem unaffected by changes in fluid shear. For large electrical double layers, it was found that above a critical size, the aggregation rate constant increases with increasing particle size.

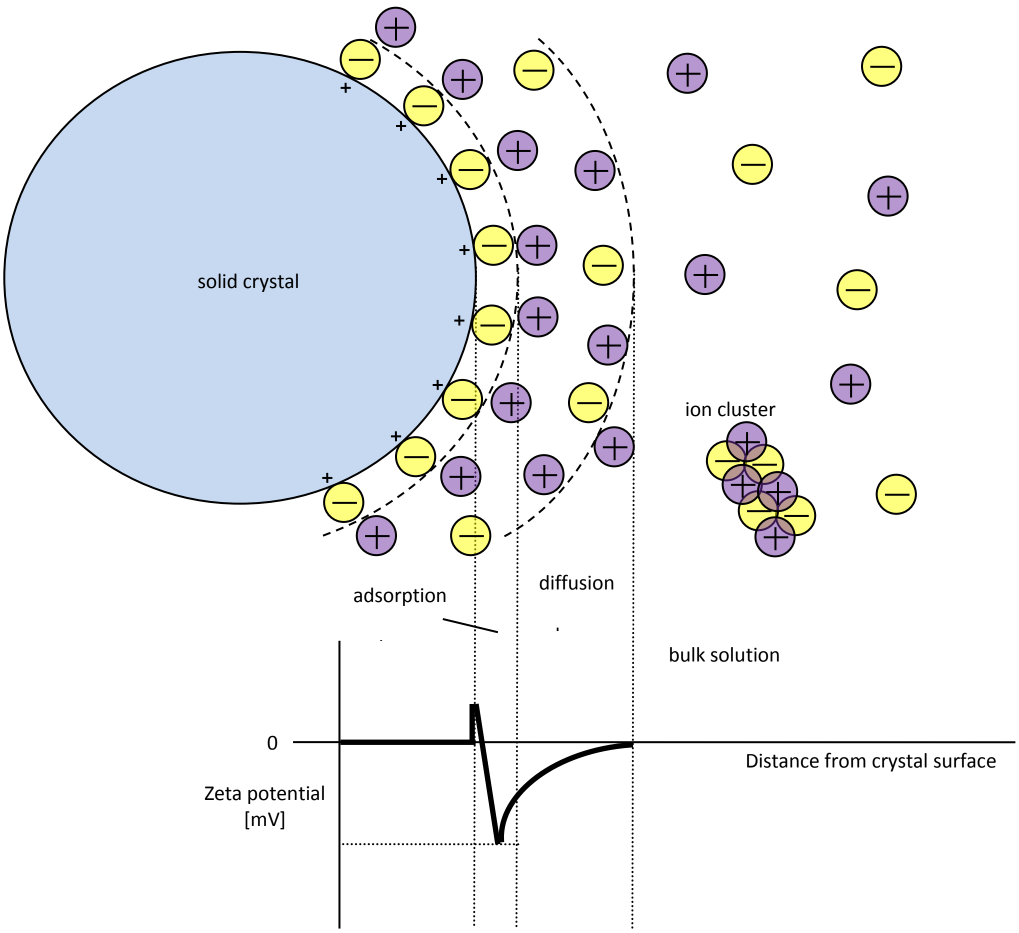

Figure 2.4 - Electrical double layer

The overall potential gradient between the solid surface and the bulk solution is called the Nernst potential, E, which is given as:

$$E = \sigma + \zeta \tag{2.46}$$

Where σ is the potential of the immobile layer and ζ, the zeta potential, is the potential of the diffusion layer. Zeta potential is a function of ionic strength, which is in turn a function of the relative charge and concentration of each component in the solution. The relationship between zeta potential and ionic strength varies depending on charges of the particles in the system. As ionic strength increases, zeta potential may reach a maximum then become smaller (mono- and bivalent ions), it may fall towards zero (bi- and trivalent ions), or it may drop to a minimum then increase (bi- and tetravalent ions). If zeta potential is large, repulsive forces are dominant, but if zeta potential is small the attractive forces are dominant.

The concept of zeta potential is well understood, but its interaction with parameters in a struvite system has not yet been fully explored. Warmadewanthi & Liu found that zeta potential became more positive as molar ratio (Mg:P) increased, reaching a maximum at a ratio of 2.5:1 (Warmadewanthi & Liu, 2009). This supports results from Bouropoulos & Koutsoukos indicating that excess Mg causes the negative surface charge on struvite to approach zero (Bouropoulos & Koutsoukos, 2000). Warmadewanthi & Liu also found that zeta potential reached a maximum at approximately pH 10. This is contrary to results from Bouropoulos & Koutsoukos who found that surface charge became more negative between pH 9.2 and 10, then saw flocculation at pH 10.5 but provided no zeta potential measurement (Bouropoulos & Koutsoukos, 2000). Warmadewanthi & Liu attributed his result to the formation of other crystals like bobbierite.

Le Corre *et al.* (Le Corre, Valsami-Jones, Hobbs, Jefferson, & Parsons, 2007a) also conducted investigations of the effect of zeta potential on struvite agglomeration by using coagulants to remove fines. Le Corre *et al.* found that struvite has a zeta potential between -27 to -17 mV, which agrees with Bouropoulos & Koutsoukos (Bouropoulos & Koutsoukos, 2000) who measured values of -26 to -20 mV over a pH range of 9.2 to 10. These values are higher than those reported by Henderson *et al.* to limit agglomeration of organic matter, algae and kaolin (Henderson, Sharp, Jarvis, Parsons, & Jefferson, 2006). How transferrable the values are to struvite is unknown, but Le Corre *et al.* showed that as zeta potential was reduced by addition of a coagulant, an increase in average particle size was observed. It was also found that floc formation was highly pH sensitive. These results may indicate that zeta potential is a controlling factor in struvite particle size enlargement, but the impact of coagulant use on the actual agglomeration process is unknown. It may very well be that although larger particles are formed, their structural properties may be different. Bouropoulos & Koutsoukos found that zeta potential was made more positive by increased magnesium concentration. Although these investigations shed some light on factors influencing struvite agglomeration and what effect it has on overall particle size enlargement, a comprehensive investigation remains to be conducted.

The other set of forces which exist between crystals in solution are Van der Waals forces. They are the sum of the attractive and repulsive forces between particles not associated with covalent bonds or electrostatic interactions *i.e.* the electrical double layer. They consist of Keesom interactions (permanent dipoles), DeBye forces (induced dipoles) and London forces (instantaneous dipoles). These forces create weak attraction forces between particles of similar material and their effect decays rapidly with particle separation distance. These forces can be described by (Jones, 2002):

$$V = A_{12}f(h) \tag{2.47}$$

Where A_{12} is the Hamaker constant for the material and h is the separation distance of two particles.

In an attempt to accurately describe particle interactions, DLVO (Derjaguin-Landau Verwey-Overbeek) theory combines estimations of energy of attraction by London and Van der Waals forces and repulsion from overlapping electrical double layers (Adamson & Gast, 1997). A limitation of this theory is that it cannot account for the effects of saturation levels or ion concentration on agglomeration (A. S. Bramley, Hounslow, Newman, & Paterson, 1997). It also ceases to work when suspensions get so dense that the separation distance of particles is in the order of the adsorbed layer (Adamson & Gast, 1997).

2.2.5.4 Aggregation rate

Various efforts have been made to describe and model steps of crystal aggregation. While this work uses a relatively simple particle size independent aggregation model, some background on alternative techniques are included for the interested reader.

Smolowchowski originally described the collision frequency of dispersed particles due to Brownian motion (Smolowchowski 1917). A general expression of aggregation describes the rate of aggregation of particles of size i with those of size j as proportional to the product of the number of particles in each size range (N_i and N_j) and includes a rate constant known as the aggregation kernel, $\beta_{i,j}$.

$$r_{agg} = \beta_{i,j} N_i N_j \tag{2.48}$$

The aggregation kernel can be broken down into two terms; β_0, representing system properties (supersaturation, fluid velocity etc.), and a particle size dependent function, $f(i,j)$, representing the aggregation frequency. The size dependence term can take various forms depending on the mechanism(s) causing aggregation (perikinetic, orthokinetic etc.). Aggregation investigations are notoriously difficult because of the many concurrent influencing factors. In the century since Smolowchowski's formulation, many investigations have been made into the agglomeration kernel and now more than 50 variants of the agglomeration kernel can be found in the literature (Mersmann, Braun, & Löffelmann, 2002).

One theoretical investigation of agglomeration accounting for Brownian motion, laminar flow and turbulent flow found that PSD properties and de-supersaturation profiles depend strongly on aggregation rate constant (contained within β_0), initial supersaturation, and hydrodynamics (David, Paulaime, Espitalier, & Rouleau, 2003). These variables are sometimes combined into a collision efficiency model including hydrodynamics, bond formation rate and bond strength.

For the calcium oxalate monohydrate system, a sparingly soluble salt which is assumed to behave similarly to struvite, aggregation has been investigated for dependency on a number of factors including: hydrodynamics (A. Bramley, Hounslow, & Ryall, 1997; M. J. Hounslow, Bramley, & Paterson, 1998); solution composition (M. J. Hounslow et al., 1998); Thiele modulus (a term describing the ratio of reaction rate to diffusion rate) (M. J. Hounslow et al., 1998); and solution ionic ratio (A. Bramley et al., 1997; Liew, Barrick, & Hounslow, 2003). It was found that a maximum aggregation rate exists with varying shear rate, due to a trade-off between increasing collision rate and increasing tensile stress between crystals (Mumtaz, Hounslow, Seaton, & Paterson, 1997). All of the abovementioned factors were able to be correlated by comparing particle collision efficiency with a number representing the ratio of aggregate bond strength of an aggregate to the force exerted on it in a collision (M. Hounslow, Mumtaz, Collier, Barrick, & Bramley, 2001).

Similar theoretical collision efficiency models have been developed incorporating hydrodynamic and colloidal interactions, accounting for particle mass, fractal dimension and a non-dimensional Hamaker constant (Babler, 2008)[8]. Babler's work concluded that collisions between particles of similar size are preferential to those with different sizes. This outcome is of importance in crystallisation applications as often it is assumed that particle surface area is not conserved during aggregation events, and that the effect of this assumption is relatively low because the majority of collisions occur between particles of significantly different sizes.

While it is physically accurate that aggregation mechanisms depend on particle size, the overall aggregation kernel can often be approximated by a size independent kernel (Jones, 2002). In a number of investigations a size independent kernel has provided a better fit to data than size dependent kernels (A. S. Bramley, 1994; M. J. Hounslow, 1990; Ilievski, 1991). This outcome has been attributed to a decrease in collision efficiency and increased particle disruption with particle size (Jones, 2002). In this scenario, the aggregation rate becomes a function of stirring rate and supersaturation only.

In this thesis, since hydrodynamics remain constant and non-turbulent, their effects on collision frequency and aggregate breakage (due to weak bond strength) are not considered. Bond formation rate is incorporated using a similar approach to previous struvite aggregation investigations by describing aggregation using a power law model (equation 2.49), where the saturation index (*SI*) is the driving force, k_{agg} and n_{agg} are the rate constant and order, respectively.

$$\beta_0 = k_{agg}(SI)^{n_{agg}} \tag{2.49}$$

2.2.5.5 Struvite aggregation

Early work on struvite crystallisation showed that for equimolar solutions of magnesium, ammonium and phosphate, twinning and aggregation occurs above a concentration of approximately 0.005M, where the

---

[8] Application to crystallisation systems would likely also require a description of the growth rate of a bridging bond.

supersaturation necessary for aggregation is approximately *SI* = 1.51, but progressively decreases with increasing concentration (Abbona & Boistelle, 1985). Struvite aggregation is evident in many industrial applications as shown by Figure 2.5 and Figure 2.6 below. Other fluidised bed reactor investigations have also reported particle sizes of 0.41 - 1.43 mm (Shimamura, Tanaka, Miura, & Ishikawa, 2003) and 2.2 - 3.5mm (Adnan, Mavinic, & Koch, 2003), which are likely only achieved by aggregation. Another FBR investigation observed pellets with a tightly bound inner core and a thick outside coating of fines (Bhuiyan & Mavinic, 2008). In addition to struvite crystallisation, one group observed 2-3 µm hydroxyapatite agglomerates forming both alone and on the surface of struvite crystals (Hutnik, Piotrowski, Wierzbowska, & Matynia, 2011).

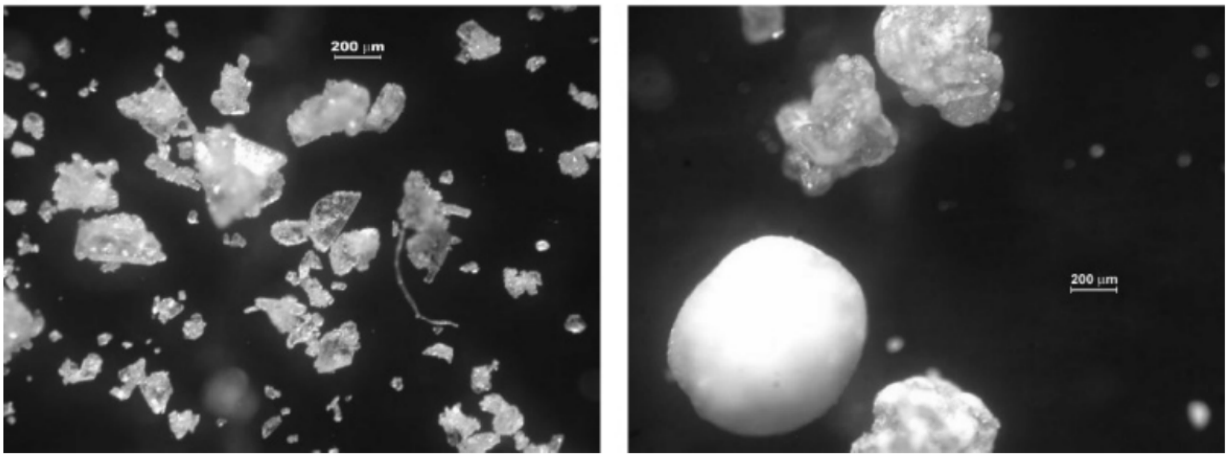

Figure 2.5 – Macroscope photos from upper fluidised section (left) and lower packed section (right) of a fluidised bed crystalliser operating for 2.29 – 7.46 days producing particles up to 1.4mm (Paolo Battistoni, Paci, Fatone, & Pavan, 2005)

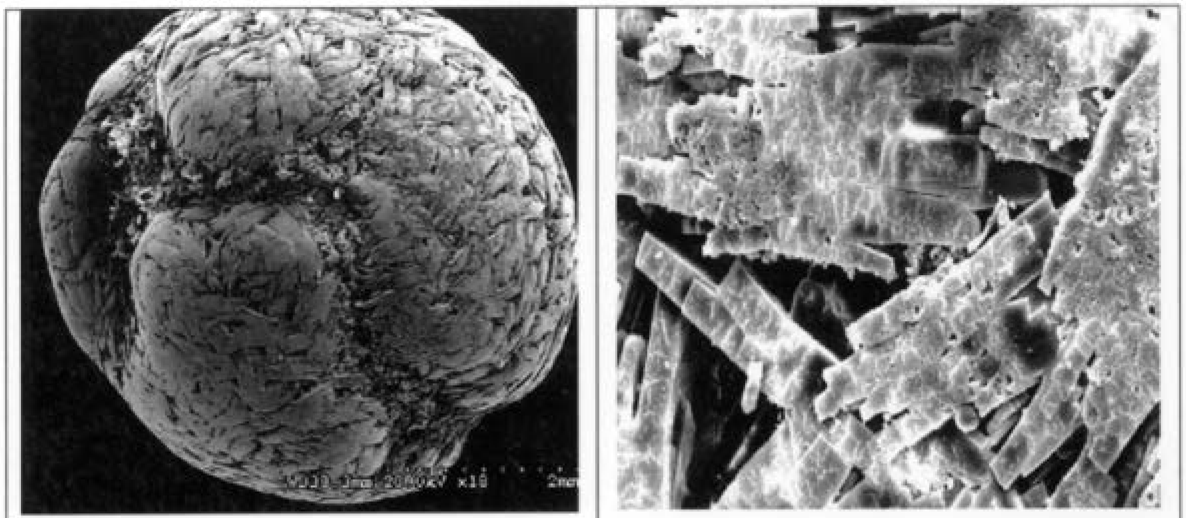

Fig.4-A: Outside appearance magnified at 18X

Fig. 4-B: Smooth surface magnified at 300X

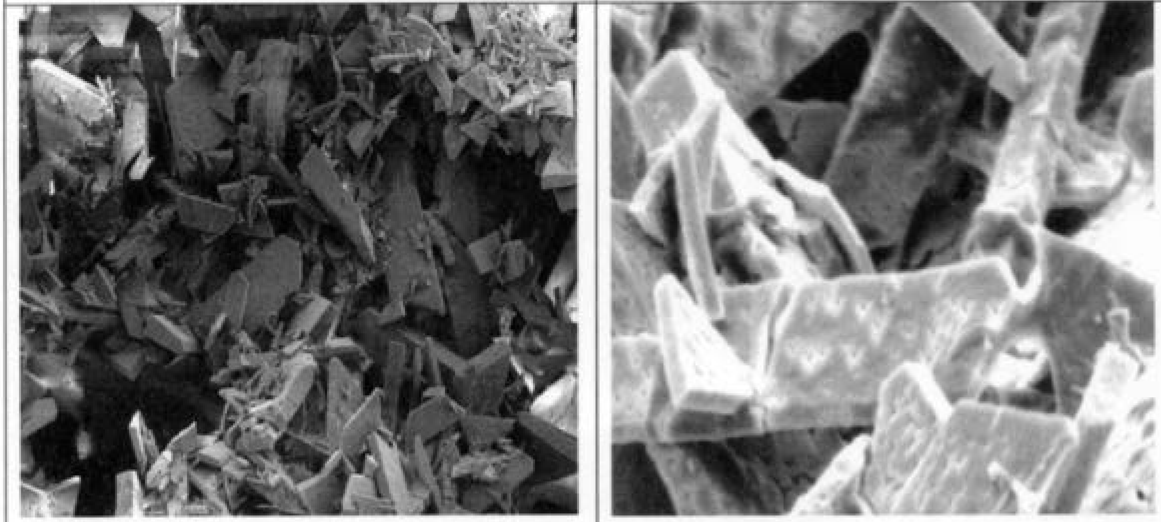

Fig. 4-C: Coarse surface magnified at 300X

Fig. 4-D: Coarse surface magnified at 3000X

Figure 2.6 – SEM images of crystals from a fluidised bed reactor fed with digester supernatant. Particle diameter reached 1.5mm in diameter with a CRT of 10 to 20 days (Huang, Mavinic, Lo, & Koch, 2005)

While struvite aggregation is commonly observed, it is not thoroughly investigated. As discussed earlier, one study using coagulants to promote aggregation, found average particle size increased from 75 – 750 µm with reduction in zeta potential (Le Corre, Valsami-Jones, et al., 2007a). However, the structural stability of agglomerates and the biological impacts of some coagulants on fertilisers are unknown. Only one work has experimentally determined kinetics of struvite nucleation, growth and aggregation (Galbraith et al., 2014). Discretised population balance methods were used to analyse data from a stirred batch vessel fed with equimolar 0.005 M feed operating at *SI* = 0.37 – 0.74. Galbraith regressed an aggregation kernel in the range of 10^{-8} to 10^{-10}, which was within a reasonable range when compared to studies of other sparingly soluble salts. While this work regresses kinetic parameters using extensive PSD and concentration data, it does finds high correlation between kinetic parameters and makes assumptions about the PSD below 2 microns. As such, work in this thesis will attempt to reduce the probability of parametric correlation and measure particles below 2 microns.

2.3 Summary

- Thermodynamics
    - Non-ideal solution chemistry modelling coupled with a charge balance is best suited to describe supersaturation and predict pH over a broad range of conditions
    - It is assumed that ion activity coefficients can be modelled at ionic strengths of <0.5 M using the DeBye-Hückel equation with Davies approximation
    - The H_3PO_4 ion is not included in the thermodynamic model as it does not affect *SI* prediction and can cause numerical problems
- Nucleation
    - Struvite induction time increases exponentially below *SI* = 0.8 and the lower saturation bound for homogeneous nucleation has been predicted to occur anywhere in the range of $SI = 0.237 - 0.69$
    - Primary nucleation rate is highly sensitive to interfacial tension
    - Secondary nucleation likely plays a significant role in struvite for particles below 100microns

    - Due to the high uncertainty in primary nucleation kinetic model and the uncertain transition between primary and secondary nucleation, a power law model may be equally as effective at describing nucleation.
- Particle size enlargement
    - Struvite particle growth rate is most likely surface integration controlled (rather than diffusion controlled)
    - Struvite particle growth rate is low below a given supersaturation level, suggesting a surface nucleation mechanism is likely
    - Uncertainty in results can be reduced by: using full PSD measurements; operating at an *SI* large enough to observe significant crystal growth; incorporating nucleation, growth and agglomeration mechanisms; and performing model parameter optimisations using multiple variables
    - Estimated struvite growth rates vary over 5 orders of magnitude and are higher under seeded conditions than unseeded conditions
    - Increased Mg:P causes an increase in zeta potential (approaching zero), which increases the probability of successful aggregate formation
    - Struvite aggregation and agglomeration have been observed extensively but only one attempt has been made to model this phenomenon
    - This work will examine size independent aggregation as a function of *SI* only

2.4 Conclusions

Thermodynamic modelling of the struvite crystallisation system under lab conditions is relatively well understood and can be used to predict a driving force (*SI* in this work) for the rate of crystallisation. Selection of a predictive kinetic model (able to match data at a different SI) is the main limitation of existing struvite crystallisation modelling. Two factors contributing to this problem are addressed in this work: (1) applying kinetic models which do not fully describe the crystallisation process (nucleation, growth and aggregation), and (2) uncertainty in nucleation and growth parameters at low SI. The first is overcome here by using a population balance model, which is described in Chapter 3 and the second is addressed by using a high supersaturation achieved by rapid mixing followed by Poiseuille flow. A continuum model for the experimental system is developed in Chapter 4.

Chapter 3 Discretised population balance development and validation

---

This chapter provides a background on population balances and describes the formulation of the cell average (CA) discretised population balance (DPB). DPBs are developed and validated against nucleation-growth and growth-aggregation analytic solutions.

3.1 Population balances

Nucleation, growth and agglomeration crystallisation processes are impossible to separate as they are coupled. This is true both in theory and reality. For example, crystal agglomeration cannot be modelled alone as the cementing of particles is dependent on the growth rate. Similarly, nucleation may continuously introduce new particles into the system, altering the number of particles growing and agglomerating. This chapter focuses on the development of a theoretical framework call a population balance model (PBM), which is necessary to describe all processes simultaneously and predict the resulting particle size distribution (PSD).

3.1.1 General formulation

Equation 3.1 shows the general form of the population balance for a batch system

$$\frac{\partial n(t,x)}{\partial t}+\frac{\partial[G(t,x)n(t,x)]}{\partial x}=B(t,x)-D(t,x) \qquad 3.1$$

Where x is the distribution domain (internal physical property/ coordinate), which is usually a characteristic particle length or particle volume and $n(t,x)$ is the number density distribution, which is related to particle number per unit volume (N) by equation 3.2. The internal coordinate x will henceforth be used to represent particle length.

$$n(t,x) = \frac{dN(t)}{dx} \tag{3.2}$$

In equation 3.1, $G(t,x)$ is the particle growth rate, which in this work is assumed to follow McCabe's ΔL law, such that the length based particle growth rate remains size independent (Jones, 2002; Alan D Randolph & Larson, 1988); $B(t,x)$ is a source term describing the birth rate of new particles, which could result from nucleation and/or aggregation events; and $D(t,x)$ is a sink term describing the death of particles due to aggregation or dissolution events. $B(t,x)$ and $D(t,x)$ can also be used to describe breakage events, but these are not considered in this work.

The PSD can be characterised by the moments of the distribution, given by equation 3.3. When the distribution domain x is chosen to be particle length, the 0th, 1st, 2nd and 3rd moments (μ_0, μ_1, μ_2 and μ_3) relate to the total particle number, total length, total surface area and total volume, respectively. When the distribution domain is chosen to be particle volume, the 0th and 1st moments relate to the total particle number and total volume, respectively.

$$\mu_j = \int_0^\infty x^j n(t,x)\, dx \tag{3.3}$$

Analytic solutions for PBMs only exist for specific conditions, so they are most commonly solved using numerical techniques. A commonly applied technique (and that used in this work) is a sectional method where the continuous distribution function $n(x)$ is approximated by a discrete distribution function as illustrated by Figure 3.1 below.

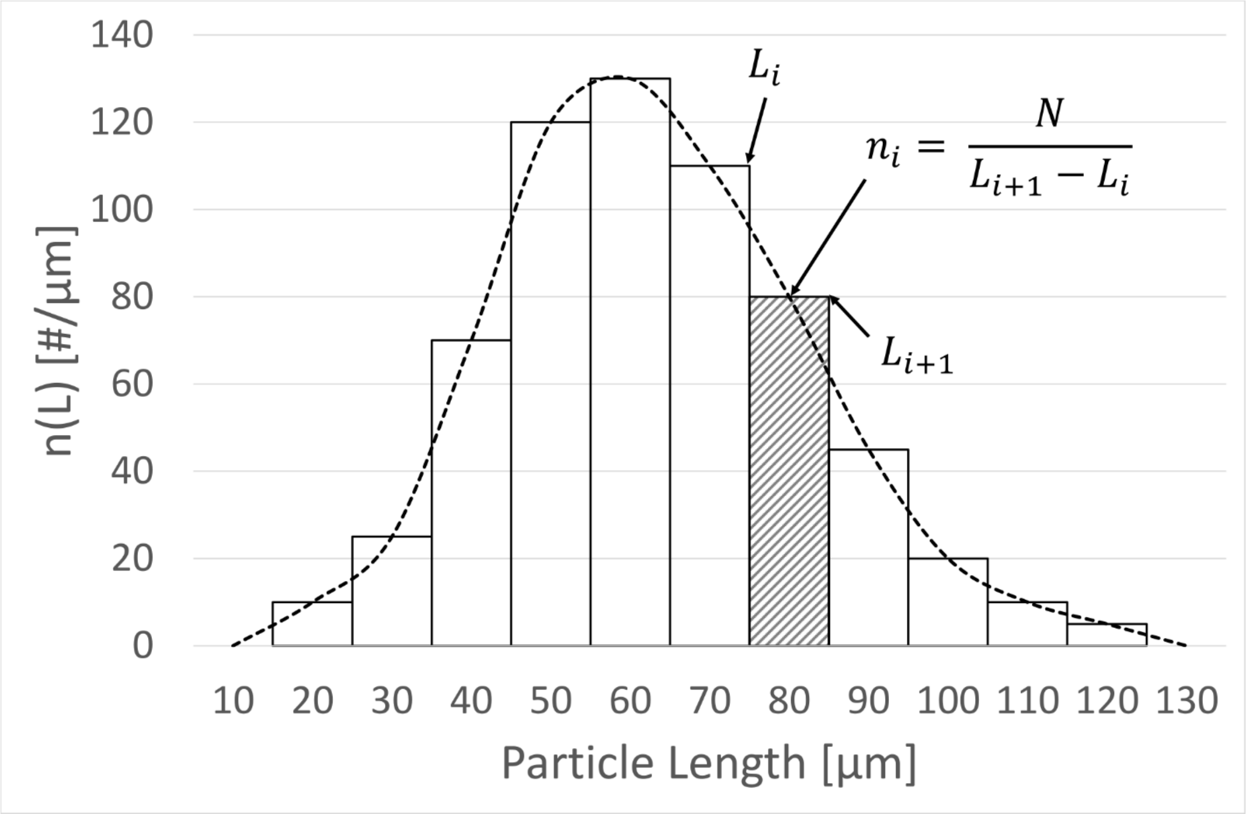

Figure 3.1 – PSD Discretisation

The PBM is approximated by a series of ordinary differential equations, creating what is referred to as a discretised population balance (DPB). The information presented below gives a brief background on DPBs with targeted information relevant to this work.

3.1.2 Discretisation methods

DPB resolution and computing requirements increase with increasing discretisation, thus a balance must be made between resolution and solution time. While using a uniformly distributed discretisation provides an accurate solution (Sutugin & Fuchs, 1970; Tolfo, 1977), often a geometric discretisation of the particle volume domain is used to achieve higher number resolution at the lower end of the scale while minimising the discretisation number necessary to represent the full domain (Michael J Hounslow, 1990a; S. Kumar & Ramkrishna, 1996b).

A geometric discretisation can follow any relationship which causes the step between representative cell sizes to increase with the cell number. The use of a geometric discretisation introduces a problem though – during aggregation events, particles in lower cell sizes do not combine to be represented by higher cell sizes. This is shown visually in Figure 3.2, where on a geometric discretisation, a particle of volume v_1 aggregates with a particle of volume v_2 to become a particle of a larger volume ($\bar{v}$), not equal to a representative size on the discretisation domain.

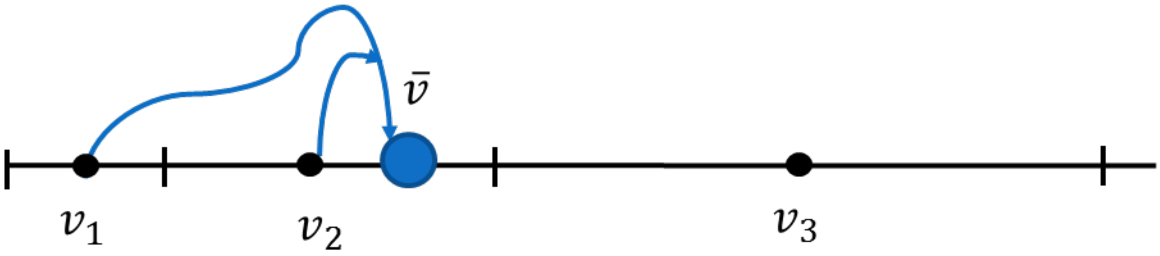

Figure 3.2 – Geometric discretisation of an aggregation event

Hounslow proposed the first DPB solution, able to reasonably conserve particle volume and number for nucleation, growth and aggregation problems using a geometric discretisation (Michael J Hounslow, 1990a). This formulation is of particular interest to this work as a hybridized version (discussed below) has been used to investigate struvite crystallisation kinetics (Galbraith & Schneider, 2014). The discretisation utilised a constant ratio in volume between one cell and the next, as described by the equivalent equations 3.4 and 3.5. This formulation was subsequently extended to enable variable discretisation coarseness (Wynn, 1996). While interesting this is not employed in this work.

$$\frac{v_i}{v_{i-1}} = 2 \qquad 3.4$$

$$\frac{L_i}{L_{i-1}} = \sqrt[3]{2} \qquad 3.5$$

3.1.3 First cell size and nucleation rate

Nuclei are expected to form on the same size scale as crystal constituents, although nuclei size is notoriously difficult to define, let alone measure (section 2.2.3). Numerically, nucleation is described by the appearance of particles at the representative size of the first cell. Setting the first cell size to an atomic scale would require a very large number of discretisation cells to represent the entire size domain, significantly increasing the computational burden. As such, the first cell size was set low enough to ensure that particles grow from their actual nuclei size to the first cell size fast enough for effects on total particle volume to be negligible. This work utilises a first cell representative size of 0.01µm, which has been estimated to be suitable for struvite (Galbraith, 2011) and coincides with the minimum resolution of the Malvern Mastersizer3000 used for particle size measurement.

3.1.4 Selected numerical methods

The nucleation and growth discretisation method initially proposed by Hounslow (equation 3.6) is numerically stable but results in some 'leakage' (*i.e.* false contribution) of particles into higher cells, creating an overestimation of the third moment of the number-length distribution and thus particle volume (Michael J Hounslow, 1990a). To account for this, Hounslow introduced and refined a 3-term nucleation and growth equation given in equation 3.7.

$$\left.\frac{dN_i}{dt}\right|_{NG} = \begin{cases} B_0 + \dfrac{G_L N_1}{(r-1)L_1} & i = 1 \\ \dfrac{G_L}{(r-1)L_i}(rN_{i-1} - N_i) & i > 1 \end{cases} \tag{3.6}$$

$$\left.\frac{dN_i}{dt}\right|_{NG} = \begin{cases} B_0 + \dfrac{2G_L}{(1+r)L_1}\left(\left(1 - \dfrac{r^2}{r^2-1}\right)N_1 - \dfrac{r}{r^2-1}N_2\right) & i = 1 \\ \dfrac{2G_L}{(1+r)L_i}\left(\dfrac{r}{r^2-1}N_{i-1} + N_i - \dfrac{r}{r^2-1}N_{i+1}\right) & i > 1 \end{cases} \tag{3.7}$$

Equation 3.8 shows the aggregation formulation proposed by Hounslow, which can be applied in conjunction with either equation 3.6 or 3.7.

$$\left.\frac{dN_i}{dt}\right|_{AGG} = N_{i-1}\beta_0 \sum_{j=1}^{i-2} 2^{j-i+1} N_j + \frac{1}{2}\beta_0 N_{i-1}^2 - N_i \beta_0 \sum_{j=1}^{i-1} 2^{j-i} N_j - N_i \beta_0 \sum_{j=1}^{N_{eq}} N_j \qquad 3.8$$

While the 3-term nucleation and growth equation (3.7) is more accurate, it is unstable when applied to a dynamic mixed suspension mixed product removal (MSMPR) reactor. In order to extend Hounslow's work to dynamic simulation, Galbraith used a sigmoid function to transition between the 2-term and 3-term forms of the nucleation and crystal growth DPBs (Galbraith et al., 2014). This approach enabled a compromise between the numerical stability of the 2-term model at lower particle size ranges and numerical resolution of the 3-term model at higher particle size ranges. Since this approach has been used for struvite investigations, it will be used in this work for comparative purposes to the new approach under consideration. This Galbraith modified Hounslow technique will henceforth be referred to as GMH.

A significant development since Hounslow's work was that of Kumar and Ramkrishna, who developed a solution method referred to as the 'fixed pivot technique', which is applicable to any discretisation scheme, and can be reduced to the Hounslow formulation when applied to the same discretisation (S. Kumar & Ramkrishna, 1996a). The fixed pivot technique assigns a fraction of each birth in a cell to an adjacent cell based on the position of the birth, taking into account the range between the representative volume below and above the cell in question. While relatively accurate, the particle property distribution results are consistently over-predicted by the fixed pivot method (J. Kumar, Peglow, Warnecke, & Heinrich, 2008). Additionally, without the particle growth term, the fixed pivot method produces some error (Alexopoulos & Kiparissides, 2005). Kumar and Ramkrishna also proposed a moving pivot technique for scenarios where growth is a dominant term (S. Kumar & Ramkrishna, 1997), however, while highly accurate, this method is difficult to apply for scenarios involving nucleation as it requires a continuously increasing number of discretisation elements (Alexopoulos & Kiparissides, 2005).

The cell average technique (abbreviated CAT), which is applied in this work, extends on work by Kumar and Ramkrishna by applying a finite volume scheme (J. Kumar et al., 2008). This technique differs from the fixed pivot technique by averaging the total births into a cell before performing a single redistribution of particles, rather than redistributing each individual birth event. A further advantage of the cell average technique is that it can be extended to conserve any number of moments of a distribution. While detailed descriptions of the cell averaged technique are available in multiple publications (J. Kumar, 2006; J. Kumar et al., 2008), they are presented in the following section for the clarity of the reader.

3.2 Cell average technique

First we must explore the formulation and nomenclature of the discretisation method. In the cell average technique, the particle number density distribution is divided into I cells, where the lower and upper bounds of the i^{th} cell are denoted by $v_{i-\frac{1}{2}}$ and $v_{i+\frac{1}{2}}$, respectively. All particles belonging to a cell are identified by a representative size, or grid point, v_i. Figure 3.3 gives a visual representation of three adjacent cells. While the representative size, v_i, could be chosen at any point between the lower and upper bounds of the cell, this work uses the mean volume between those bounds *i.e.* $v_i = \left(v_{i-1/2} + v_{i+1/2}\right)/2$.

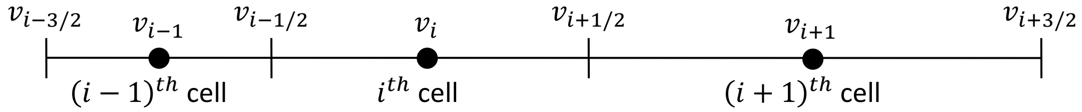

Figure 3.3 - Cell average discretisation

The cell average technique transforms the general continuous population balance into a set of I ODEs of the form:

$$\frac{dN_i}{dt} = \underbrace{B_i^{CA}}_{birth\ events} - \underbrace{D_i}_{death\ events} \quad , i = 1,2, \dots I \tag{3.9}$$

Where N_i is the total number of particles in cell i, B and D represents the “birth” and “death” rates of particles into cell i (alternatively the net inflow and outflow of particles from cell i) and CA denotes that cell averaging is used. The CA technique is constituted by the following four steps.

1. Calculate particle births and deaths resulting from particle processes (growth, agglomeration and nucleation events)
2. Calculate average volume of particles born into a cell
3. Distribute particles between current and adjacent (above or below) cells based on their relative position to the cell representative size
4. Solve ODEs expressing the total change of particle number at the representative size in each cell resulting from particle births and deaths (equation 3.9)

3.2.1 Step 1 - expression for total births

Consider P particle births $B_{i,1}, B_{i,2}, \dots, B_{i,P}$ at corresponding positions $v_{i,1}, v_{i,2}, \dots, v_{i,P}$ within the i^{th} cell. Each birth could have resulted from any process (nucleation, growth, agglomeration and/or breakage), meaning that it may not necessarily occur at the representative volume v_i. This is especially true for aggregation events, as discussed earlier. Methods for calculating these birth volumes are described in section 3.3 below. In general terms, the total birth rate of particles in the i^{th} cell is calculated by summing the birth rates resulting from each process:

$$B_i = \sum_{p=1}^{P} B_{i,p} \qquad 3.10$$

3.2.2 Step 2 - expression for average volume:

The average volume of newborn particles in cell i is then given by

$$\bar{v}_i = \frac{\sum_{j=1}^{n} v_{i,j} B_{i,j}}{B_i} \qquad 3.11$$

Using equations 3.10 and 3.11, the total contribution of particle number and mass can be equated to B_i particles located at size $\bar{v}_i$. If the average size $\bar{v}_i$ matches the representative size, v_i, then the total birth rate B_i can be assigned to the cell v_i. In the more likely alternative, where the average size is not equal to the representative size, a fraction of the total birth rate, B_i, is assigned to v_i and the remainder is assigned to the representative volume of a neighbouring cell (either v_{i-1} or v_{i+1}), conservation of particle number and volume. The proportion of particles assigned to the neighboring cells is calculated based on the average volume of newborn particles in the cell, $\bar{v}_i$, relative to the representative sizes of cell i and the neighboring cell. If the average volume is greater than the representative cell size then a fraction of the volume is assigned to the upper cell, (v_{i+1}). Similarly if the average volume is less than the representative cell size, a fraction of the volume is assigned to the lower cell, (v_{i-1}). The manner of redistribution will be discussed in detail below.

3.2.3 Step 3 - expression for redistribution

Redistribution of the birth rate into cell i will be demonstrated by examining the scenario where $\bar{v}_i > v_i$ (Figure 3.4), although the process remains the same for $\bar{v}_i < v_i$. In either case the overriding goal is to conserve (preserve) the number of particle born in the cell, so as not to gain/lose particles due to the approximate nature of the discretisation. The birth rate of particles distributed to v_i and v_{i+1}, are denoted a_i and a_{i+1} respectively. Equation 3.12 shows that the sum of b_i and b_{i+1} is equal to the total birth rate of particles, B_i, calculated in step 1.

$$B_i = b_i + b_{i+1} \tag{3.12}$$

Conservation of particle volume is ensured by equating the total rate of change of volume at $\bar{v}_i$ to the rate of change of volume resulting from the reassignment to v_i and v_{i+1} (equation 3.13):

$$B_i \bar{v}_i = v_i b_i + v_{i+1} b_{i+1} \tag{3.13}$$

By combining equations 3.12 and 3.13, we can solve for a_i and a_{i+1}. The ratios of volume in a_i and a_{i+1} are expressed visually in Figure 3.4

$$b(\bar{v}_i, v_i) = B_i \frac{\bar{v}_i - v_{i+1}}{v_i - v_{i+1}} \tag{3.14}$$

$$b_{i+1}(\bar{v}_i, v_{i+1}) = B_i \frac{\bar{v}_i - v_i}{v_{i+1} - v_i} \tag{3.15}$$

Figure 3.4 - Reassignment of particles into adjacent cells. Adapted from (J. Kumar et al., 2008).

In the scenario where $\bar{v}_i = v_i$, no births are assigned to v_{i+1}, while in the scenario where $\bar{v}_i = v_{i+1/2}$, 50% (assuming uniform spacing of representative volumes) of births are assigned to v_{i+1}. To generalise, for the average volume being either higher or lower than the representative volume, the lambda function is defined:

$$\lambda_i^{\pm}(v) = \frac{v - v_{i\pm1}}{v_i - v_{i\pm1}} \qquad 3.16$$

Where the i in $\lambda_i^{\pm}(v)$ denotes the cell to which the particles will be assigned, v is a variable representing the average volume under consideration (*i.e.* $\bar{v}_{i-1}$, $\bar{v}_i$ or $\bar{v}_{i+1}$) and $\pm$ is the sign used to indicate the upper or lower reference cell (all signs in the expression are either + or -).

Equation 3.14 can be rewritten as:

$$b_i(\bar{v}_i, v_i) = B_i \lambda_i^{+}(\bar{v}_i) \qquad 3.17$$

Where

$$\lambda_i^{+}(\bar{v}_i) = \frac{\bar{v}_i - v_{i+1}}{v_i - v_{i+1}} \qquad 3.18$$

Similarly, equation 3.15 can be written as:

$$a_{i+1}(\bar{v}_i, v_{i+1}) = B_i \lambda_{i+1}^{-}(\bar{v}_i) \qquad 3.19$$

Where

$$\lambda_{i+1}^{-}(\bar{v}_i) = \frac{\bar{v}_i - v_i}{v_{i+1} - v_i} \qquad 3.20$$

Equation 3.20 refers to an assignment of a fraction of particles away from cell i. In practice this quantity is not calculated when examining the rate of change of particles in cell i, rather, it is accounted for by the birth term of the cell receiving the assignment. The standard expressions for distributions of birth rates into cell i are given in step 4.

3.2.4 Step 4 - development of ODEs describing change in total particle number

The cell average birth rate may be contributed to by four potential redistributed rates. Two potential contributions come from fractions of the birth rates in the lower (v_{i-1}) and upper (v_{i+1}) cells. Another two potential contributions exist within cell i, depending on whether $\bar{v}_i$ is greater or less than v_i. The specific contributions which occur are determined by the relative position of the average volume of particles born into each cell in the previous time step. The associated lambda function for each potential redistribution are given by equations 3.21 to 3.24.

For $\bar{v}_{i-1} > v_{i-1}$, a fraction of $B_{i-1}$is assigned to v_i:

$$\lambda_i^-(\bar{v}_{i-1}) = \frac{\bar{v}_{i-1} - v_{i-1}}{v_i - v_{i-1}} \tag{3.21}$$

For $\bar{v}_i < v_i$ a fraction of B_i is assigned to v_i:

$$\lambda_i^-(\bar{v}_i) = \frac{\bar{v}_i - v_{i-1}}{v_i - v_{i-1}} \tag{3.22}$$

For $\bar{v}_i > v_i$ a fraction of B_i is assigned to v_i:

$$\lambda_i^+(\bar{v}_i) = \frac{\bar{v}_i - v_{i+1}}{v_i - v_{i+1}} \tag{3.23}$$

For $\bar{v}_{i+1} < v_{i+1}$, a fraction of $B_{i+1}$is assigned to v_i:

$$\lambda_i^+(\bar{v}_{i+1}) = \frac{\bar{v}_{i+1} - v_{i+1}}{v_i - v_{i+1}} \tag{3.24}$$

A general description of births into cell i is given by equation 3.25.

$$\begin{aligned} B_i^{CA} = {} & B_{i-1}\lambda_i^-(\bar{v}_{i-1})H(\bar{v}_{i-1} - v_{i-1}) \\ & + B_i\lambda_i^-(\bar{v}_i)H(v_i - \bar{v}_i) \\ & + B_i\lambda_i^+(\bar{v}_i)H(\bar{v}_i - v_i) \\ & + B_{i+1}\lambda_i^+(\bar{v}_{i+1})H(v_{i+1} - \bar{v}_{i+1}) \end{aligned} \tag{3.25}$$

Where the Heaviside step function, $H(x)$, (*i.e.* the unit step function) is defined by:

$$H(x) = \begin{cases} 1, & x > 0 \\ \frac{1}{2}, & x = 0 \\ 0 & x < 0 \end{cases} \quad 3.26$$

This expression is used to isolate the correct contributions to the total birth rate at v_i. For example, in the scenario where $\bar{v}_i > v_i$, the second term in equation 3.25 becomes zero as the lambda function in this term (given by equation 3.22) represents the alternate scenario where $\bar{v}_i < v_i$.

At this point, a method has been developed for reassigning fractions of the total particle number born into a cell to the representative volumes of that cell and a neighbouring cell. The reassignment is based on the average volume relative to the representative volumes and conserves particle number and volume. In the following sections, the model implementation is presented and numerical models for different combinations of crystallisation mechanisms are compared to analytic solutions to assess their relative resolution. Formulations of these numerical models are presented in Appendix B, analytic solutions are presented in Appendix C and sample code for these models, coded in the software package gPROMS, is presented in Appendix E.

3.3 DPB implementation

The following section describes formulations of the total particle birth and death rates $[particles. L^{-1}. \min^{-1}]$ and volume growth rate $[\mu m^3. L^{-1}. \min^{-1}]$ in each cell, resulting from each crystallisation mechanism. The birth rates are used to calculate the volume rates, which are then used in birth rate reassignment calculations (sections 3.2.3 and 3.2.4). The resulting birth rates, modified by the cell average technique, are then combined with the death rates to create the overall DPB which conserves particle number and volume.

3.3.1 Nucleation

Nucleation was assumed to occur at a fixed rate of B_{nuc} $[particles. L^{-1} min^{-1}]$ in the first cell representative size, $v_1 [um^3. particles^{-1}]$. The volume rate, $V_{nuc,1} [um^3. L^{-1} min^{-1}]$, was then calculated using equation 3.27 below. No particle deaths result from particle nucleation.

$$V_{nuc,1} = B_{nuc} v_1 \tag{3.27}$$

3.3.2 Growth

Growth is represented by the birth of particles in a cell ($B_{growth,i}$ $[particles. L^{-1}.\min^{-1}]$) slightly larger than the representative size of the cell (equation 3.28), balanced by an equal death rate of particles from the representative size of the cell (equation 3.29). This ensures that a positive crystal volume rate exists ($V_{growth,i}$ $[um^3. L^{-1} min^{-1}]$ in equation 3.30), adding crystal volume to each cell, while the number of particles goes unchanged. The volume, $v_{0,g}$ $[um^3]$, in equations 3.28 and 3.29 represents the small mass increment used to approximate growth – in this work it was arbitrarily set to 10% of the first cell volume and found to have no significant difference on results when compared to an analytic solution.

$$B_{growth,i} = \frac{G_v N_i}{v_{0,g}} \tag{3.28}$$

$$D_{growth} = \frac{G_v N_i}{v_{0,g}} \tag{3.29}$$

$$V_{growth,i} = B_{growth,i}\left(v_i + v_{0,g}\right) \tag{3.30}$$

3.3.3 Aggregation

Particle births in each cell resulting from aggregation are calculated by adding contributions from all possible combinations of smaller particles (equation 3.31). The aggregation rate from each combination depends on the number of particles in each cell (N_j and N_k) and the aggregation kernel ($\beta_{j,k}$), which describes the likelihood of a successful aggregation event. The Dirac function $\left(1 - \frac{1}{2}\delta_{j,k}\right)$ is used to avoid double counting of particle interactions; it is equal to ½ when $j = k$ and 1 for all other scenarios. To avoid logic statements within the code, the summation is generalised to occur over all cells (where NEQ is the final cell) and the AGG_INDEX term (equation 3.32) describes whether two colliding particles from cells j and k would result in the birth of a particle in cell i. .

$$B_{agg,i} = \sum_{j,k=1}^{NEQ} AGG\_INDEX_i \times \left(1 - \frac{1}{2}\delta_{j,k}\right) \beta_{j,k} N_j N_k \tag{3.31}$$

$$AGG\_INDEX = \left(0.5 + 0.5H\left(v_{i+1/2} - v_{agg}\right)\right)\left(0.5 + 0.5H\left(v_{agg} - v_{i-1/2}\right)\right) \tag{3.32}$$

Where $v_{agg} = v_j + v_k$. The death rate resulting from aggregation is given by the sum of all possible aggregation events that could occur between the cell and other cells (equation 3.33).

$$D_{agg,i} = N_i \sum_{k=1}^{NEQ} \beta_{i,k} N_k \tag{3.33}$$

The total volume added by aggregation is calculated by introducing the aggregate volume into equation 3.31, as shown in equation 3.34 below:

$$V_{agg,i} = \sum_{j,k}^{NEQ} AGG\_INDEX_i \times \left(1 - \frac{1}{2}\delta_{j,k}\right) \beta_{j,k} N_j N_k \, v_{agg,j,k} \tag{3.34}$$

3.3.4 Combined processes

Finally, total birth rate (equation 3.35) and volume (equation 3.36) are used to calculate the average volume of particles being born into cell i (equation 3.37).

$$B_{tot,i} = B_{nuc,i} + B_{growth,i} + B_{agg,i} \tag{3.35}$$

$$V_{tot,i} = V_{nuc,i} + V_{growth,i} + V_{agg,i} \tag{3.36}$$

$$\overline{v_i} = \frac{V_{tot,i}}{B_{tot,i}} \qquad 3.37$$

Total death rate in cell i is given by equation 3.38

$$D_{tot,i} = D_{growth,i} + D_{agg,i} \qquad 3.38$$

The overall DPB is the constructed by substituting each of the abovementioned terms into equation 3.25 and calculating Heaviside and Lambda functions.

3.4 Validations

Validations were conducted by comparing numerical solutions to analytic (exact) solutions for specific scenarios where analytic solutions are possible. This was done for nucleation-growth and growth-aggregation scenarios, covering all mechanisms which are expected to affect struvite PSDs in this work. For all validations, the PSD was discretised using the geometric progression defined by equations 3.4 and 3.5 to allow comparison between the CAT and GMH techniques, where possible. For nucleation and crystal growth scenarios, residence time was set to that of the reactor defined in section 4.1.3, while for the aggregation and crystal growth scenario, the dimensionless growth time was used (appendix section B.3). The nucleation, growth and aggregation rates were arbitrarily assigned values shown below Table 3.1. In later analyses, these rates were described using power law functions of supersaturation, enabling them to reduce as supersaturation decrease.

Table 3.1 below summarises the error between analytic and numerical solutions for zeroth and first moments, showing that all errors were <5%, which is considered acceptable. The CAT was found to be more accurate than the GMH method for the nucleation-growth scenario, justifying its use to model this condition. However the GMH gave superior simulation times when modelling nucleation growth and aggregation simultaneously. Therefore, the CAT method was used to model nucleation and growth while the GMH method was used to model aggregation. The growth rate description utilised in the GMH solution was not compatible with the analytic solution and was therefore not included.

Table 3.1 – Error in numerical solutions for PSD moments

Scenario	Cell Average		Galbraith Modified Hounslow	
	μ_0 error [%]	μ_1 error [%]	μ_0 error [%]	μ_1 error [%]
Nucleation & Growth*	-1.30×10^{-16}	6.83×10^{-6}	2.59×10^{-14}	4.55
Aggregation & Growth**	5.02×10^{-4}	-4.15	N/A	N/A

$*G_L = 10, B_{nuc} = 1 \times 10^7; ** \; G_0 = 10, \beta_0 = 1 \times 10^{-6}$

Figure 3.5, Figure 3.6 and Figure 3.7 compare final numerical and analytic PSDs for each scenario. Figure 3.5 and Figure 3.6 show numerical diffusion around the discontinuity for the nucleation and crystal growth scenario – this diffusion is greater for the GMH technique. Similarly, Figure 3.7 shows reasonable agreement between numerical and analytic solutions at high particle numbers and deviations at low particle numbers, on either side of the distribution – this is also attributed to numerical diffusion. These results are expected for these DPB solutions (Michael J Hounslow, 1990b; J. Kumar, 2006).

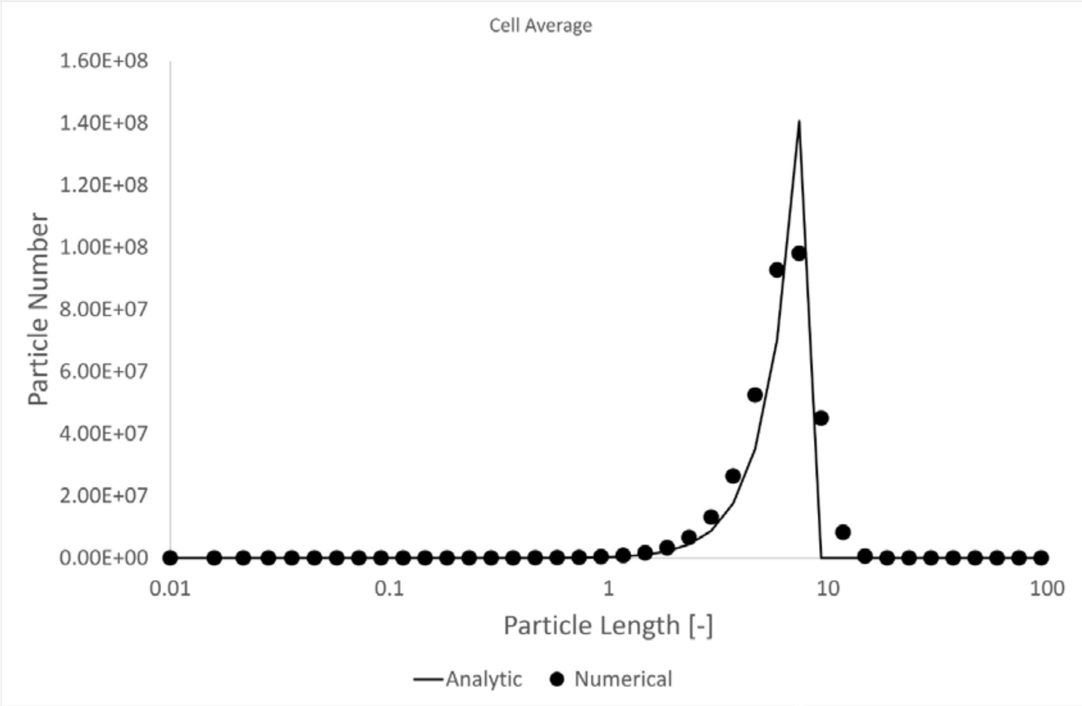

Figure 3.5 – Comparison of numerical and analytic results using the cell average technique formulation for nucleation and crystal growth

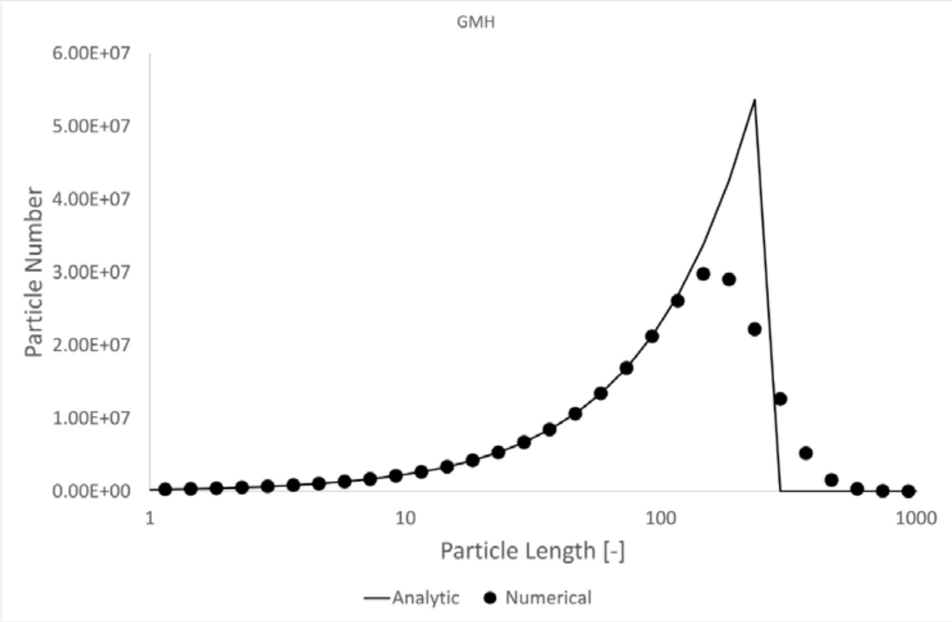

Figure 3.6 – Comparison of numerical and analytic results using the Galbraith Modified Hounslow formulation for nucleation and crystal growth

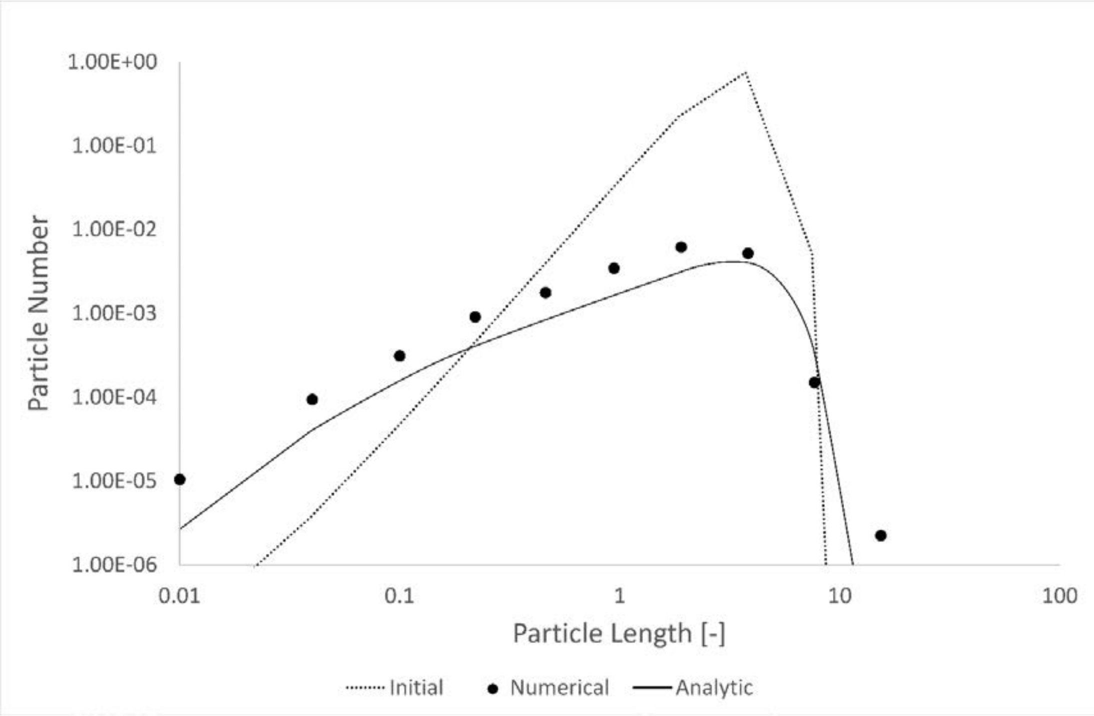

Figure 3.7 – Comparison of numerical and analytic results using the CAT formulation for aggregation and crystal growth

3.5 Summary

- Population balances are necessary to model concurrent crystallisation mechanisms
- Geometric discretisation is necessary for the efficient solution of population balance equations
- Weighting factors (GMH technique) or particle mass reassignment (CAT technique) are necessary for mass conservation in geometrically discretised population balances
- The CAT technique is slightly more accurate than the GMH technique and both conserve particle mass to within 5% of the analytic solution

3.6 Conclusion

Formulations of the Cell Average Technique and Galbraith Modified Hounslow technique were tested against analytic solutions where possible. For the nucleation and growth scenario, both techniques were accurate to within 5%, although the CAT was more accurate than GMH. While an analytic solution was not possible for the nucleation, growth and aggregation scenario, the GMH delivered significantly better simulation times. Based on these results, modelling and parameter optimisation for nucleation and growth was conducted using the CAT, and that for aggregation was conducted using GMH method. Further detail on parameter optimisation procedures is given in chapter 7.

Chapter 4 Poiseuille flow crystalliser model development

This chapter describes the Poiseuille flow crystalliser (PFC) experimental apparatus used in this work, followed by the development of an advection-diffusion-reaction model used to represent it. Following that, numerical solution methods and steps taken to improve model robustness and speed are presented, including a grid convergence study and scaling. Combining this model with previously described thermodynamic and kinetic models (Chapters 3 and 4) results in a full process model, which will be used for sensitivity analysis in the next chapter.

4.1 Experimental apparatus

Figure 4.1 shows the Poiseuille flow reactor (PFR) used in this work and details the analysis performed. Details of reactor design are presented, including assessment and quantification of associated trade-offs.

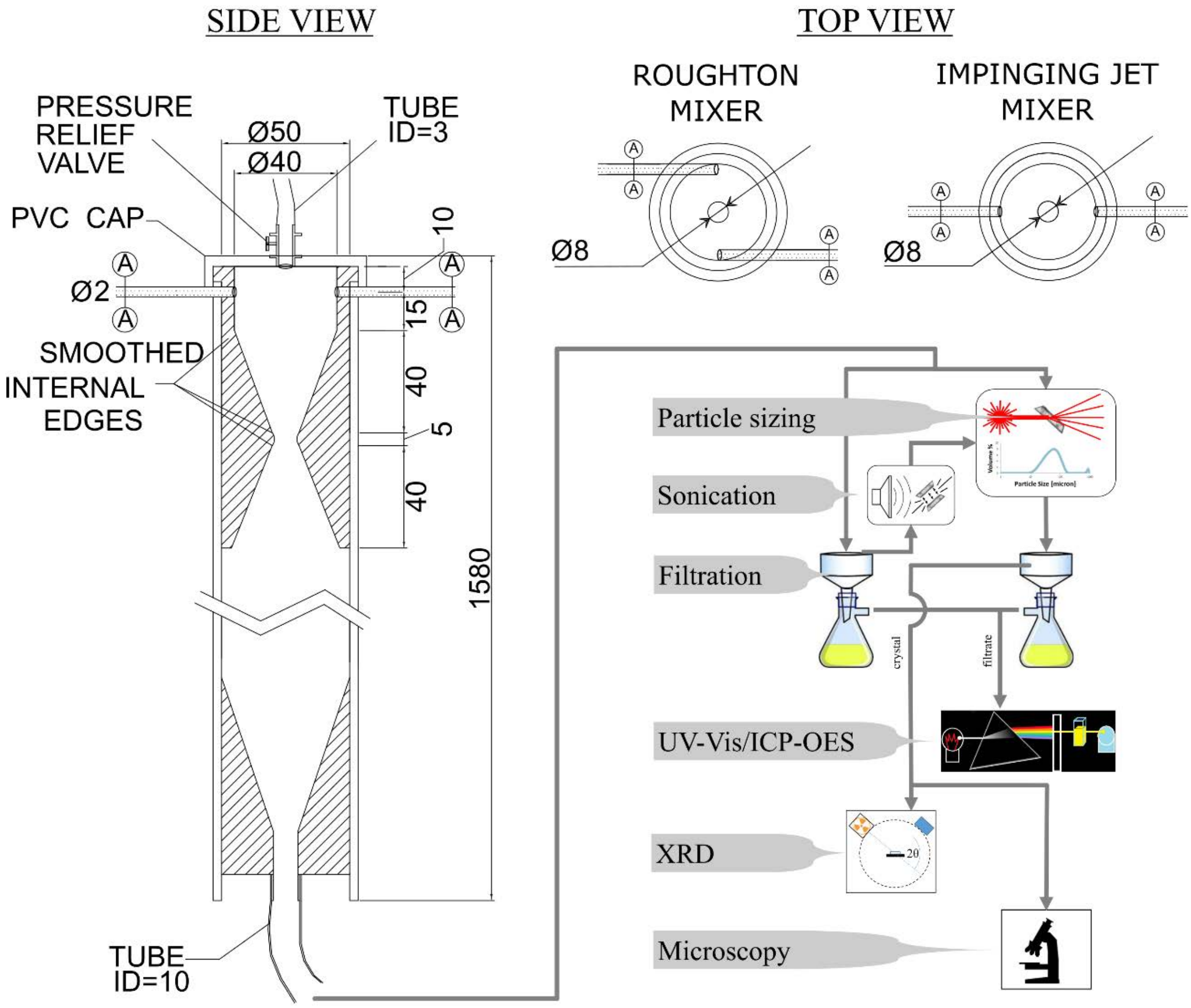

Figure 4.1 – Poiseuille flow crystalliser with rapid mixing via Roughton (R) and submerged impinging jet (IJ) mixers. All dimensions in mm.

4.1.1 Orientation

The reactor was operated vertically with downwards flow after various design iterations. Preliminary experiments showed that:

- Particles can be visually observed to settle in a horizontal pipe below fully developed turbulence (Re>4000)

- Vertical upward laminar flow creates a fluidised bed as fluid velocity near the reactor wall is less than settling velocity of larger particles. These particles then form weakly bound aggregates which contributed to blockages.
- Vertical downwards flow narrows the PSD, since larger particles tend to exit the reactor faster due to settling. Settling increases with particle size, exceeding the centreline fluid velocity for particles >100µm as shown by Figure 4.2 below.

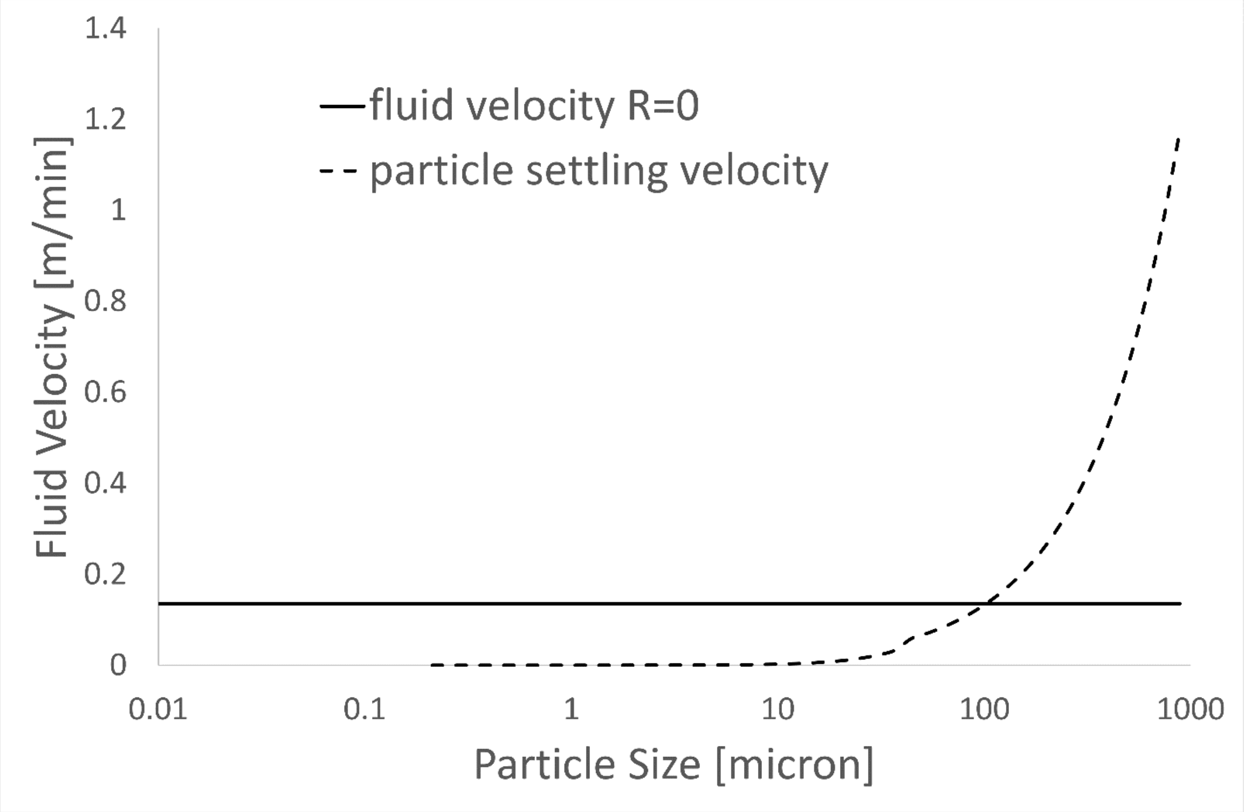

Figure 4.2 – Particle settling velocity profile

4.1.2 Length

Reactor length (1.58m) was limited to the ceiling-to-bench distance, while the diameter was selected to enable a range of residence times to be achieved (11.5 – 23min).

4.1.3 Residence time

The minimum residence time (on the flow centreline) was selected to be the time taken for 90% de-supersaturation to occur. This time was estimated by measuring pH response in batch experiments using a variety of synthetic feeds (Synthetic urine - 0.02M P Mg:N:P = 1.5:7:1 (Maurer, Pronk, & Larsen, 2006; Udert, Larsen, Biebow, & Gujer, 2003); Synthetic equimolar 0.02M P; Synthetic digester centrate - 0.0028M P Mg:N:P = 1.5:11:1 (Cleveland Bay Purification Plant, Townsville)). The average residence time used was 23.12min.

4.1.4 Diameter

Reactor diameter $D_{reactor}\ [m]$ was calculated based on selected feed flow rate $Q\ [m^3 min^{-1}]$ (section **5.2.1**), mean residence time $\bar{t}\ [min]$ and reactor length $Z\ [m]$ using equation 4.1.

$$D_{reactor} = \sqrt{\frac{4Q\bar{t}}{\pi Z}} \tag{4.1}$$

The mean residence time, residence time distribution (RTD) and variance of the residence time distribution of a pipe undergoing Poiseuille flow are given by equations 4.2, 4.3 and 4.4, respectively (Levenspiel, 1999).

$$\bar{t} = \frac{V}{Q} \tag{4.2}$$

$$E(t) = \frac{\bar{t}^2}{2t^3}, t > \frac{\bar{t}}{2} \tag{4.3}$$

$$\sigma^2 = \int_0^\infty (t - \bar{t})^2 E(t)\, dt \tag{4.4}$$

Where $V\ [m^3]$ is reactor volume, $Q\ [m^3\ min^{-1}]$ is the total flow rate, $E(t)[s^{-1}]$ represents the exit age distribution of fluid elements in the reactor, $t\ [min]$ is time, $\bar{t}\ [min]$ is the mean hydraulic residence time (HRT) and $\sigma^2\ [min^2]$ is the standard deviation of the RTD. These equations show that the exit age distribution and its variance are independent of reactor dimensions for a reactor undergoing Poiseuille flow, at a given residence time. The length to diameter ratio does however affect the fraction of the reactor length necessary for full laminar flow development, known as the entry length (L_e). The entry length was calculated to be <11% of the reactor length using equation 4.5 (Munson, Young, & Okiishi, 2006).

$$L_e = 0.12Re \cdot R \tag{4.5}$$

Where Re is the Reynolds number and R $[m]$ is the reactor radius. The applicability of this entry length estimation is uncertain though since the conical diffuser expansion angle is larger than the 5° recommended to avoid flow separation in laminar flows (Sparrow, Abraham, & Minkowycz, 2009). The fluid rotation from the mixer may have reduced this effect, but without detailed investigations (via CFD for example), this cannot be quantified. For a given flow rate, the fraction of the reactor length (and the induction time) taken up by the entry length can be reduced by reducing the reactor radius. This, however requires an increase in the necessary length, something not possible in this scenario. Therefore, the flow development is an operational constraint that had to be accepted in this work.

Simulation results shown in section 4.8 predicted that 20% of the thermodynamic yield would be achieved by the reactor length where full laminar flow has developed. This means that a lower crystal mass and surface area would exist in this region and crystal growth would not be significantly affected by the transition flow.

4.1.5 Flow regime

The flow regime for the reactor was determined to be completely convective (*i.e.* Poiseuille flow model can be used and axial dispersion effects ignored) by locating the flow regime on a flow map where the Bodenstein number (Reynolds number × Schmidt number) and reactor geometry are considered (Levenspiel, 1999). This result was confirmed by modelling the reactor using an axially and radially discretised advection-diffusion-reaction model, which showed no measureable change in reactor outlet concentrations or particle size when axial and radial ion diffusion terms were excluded (section 6.3).

4.1.6 Feed stream mixing

Two feed mixing arrangements were tested. The impinging jet mixer was used to represent pilot scale fluidised bed reactors where impinging feed streams are used (Britton et al., 2005; Shimamura, Ishikawa, Tanaka, & Hirasawa, 2007), and the Roughton mixer was trialled as a more efficient alternative. The R mixer was designed to meet three criteria:

1. The mixer Reynolds number was greater than 1600 (Liu, Cheng, Prud'homme, & Fox, 2008). This is calculated using mixer diameter (40mm as shown on Figure 4.1) and inlet jet velocity. The actual mixer Reynolds number was 28,181
2. The mixing time (0.23s) was less than the mixer HRT (4.86s), which was in turn less than the lowest expected induction time (15.16s) (Alison et al., 2003; Alvarez & Myerson, 2010)
3. The mixer inlet jet diameter (2mm) was not greater than that predicted using scaling methods based on constant meso- and micro-mixing (2mm) (Gillian & Kirwan, 2008).

Mixing time was calculated based on the Kolmogorov mixing timescale (Lindenberg & Mazzotti, 2009; Liu et al., 2008). The impinging jet mixer was given the same dimensions as the Roughton mixer, with an altered jet direction as shown in Figure 4.1 (b).

4.2 Model structure

Figure 4.3 shows how the solid and liquid phase mass balance equations detailed in this chapter were linked to the thermodynamic model (section 2.1) and kinetic model (Chapter 3). All equations describing the system are distributed over the length and radius of the reactor. The liquid mass balances are used to infer the driving force for crystallisation, which are used in the kinetic models within the discretised population balance. The population balance is then used to determine the amount of crystal formed and corresponding depletion of reactants in the mass balance. The continuum equations for the solid and liquid phases describe the flow of each phase as a result of convection, diffusion and settling. These are necessary to differentiate the flow of solids and liquids in the system.

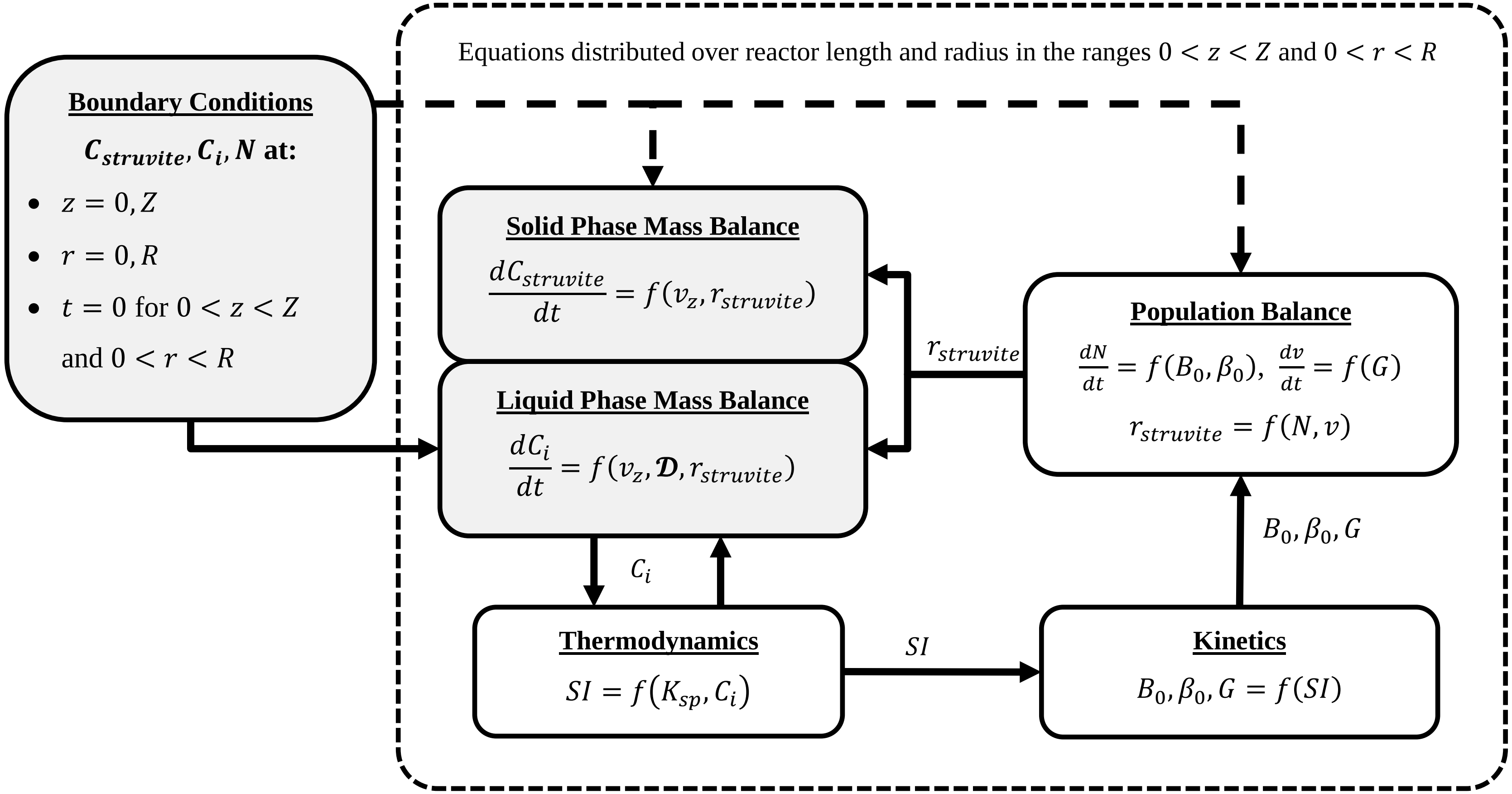

Figure 4.3 – Modelling topology highlighting the place of mass balance within the model architecture

4.3 Model equations

Reagents are fed into one end of a cylindrical reactor and allowed to react over its length, as shown in Figure 4.4.

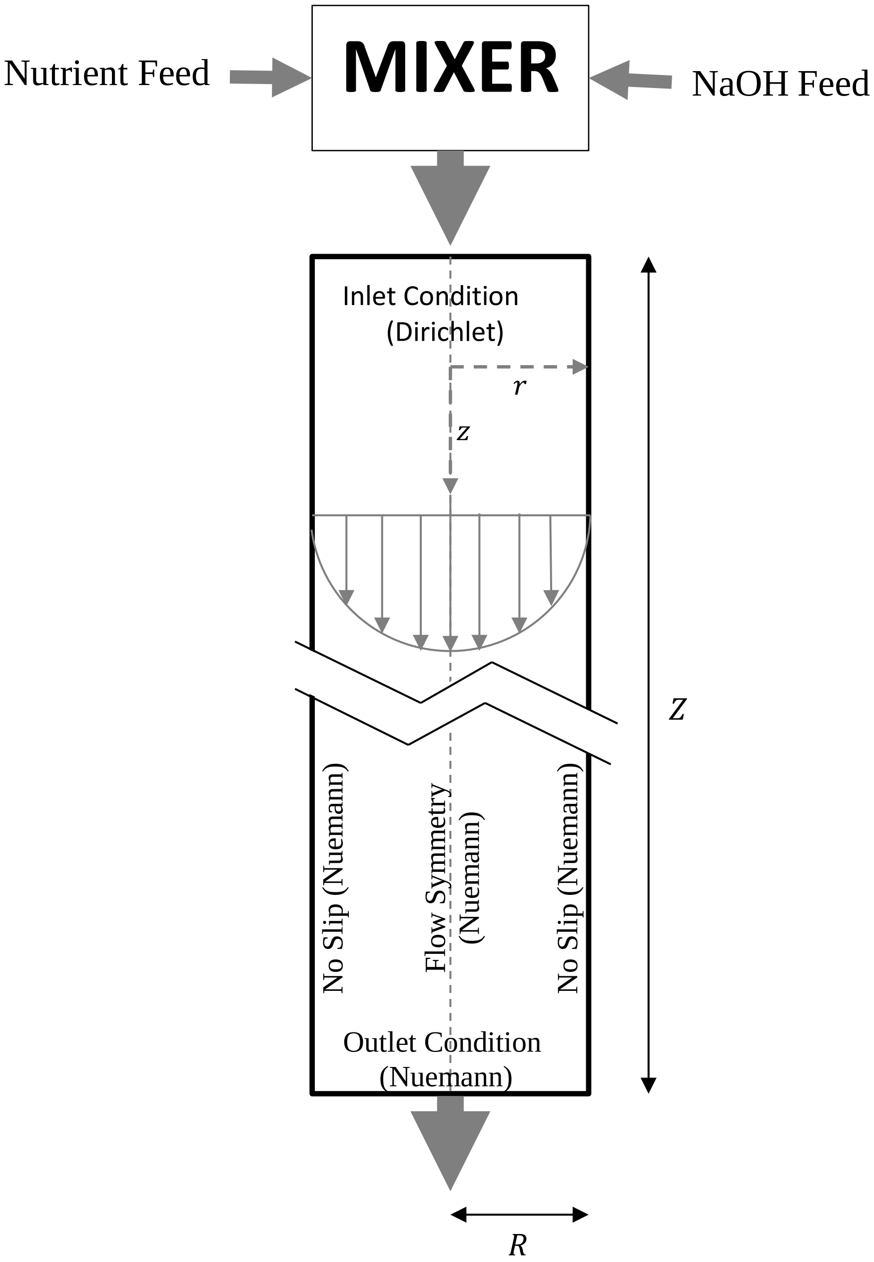

Figure 4.4 – Poiseuille flow reactor model schematic showing boundary conditions and distribution domains

Equation 4.6 is the advection-diffusion-reaction (ADR) liquid phase mass balance which describes the change in ion concentration C_i [mol/L] along the length (z) and radius (r) of the reactor. A derivation of this equation can be found in Appendix D.

$$\frac{\partial C_i}{\partial t} = -v_z(r)\frac{\partial C_i}{\partial z} + \boldsymbol{\mathcal{D}_i}\frac{\partial^2 C_i}{\partial z^2} + \boldsymbol{\mathcal{D}_i}\frac{\partial^2 C_i}{\partial r^2} - r_{struvite} \tag{4.6}$$

Similarly, Equation 4.7 is the solid phase mass balance, which excludes diffusion.

$$\frac{\partial C_{struvite}}{\partial t} = -v_{MAP}(r)\frac{\partial C_{struvite}}{\partial z} + r_{struvite} \tag{4.7}$$

In the 1st term on the right hand side (advection), $v_z(r)$ [m/min] is the fluid velocity in the axial direction. Fluid advection is described by equation 4.8.

$$v_z(r) = 2\overline{v_z}\left(1 - \left(\frac{r}{R}\right)^2\right) \tag{4.8}$$

Where $v_z(r)$ is the axial fluid velocity as a function of the radial coordinate r, $\overline{v_z}$ is the average fluid axial velocity and R is the reactor radius. In equation 4.7, the solid phase advection also incorporates particle settling to describe the axially vertically reactor, as described by equations 4.9 to 4.11.

$$v_{MAP} = v_z(r) + v_{settling} \tag{4.9}$$

$$v_{settling} = \begin{matrix} \dfrac{2(\rho_p - \rho_f)gR^2}{9\mu} & L < 40\mu m \\ \dfrac{8(\rho_p - \rho_f)gR}{3\rho_f C_D} & L \geq 40\mu m \end{matrix} \tag{4.10}$$

Where L describes particle equivalent diameter and C_D, the laminar drag coefficient, is calculated as follows.

$$C_D = \left(\frac{24}{Re_p}\right)\left(1 + 0.14Re_p^{0.7}\right) \tag{4.11}$$

Where ρ_p and ρ_f are the densities of the particle and fluid, g is acceleration due to gravity, R is the particle radius, μ is the dynamic viscosity of the fluid, C_D is the drag coefficient. Equation 4.10 describes the Stokes settling for particles below and above a particle Reynolds number of 0.1, and equation 4.11 is an empirical approximation accurate to within 6% for the range $0.1 < Re_p < 1000$, which corresponds to 40 – 860 microns (Perry, Green, & Maloney, 1999). The 2nd term in equation 4.6 (excluded from 4.7), describes ion diffusion, where $\boldsymbol{D_i}$ [m^2/min] is the diffusivity of species i. Finally, the last term in both 4.6 and 4.7, $r_{struvite}$ [mol/L.min] is the formation rate of struvite, which couples the fluid and solid mass balance models to the population balance kinetic model via equation 4.12 below.

$$r_{struvite} = \frac{\rho_p}{MM_{struvite}} \sum_i \frac{\partial N_i}{\partial t} v_i \qquad 4.12$$

Where ρ_p is the particle density and $MM_{struvite}$ is the molar mass of struvite. The formulation in equation 4.6 assumes fully developed axisymmetric steady state flow with zero radial velocity, which is reasonable in fully developed laminar flow (Munson et al., 2006). To validate this assumption, the distance from the pipe entry to full flow development is defined by the convergence of viscous boundary layers, which can be approximated by equation 4.13 (Munson et al., 2006).

$$L_e = 0.12Re \cdot R \qquad 4.13$$

Where L_e is the entry length and Re is the Reynolds number. In the experiments conducted in this work, L_e was <10% of the reactor length. While not ideal, this was deemed acceptable considering the estimated induction time (no nucleation) took ~10% of reactor length and crystal surface area for growth is initially low after nucleation begins.

4.4 Boundary conditions

Spatial boundary conditions used to solve equation 4.6 are shown schematically in Figure 4.4 and described by equations 4.14 to 4.17 below. These are standard conditions applied to this type of problem (Rice & Do, 1995). The no slip and symmetry conditions dictate that the radial concentration change at the centreline ($r = 0$) and the reactor wall ($r = R$) are zero. The outlet condition dictates that the outlet ($z = Z$) axial change in concentration is zero. And finally, the inlet conditions define the reagent concentrations immediately after the mixer (*i.e.* the feed conditions). These can be found in section 5.2.3.

$$\left.\frac{\partial C_i}{\partial r}\right|_{r=0} = 0 \quad 4.14$$

$$\left.\frac{\partial C_i}{\partial r}\right|_{r=R} = 0 \quad 4.15$$

$$\left.\frac{\partial C_i}{\partial z}\right|_{z=Z} = 0 \quad 4.16$$

$$C_{i_{z=0}} = C_{i,0} \quad 4.17$$

Initially, the reactor was initially filled with saturated solution ($C_{NH_4^+} = 0.01M, C_{PO_4^{3-}} = 0.01M, C_{Mg^{2+}} = 0.015M, C_{NaOH} = 0.005378M, C_{Cl} = 0.03M, C_{struvite} = 0$) to avoid particle dissolution, both experimentally and numerically. Concentrations at all spatial elements not defined by equations 4.14 to 4.17 were defined to represent this.

4.5 Derivative solution

The advection $\left(-v_z(r)\frac{\partial C_i}{\partial z}\right)$ and reaction $(v_i \cdot r_{struvite})$ terms were approximated in the radial and axial domains using a first order backwards finite difference method (BFDM). It is recognised that alternative and higher order methods can achieve lower truncation errors, but the first order BFDM method was most robust, delivering solutions under all conditions without oscillation.[9] The diffusion terms $\left(\boldsymbol{\mathcal{D}_i}\frac{\partial^2 C_i}{\partial z^2} + \boldsymbol{\mathcal{D}_i}\frac{\partial^2 C_i}{\partial r^2}\right)$ were approximated using a second order centered finite difference scheme (CFDM) to account for the multi directional nature of diffusion. Differential equations were solved using a variable time step, fully-implicit Runge-Kutta method. Model robustness was improved by providing accurate initial guess values from previous simulations, which were found to be key to obtaining fast solution convergence, especially for low concentration systems (*e.g.* real digester centrate).

Variables within the model range over approximately 30 orders of magnitude. Accuracy for both small concentration ($< 10^{-8}$) and large particle number ($> 10^{9}$) values can be achieved in multiple ways. Increasing the number of iterations to ensure all variables are solved to the lowest absolute tolerance is possible but is time consuming and some variables are solved to a tolerance far beyond what is necessary.

---

[9] Confirmed by personal communication with software developer

In this work variables were scaled so that they were of similar orders of magnitude and a higher (more relaxed) solution tolerance was applied. Numerical solutions are easier to achieve for variables with similar orders of magnitude as integration is performed over smaller gradients. Compared to tightened solution tolerances, particle numbers scaled by a factor of 10^{-9}, such that one simulated particle unit represented 10^9 actual particles, reduced simulation times by 20%. However, it should be realised that scaling increases uncertainty when small particle numbers are involved. This is deemed acceptable as they contribute less to mass balance. Concentrations within the thermodynamic equilibrium model were logarithmically scaled as per equations 4.18 to 4.20.

$$Z \rightleftharpoons X + Y \tag{4.18}$$

$$K_{eq} = \frac{C_X C_Y}{C_Z} \tag{4.19}$$

$$\log_{10}(K_{eq}) = \log_{10}(C_X) + \log_{10}(C_Y) - \log_{10}(C_Z) \tag{4.20}$$

Where K_{eq} is an equilibrium constant for the reaction equation 4.18. Model tolerances (relative and absolute) were determined in an iterative process. First, the minimum acceptable tolerance of each variable was defined to be one order of magnitude lower than the respective measurement tolerances. Secondly, the absolute and relative tolerances were decreased until solution time was significantly affected. This resulted in absolute and relative tolerances being set to 10^{-9}.

Initialisation of the numerical model with no particles present causes solution difficulties and creates problems with PSD statistical descriptions (*i.e.* percentiles and moments). As such, the model was initialised with a small number of particles (<10^3) in the the first cell/smallest predicted size – 0.01 microns. Starting with some particles present in a very low size range is also physically more realistic as it is likely impossible that reagents will be completely free of particles (Mullin, 2001).

4.6 Grid convergence study

This section details the methods used to determine the minimum number of spatial elements (axial and radial) required to ensure accuracy of the numerical solution to equation 4.6. Traditionally, grid independence is defined by the number of discrete elements required for the solution to stop changing within machine (computer) tolerance. Here, grid convergence was deemed to be achieved when the difference between the numerical and exact[10] solution, for a variable, was less than 10% of that variable's outlet measurement uncertainty. The population balance model was decoupled from ADR model to decrease simulation time. All grid convergence studies were performed under steady state operation, determined to occur after 60 min.[11] Phosphorus concentration and flow rate were used to indicate grid convergence as their measurement uncertainties were known. Phosphorus concentration was also identified as the slowest concentration variable to stabilise after changes to reactor feed, thereby indicating that all other species concentrations would be stabilised. These "indicator" variables were examined at all axial and radial grid elements. An arbitrary grid coarseness (65 elements in both dimensions), assumed to be greater than that required for grid independence, was used to determine steady state. This assumption was later validated. The grid convergence study found that a solution could be achieved within this tolerance using 41 radial and 18 axial grid elements.

4.6.1 Methods

The number of grid elements has a significant impact on the computation time, so it is imperative that only sufficient granularity is selected to achieve a reasonable solution. Grid convergence methods are detailed in Appendix F. The solution is achieved when the absolute error in a predicted variable E_f was less than the absolute measurement tolerance for that variable ϵ_f. Here ϵ_f was defined as 10% of measurement tolerance – error in phosphorus concentration, $\epsilon_{C_P} = 8.88 \times 10^{-6} \, [\frac{mol}{L}]$ and error in feed flow rate, $\epsilon_{Q_{feed}} = 5 \times 10^{-4} \, L/h$. A dimensionless error term was used to describe this phenomenon (equation 4.21), where for a given grid coarseness, if $\widehat{E_f} < 1$, the variable f can be considered grid independent.

---

[10] Exact solution was approximated using 512 grid elements in both domains.

[11] Negligible change was observed between 60min and 300min of operation.

$$\widehat{E_f} = \frac{E_f}{\epsilon_f} \tag{4.21}$$

Phosphorus concentration uncertainty was estimated by combining variances of 54 measurements (using molybdo-vanadate UV-Vis method) and flow uncertainty was assumed based on pump flow rate resolution *i.e.* the pumps used in experiments were accurate to 0.01 L/h.

4.6.2 Kinetic model decoupling

The population balance was decoupled from the ADR model to reduce computation time.[12] Instead the rate term ($v_i \cdot r_{struvite}$) was described using a 6th order polynomial as a function of total phosphorus concentration. The polynomial ($R^2 = 0.9997$) was fit to rate data at inner, middle and outer reactor radii to ensure accurate representation in all regions. Concentration and rate data are shown in Figure 4.5 (a) and (b), respectively. They were obtained using 41 radial grid elements, 65 axial grid elements and an operating time of 300 min, assuming kinetics from Galbraith (Galbraith, Schneider, & Flood, 2014).

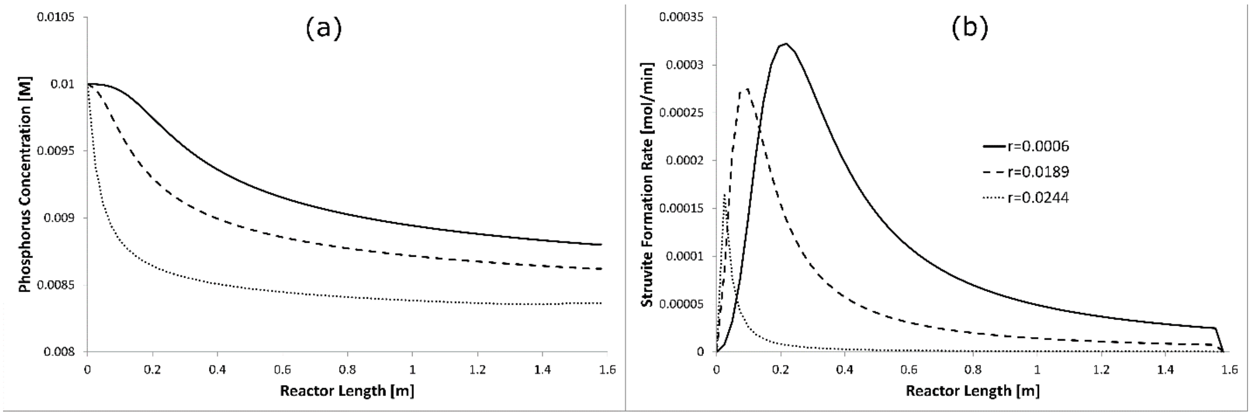

Figure 4.5 – (a) Phosphorus concentration and (b) struvite formation rate variation with reactor length

4.6.3 Grid independence measure

Grid independence was determined for all radial and axial grid elements. This is important because phosphorus concentration may be within measurement uncertainty at the reactor outlet, but exhibit

---

[12] The cell average population balance model inherently conserves particle mass and number so is not considered for grid independence here

significant error upstream at varying radial positions. This effect is visualised in Figure 4.6, where on the centreline (r=0), phosphate concentrations given by coarser grids (Nz=3-5) are above the upper error limit, while for the outer perimeter (r=0.025 m), they are below. This is because at the outer perimeter, phosphate concentration has reached equilibrium before the outlet.

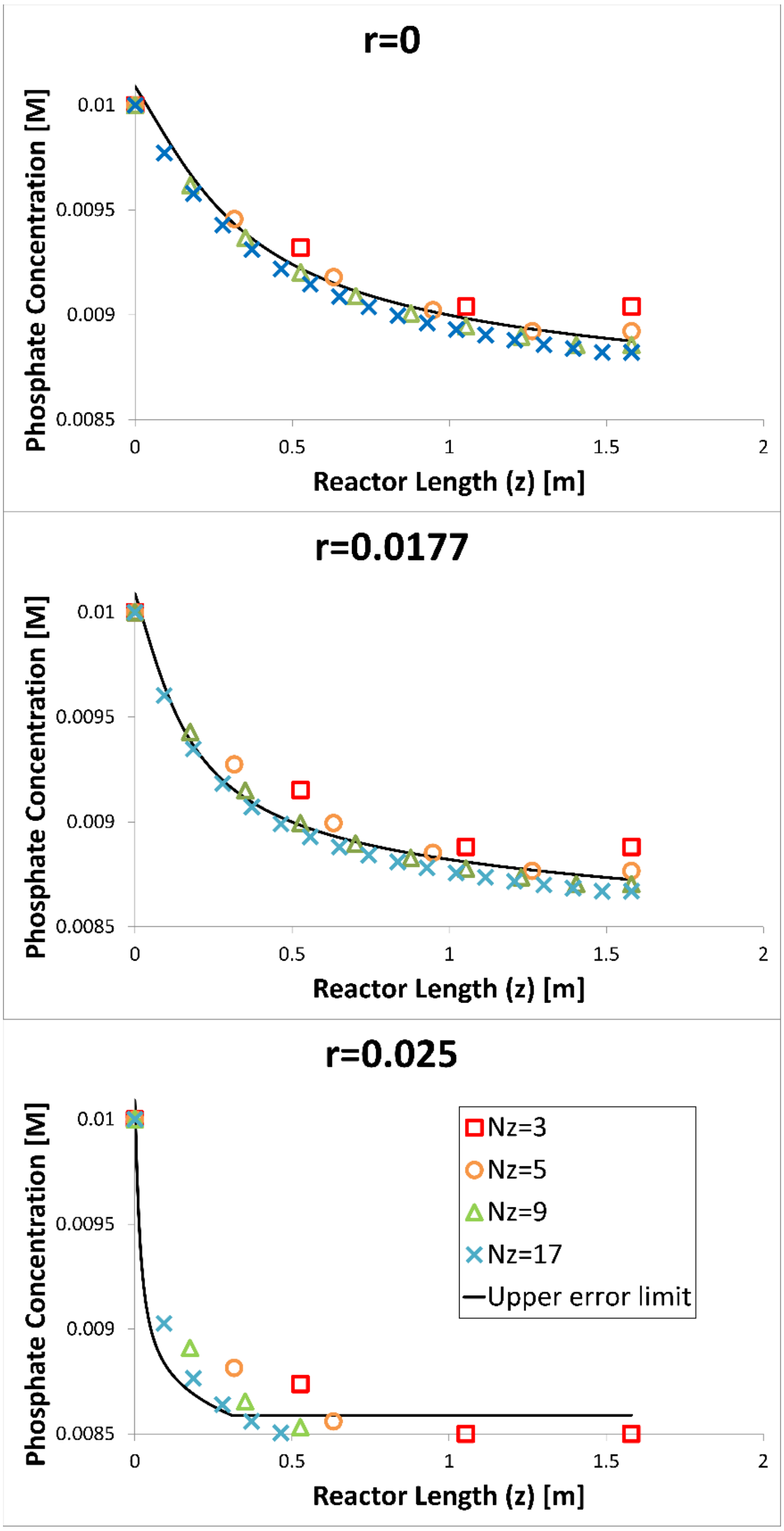

Figure 4.6 – Phosphorus concentration profile along the reactor length, simulated using varying axial elements (Nz), at the centreline (r=0), half reactor cross sectional area (r=0.0177) and outer perimeter (r=0.025). Measurement upper error limit is given by adding the phosphate measurement tolerance to the assumed exact solution (Nz=513).

This effect can also be observed by comparing results of the grid convergence method applied over the reactor length and radius to those where it is applied only on the outlet mixed concentration. The outlet mixed phosphorus concentration was calculated by integrating phosphorus concentration (C_{PO_4}) and fluid velocity (v_z) over all radial elements in Figure 4.4, as shown by equation 4.22.

$$C_i = \frac{moles_{i,T}}{Q_T} = \frac{\int_0^R C(r) v_z(r) 2\pi r \, dr}{\int_0^R v_z(r) 2\pi r \, dr} \tag{4.22}$$

Figure 4.7 shows that the number of axial grid elements necessary for grid convergence at all elements is significantly larger (18 elements) than that necessary for convergence using the mixed outlet concentration only (7).

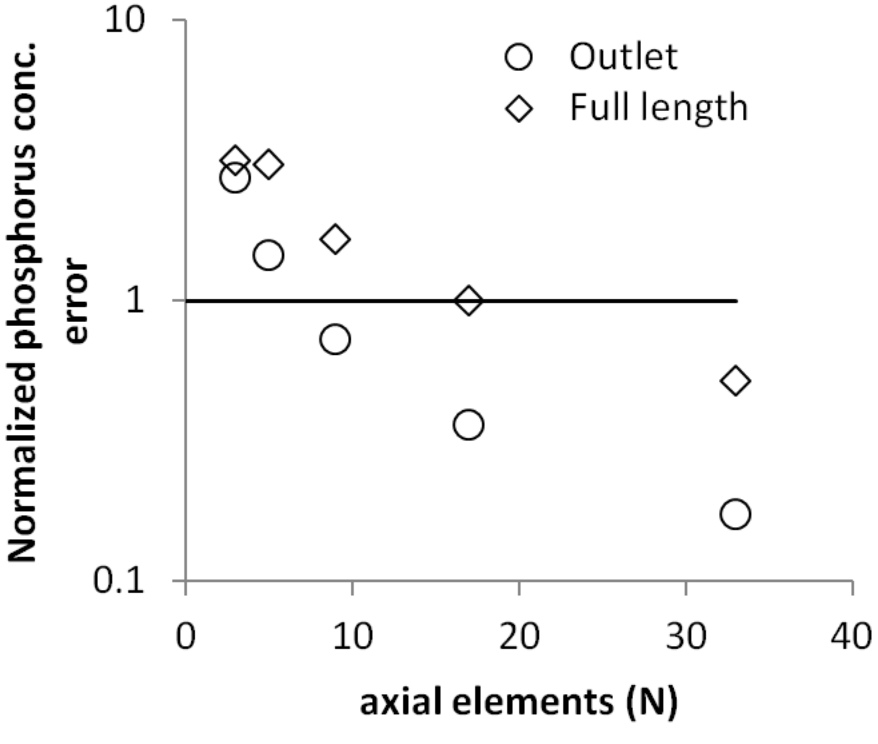

Figure 4.7 - Dimensionless phosphorus concentration error as a function of axial elements, calculated at the reactor outlet and maximum of any point in the reactor at $r = 0.0213$

4.6.4 Results

Figure 4.8 summarises the grid convergence study results. Radial grid coarseness was analysed before axial grid coarseness because mass conservation independent of the axial coordinate. This allowed for the use of a coarse axial grid during the radial analysis. Grid convergence order (discussed in Appendix F) indicated that radial grid coarseness was limited by flow rate resolution – this is also shown in Figure 4.8 where the radial phosphorus concentration line crosses the error boundary of 1 before the radial flow line. Radial grid independence was achieved using 41 elements, equivalent to a step size of $h_r \sim 0.61\ mm$. Using the identified radial grid coarseness, axial grid convergence was determined to occur in 18 elements.[13]

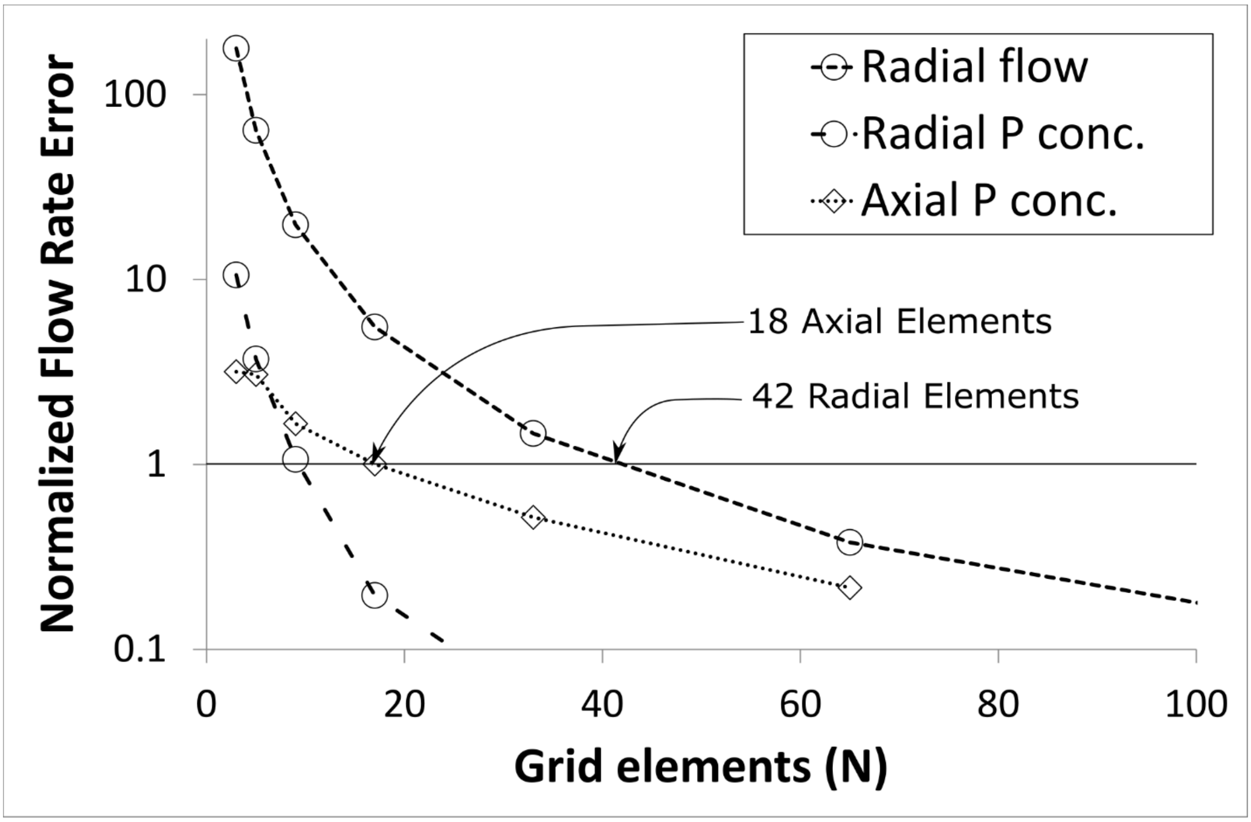

Figure 4.8 – Grid convergence using normalised flow rate error for radial and axial elements

---

[13] Axial grid convergence only considered phosphorus concentration since flow rate is independent of axial coarseness.

4.7 Mass conservation check

The grid convergence was checked by ensuring that overall phosphorus removal was achieved to within an acceptable tolerance, using the full population balance model. This was done by calculating the amount of MAP formed as a percentage of the change in phosphorus concentration over the reactor, then comparing this to the acceptable uncertainty. Phosphorus measurement uncertainty corresponded to a conservation of the solid phase of within 0.48%. Figure 4.9 shows that the percentage error between the solid and liquid mass balance was within this range at a lower number of axial grid elements than was identified by the grid convergence. Therefore the overall conservation of mass was achieved to within an acceptable limit using 41 radial and 18 axial grid elements. The asymptotic nature of the mass conservation error suggests that other numerical factors make contributions, although these are not considered of importance since uncertainty is already within and acceptable tolerance.

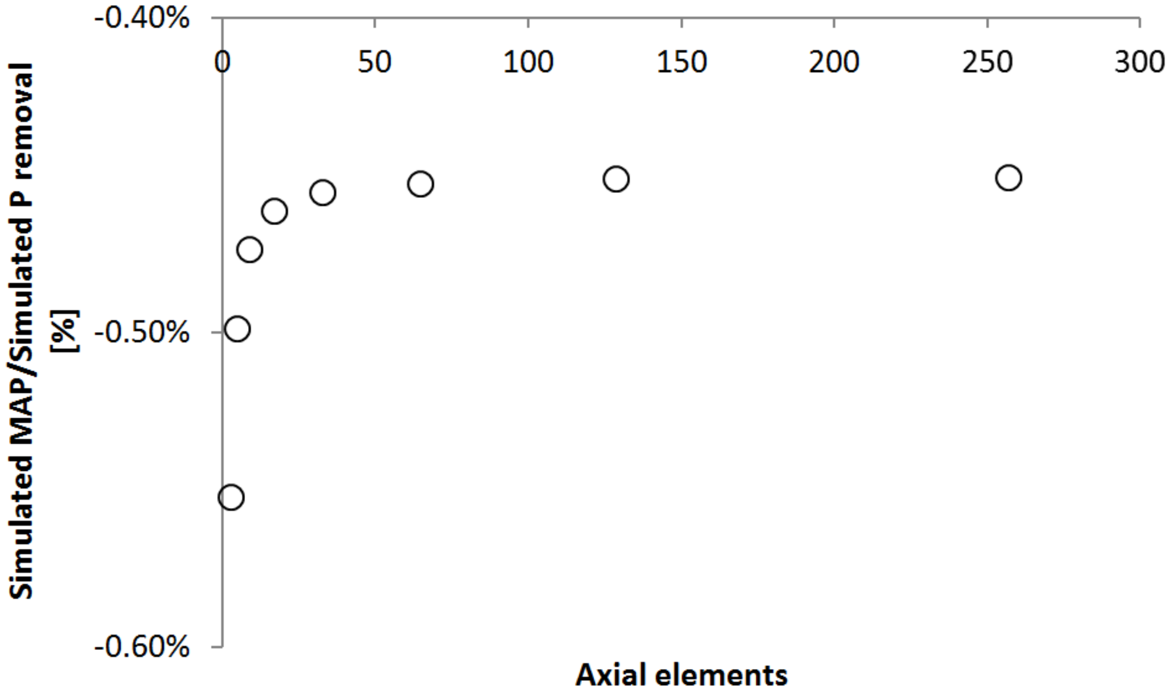

Figure 4.9 – Struvite mass balance closure described by the ratio of struvite to phosphorus removed at the reactor outlet.

4.8 Reactor simulations

Once tuned for accuracy, the reactor model was used to examine (1) how much crystallisation is likely to have occurred in the entry length region and (2) the difference between using a more common 2nd order particle growth model and the 5th order model found by Galbraith. Simulations used for these investigations used initial and boundary conditions given in section 4.4 and feed conditions and simulation parameters given in Table 4.1 and Table 4.2 below.

Table 4.1 – Reactor simulation feed conditions

Variable	Nutrient feed	NaOH feed
Flow rate [L/h]	4	4
$NH_4H_2PO_4$ conc. [mM]	20	-
$MgCl_2 \cdot 6H_2O$ conc. [mM]	30	-
NaOH conc. [mM]	-	17.61

Table 4.2 – Reactor simulation parameters

Parameter	Value
Growth rate constant (k_g) [µm/min]	12.49
Nucleation rate constant (k_{nuc}) [1/L.min]	8.5×10^7
Aggregation rate constant (k_{agg}) [L/min]	3.72×10^{-7}
Growth rate order (n_g)	5.06
Growth rate order (n_g)	2
Nucleation rate order (n_{nuc})	1.68
Aggregation rate order (n_{agg})	5.26
Induction time [min]	0.908

4.8.1 Entry length investigation

As noted earlier, developing flow at the entry to the reactor would not exhibit the well defined Poiseuille flow described by the model. Because of this, it is of interest to know how far the reaction has progressed in this region. Reaction progress is described by *SI* and the fraction of recoverable phosphorus which has been recovered (thermodynamic yield), given by equation 4.23 below.

$$Yield_{thermo} = \frac{\left(C_{PO_4^{3-}} - C_{PO_4^{3-},eq}\right)}{C_{PO_4^{3-},eq}} \tag{4.23}$$

Where $C_{PO_4^{3-}}$ is the orthophosphate concentration and $C_{PO_4^{3-},eq}$ is the orthophosphate concentration at equilibrium. Simulations of *SI* and thermodynamic yield are shown in Figure 4.10 and Figure 4.11 below.

Equation 4.13 was used to estimate the entry length to be 0.17m. At this length, Figure 4.10 and Figure 4.11 show that a 20% drop in *SI* has occurred, resulting in 20% of thermodynamic yield (at the approximate equilibrium time of 60 min). This indicates that a significant portion of the crystal growth occurs within developed flow. The entry length equates to two axial grid elements. Figure 1.6 shows that if the axial grid resolution were halved so that the entry length occurs within the first grid element, error in phosphate concentration along the reactor length would have remained below the arbitrary limit (10% of measurement tolerance) for most radial elements, only exceeding the limit near the reactor wall. On this basis, the error in the simulation resulting from a poor description of the flow development is not considered to be of significance. However, this analysis does not quantify the effects of the diffuser or the circular motion caused by the mixer. Future work should quantify these effects using CFD.

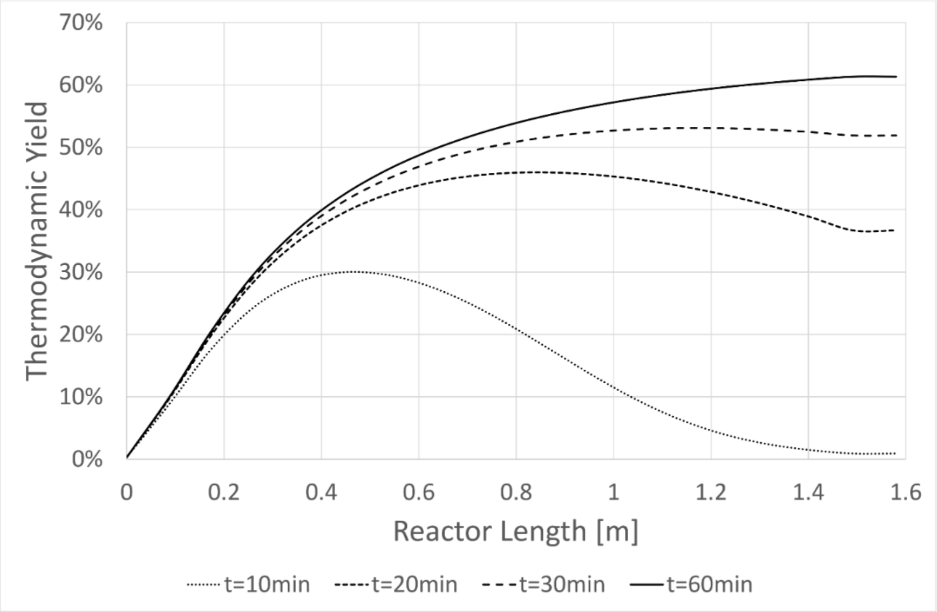

Figure 4.10 – Average thermodynamic yield along the reactor length at various operating times. Average thermodynamic yield was calculated using the thermodynamic model and reagent concentrations integrated over the reactor radius.

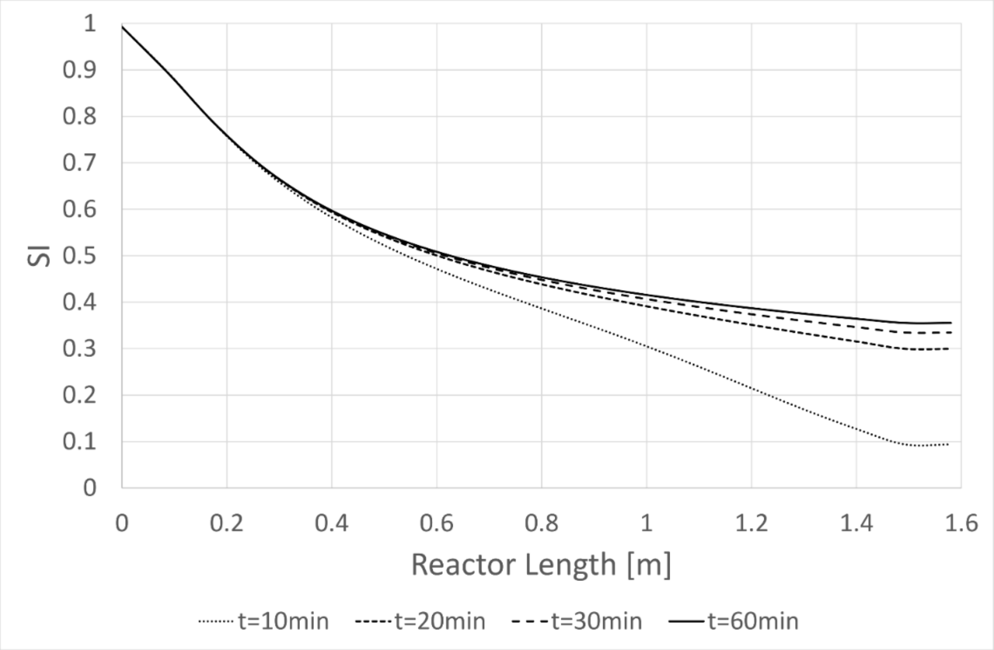

Figure 4.11 – Average SI along the reactor length at various operating times. Average SI was calculated using the thermodynamic model and reagent concentrations integrated over the reactor radius.

4.8.2 Growth rate order impact

As noted in Chapter 2, all struvite crystal growth power law models exhibited an order between 1.68 and 2 – this is a common finding for surface integration controlled crystallisation. However, the only model which used a DPB found a growth rate order of 5.06 (Galbraith, Schneider, & Flood, 2014). These models were shown to give similar rates above *SI* = 0.3 but deviate below. In the event that the parameter estimation problem in this work becomes over-parameterised, the growth rate order can be fixed to an already measured value to allow better estimation of the growth rate constant. Since the output *SI* in this reactor is unknown, it is important to examine the impact of growth rate order on the reactor *SI* profile and resulting crystallisation mechanism rates. Simulations visualised below show profiles of the *SI,* growth rate, nucleation rate and aggregation rate using a growth rate order of n=2 and n=5.06.

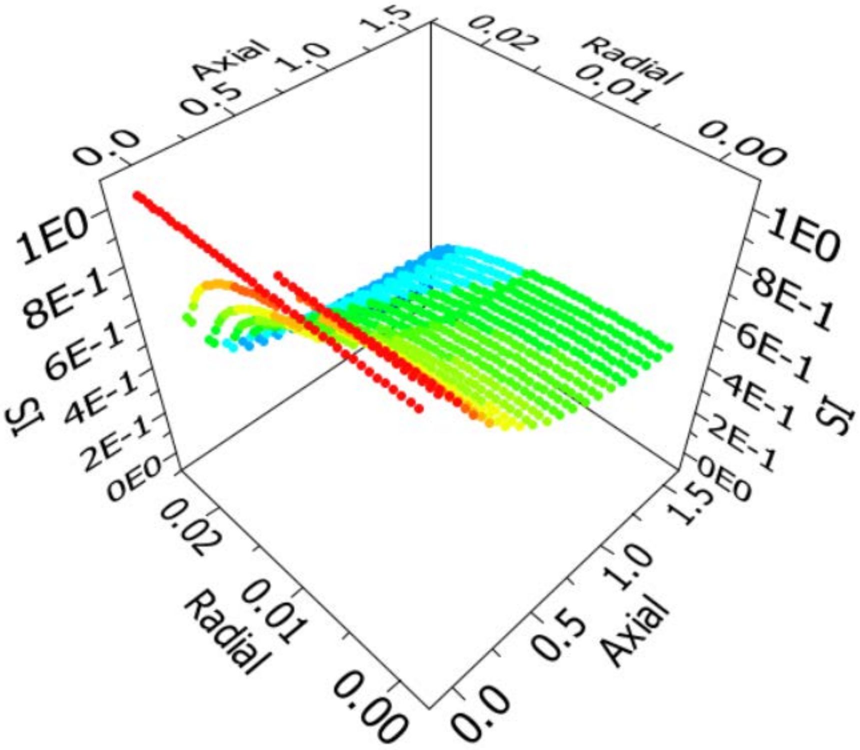

Figure 4.12 – SI profile at steady state simulated by the nucleation and crystal growth model with growth rate order $n_g = 5.06\ [\mu m.min^{-1}]$

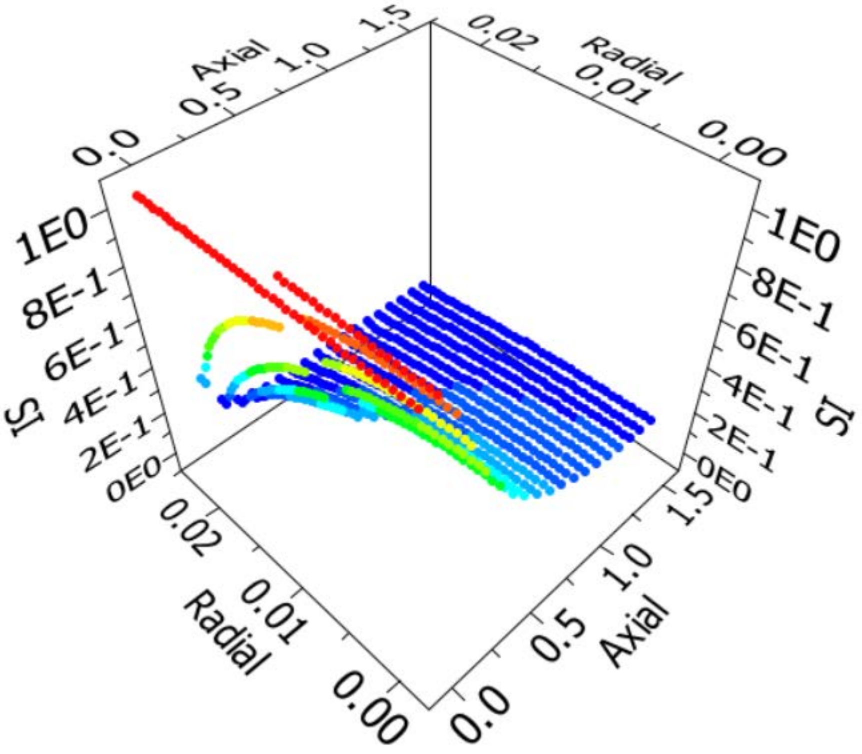

Figure 4.13 - SI profile at steady state simulated by the nucleation and crystal growth model with growth rate order $n_g = 2\ [\mu m. min^{-1}]$

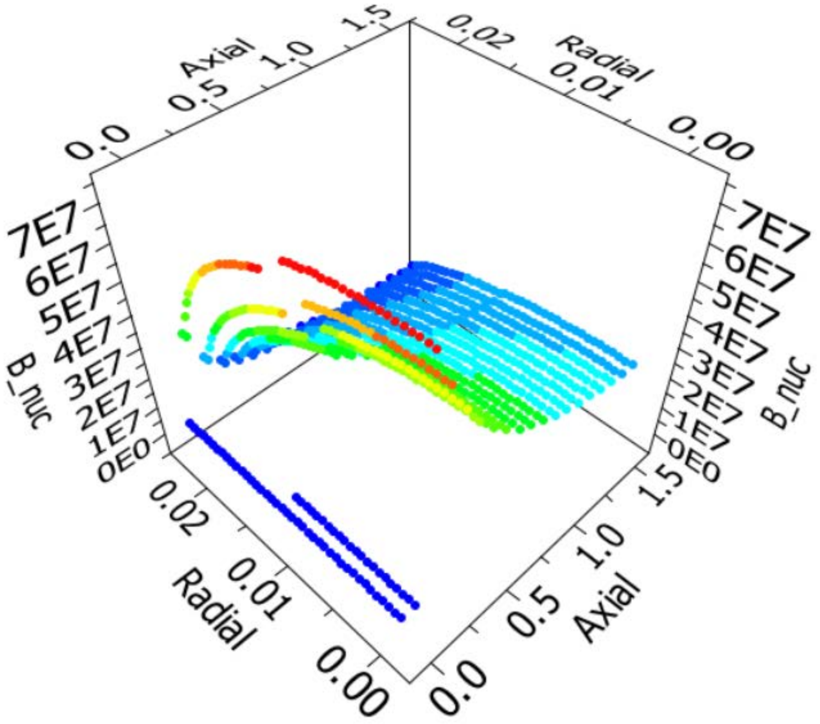

Figure 4.14 – Nucleation rate ($B_{nuc}\ [L^{-1}min^{-1}]$ *) profile at steady state simulated by the nucleation and crystal growth model with growth rate order* $n_g = 5.06\ [\mu m. min^{-1}]$

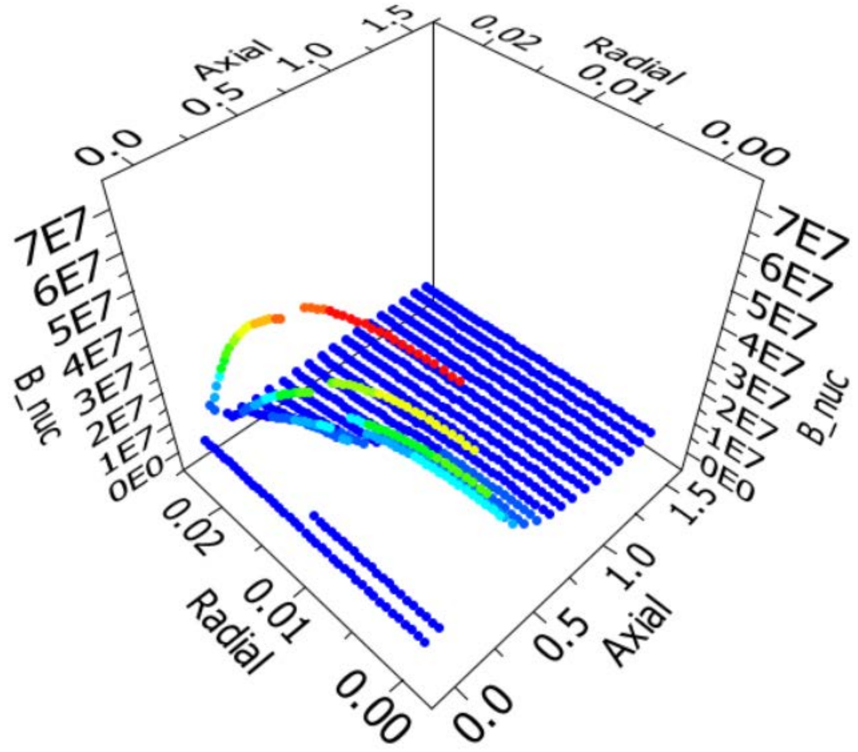

Figure 4.15 - Nucleation rate (B_{nuc} $[L^{-1}min^{-1}]$) profile at steady state simulated by the nucleation and crystal growth model with growth rate order $n_g = 2$ $[\mu m. min^{-1}]$

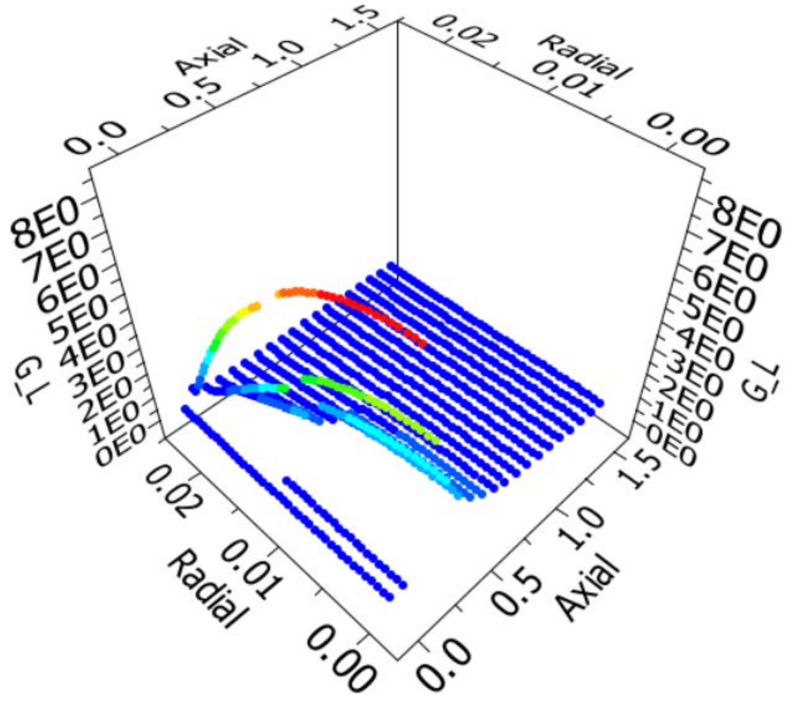

Figure 4.16 – Growth rate (G_L $[\mu m. min^{-1}]$) profile at steady state simulated by the nucleation and crystal growth model with growth rate order $n_g = 5.06$ $[\mu m. min^{-1}]$

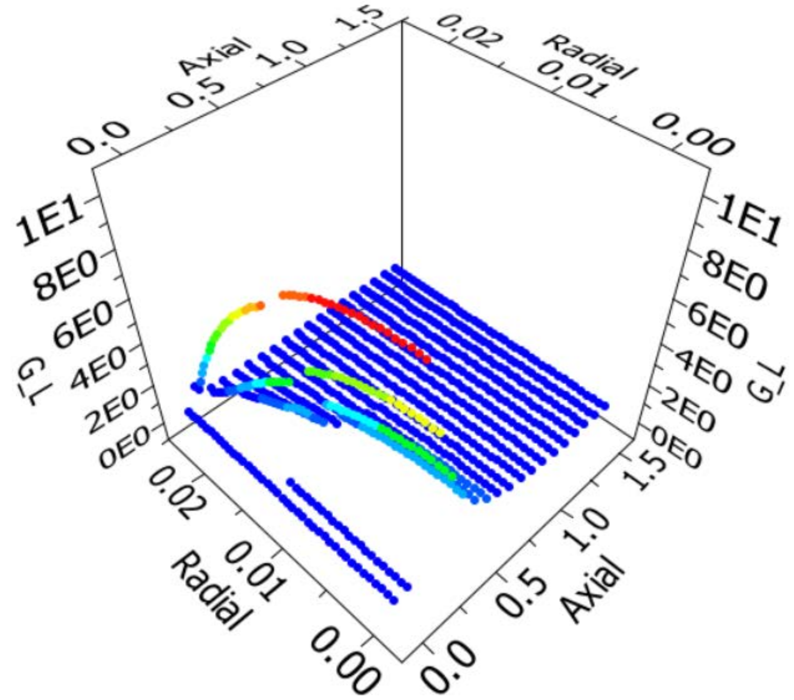

Figure 4.17 - Growth rate (G_L $[\mu m.min^{-1}]$*) profile at steady state simulated by the nucleation and crystal growth model with growth rate order* $n_g = 2$ $[\mu m.min^{-1}]$

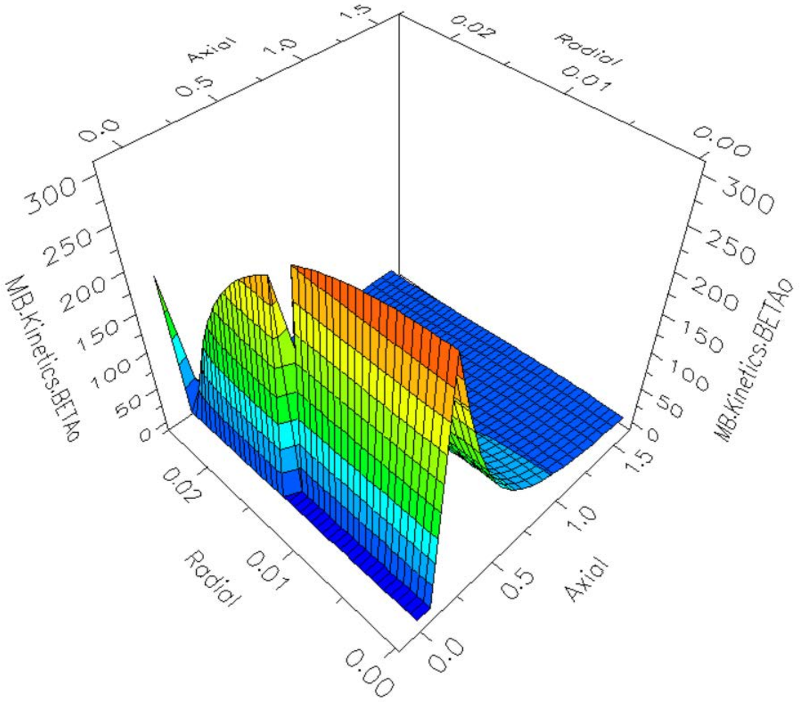

Figure 4.18 – Aggregation rate $[L^{-1}min^{-1}]$ *profile at steady state simulated by nucleation crystal growth and aggregation model with growth rate order* $n_g = 5.06$ $[\mu m.min^{-1}]$

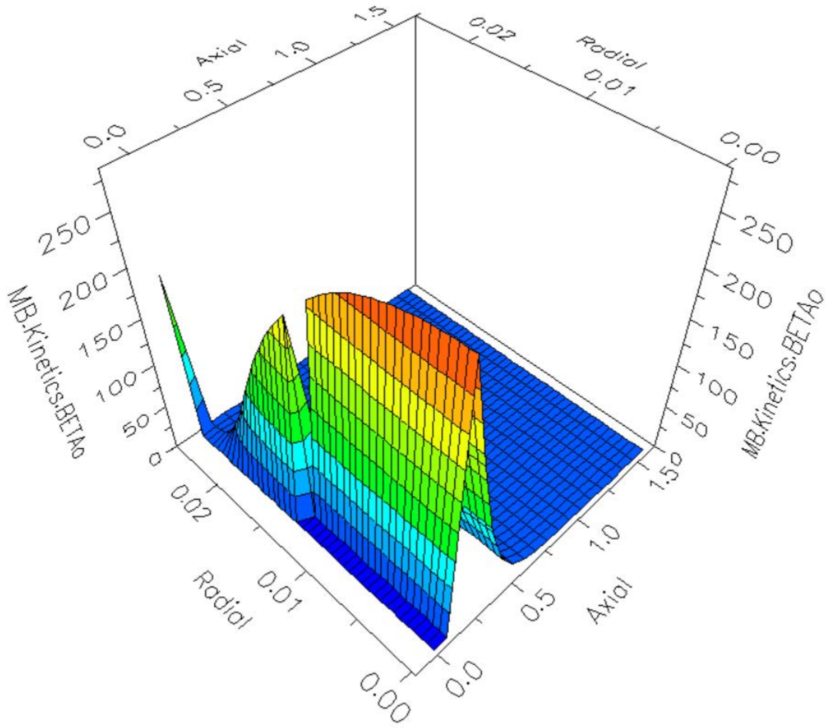

Figure 4.19 – Aggregation rate $[L^{-1}min^{-1}]$ *profile at steady state simulated by nucleation crystal growth and aggregation model with growth rate order* $n_g = 2\ [\mu m. min^{-1}]$

It can be seen that for $n_g = 5.06$, the growth rate is lower initially and plateaus towards the end of the reactor, showing the ‘growth rate dead zone’ discussed by Galbraith. This results in a sustained *SI* and subsequent nucleation and aggregation rate throughout the reactor, meaning that the choice of growth order has a significant impact. If growth order needs to be fixed, the selection of order can be determined by the supersaturation observed at the outlet. If the supersaturation reaches zero, then no dead zone exists and a lower growth order can be used. If supersaturation plateaus, then a dead zone is likely and a higher order growth model can be used.

4.9 Summary

- A reactor model incorporating fluid and particle advection, axial and radial solute diffusion, struvite crystallisation via a discretised population balance, particle settling, non-ideal solution thermodynamics and a mass balance was developed to represent changes in solid and liquid phase concentrations in a Poiseuille flow reactor.

- Numerical solution methods, scaling techniques and initialisation techniques were examined before conducting a grid convergence study.
- A Grid convergence study was used to determine an adequate axial and radial grid size to ensure the uncertainty introduced by using a numerical solution was <10% of key measurement uncertainties.
- Conservation of mass was confirmed to within an acceptable range, providing confidence that the model could be used for sensitivity analysis and parameter optimisation purposes.

4.10 Conclusions

The model developed in this chapter describes crystal nucleation, growth and aggregation in Poiseuille flow. The complexity of this model makes it broadly useful for describing any particulate system in Poiseuille flow. This means that it can be adapted to investigate kinetics of other crystal systems or, if kinetics are known, it can be applied to Poiseuille seed reactor simulation and design. The model is used in subsequent chapters for struvite nucleation, growth and kinetic parameter optimisation based on experimental results. Simulations conducted here show that varying growth rate order based on previous work significantly affects *SI* profile throughout the reactor and is therefore important to consider when conducting parameter estimation. Chapter 6 provides a detailed comparison of the sensitivity of the reactor outputs to each kinetic parameter. The entry region remains a key limitation of the models ability to describe the experimental apparatus however simulations show that the impact on simulation accuracy is not very large. While steps could be taken to increase model complexity, removing the constriction between the mixer and Poiseuille section may prove to be an easier solution.

Chapter 5 Poiseuille flow reactor design and testing

This chapter details the operation of the Poiseuille flow experimental reactor (detailed in Chapter 4) for the continuous production of controlled seeds at varying levels of feed supersaturation.[14] *The reactor flow behaviour was examined to confirm the creation of a high supersaturation region, resulting in primary nucleation. The crystal product was analysed for phase composition and particle size distribution (PSD). Sonication was utilised to distinguish nucleation and growth mechanisms from aggregation. In experiments, non-equilibrium feed saturation index (SI) was varied from 0.8 to 1.4. A Roughton (R) style vortex mixer was compared to the more common impinging jet (IJ) mixer to assess differences in mixing performance and PSD. Results showed that all particles produced in this work were within the range of those produced in previous struvite seeding studies. Increasing feed SI increased PSD properties (distribution width and median diameter) measured in line, but after sonication the difference was not significant, indicating the presence of weakly-bound aggregates. The R mixer achieved a narrower PSD at SI = 0.8 and improved phosphorus recovery at all supersaturation levels. Scatter in PSD data at higher SI values indicated incomplete mixing in both mixers, calling into doubt the applicability of the induction time and mixing models utilised in this study.*

---

[14] Note: The contents of this chapter resulted in the following publications: M. Burns, L. Natividad Marin, P. Schneider, Investigations of a continuous Poiseuille flow struvite seed crystalliser - Mixer performance and aggregate disruption by sonication, Chem. Eng. J., 295 (2016) 552-562. doi:10.1016/j.cej.2016.03.061.

Discrepancies between particle mass measurements and predictions at the reactor outlet, suggest that between 5% and 13% of particle mass was likely retained within the reactor.

5.1 Introduction

The work outlined in this chapter served two goals. The first was to investigate Poiseuille flow reactor performance for generating struvite seed particles suitable for subsequent size enlargement. Reactor performance was investigated with respect to fluid mixing and inlet supersaturation, which were varied while product PSD and recovery were examined. Fluid mixing was varied by using both a Roughton and an impinging jet mixer and inlet supersaturation was varied using caustic feed concentration. The second goal was to generate data in a well-defined flow regime which can be used for optimisation of nucleation growth and aggregation kinetic parameters. This is important since the only DPB work on all three mechanisms of struvite did not investigate primary nucleation and has not been conducted in well characterised fluid dynamics. Reliable primary nucleation data requires generation of a region of high supersaturation since induction times become increasingly uncertain with lower supersaturation. Therefore, tracer studies were used to show that high supersaturation was achieved early in the reactor, indicating the onset of primary nucleation. Finally, this work attempted to address the issue of parameter correlation when simultaneously determining nucleation, growth and aggregation kinetic parameters. This was done by employing a novel data collection method to separate nucleation and growth mechanisms from aggregation.

5.2 Reactor operation

5.2.1 Inlet supersaturation

Supersaturation, the driving force for crystallisation, was quantified by *SI*. Maximum *SI* achieved at the reactor inlet was predicted by modelling non-ideal thermodynamics as described in section 2.1.

$$SI = \log_{10}\left(\frac{IAP}{K_{sp}}\right) \tag{5.1}$$

Where *IAP* is the ion activity product and K_{sp} is the equilibrium solubility product for struvite (13.26) (K. N. Ohlinger et al., 1998). Code used to solve the thermodynamic model is provided in Appendix E.

5.2.2 Flow rate

Two Grundfos DME12 diaphragm pumps were used to supply 4.00±0.005 L/h of both nutrient and $NaOH$ solutions. This flow rate was selected to ensure particle flow through the Mastersizer3000 flow cell by taking the following steps:

1. Struvite crystals were suspended in saturated solution in the Mastersizer3000 sampling container, by mixing at 1200rpm, to ensure even sampling
2. The suspension was then recirculated through the flow cell at flows ranging 4 – 12 L/h while PSD was repeatedly measured

For recirculation flows >7 L/h, PSD remained unchanged. Settling in dead zones at lower flow rates was checked by operating at a given flow rate for 5 residence times then increasing flow to maximum to observe flush through of any build-up. No flush through was observed for flows >8 L/h. As such minimum reactor flow rate was set to 8L/h. Nutrient and caustic were fed at an equal volumetric flow rate to achieve consistent and reliable mixing in the IJ mixer.

5.2.3 Feed concentrations

All experiments were conducted using 20-L batches of nutrient solution with an elemental phosphorus concentration of 0.02 M and elemental Mg:N:P molar ratios of 1.5:1:1. Feed concentration selection is discussed in detail in sections 5.2.3.1 to 5.2.3.4 below. Stock nutrient solutions were made using $NH_4H_2PO_4$ and $MgCl_2{\cdot}6H_2O$ and *SI* values of 0.8, 1.0 and 1.4 were achieved by the addition of 16.5, 17.6 and 19.3 mM caustic ($NaOH$) solution, achieving predicted non-equilibrium pH values of 7.172, 7.351 and 7.727 respectively. Solutions were made with Sigma-Aldrich analytical grade reagents and RO filtered water, subsequently filtered through 0.2-μm cellulose nitrate membrane filter. All solutions were stored in sealed vessels to minimise CO_2 intrusion, which can impact solution thermodynamics through carbonate chemistry.

5.2.3.1 Phosphorus concentration

Phosphorus concentration was selected to ensure that uncertainties in reagent composition contributed < 1% uncertainty in saturation index (SI). Uncertainty propagation was evaluated with a thermodynamic model (Ali & Schneider, 2008a) in EES software package.[15] When all other uncertainties in the thermodynamic model are accounted for (most of which are attributed to solubility and stability constants), the resulting uncertainty in saturation index is 6%. Although this is significant, all uncertainties other than solution concentration are expected to be constant between experiments. Using a phosphorus concentration higher than typical wastewater enabled a sufficient crystal mass to be collected in a shorter period.

5.2.3.2 Ammonia Concentration

Using a 1:1 N:P ratio produces a greater pH change during crystallisation than that observed in urine and digester wastewaters where N:P can vary from 4 to 49 (Maurer et al., 2006; Md. Mukhlesur Rahman et al., 2014; Ronteltap et al., 2010). Greater pH change, relative to measurement uncertainty, reduces the uncertainty in subsequent thermodynamic model predictions.

5.2.3.3 Magnesium Concentration

Investigations of element molar ratio are regularly made on laboratory and pilot scale studies, but are seldom comparable, due to variations in experimental conditions. A common finding is that increasing Mg:P ratio produces an increase in phosphorus recovery (Bhuiyan et al., 2008; Nelson et al., 2003; Stratful, Scrimshaw, & Lester, 2001a). Mg:P ratios from 1.5:1 to 3.5:1 resulted in increased particle size of 30 % – 60 %, of high purity struvite, while maintaining >90% P removal, in fluidised bed reactors fed with anaerobic supernatant (Huang et al., 2005). It is uncertain whether steady state was achieved in the two reactors examined by Huang et al, as particle size was trending upwards at different rates. In another study, struvite formation rate was shown to double when Mg:P ratio increased from 1.1 to 1.5 (Quintana, Colmenarejo, et al., 2005). On the basis of the abovementioned studies, Mg:P ratio was set at 1.5:1.

---

[15] http://www.fchart.com/ees/

5.2.3.4 NaOH Concentration/ Supersaturation Range

NaOH concentration was varied to achieve *SI* levels between 0.8 and 1.4. This range was selected to ensure sufficiently low induction times (15 – 237 s at *SI* = 0.8) while avoiding dendritic crystal growth (*SI*>1.4). The minimum *SI* was set based on previously determined induction time models and the maximum *SI* was determined by qualitatively assessing when unwanted dendritic crystal growth became dominant.

Struvite induction time models, which operate in the same *SI* range as this work, are all based on classical nucleation theory, but vary in form, aqueous species considerations and solubility description (Bhuiyan et al., 2008; Bouropoulos & Koutsoukos, 2000; Kabdasli et al., 2006; K. N. Ohlinger et al., 1999). Induction time data were consolidated using methods described by Galbraith (Galbraith, 2011), incorporating more recent data (Le Corre, Hobbs, et al., 2007b; Mehta & Batstone, 2013). Results from Mehta 2013 were calculated using induction time model parameters rather than thermodynamic modelling, as raw data were not provided. The model from Bhuiyan *et al.* was not considered accurate as pH change was used to identify the end of induction time in a solution which likely had significant ammonia buffering (N:P ratio of 17:1). Several models indicated that induction time increased exponentially below *SI* = 0.8, therefore only higher saturations were considered (Figure 5.1). For mixer design, the lowest predicted induction time was used to ensure complete mixing before nucleation.

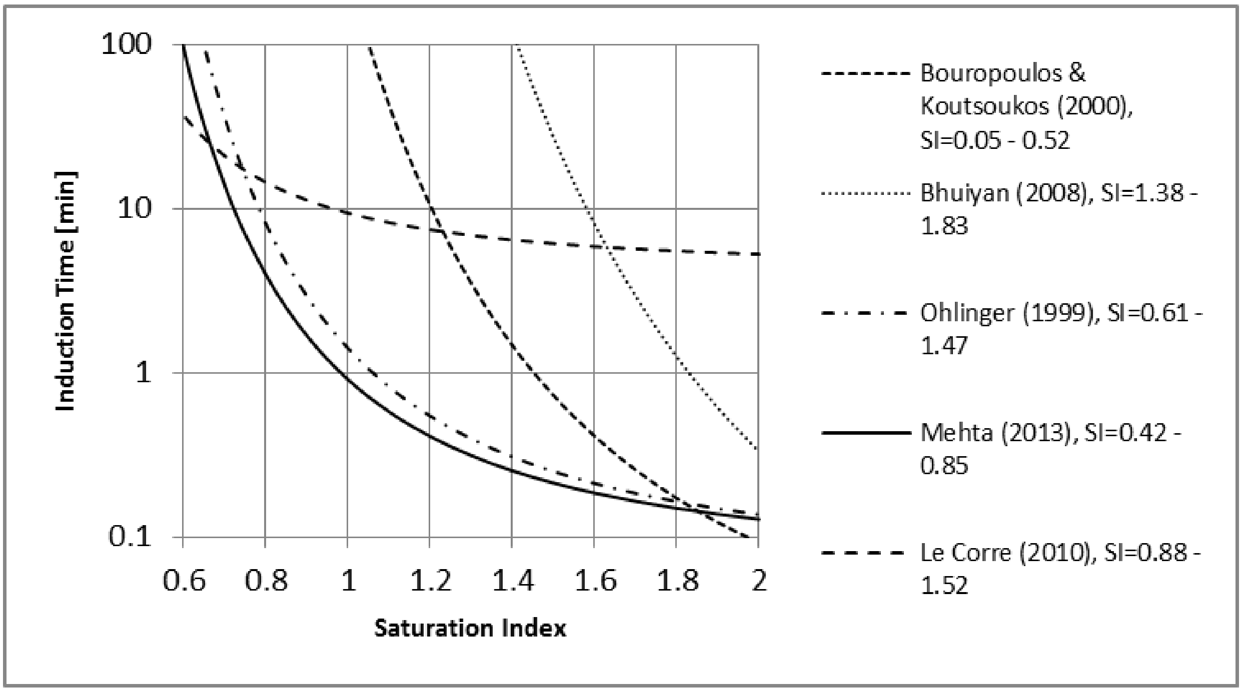

Figure 5.1 – Induction time models from various authors processed using a common thermodynamic basis.

Dendritic growth at higher *SI* results from the increased availability of PO_4^{3-} and NH_4^+. These ions preferentially absorb on the crystal c-axis, because of electrostatic inhibition of rectangular facet to facet particle adsorption created by Mg[H2O]$_6^{2+}$ species (Ye et al., 2014). Preliminary tests in this work showed that dendritic growth was prevalent at *SI*>1.4 (Figure 5.2). This was set as the upper limit of testing to reduce laser diffraction PSD measurement uncertainty introduced by apparent *D[50]* increases with particle aspect ratio (Kelly & Kazanjian, 2006).

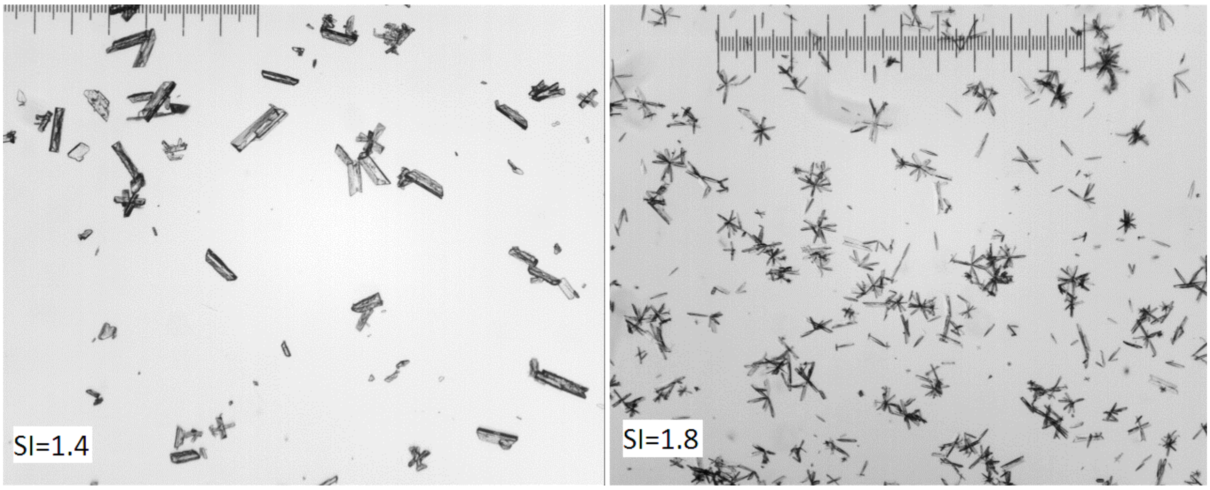

Figure 5.2 – Microscope images of crystals at SI = 1.4 and SI = 1.8 after 20min growth in a stirred vessel.

5.2.4 Tracer studies

Hydraulic and crystal tracer studies were conducted and repeated to ensure consistent reactor operation. To measure hydraulic residence time distribution (RTD), a 5-mL volume of 5% mass fraction of NaCl solution was injected into the feed stream and outlet conductivity was measured using a Thermo Orion 013605MD conductivity probe. NaCl was selected due to its availability and highly linear relationship between concentration and conductivity. A pulse of struvite crystals, suspended in saturated solution to avoid crystal dissolution, was used to measure crystal RTD. Their PSD is shown in Figure 5.3 below. Crystals were collected from a previous experiment using the PFR to ensure similar PSD and habit to experimental conditions. The outlet PSD was sized in-line by feeding reactor output directly into the Malvern Mastersizer 3000. Laser obscuration was used as a surrogate for mass concentration to calculate the crystal residence time (CRT). HRT and CRT were calculated as the first moment of the respective RTDs (Levenspiel, 1999).

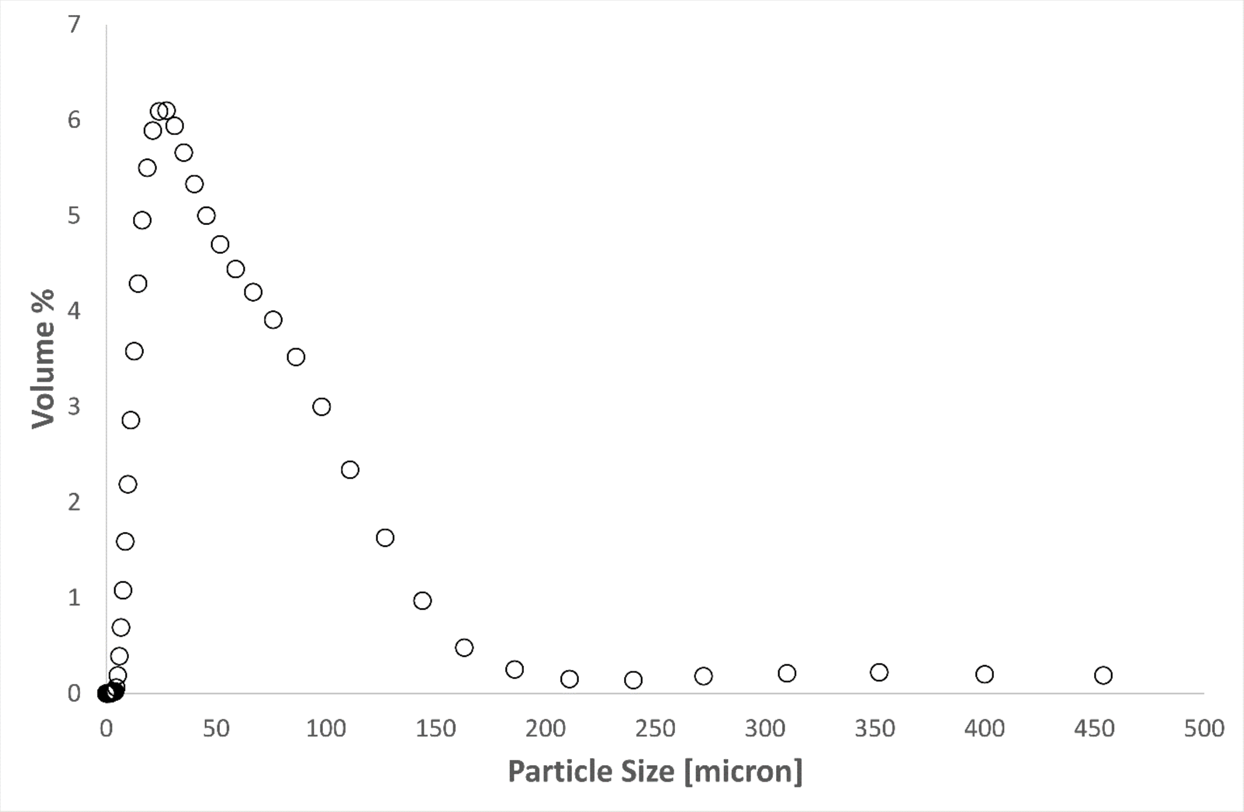

Figure 5.3 – PSD of struvite crystal pulse used in tracer study

Figure 5.4 presents hydraulic RTD (NaCl tracer) and crystal RTD tracer study results, averaged from two repeats. Theoretical hydraulic and crystal RTDs are provided for reference. The theoretical crystal RTD differs from the hydraulic RTD as it accounts for settling effects based on the PSD given in Figure 5.3. Uncertainty in the theoretical hydraulic RTD resulting from feed flow rate uncertainty is negligible when viewed on this figure. Hydraulic and crystal RTD error bars represent sample standard deviation based on two repeats. While uncertainty is high around discontinuities, it remains low at all other points. As such, no further repeats were deemed necessary.

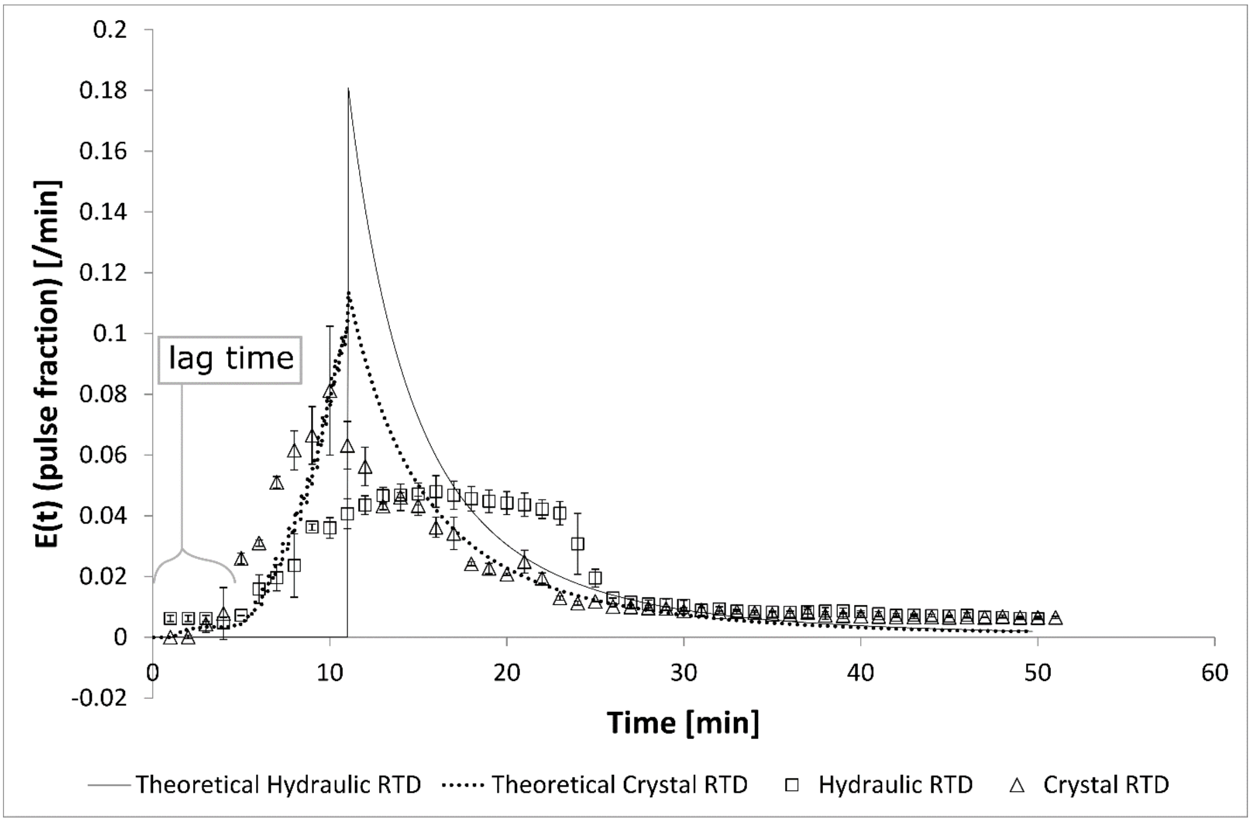

Figure 5.4 – Hydraulic and crystal tracer responses in the Poiseuille seed crystalliser

The given reactor dimensions, operating conditions and entry length should have resulted in close-to-ideal Poiseuille flow (Section 4.1.5). Figure 5.4 shows that hydraulic and crystal RTDs exhibit a partial lag time, suggesting an initial period of high *SI* was achieved. This confirms the suitability of the proposed reactor for investigation of narrow crystal size distribution production. The hydraulic RTD in Figure 5.4 shows fluid elements exiting the reactor faster than predicted by the theoretical fluid RTD for Poiseuille flow, an effect known as short circuiting. The HRT was 16% lower than the theoretical value and its standard deviation was 19.3% greater, which is also an indication of short circuiting. In addition to fluid elements exiting the reactor early, some remain in the reactor for longer than expected by theory. These results indicate plume formation, where some fluid elements, exiting the centre of the orifice between the mixer and Poiseuille flow section, move faster than theoretically anticipated, while others exiting near the edge of the orifice recirculate and spend longer than expected in the entry of the reactor. PSD spreading might be reduced by increasing reactor length-to-diameter ratio or decreasing the reactor-diameter to orifice-diameter ratio. The crystal RTD in Figure 5.4 shows that a fraction of crystal tracer exits the reactor earlier than the theoretical crystal RTD, indicating that the crystals used in the tracer also short circuited. It is likely that they were entrained with the short circuiting fluid. It must be noted that in reality, particles would not have exited as early as measured since they would have begun as nuclei, whereas the crystals used in the tracer entered the reactor at full size ($D[50] = 34.2\mu m$) and were therefore subject to maximum settling force. The separation of the crystal tracer based on particle size is visualised in Figure 5.5 below which shows larger particles exiting the reactor faster. Calculations incorporating particle growth and settling effects estimated that during seed production experiments, particles would begin to exit the reactor after 10.05min, rather than after the 5min mark as observed in the crystal tracer. This indicates that the crystal RTD would be translated right, putting it in line with the fluid RTD. Although some short circuiting was evident, the agreement between theoretical and measured crystal RTDs gave confidence that the reactor operated as intended and could be modelled using Poiseuille flow and settling theory.

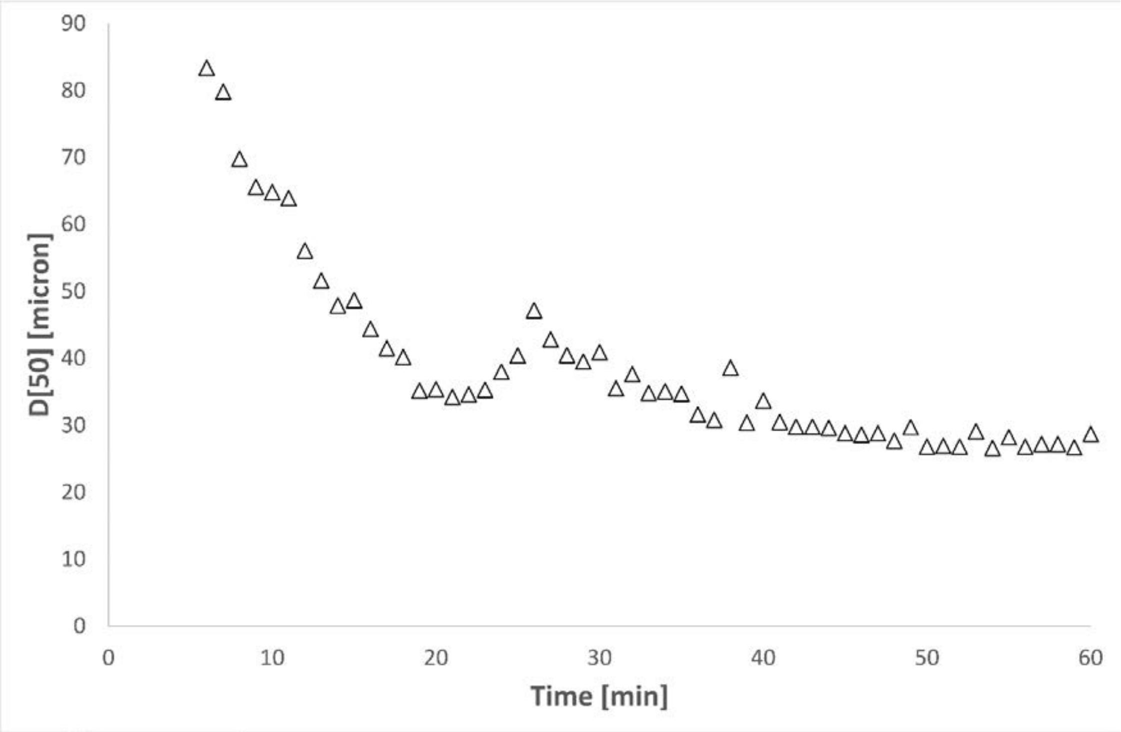

Figure 5.5 – Outlet median particle diameter during crystal tracer study decreasing with time as larger particles settle faster

5.3 Experimental design

Table 5.1 describes the experimental campaign undertaken. In experiment set 1, in-line PSD sampling was conducted with a minimum of three runs for each level of *SI* to address the significant scatter encountered. Additional runs were conducted at *SI* = 0.8 and 1.0 when an equipment modification was made to the reactor. Their inclusion had negligible impact on averaged results so they were included in the analysis. In experiment set 2, filtered and sonicated sampling was conducted with a single run under each condition due to the low variance in data and the time and resource intensive nature of manual sampling. At *SI* = 1.4, the beginning of transfer line blockage formation reduced the number of reliable filtered samples.

Table 5.1 – Experimental campaign for Poiseuille flow reactor with either in-line or filtered and sonicated PSD measurement techniques

SI	**Mixer**	**Experimental Set 1 – In-line**		**Experimental Set 2 – Filter/ Sonicate**	
		Runs	Number of PSD Samples taken	Runs	Number of PSD Samples taken
0.8	R	4	10	1	10
	IJ	4	10	1	10
1.0	R	5	10	1	10
	IJ	6	10	1	10
1.4	R	3	10	1	7
	IJ	3	10	1	7

5.4 Sampling and analysis

5.4.1 Analysis methods

All *pH* measurements were taken at the reactor outlet before filtration using a Ross Ultra Sureflow Semi-micro probe (8175BNWP) in a flow cell. Phosphate concentration was determined with an Agilent 8453 UV-Vis spectro-photometer using the molybdo-vanado-phosphoric acid method (APHA, AWWA, & WEF, 1999). Precipitant phosphate and magnesium ratio were determined by dissolving crystal in de-ionised water and analysing using ICP-OES. PSD analysis was performed by laser diffraction (LD) using a Malvern

Mastersizer3000. In one set of experiments the PSD was measured in-line and in another set of experiments it was measured after filtering particles and subjecting them to sonication (40 W at 40 kHz for 5 min) in saturated solution. In-line sonication, although desirable, was not possible with the Mastersizer3000 without introducing a mixed volume that would have sustained crystal growth and allowed sample back-mixing. Sample collection was conducted using vacuum filtration using 0.2-µm cellulose nitrate filters. Filters were changed and washed with saturated solution in 10-min cycles to avoid bridging of crystals in the filter cake as this would compromise subsequent PSD measurements. Saturated solution was prepared by collecting filtrate, allowing it to rest for at least 24 hours and filtering again. All equipment was calibrated as per manufacturer specifications before each experiment. We employed four measures/inferences of struvite suspended solids, measured in g/L. It was directly measured at the reactor outlet by crystal filtration and mass measurement over a known time frame at a given average flow rate. The filtrate phosphorus concentration was also used to determine phosphorus removal from solution by mass balance. Suspended solids was also measured by inference from laser diffraction measurements using the Beer-Lambert Law and finally by using thermodynamic modelling based on pH measurements (Figure 5.8).

5.4.2 Scale formation in Mastersizer

Preliminary tests showed in-line particle size to increase with run time at fixed operating conditions. Scaling of the Mastersizer flow cell was identified by injecting 60-mL pulses of 2-M HCl *in the line after the reactor, but before the Mastersizer3000. Reduction of particle size and return of laser obscuration to the base line were achieved (Figure 5.6). Note that the multiple downward spiking of pH results from HCl moving both upwards and downwards from the injection point. On this basis, the particle size measurements taken in line were considered correct for only the first 10 minutes after application of acid flush, once a stable pH was achieved.*

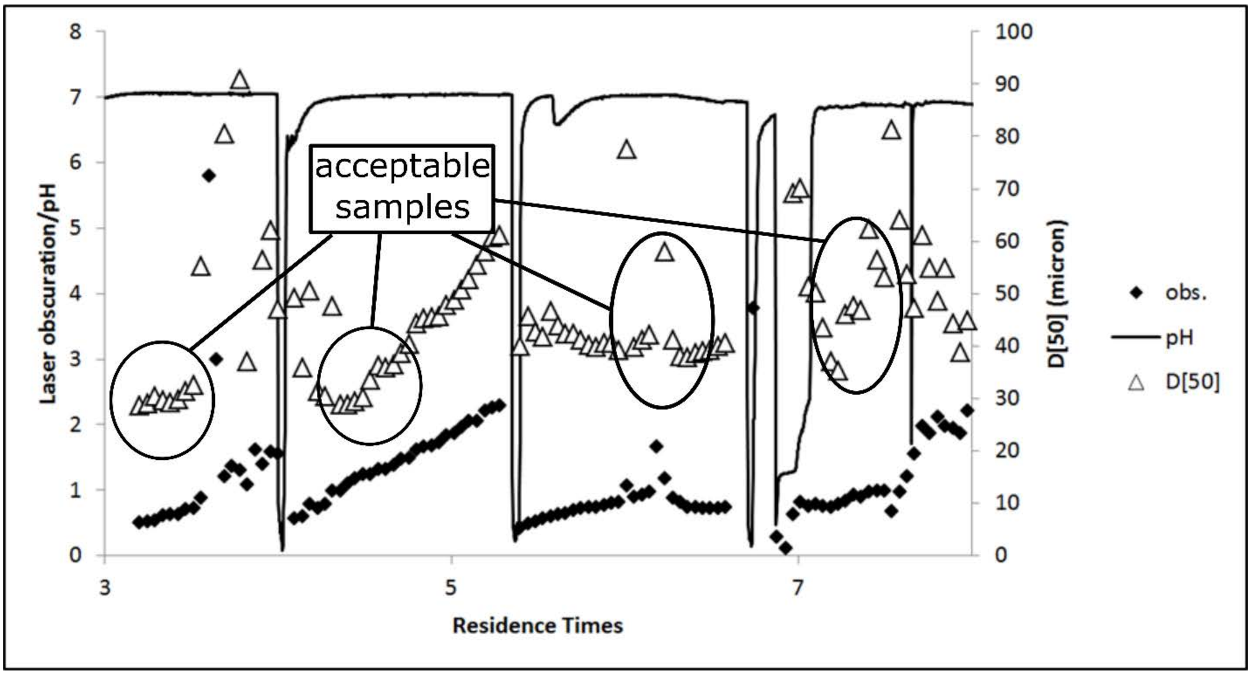

Figure 5.6 – Flushing of HCl through laser diffraction flow cell to remove scaling. Obs.= laser obscuration %.

5.4.3 pH probe drift and response time

Drift of the pH measurements was determined to be negligible (<0.01) over test durations of up to 3h. Although, crystallisation experiments showed that the effects of probe encrustation were significant. The crystallisation experiments involved measuring the pH of nutrient solutions with two probes. One probe remained clean, while the other was encrusted with struvite under the same solution thermodynamic and hydrodynamic conditions as in Poiseuille flow tests. Tests were repeated in triplicate and probes were calibrated before each test. Before encrustation, the pH difference between probes averaged 0.04, showing that in solutions of low ionic strength (0.045M), pH agreement is worse than the manufacturer's specification (±0.01), but better than the uncertainty of buffer solutions used for calibration (±0.05). After encrustation took place, the difference in pH between the clean and encrusted probe was 1.585 after 30s and 0.176 after 5min, illustrating high response time of the crystal encrusted probe. This significantly reduces reliability of pH as an indicator of the thermodynamic state in this study and raises questions of the applicability of pH as a meaningful variable in industrial scenarios, where probe encrustation is likely.

5.5 Results and discussion

5.5.1 XRD characterisation

Figure 5.7 shows XRD of the product crystals created at *SI* = 0.8, 1.0 and 1.4. The figure also includes indication of the major responses, which are expected to be associated with either struvite and newberyite, although struvite responses are much stronger. Many minor responses associated with each of these minerals (not presented here) overlap due to the similar ionic structure of struvite and newberyite. The key responses suggesting the occurrence of newberyite, which do not overlap with struvite, occur at 2θ=18.82, 19.18, 20.04, 25.82, 28.86, 29.30 and 34.94. Miller indices for each phase are also included to indicate crystal faces upon which preferential growth occurs.

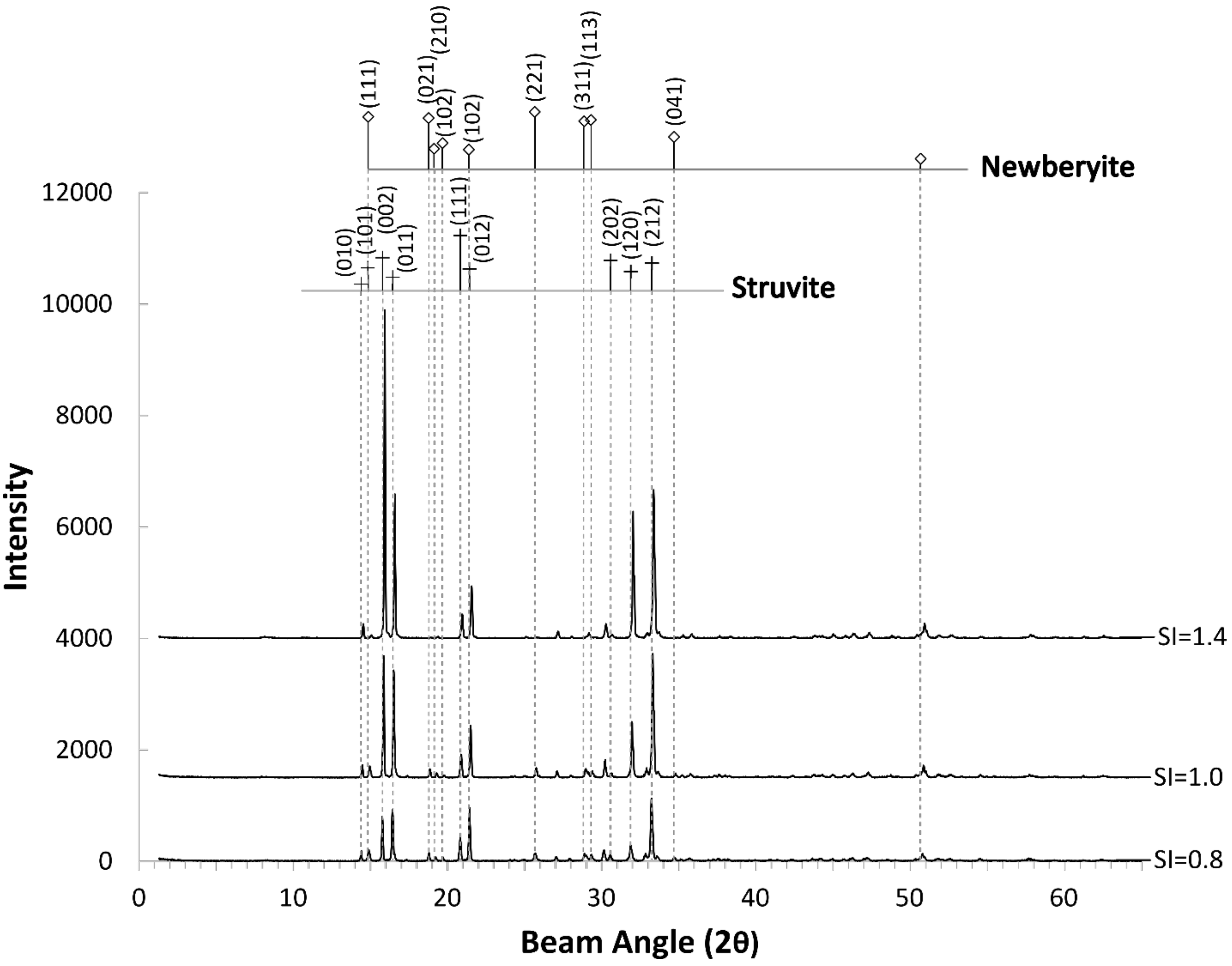

Figure 5.7 – XRD patterns taken from samples at SI = 0.8, 1.0 and 1.4

XRD patterns (Figure 5.7) of the solid phase produced matched that of struvite. Preferential growth of the struvite 002, 011 and 120 faces with increasing *SI* was indicated by increasing intensity of responses at 2θ = 15.78, 16.60 and 32.06, respectively. This supports the observation of increasing aspect ratio with increasing *SI* shown in Figure 5.9 and the needle-like particles shown at *SI* = 1.8 in Section 5.2.3.4. Similar results have been observed by other authors (Chauhan, Joseph, Parekh, & Joshi, 2008; Korchef, Saidou, & Ben Amor, 2011; Ye et al., 2014). Peak heights at 2θ = 20.84^0 (111) were lower than expected at all *SI* values, indicating low growth on this face, or possibly orientation bias, where crystals preferentially orient in one direction during measurement. The XRD patterns also suggest small quantities of newberyite ($MgHPO_4 \cdot 3H_2O$) formation at *SI* = 0.8 and 1.0. ICP analysis gave an Mg:P ratio of the crystal product as 1.15±0.02, 1.13±0.04 and 1.18±0.02 in tests using $SI = 0.8, 1.0\ and\ 1.4$, respectively, suggesting that an additional magnesium phosphate solid phase is forming. Incorporating magnesium phosphate solid phases to the model suggested that under the conditions tested, it was thermodynamically possible for formation of bobbierite, $Mg_3(PO_4)_2 \cdot 8H_2O$, and newberyite, $MgH(PO_4)$, which at the inlet would have supersaturations of *SI* = 1.07 and *SI* = 0.2823, respectively.[16] Previous work has observed XRD patterns indicating the formation of cattiite, $(Mg_3PO_4)_2 \cdot 22H_2O$ at Mg:P of 3-4 (Korchef et al., 2011), although thermodynamic modelling and XRD results do not suggest its formation here. The presence of newberyite did not explain the excess Mg in the crystal, since newberyite has the same Mg:P ratio as struvite. Therefore bobbierite is the most likely secondary mineral forming although XRD patterns for bobbierite and cattiite do not significantly match any unexplained XRD peaks. If the excess magnesium does exist in the form of bobbierite, thermodynamic modelling shows that struvite purity on a mass fraction basis was 73.78±3.69%; 77.44±3.63%; 68.19±3.77% at *SI* = 0.8, 1.0 and 1.4, respectively.

---

[16] It should be noted that SI values are not comparable between minerals in relation to crystallisation kinetics nor even to the equilibrium state. SI simply indicates whether the system is at, or away, from thermodynamic equilibrium.

5.5.2 Phosphorus recovery measurement/ estimation

Figure 5.8 shows the suspended solids of the flow exiting the reactor between two residence times duration towards the end of each reactor operation, typically 5 residence times. This should reflect steady state operation of the system. Operating times beyond this were not possible due to transfer tube fouling (Figure 4.1). Four different precipitation measurement methods were utilised for validation purposes – solution phosphorus concentration, filtered crystal mass, suspended solids based on laser obscuration, and crystal mass inferred from pH change. Their uncertainties are described in Table 5.2.

Table 5.2 – Phosphorus concentration measurement methods and uncertainties

Crystal mass concentration [g/L] calculation method	Uncertainty estimation method	Crystal mass concentration uncertainty [g/L]
Solution phosphorus concentration	Spectrophotometer (average S.D. = $8.88 \times 10^{-5} M$ from 10 repeat measurements), dilution (0.66%) and thermodynamic model uncertainties	0.039 – 0.061 (S.D.)
Filtered crystal mass	Electronic balance precision (5×10^{-5}), filtrate volume (0.029)	$4.29 \times 10^{-5} - 594 \times 10^{-5}$ (min/max)
Suspended solids (laser obscuration)	10 repeat measurements per sample	0.007 – 0.167 (S.D.)
pH	Buffer solution (0.05 min/max) and thermodynamic model uncertainties	0.001 – 0.029 (S.D.)

The most reliable measurement of crystal formation was that based on the remaining liquid phosphorus concentration. The filtration and weighing technique tended to underreport suspended solids, due to scaling losses within the reactor. Obscuration-based suspended solids, shown in Figure 5.8, displayed a high variance in repeat measurements of the same sample and between samples. This effect was more prominent at higher *SI* and may have been caused by higher particle aspect ratio at higher *SI*, as seen in Figure 5.9 below. Higher particle aspect ratios have been shown to reduce the accuracy of laser diffraction PSD measurements (Kelly & Kazanjian, 2006), an effect which has also been observed for the struvite system (Ariyanto et al., 2014). Crystal formation inferred from pH measurements was also uncertain due to encrustation of the pH probe, which occurred mostly on the leading edge of the pH probe, reducing accuracy and increasing response time (Section 5.4.2). These issues highlight the need to be meticulous when measuring phosphorus recovery. Despite these issues it is still comforting that all four techniques were in the same order of magnitude.

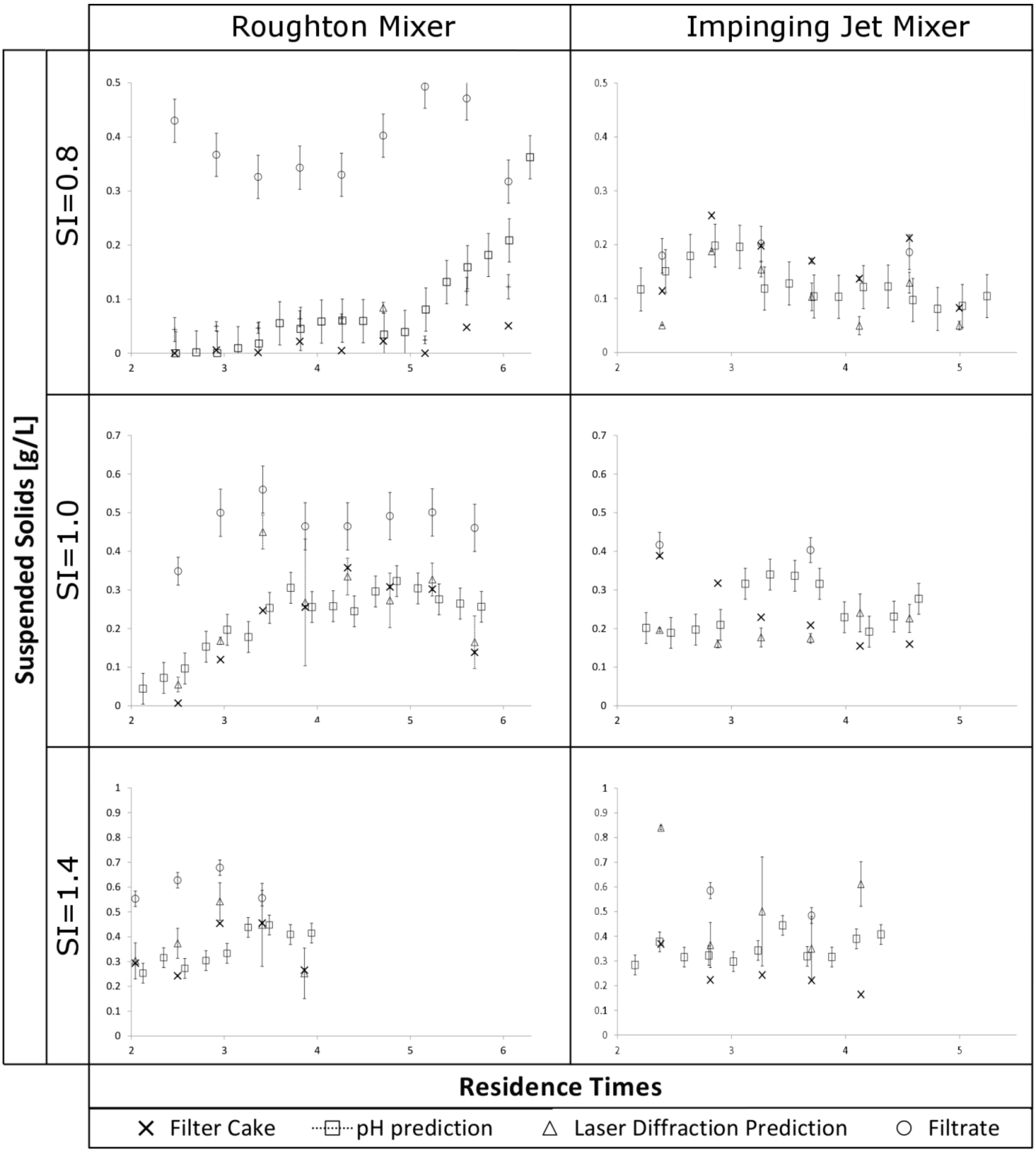

Figure 5.8 – Transient struvite suspended solids [g/L] produced in Poiseuille flow crystalliser with impinging jet (IJ) and Roughton (R) mixers at SI = 0.8, SI = 1.0 and SI = 1.4. Legend indicates method by which suspended solids was measured/inferred.

Figure 5.9 shows photomicrographs of crystals at increasing *SI*, using R and IJ mixers before and after sonication. Extra images are provided in Appendix A. A 1-mm scale is provided in the bottom right and individual images contain a scale, where minor divisions are 10 µm and major divisions are 100 µm. The images show that aggregates broke apart and aspect ratios of individual crystals observed before and after sonication suggest that crystal breakage was insignificant. A detailed discussion of how sonication impacted the results is given later in section 5.5.5.

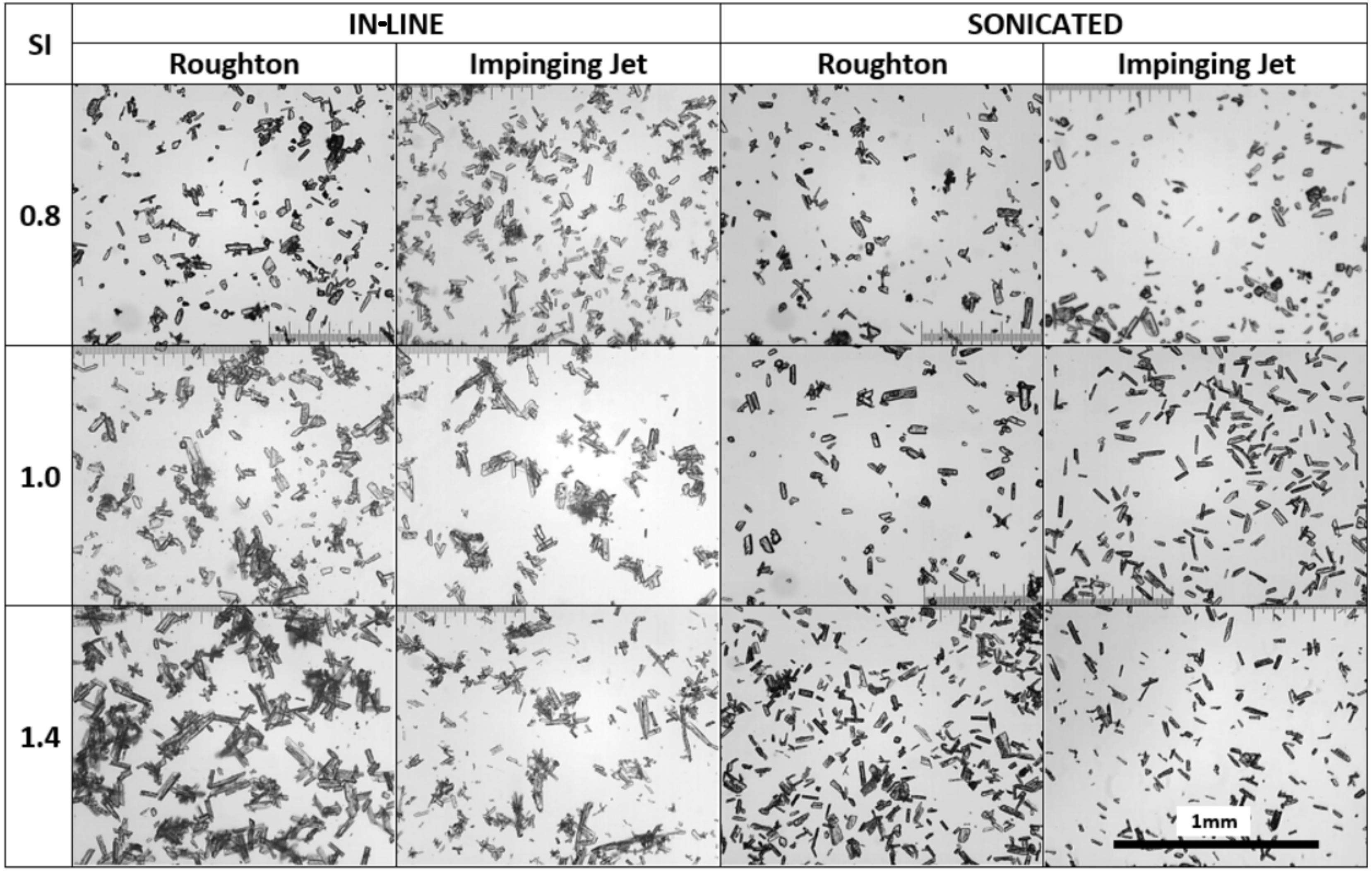

Figure 5.9 – Photomicrograph of crystals exiting the Poiseuille flow crystalliser, comparing in-line and sonicated samples from both Roughton (R) and impinging jet (IJ) mixer apparatus at SI of 0.8, 1.0 and 1.4.

5.5.3 Effects of mixing on phosphorus recovery

Figure 5.10 shows ‘recovery curves’ for this system, which represent the de-supersaturation pathway of the outlet phosphorus concentration for a given inlet SI. The curves are created by solving the thermodynamic model for this system (Galbraith & Schneider, 2014), using a particular feed condition. Three feed conditions are shown on the plot: high, medium and low non-equilibria SI. All curves start at a positive SI, decreasing to $SI = 0$, which is the theoretical thermodynamic end-state of the feed solution. Each point is superimposed on its respective inlet condition curve based on the measured outlet phosphorus concentration. Each phosphorus concentration data point and uncertainty (standard deviations) are the combination of all sonicated runs, all samples, all repeat measurements and include dilution uncertainties. Thermodynamic model uncertainty has not been included since it would be consistent between phosphorus recovery curves. The grey dashed line shows an apparent plateau of minimum SI for the IJ mixer.

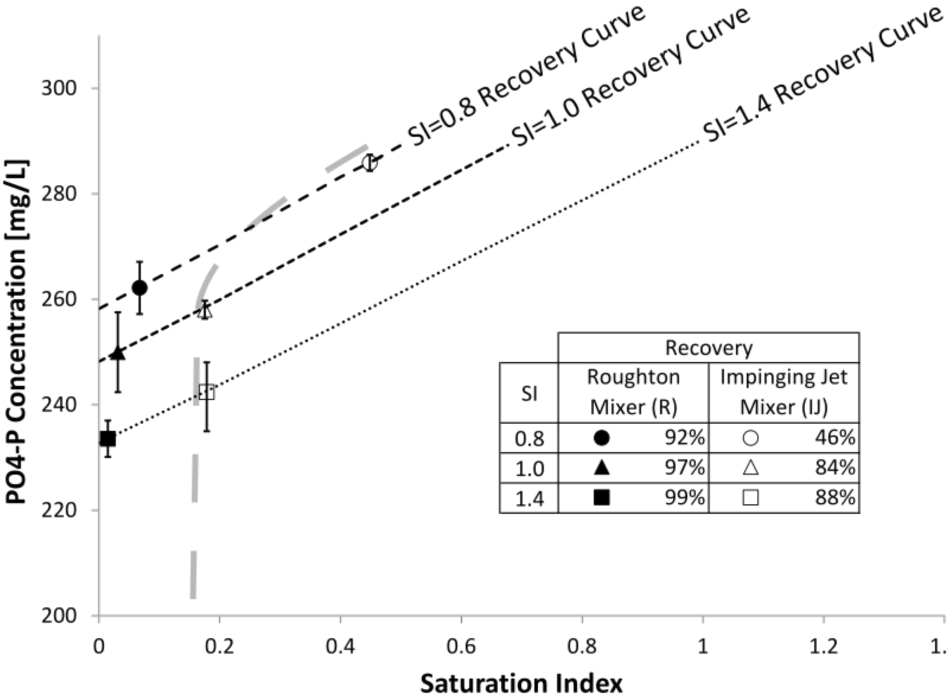

SI	Recovery Roughton Mixer (R)		Impinging Jet Mixer (IJ)	
0.8	●	92%	○	46%
1.0	▲	97%	△	84%
1.4	■	99%	□	88%

Figure 5.10 – Phosphorus recovery and exit saturation index (SI) for Roughton (R) and impinging jet (IJ) mixers at SI = 0.8, 1.0 and 1.4. Dashed line shows the limiting phosphorus recovery performance of the IJ mixer.

Figure 5.10 shows that reactor outlet *SI* plateaued with the IJ mixer for all feed conditions studied (grey dashed line), since none of the outflows reached the equilibrium target phosphorus concentration. The R mixer did a much better job of achieving close-to-equilibrium recoveries. Although the IJ mixer would produce equilibrium results at a longer residence time, this shows that the IJ mixer lags behind the R mixer. While slower kinetics have been observed below *SI* = 0.2 (Galbraith et al., 2014; Mehta & Batstone, 2013; Schneider et al., 2013), excellent recoveries achieved using the R mixer contradict this observation. This suggests that phosphorus recovery depends significantly on mixing and not only on *SI* level in the inlet. Insufficient mixing could affect phosphorus recovery by causing a number of effects:

First, poorer mixing creates localised zones of high *SI* and resulting nucleation rates. However, the interfacial area between feed fluids is lower, resulting in a lower average *SI* and nucleation rate, when integrated over the radial cross section. This means that uniform mixing generates a greater overall nucleation rate as all of the reagents are able to react simultaneously. This results in a greater crystal surface area for subsequent crystal growth. Reduced mixing has previously been shown to cause PSD spreading, and decreased recoveries (Hacherl et al., 2003) and computational fluid dynamics (CFD) has been used to show that mixing is lower in IJ applications (Lindenberg & Mazzotti, 2009), but no work could be found investigating the *SI* distribution in a tubular reactor. Therefore, lower ultimate phosphorus recovery in the IJ mixer at *SI* = 0.8 suggests lower nucleation rates, a result of poor mixing.

Second, poor mixing means that small volumes of one feed can be mixed with larger volumes of the other and vice-versa, creating localised SI variations. This means that fluid elements of undersaturated feed exist, enabling nuclei dissolution. For example, Figure 5.11 shows that for the non-equilibrium feed SI of 1.4, when the ratio of caustic to feed fluid element volume varies from 1:10 to 20:10, SI varies from -1.41 to 2.46. Higher caustic feed ratios (>20:10) introduce a dilution effect causing SI to decline.

These first two explanations hinge on the assumption that the increase in nucleation rate and decrease in dissolution zones due to complete mixing outweighs the increase in nucleation rate in localised zones of high supersaturation created by incomplete mixing. The results seem to support this assumption but it can only be truly tested with a sound knowledge of nucleation kinetics and a detailed hydrodynamic model e.g. a CFD model.

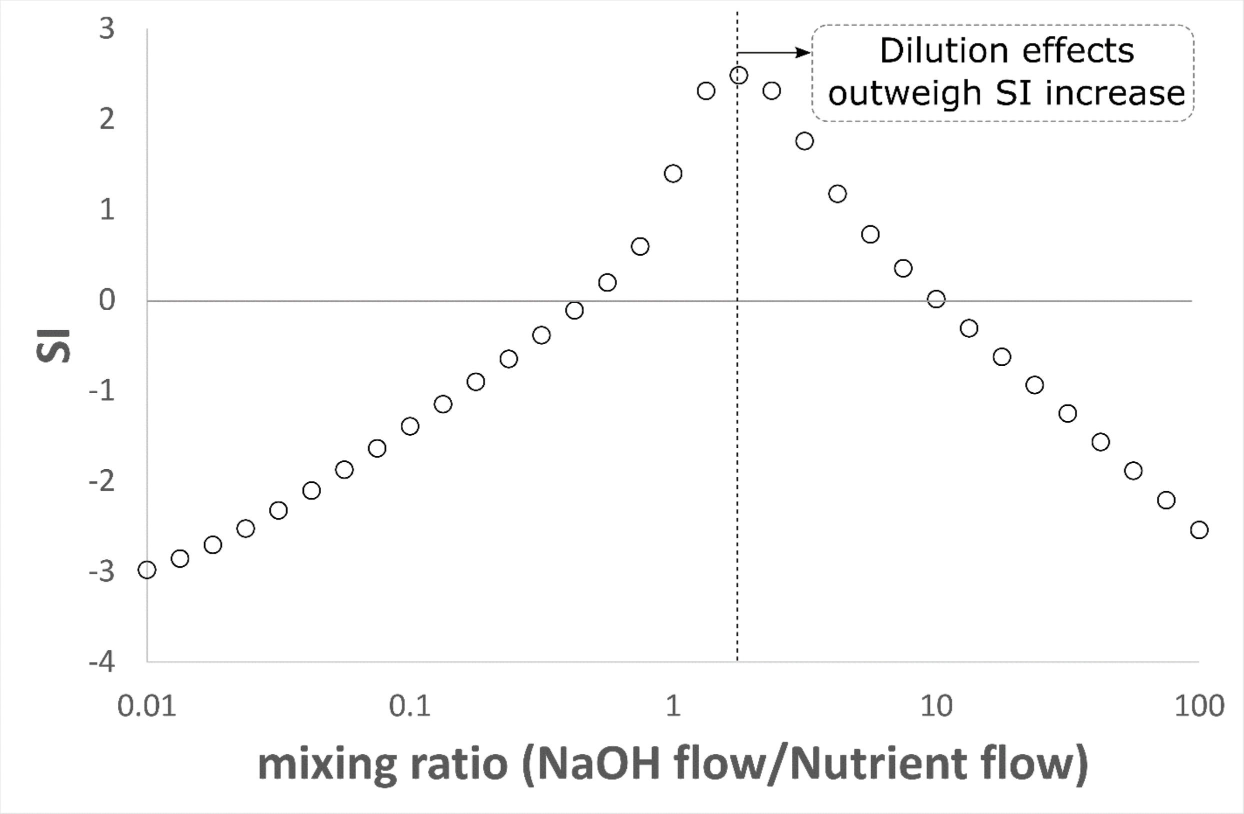

Figure 5.11 – Effects of increasing ratio of sodium hydroxide to nutrient feed flow rate on SI

A third way that insufficient mixing might affect phosphorus recovery is by aggregation. Concentration gradients created by incomplete mixing may promote aggregate formation by a number of mechanisms. Firstly, collisions in high supersaturation regions are more likely to form a bridge due to high growth rates (M. Hounslow et al., 2001). Lower shear forces in the IJ mixer reduce the probability of aggregate disruption (Balakin, Hoffmann, & Kosinski, 2010; M. Hounslow et al., 2001). The resulting increase in aggregation can then limit surface area available for crystal growth. Larger aggregates observed in the IJ mixer contribute to lower phosphorus removal due to reduced crystal surface area and diffusion limitations of fractal aggregates. Figure 5.13 shows that at *SI* = 1.0, particle size is 53% larger in the IJ mixer than in the R mixer, yet phosphorus recovery is 13% lower. Similarly, at *SI* = 1.4, aggregate size is

35% greater (in the IJ mixer case), while phosphorus recovery is 11% lower. These results support the abovementioned potential mass transfer limited growth,

Finally, secondary nucleation caused by fluid shear of scale formation in the R mixer (Figure 5.12) may also contribute to the greater observed phosphorus recovery. Higher turbulence is created in the R mixer than the IJ mixer, which is known to increase struvite scale formation (K. N. Ohlinger et al., 1999). The reason for this is twofold: firstly, improved mixing results in more uniform supersaturation; and secondly, rotational fluid motion creates a wider distribution of fluid element residence times (Lindenberg, Schöll, Vicum, Mazzotti, & Brozio, 2008). Both of these factors increase the probability that the mixer surface is exposed to supersaturated solution and subject to scale formation. Scaling could be reduced in future work by polishing the inside of the mixer to reduce surface roughness.

Figure 5.12 – Long term mixer scaling from Roughton mixing operation

5.5.4 Supersaturation impacts on PSD

Figure 5.13 and Figure 5.14 show the average volume median particle diameter (*D[50]*) and PSD width (*D[90]-D[10]*) of the reactor outflow across the range of inlet SI values, using R and IJ mixer types, measured in-line and after sonication. Results for sonicated samples and in-line samples are from unrelated runs. Data points and uncertainties (one standard deviation) are the combination of all runs, all samples, all repeat measurements and include dilution uncertainty propagation. The statistically significant outcomes of results presented in Figure 5.13 and Figure 5.14 are summarised in Table 5.3, where each result was determined using a two-tailed test at 95% confidence interval.

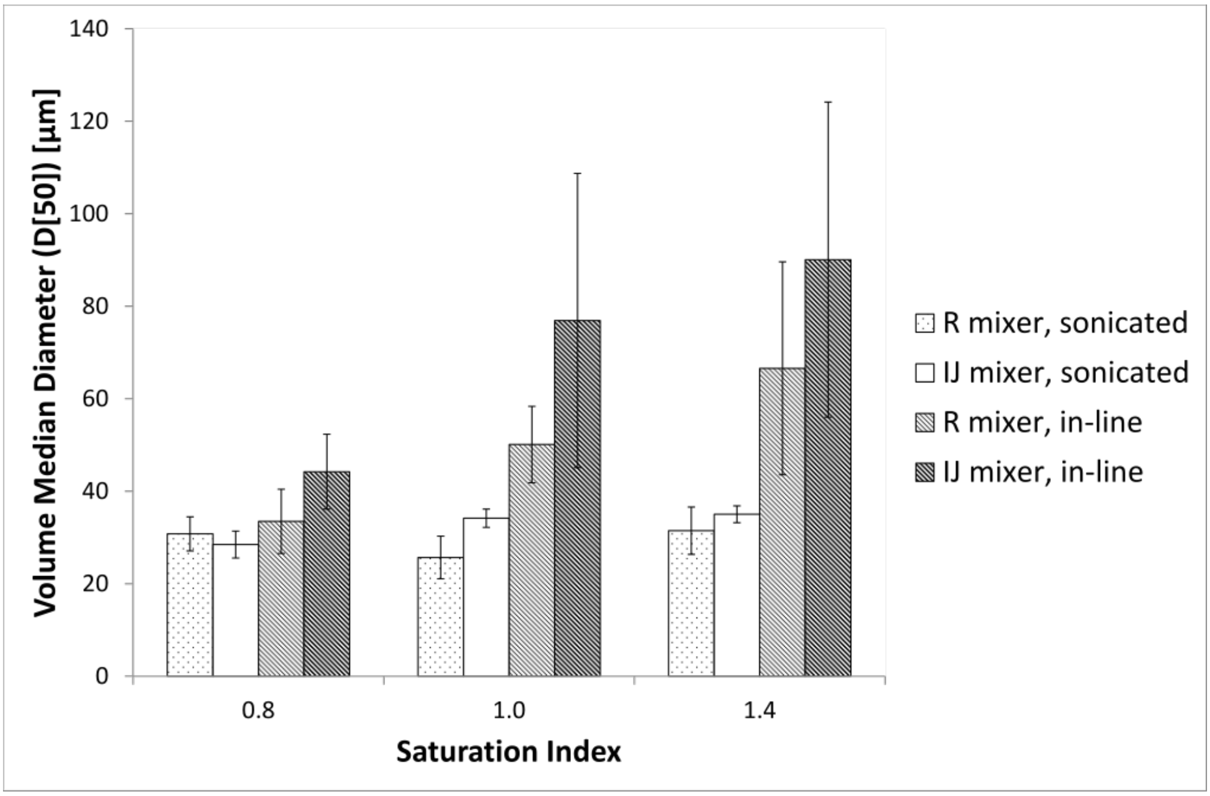

Figure 5.13 – Volume Median Diameter (D[50]) averaged over repeat experiments for varying saturation index (SI) levels using Roughton (R) and Impinging Jet (IJ) mixers. Uncertainty defined as ±1σ of all experimental D[50] values.[17]

---

[17] Note that the standard deviation of *D[50]* values differs from the standard deviation of an individual distribution, which is a measure more akin to the distribution width described later.

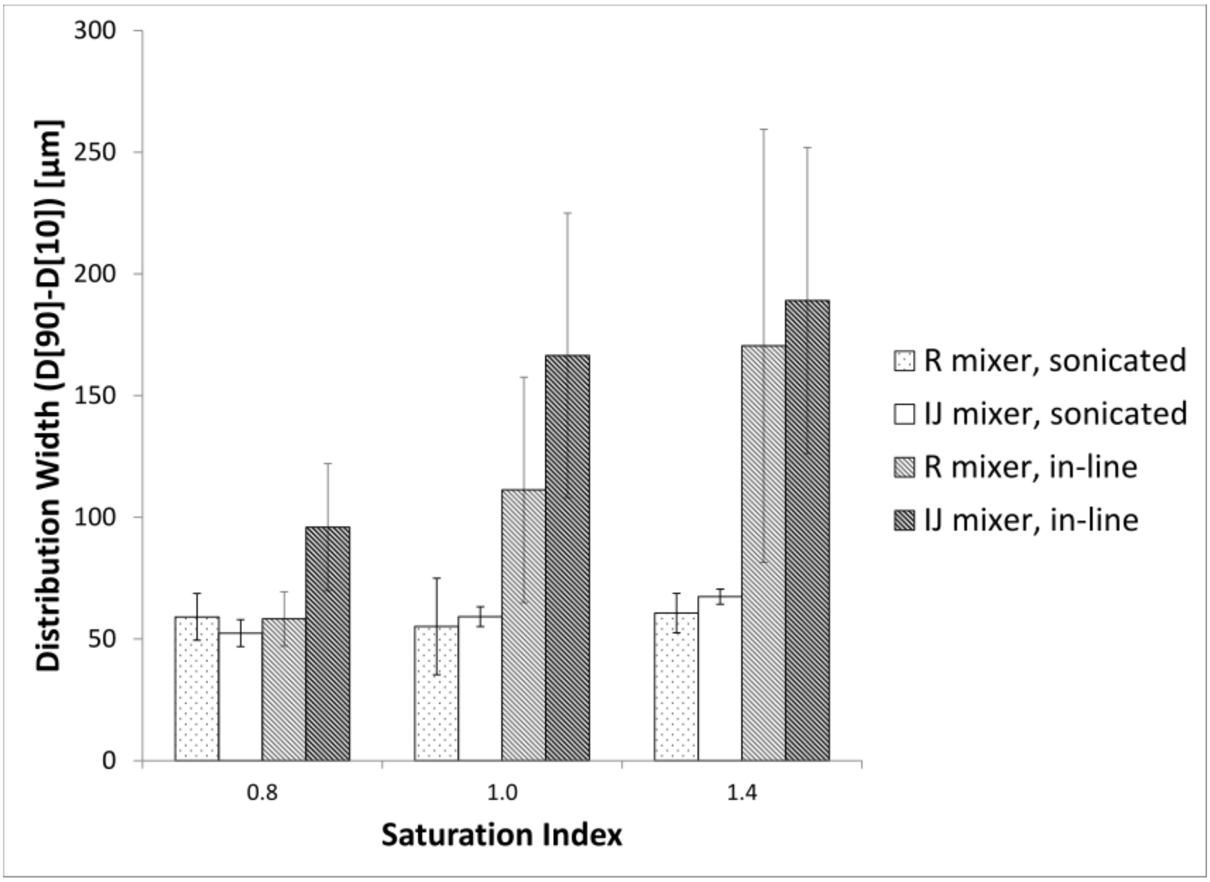

Figure 5.14 – PSD width (D[90]-D[10]) obtained in a Poiseuille flow reactor at different saturation indices (SI) with Roughton (R) and Impinging Jet (IJ) mixers using In-Line (IL) PSD measurement and filtration followed by sonication (FS) PSD measurement.

Table 5.3 – Summary of significant differences in averaged volume median diameter and PSD width results between supersaturation levels and sonication conditions for the Poiseuille flow reactor. Conditions 1 and 2 describe the comparison made using a Z or t test

PSD property	Mixer	Measurement technique	SI	Condition 1	Condition 2	Statistical Test	Change in PSD property ± 95% CI [μm]
D[50]	R	In-line	-	*SI* = 0.8	*SI* = 1.4	Z	33.1 ± 8.5
D[50]	IJ	In-line	-	*SI* = 0.8	*SI* = 1.4	Z	45.9 ± 12.5
D[50]	IJ	Sonicated	-	*SI* = 0.8	*SI* = 1.0	t	5.7 ± 2.5
D[50]	IJ	N/A	0.8	In-line	Sonicated	t	15.8 ± 3.5
D[50]	IJ	N/A	1.0	In-line	Sonicated	t	42.8 ± 9.3
D[50]	IJ	N/A	1.4	In-line	Sonicated	t	55.1 ± 14.8
D[50]	IJ	N/A	1.4	In-line	Sonicated	t	121.7 ± 27.3
width	R	In-line	-	*SI* = 0.8	*SI* = 1.4	Z	112.2 ± 32.0
width	IJ	In-line	-	*SI* = 0.8	*SI* = 1.4	Z	93.2 ± 23.9
width	IJ	N/A	0.8	In-line	Sonicated	t	43.5 ± 10.0
width	IJ	N/A	1.0	In-line	Sonicated	t	107.3 ± 24.0
width	R	N/A	1.4	In-line	Sonicated	t	35.1 ± 10.9
width	R	N/A	1.4	In-line	Sonicated	t	109.8 ± 39.1

Under all supersaturation levels considered, the seeds produced in this work, before and after sonication, are in the size range of those encountered in previous work: 5 – 20 μm (Galbraith et al., 2014); 35±3 μm (Mehta & Batstone, 2013); 45 – 63 μm (Ali, Schneider, & Hudson, 2005) and; 75 - 150 μm (Kim et al., 2007; Jun Wang et al., 2006). This enables the results of those investigations to inform future investigations of a continuous seeding reactor followed by a growth reactor. The continuous seeding reactor should be investigated as a method of process control. This requires two sets of experiments to: 1) examine the influence of *SI* and shear rate on PFR output PSD; and 2) examine the effects of seed size and mass loading on the growth reactor phosphorus recovery and PSD. Designing such a system requires the use of existing kinetic models. Since this reactor has produced seed crystals similar to those used in previous kinetic investigations, the results of those investigations can be used in the growth reactor design process.

Figure 5.13 and Figure 5.14 show increased magnitudes of both the *D[50]* and distribution width (difference between volume based PSD 90th and 10th percentiles), respectively, with increasing feed *SI* for in-line samples. A summary of the PSD and width differences, between a variety of *SI* and sonication conditions, at 95% confidence is presented in Table 5.3. These results also exhibit an increasing degree of scatter with increased *SI*. Thus, as feed *SI* is increased, particles observed at the outlet get larger and more variable in size. Other work on struvite crystallisation has shown increasing *SI* to cause an increase in *D[50]* (Koralewska et al., 2007). Koralewska *et al.* also found that increasing *SI* generated no discernible trend in PSD standard deviation, which is analogous to PSD width, because of large scatter in the data. In this work, some PSD width increase is likely due to uncertainties in laser diffraction measurement of high aspect ratio particles, but is primarily attributed to aggregation.

5.5.5 Sonication impacts on PSD

Figure 5.15 shows the change in *D[50]* with time of various crystal samples undergoing sonication. These tests were performed to identify whether attrition (*i.e.* destruction of particles) caused significant change in the PSD over time. The most significant reduction in particle size had occurred by 3 min and a stable trend was observed after 5 min.

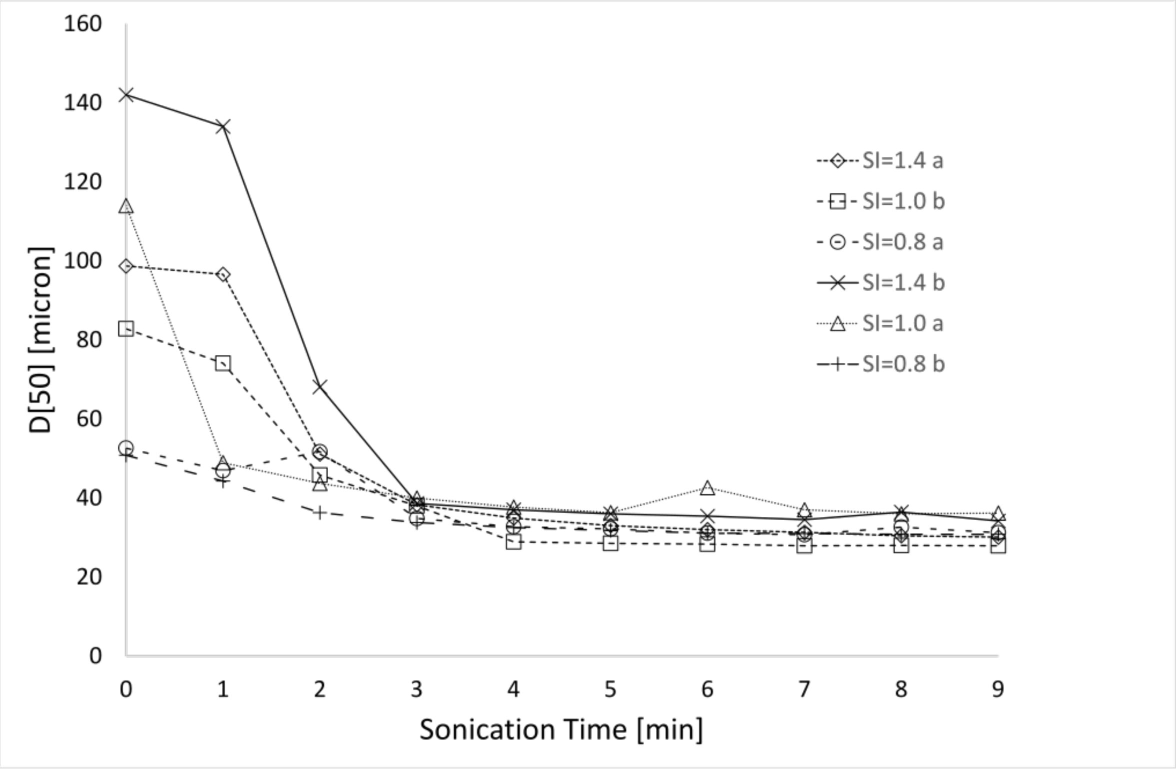

Figure 5.15 – Volume median diameter of particles during sonication.

Sonication easily disrupted aggregates, suggesting that they are only weakly bound.[18] Figure 5.15 shows plateauing particle size reduction with ongoing sonication. We assume that this represents individual particles that have been released from aggregate structures and that the sonication used does not cause significant struvite particle attrition. In sonicated samples, mixer type and feed *SI* had little effect on the *D[50]* and distribution width, unlike the in-line (non-sonicated) sampling strategy. Figure 5.13 shows that the sonicated *D[50]* did not change significantly with increasing feed *SI* using the R mixer and only slightly increased between *SI* = 0.8 and 1.0 using the IJ mixer (Table 5.3). Figure 5.14 shows that distribution width did not change significantly in sonicated samples for any condition examined. Microscopy, shown in Figure 5.9, corroborates these results. At *SI* = 0.8, in the R mixer *D[50]* and distribution width were almost identical for in-line and sonicated samples. Conversely, in the IJ mixer, in-line *D[50]* was 55±12% greater and in-line distribution width was 83±19% greater than sonicated samples (Table 5.3). This shows that at *SI* = 0.8, aggregation is negligible in the R mixer, but significant in the IJ mixer, supporting the idea that aggregation is increased when mixing is incomplete before crystallisation begins.

Aggregation is also more evident at higher *SI* levels. The difference between sonicated and non-sonicated *D[50]* and width are significant at *SI* = 1.0 for the IJ mixer and at *SI* = 1.4 for both mixer types (Table 5.3). This again shows that aggregation is significant at higher *SI*. Increased distribution width shows that aggregates cause increased *D[90]*, but that small particles remain present in all samples. Comparing mixer types at *SI* = 1.0 and 1.4 using non-sonicated measurements gives no significant conclusions, owing to excessive scatter in the data. While scatter is much lower in sonicated samples, no trends are observed. Increasing scatter and converging average *D[50]* and width suggest that differences between R and IJ mixers become less important at higher SI levels. The implication is that mixing time and/or induction time models utilised were not an accurate representation of this system.

---

[18] Note that aggregates are different to agglomerates, which exhibit the same strength as their constituent particles.

5.5.6 Contributions of nucleation, growth and aggregation

Under all conditions tested, all individual particles reach a similar ultimate size, whether aggregation occurred or not. The observed in-line PSD differences primarily result from weak aggregate formation. The similarity of the de-aggregated (*i.e.* sonicated) crystal PSDs at different *SI* levels across a range of mixing regimes, suggests that individual crystals continue growing after they aggregate. The difference in phosphorus removed from solution at different *SI* values and in different mixers, shown in Figure 5.10, means that higher feed *SI* levels create more particles. Quantification of differences in nucleation rate under different operating conditions would be best achieved with an accurate measurement of particle number density, which is better delivered using particle counting and sizing techniques, rather than particle-ensemble, volume-based laser diffraction techniques. This is, unfortunately, a limitation of this work.

Comparing sonicated to in-line samples shows that greater aggregation occurs at higher *SI* levels, which could result from a number of mechanisms. First, increased *SI* increases particle number density due to increased nucleation rates, increasing the rate of particle collisions. Second, it increases the driving force for aggregate bridge formation, reducing the time between particle collision and bridging. Finally, increased *SI* causes dendritic growth, due to preferential adsorption of ions onto one crystal face, increasing the probability of particle collisions and resulting in the formation of more loose and porous aggregates (Ye et al., 2014). Microscopy shows that the contact between aggregate constituents is minimal, which means that the crystal mass increase associated with bond formation between constituent particles in the aggregate is also small. As such, the sonicated samples could be used as a proxy for nucleation and growth mechanisms only. This result is not trivial as it offers a method of extricating aggregation from nucleation and growth mechanisms, a task which has not been properly addressed for struvite, and many other crystal systems. Elucidating true kinetic mechanisms of crystallisation can reduce risk and enhance crystalliser design.

Applying the model developed in Chapter 4, using the cell average technique and nucleation and growth kinetics based on work by Galbraith (Galbraith et al., 2014), shows some agreement between experimental and simulated PSD and phosphorus recovery (Figure 5.16, giving validity to these kinetic parameters. It can be seen though that phosphorus recovery is under-predicted for all supersaturation levels and PSD is under-predicted for *SI* = 0.8, indicating that improved parameter optimisation is necessary. Varying levels of kinetic parameter regression/ optimisation complexity are discussed in section 2.2. This work implements a least squares approach accounting for PSD and phosphorus recovery data from multiple datasets simultaneously, presented in detail in Chapter 7.

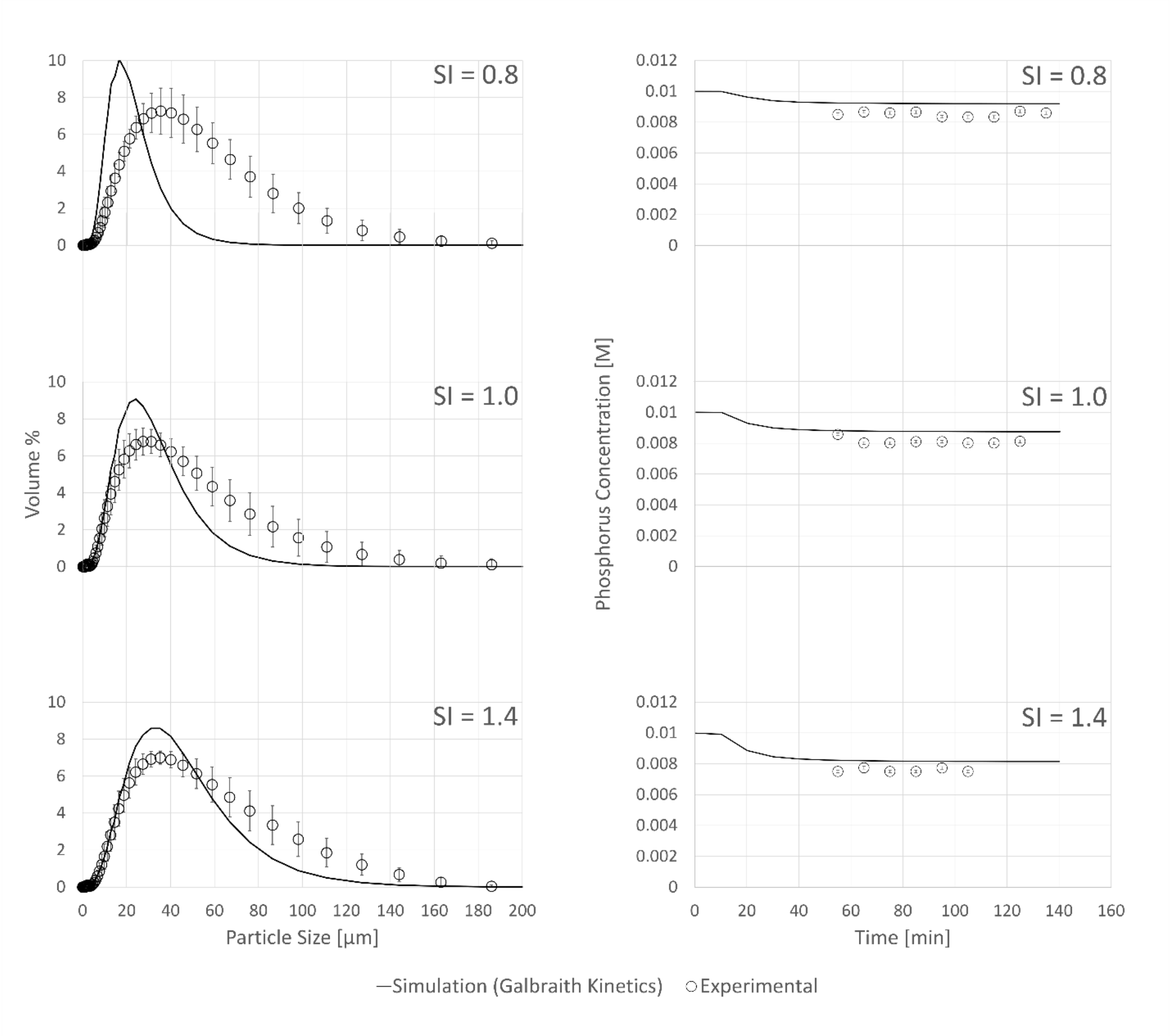

Figure 5.16 – Roughton mixer PFR PSD and outlet phosphorus concentration compared to those predicted by kinetics estimated by Galbraith (Galbraith et al., 2014)

5.5.7 Mixer design evaluation

The method used to specify the inlet jet diameter for both mixers is based on a generalised model for meso- and micro-mixing (Gillian & Kirwan, 2008). The method was previously validated for confined impinging jet mixers, while in this work, the base model applied was a vortex mixer with multiple inputs (Liu et al., 2008). Very little difference in mixing time was observed in the work by Liu between two and four jet scenarios, so the difference between that scenario and this application is not considered of significance. The jet diameters predicted here are considered reasonable due to the generalised nature of the mixing model. In addition, jet Reynolds number (calculated using jet diameter and jet velocity) used in this work ($Re_{jet} = 705$) was far larger than the jet Reynolds number in the vortex mixer used as a base for jet diameter design ($Re_{jet} = 73$), indicating that the jet diameter used for this work produced more turbulent mixer jets with the feed flows used. Mixer Reynolds number in this work as described by Figure 5.17 below, was 28,181. That is more than 20 times the Reynolds number reported for reaction mixing independence using acid/base neutralisation reactions (Liu et al., 2008), which are much faster than struvite formation rates.

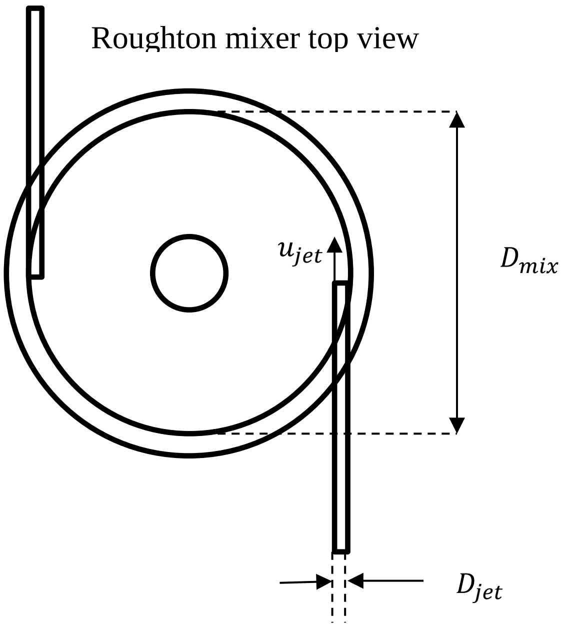

$$Re_{mix} = \frac{\rho u_{jet} D_{mix}}{\mu}$$

$$Re_{jet} = \frac{\rho u_{jet} D_{mix}}{\mu}$$

Figure 5.17 – Mixer characteristic Reynolds number calculation methods

Section 5.5.5 suggests that the mixing time and induction time models utilised do not adequately describe the system at high *SI* as nucleation (resulting in scale formation) occurs in the R mixer before mixing is complete. The mixing time model utilised in this work was previously validated using an inlet jet Reynolds number of approximately 5200 (Lindenberg & Mazzotti, 2009), compared to 700 in this work. Using the Lindenberg & Mazzotti model as a base for design, rather than the model by Liu (described above), yields a jet diameter 5 times smaller than that used in this work, although in their model mixing times were below 1ms, which is well under our requirements. Despite differences between this work and previous work, the design criteria used suggest that it is very unlikely that mixing would be incomplete since the predicted mixing time (0.23 s) was 66 times lower than the lowest predicted induction time (15.15 s at *SI* = 1.4).

This early nucleation may indicate that the mixer Reynolds number, defined by the mixer diameter and jet velocity is not the best indication of mixer turbulence. This is because for a fixed jet velocity, mixer Reynolds number increases proportionally with mixer diameter, but increased fluid volume results in a lower vortex velocity. To test this theory, a series of tracer studies was performed. A small piece of Styrofoam was placed on the open surface of the fluid in the mixer and showed that the average rotational velocity was 1.39 rev/s, which equates to 0.349m/s, almost equal to the jet velocity of 0.354m/s. This indicates that for the reactor geometry and operating conditions, viscous fluid dissipation has a negligible effect on vortex velocity. Nonetheless, we suggest that an improved mixer description for future design and optimisation purposes incorporates mixer aspect ratio and mixer diameter to exit orifice diameter ratio. These tests also showed that the rotational velocity is higher in the center, an effect driven by the fluid exiting the orifice in the bottom of the mixer.

An estimate of the rotational velocity was also made by measuring the depth between the top of the mixer and the fluid surface in the center (Δh=2.5mm). By assuming a rotating body, where linear slopes represent the surface from the outer circumference to centre, then equating the centripetal force to the pressure force, it can be shown that $v=(g\Delta h)^{0.5}$, where v [m/s] is the fluid velocity at the wall and g [m/s^2]

is acceleration due to gravity. This relationship estimates the rotational velocity to be 1.25rev/s (0.157m/s); less than the measured velocity on the surface. By assuming that the outer velocity, created by the jets, is the average of the two estimates given above, the Blasius solution can be used to estimate the viscous sub-layer thickness to be 0.0037m and the maximum viscous sub-layer velocity to be 0.055m/s (Munson et al., 2006). While this estimate is uncertain, it indicates that around 34% of the mixer volume, consists of laminar flow as a result of the no slip condition on the mixer wall. At the maximum laminar velocity, the fluid would exit the mixer in 9.94s, which is over triple the mixer residence time, but still less than the lowest expected induction time. Applying the same methods, it is estimated that the thickness from the laminar layer, wherein the fluid resides in the mixer longer than the crystal induction time is 0.0002m. This is considered a reasonable explanation for the crystal scale observed on the mixer wall (Figure 5.12). An improved mixer design would reduce the mixer diameter, thus reducing any difference between jet and vortex velocities. In addition, the orifice separating the mixer and PFR (Figure 4.1) could be removed to assess whether its shape contributes to scale formation.

A more accurate description of the system would represent mixing time, fluid residence time and induction time as distributed variables. Mixing time and residence times are a function of fluid hydrodynamics, which are distributed because of the laminar layer. Induction time becomes distributed because of supersaturation gradients during the mixing process. The combination of these effects is that some fluid elements stay in the mixer longer than their induction time. This may also be compounded by scale formation facilitating secondary nucleation. In short, the averaged models for mixing time, fluid residence time and induction time are not an adequate description of the complex processes occurring in the mixer.

Future designs can account for these RTD effects by ensuring that a large fraction (*e.g.* 99%) of the mixer residence time is below the induction time, rather than using average mixer residence time. This will reduce the probability of distributed nucleation and scaling by ensuring that fluid elements are well and truly mixed and outside of the mixer before nucleation. Additionally, if a computational fluid dynamics model were applied, supersaturation and resulting induction times could be modelled as distributed variables. Unfortunately, this level of model complexity was outside the scope of this thesis.

5.5.8 Operational considerations

Various operational considerations were identified as important for future investigations. Reactor and transfer line fouling made long term reactor operation unachievable and meant that true steady state operation was not achieved. Despite this, phosphorus removal remained relatively constant over the timescale considered (implying that there was sufficient surface area for mass transfer). Scaling of the flow cell in the PSD measuring device also reduced the number of acceptable in-line (*i.e.* unsonicated) data points (Section 5.4.2). Flow through the orifice separating the mixer from the main reactor became restricted after extended operating times in some runs. This phenomenon indicates that while the residence time of the mixer was 5-fold lower than the induction time at the maximum SI considered, nucleation and subsequent scaling persist. Some degree of stock solution particulate contamination was also inevitable, despite filtration, meaning that true homogeneous nucleation is highly unlikely and that heterogeneous nucleation effects are important. Despite this, past experiments used to determine induction time models were conducted under similar conditions and therefore account for these effects. If both induction time and scaling follow probability distributions, then scaling is unavoidable under long-term operation of any reactor. To quantify scaling, after selected tests, the reactor was drained and filled with 1M HCl, dissolving the accumulated scale. The phosphorus concentration in this volume was then measured and showed that the mixer and reactor scaling contributed between 5% and 13% of total phosphorus removal for SI = 0.8 and 1.4, respectively.

5.6 Conclusions & recommendations

A Poiseuille flow reactor can be used as a low pressure drop method for continuous production of struvite seeds of comparable properties to those used in other work. The PFR produced a significantly narrower hydraulic RTD than a well-mixed tank of equivalent residence time, although some short circuiting and PSD spreading were evident. Scale formation within the reactor and transfer line blockages were identified as an operational limitation, which must be addressed if this reactor is to be used for future work. Mixer scaling indicates slow moving fluid within the mixer and/or issues with induction time estimates. XRD results showed that struvite was primarily formed, with minor formation of newberyite. Crystal elemental molar ratios suggested bobbierite formation, although this was not observed in XRD analysis.

Analysis of PSD and phosphorus recovery data provided a number of insights about mixing and aggregate formation. First, phosphorus recovery data showed that the R mixer was superior to the IJ mixer, under all conditions examined. Second, examining PSD differences between in-line and sonicated samples suggested the formation of weakly-bound aggregates. This was also observed using microscopy. Aggregate formation was found to be insignificant at *SI* = 0.8 in the R mixer, but significant in the IJ mixer. Finally, aggregate formation increased at *SI* = 1.0 and 1.4, making R and IJ mixers' performance indistinguishable.

Increased aggregate formation at higher *SI* in both mixers is likely due to higher particle number densities, increased bridge formation rate, incomplete mixing, and higher particle aspect ratios. In addition, increased scatter in PSD measurements at higher *SI* levels suggests poorer mixing in both mixing configurations. Sonicated PSD properties remained unchanged for all conditions accept for a minor change between *SI* = 0.8 and 1.0 in the IJ mixer, indicating that individual crystals grow to a similar size, irrespective of their participation in aggregation. The results brought into question the characteristic Reynolds number used for mixer design and highlighted the need for larger differences between mixer residence time and induction time.

Results of this investigation are of relevance to both struvite seed production and modelling of struvite formation in Poiseuille flow, for example in catheter encrustation. The applicability of this reactor as a means of continuously producing consistent seed particles will depend on product requirements. If seed requirements match those used in previous research, then an un-sonicated product is acceptable. Alternatively, if a narrower and more repeatable product is required, sonication or another method of de-aggregation should be implemented. In addition, because contact area of individual crystals making up aggregates is small, sonicated samples may provide reasonable data to determine nucleation and growth rates, essentially ignoring the impact of aggregation. In any case, if this reactor design is to be used for struvite crystallisation, crystal scaling mechanisms require further investigation.

Chapter 6 Poiseuille flow crystalliser sensitivity analysis

Basic sensitivity analyses of the Poiseuille flow reactor (PFR) were conducted using the PFR model discussed in earlier chapters. Analyses are presented with three key goals in mind. Firstly, unnecessary model complexity was identified and removed to reduce simulation time. Secondly, propagation of input variable uncertainty to output variable uncertainty was quantified, determining those input variables that have the greatest influence and which output variables vary most significantly. Finally, the propagation of kinetic parameter uncertainty to output variables was quantified, showing which kinetic parameters have the greatest influence on output variables and what variation would be expected based on kinetic models available in the literature. Kinetic uncertainty propagation was also used to identify suitable kinetic parameter boundaries for parameter optimisations, which are presented in the following chapter.

6.1 Introduction

Experimental work in chapter 5 will be used for kinetic parameter optimisation in chapter 7. This chapter analyses the model to help make the parameter optimisation more efficient. This is done by (1) reducing unnecessary model complexity – since kinetic parameter optimisation is an iterative process, it can be very time consuming. Therefore simulation time reduction can be very useful. The first part of this chapter aims to reduce simulation time by identifying aspects of the model developed in chapter 4 which do not make a significant contribution to reactor outlet variables used for kinetic parameter optimisation (PSD and phosphorus concentration). (2) determining whether output variable measurement uncertainties can be used during parameter optimisation – output variable uncertainty must be defined for (or found during) the kinetic parameter optimisation process. These uncertainties could be defined based on output measurement device uncertainty or input uncertainty propagated through the model. The larger of the two will be used in parameter optimisation to ensure kinetic parameters do not have unrepresentatively low uncertainties. While measurement uncertainty is known, propagated uncertainty must be calculated. This can be done in the kinetic parameter optimisation process. Preliminary sensitivity analysis was used to identify whether this is necessary. This was done by varying input variables and observing output variables. The expected output variable uncertainty must be calculated based on input variable uncertainty only (not kinetic parameter uncertainty), as the kinetic parameter uncertainty will be calculated in the parameter optimisation. This chapter details the calculation of propagated uncertainty using the same experimental conditions as in chapter 5. No experimental data is used in this chapter though. (3) identifying which kinetic parameters have the greatest influence on the output variables during simulations – kinetic parameters which have the greatest influence on output variables are of most interest during kinetic parameter optimisation. These parameters are identified in this chapter with the intention of limiting the number of kinetic parameters to be optimised in chapter 7, to avoid over-parameterisation.

These three objectives were achieved using simple delta analysis and it was deemed that Monte Carlo simulations were not necessary to reiterate the outcomes considering the much higher computational requirements. Monte Carlo analyses were however used to examine the effects of kinetic parameter variation and industrial feed input variations using a generalised model.

In addition to improving parameter optimisation efficiency, kinetic parameter variations provided output variable boundaries for parameter optimisation in chapter 8, while industrial feed variations were used to show how this reactor might perform in real life. It should be noted that the generalised model is useful for describing a broad range of experimental data in the literature but contains multiple parameters which are highly uncertain, making its application difficult. Further analysis in chapter 7, is therefore devoted primarily to the standard power law model. This also facilitates ease of comparison with other struvite DPB work.

6.2 Methods

The full PFR model combining fluid flow, cell average population balance techniques and thermodynamic models discussed in earlier chapters was used to conduct sensitivity analyses of the experimental system being examined. In this chapter, key input variables are fixed but have some experimental uncertainty, like flow rate and feed concentration. Output variables refer to measures of system performance which could be measured directly or calculated based on other measurements. These change with time and have uncertainty resulting from input variable uncertainty. Finally, kinetic parameters are fixed with time and exhibit some degree of uncertainty, either as a result of parameter optimisation techniques or data variance.

6.2.1 Key output variable identification

Output variables selected for consideration were the SI, pH, thermodynamic yield, volume median diameter (D[50]) and PSD width (difference between D[90] and D[10]). These variables differ from those used in chapter 5 and 7 since they are better representations of reactor performance. PSD uncertainty is difficult to display since individual size range measurements may have variable uncertainties. The actual uncertainties are analysed as part of the parameter optimisation process in chapter 7. The output variables examined here are analogous to the direct measurements used for parameter optimisation. Thermodynamic yield is analogous to phosphorus concentration and D[50] and width are representative of PSD. The rationale for their selection and their measurement uncertainties are given below in Table 6.1.

Table 6.1 – Output variable uncertainty

Variable	Rationale	Uncertainty	Uncertainty Basis	Used in Parameter Regression
SI	Driving force for all kinetic mechanisms	0.063 (abs)	Propagation through thermodynamic model**	N
pH	Easy to measure and is linked to many thermodynamic equilibriums	0.05 (abs)	Buffer solution	N
D[50] [µm]	An indication of average product size	1% (relative)*	Instrument specification	Y
PSD width [µm] (D[90] – D[10])	An indication of variation in product size	1% (relative)*	Instrument specification	Y
Thermodynamic yield*** [%]	An indication of the performance of the reactor	6.34	Propagation through thermodynamic model**	Y

* If D[50] or width are <1 micron, uncertainty is fixed at Mastersizer3000 lower detection limit (0.01 microns)

** using methods described by NIST (Taylor & Kuyatt, 1994)

*** Thermodynamic yield is calculated based on phosphorus concentration uncertainty relative to the phosphorus concentration at equilibrium

While not all of these variables were used in later parameter optimisations, they remained of interest for their description of reactor operation/performance. Propagated *SI* uncertainty was calculated based on phosphorus concentration measurement uncertainty ($\pm 8.88 \times 10^{-5} [M_{PO_4^{3-}-P}]$), flow rate uncertainty ($\pm 0.005\ [L/h]$) and the struvite equilibrium constant uncertainty (± 0.04) (K. N. Ohlinger et al., 1998). Approximately half of the SI uncertainty given above resulted from assumed equilibrium constant uncertainty.

The uncertainty in PSD measurements is difficult to accurately define, so its propagated uncertainty was investigated under high and low growth rates. The Mastersizer3000 operating manual suggests that its relative uncertainty is less than 1%. Using a percentage measurement uncertainty means that propagated uncertainty may exceed this expected measurement uncertainty for low particle sizes.

6.2.2 Preliminary sensitivity analysis

Preliminary sensitivity analyses were conducted to quantify the impacts of input variable uncertainty and kinetic parameter uncertainty on the key variables listed in Table 6.1 above (sections 6.4 and 6.5, respectively). These were favoured over stochastic analysis as they are far less computationally demanding but still provide useful information. In all preliminary simulations, input variables and kinetic parameters were varied, individually and in combination, to the extremes of their uncertainties, to generate the greatest possible deviation from baseline. In the worst case scenario, NaOH flow was increased, feed flow was decreased, and the concentration of both feed and caustic were maximised.

Preliminary simulations were run for 60 minutes, since all output variables of interest were at steady state (within 10% of their measurement tolerances) by that time. The experimental feed condition of *SI* = 1.0 (non-equilibrium immediately after mixing) was used and fixed kinetic parameters were assumed. The assumed kinetic parameters were based on work by Galbraith *et al.* (Galbraith et al., 2014).

6.2.3 Stochastic simulations

The propagation of uncertainty through complex systems can be analysed using stochastic simulations (Monte Carlo simulations), which are discussed in section 6.6. In stochastic analysis, simulations are repeated, using values randomly selected from appropriate probability distributions. Results of these simulations are combined to construct probability distributions of output variables and the standard deviations of these can be used to describe their uncertainty.

Stochastic simulations were carried out in the gPROMS platform by generating an array of the process model of size $n = 200$, where each element of the array is an instance of the model. This can be conceptualised as n reactors operating in parallel. In each reactor instance, the input variables and parameters which are expected to make a significant contribution to the uncertainty of key output variables are randomly assigned using a probability distribution. Simulating a large array of reactors generates a large number of variables considering that each axially and radially distributed element contains a fluid flow model, a discretised population balance model and a non-ideal solution thermodynamic model. In a simulation containing 20 reactor instances, 3.3 million equations were generated, requiring 12GB RAM. To enable this type of simulation to run on machines with limited RAM without creating a bottle-neck, a novel technique was used where the outlet conditions of each reactor were recorded at a specified simulation time, then key variables and parameters in each reactor were reassigned new values from their respective distributions and the model was allowed to continue running.

6.3 Model simplification

Model simplification is important since elimination of a single term can significantly reduce the number of equations if that term is distributed over axial, radial and particle size domains.

6.3.1 Diffusion and settling effects

Equations representing diffusion (equation 4.6) and particle settling effects (equations 6.2 and 6.3) were examined to determine their impact on key output variables (Figure 6.1).

$$\frac{\partial C_i}{\partial t} = -v_z(r)\frac{\partial C_i}{\partial z} + \boldsymbol{\mathcal{D}_i}\frac{\partial^2 C_i}{\partial z^2} + \boldsymbol{\mathcal{D}_i}\frac{\partial^2 C_i}{\partial r^2} - r_{struvite} \qquad 6.1$$

Where C_i [mol/L] along the length is ion concentration alone the reactor length (z) radius (r).

$$v_{settling} = \begin{cases} \dfrac{2(\rho_p - \rho_f)gR^2}{9\mu} & L < 40\mu m \\ \dfrac{8(\rho_p - \rho_f)gR}{3\rho_f C_D} & L \geq 40\mu m \end{cases} \qquad 6.2$$

Where $v_{settling}$ is the settling velocity incorporated into v_z for particle advection, L describes particle equivalent diameter and C_D, the laminar drag coefficient, is calculated as follows.

$$C_D = \left(\frac{24}{Re_p}\right)\left(1 + 0.14Re_p^{0.7}\right) \qquad 6.3$$

Where ρ_p and ρ_f are the densities of the particle and fluid, g is acceleration due to gravity, R is the particle radius, μ is the dynamic viscosity of the fluid, C_D is the drag coefficient.

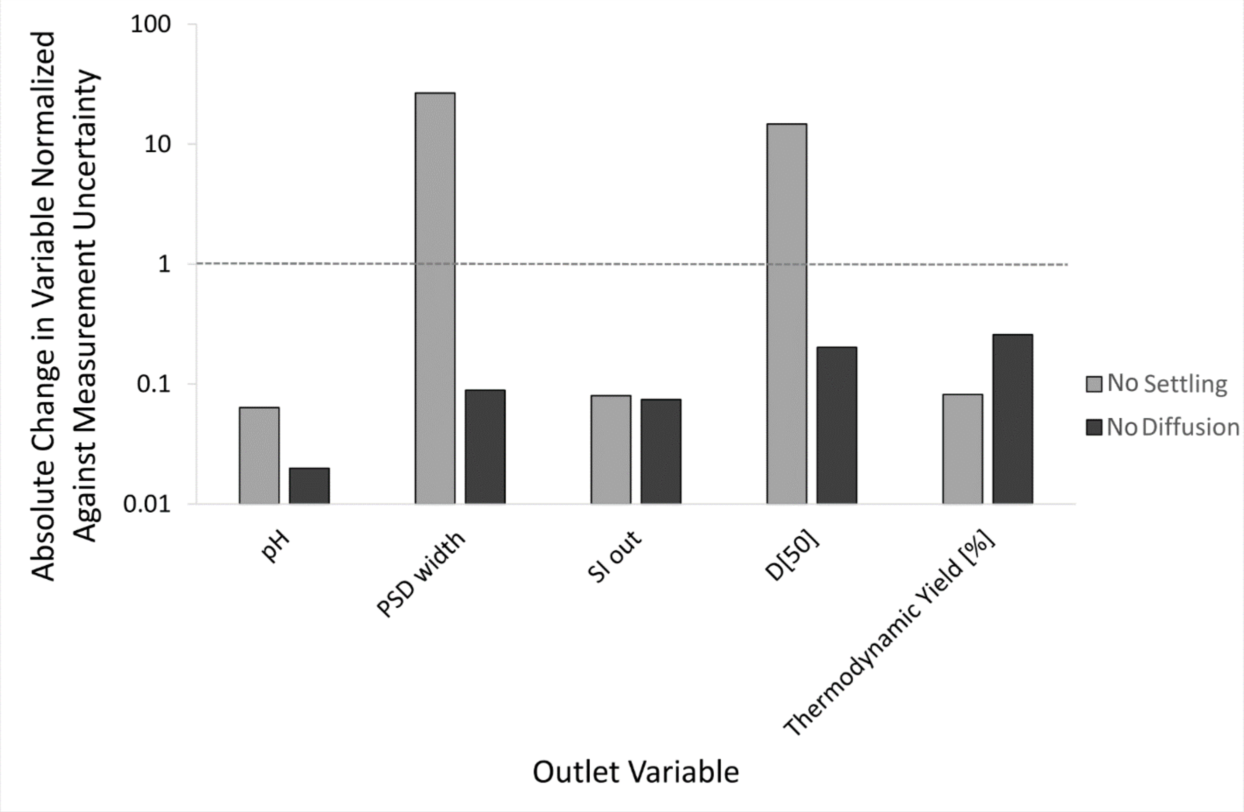

Figure 6.1 – Particle settling and ionic diffusion effects on key output variables

Particle settling effects had a negligible impact on thermodynamic properties but significantly affect outlet PSD. Exclusion of settling effects resulted in a 30% increase in PSD width, a 15% increase in volume median diameter and an 8% decrease in solution time. On this basis, settling effects were incorporated into all further modelling. The exclusion of diffusion resulted in a 44% decrease in computation time and no significant differences in key output solution parameters, which all varied by less than 30% of their respective measurement uncertainties. The diffusivity was approximated by that of hydrogen ($4.5 \times 10^{-5} [cm^2 s^{-1}]$), an overestimate since most ions in the system are significantly larger and therefore exhibit lower diffusion rates. This result does not imply that diffusion can be ignored when simulating *all* struvite crystallisation scenarios though, as its relative impact depends on concentration gradients and fluid velocity.

6.4 Sensitivity to experimental input variables

An accurate description of output variable uncertainty, resulting from input uncertainty, is necessary for parameter optimisations and provides an understanding of which input variables have the most influence on results. In this section output uncertainties propagated from input uncertainties are presented. Output uncertainties were normalised against measurement tolerances to indicate whether the propagated uncertainty was of significance. A significant result is therefore defined by a normalised value greater than 1.

6.4.1 Input variables

Input variables were selected for investigation if their uncertainty could be estimated and controlled. These are shown in Table 6.2 below.

Table 6.2 – Input variable uncertainties

Variable and units	Value ± Uncertainty	Uncertainty Basis
C_P **[M]**	$0.02 \pm 5.19 \times 10^{-6}$	Scales, glassware
C_{NaOH} **[M]**	$0.0176 \pm 1.067 \times 10^{-5}$	Scales, glassware
$Q_{NaOH}, Q_{nutrient}$ **[L/h]**	$4.00 \pm 5 \times 10^{-3}$	Pump resolution
Q_{tot} **[L/h]**	7.976 ± 0.146	Outlet flow measurements

Methods described by NIST (Taylor & Kuyatt, 1994) were used to calculate uncertainty propagation for total flow and feed concentrations. Experimental total flow was defined as a separate variable to inlet flow rate because during experiments, total flow was controlled using a valve on the outlet, while inlet flows were determined by pumps. The variance in outlet flow was buffered by headspace above the mixer. Changes in total flow rate affect the residence time, while variations in individual pump flow rates also affect the inlet supersaturation level.

6.4.2 Preliminary (min/max) sensitivity analysis

Figure 6.2 shows that no single experimental input uncertainty had a significant impact on output variables. However, the combined effect of uncertainty in all input variables may cause D[50] and PSD width to vary up to 15% and 18% more than their measurement tolerance, respectively.

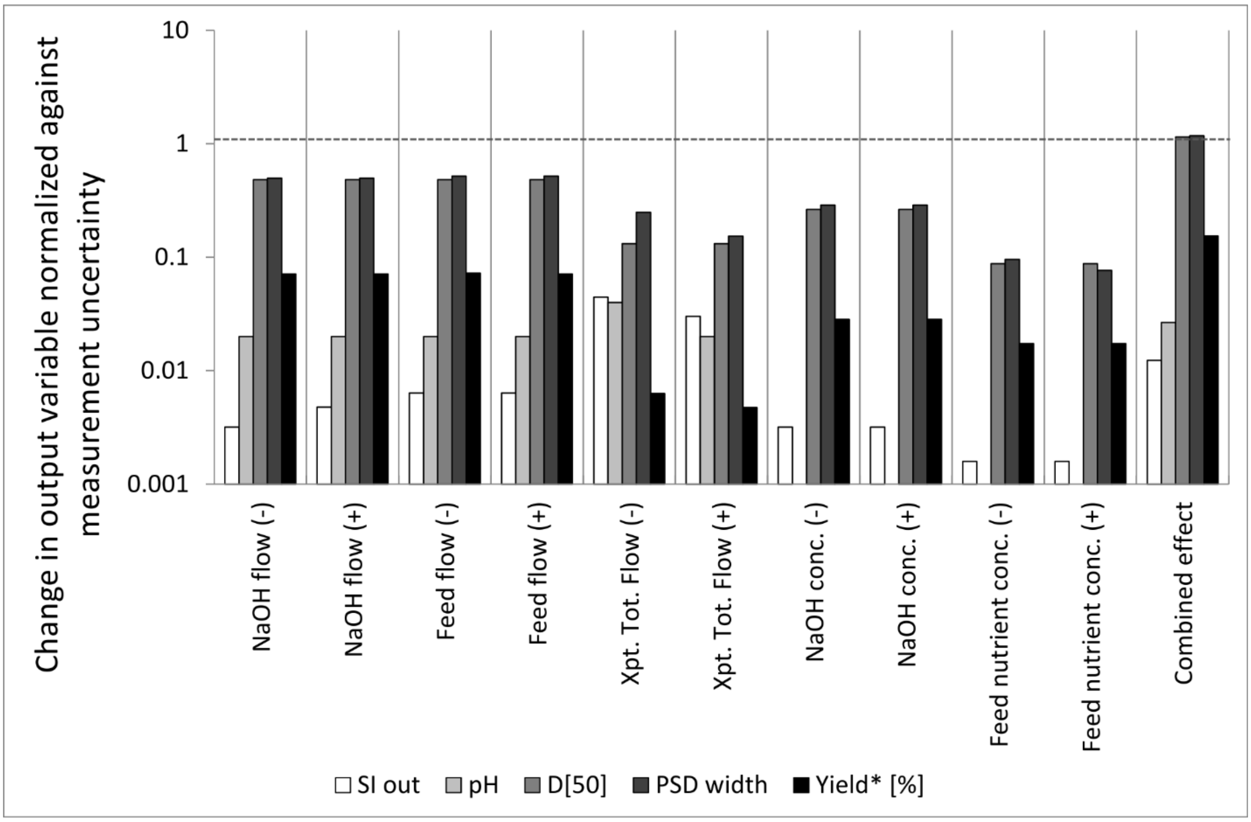

*Figure 6.2 – Sensitivity to experimental parameters presented as normalised key output variable change resulting from changes in individual key input variables. *Yield is given as thermodynamic yield*

These results suggest that it is possible, although unlikely, that uncertainties in experimental conditions can cause output variable changes greater than their respective measurement tolerances, using the assumed kinetic parameters. The symmetrical nature of + and – responses indicates that the system behaved linearly within the range examined. Flow rate of NaOH and nutrient feed had the greatest impact on reactor outputs and PSD properties were the most sensitive outputs, irrespective of the input variable. Other output variables were relatively insensitive to input uncertainties, and interestingly, outlet pH was completely insensitive to feed phosphorus and NaOH concentration. This shows that pH may not be an ideal variable for reactor control (a common practice). Additionally, the uncertainties in total experimental flow rate had less effect on all output variables than uncertainties in individual pump flow rates, despite being 29.2 times greater, highlighting that the feed component ratios are more important than reactor residence time.

6.4.3 Preliminary (min/max) sensitivity analysis at low growth rate

Assuming a 1% relative uncertainty in PSD measurements (section 1.1) creates reduced uncertainty at low particle sizes. Therefore, propagated PSD uncertainty may exceed measurement uncertainty at low growth rates. To examine this effect, the growth rate constant was reduced to a constant 0.043 µm/min, which is at the low end of the spectrum of those measured for struvite (section 2.2.4.5). In Figure 6.3 12% of the volume based PSD produced in the lower growth rate scenario resides below 1µm. In this region, measurement relative uncertainties are greater than 1% because 1% of any measurement made below 1µm exceeds the 0.01µm lower detection limit.

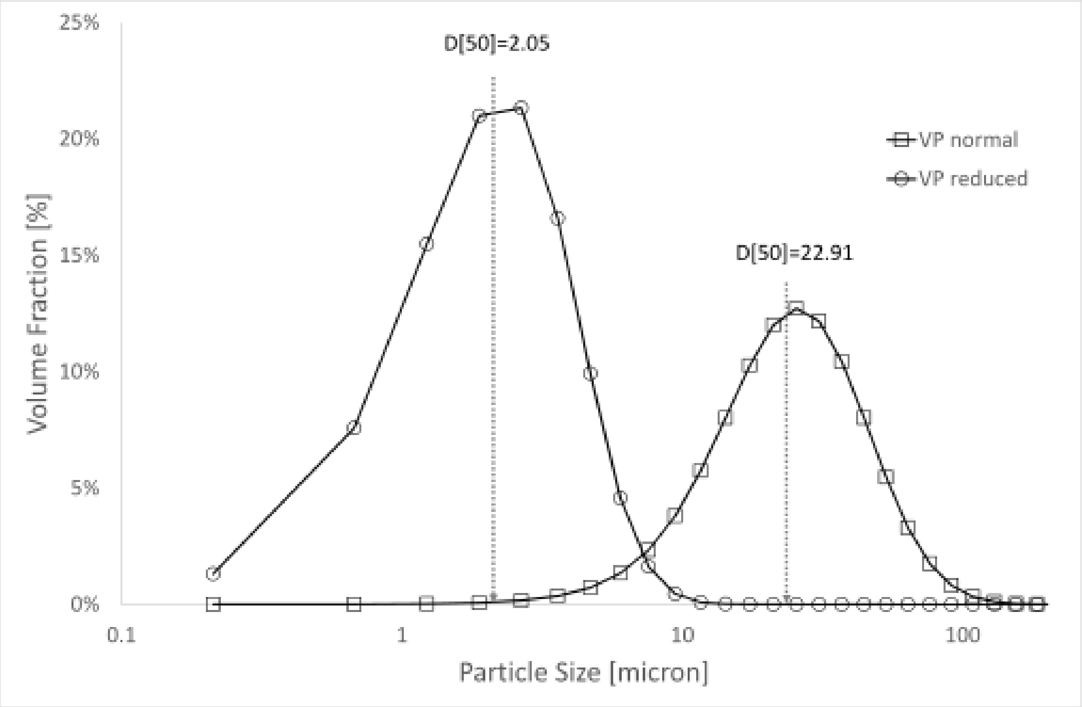

Figure 6.3 – Volume based particle size distributions for Galbraith et al. kinetic model and reduced particle growth rate.

The results shown in Figure 6.4 below confirm that at lower growth rates D[50], PSD width and yield uncertainties exceed their respective measurement uncertainties. For parameter optimisation purposes, this means that if a significantly low growth rate is encountered experimentally, the expected output variable uncertainty must be updated from the measurement uncertainty to the new expected variance. Since both the particle growth rate models vary significantly (section 2.2.4.5), it is possible that a low growth rate may be encountered. Therefore, the uncertainty of PSD properties and thermodynamic yield must be included as an estimated variable during parameter optimisations. Stochastic simulations discussed in section 6.6 will be used to provide limits to this uncertainty estimation.

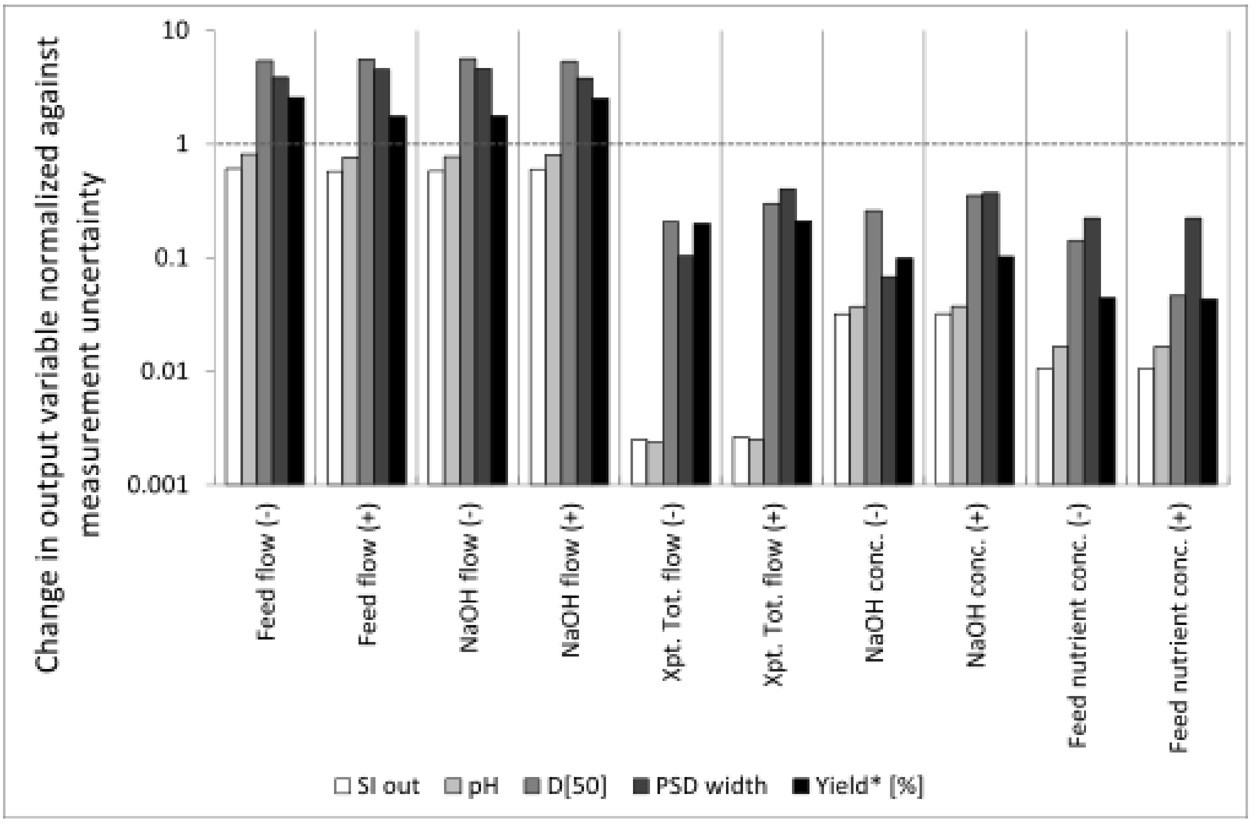

*Figure 6.4 – Normalised key output variable change resulting from changes in individual key input variables at a reduced growth rate. *Yield is given as thermodynamic yield*

When contrasting Figure 6.4 with the higher growth rate data in Figure 6.2, it becomes evident that the feed flow rates have a more significant impact at lower growth rates and their impact on thermodynamic properties is also larger. More generally, all thermodynamic variables are more sensitive at lower growth rates because of reduced levels of phosphorus removal in the reactor, creating higher levels of supersaturation throughout the reactor.

Observing the reactor output in the low growth scenario, where *SI* remains high, magnifies the effects of feed ratio and NaOH concentration changes. Additionally, all output uncertainties, while different to the higher growth rate scenario, remained relatively symmetrical. This showed that although the kinetic power law models were high order, they still exhibited a nearly linear response to the range of input variances examined. However, this may not remain the case if greater input variances were examined.

6.5 Kinetic model effects on output uncertainties

Kinetic parameters offer the greatest potential uncertainty in the model. This section examines the impact individual kinetic parameter uncertainties as detailed below:

1) Fixed percentage (10%) change in uncertainties – to show which kinetic parameters have the greatest impact, assuming equal variance
2) Boundaries of mathematically feasible kinetic parameters based on work by Galbraith *et al.* – to show that the parameter constraints used by Galbraith *et al.* encompass the data collected in this work
3) Expected kinetic parameter uncertainties from Galbraith *et al.* – to show the output uncertainties, continuing with the assumed model in section 6.4
4) Generalised kinetic model uncertainty, based on many kinetic studies available in the literature – to show what uncertainties could be expected based on the variations in struvite kinetics reported in the literature

6.5.1 Relative effect of kinetic parameters

To assess the relative effects of changes in kinetic parameters, each kinetic parameter was varied by ±10%. For consistency the kinetic parameters proposed by Galbraith *et al.* were used (Galbraith et al., 2014). Output variable uncertainties used for normalisation are given in Table 6.1 in section 6.2.1. This analysis shows how sensitive each output variable is to each kinetic parameter and allows for comparison between results. Table 6.3 and Figure 6.5 show the relative influence of each kinetic parameter.

Table 6.3 – Relative influence of kinetic parameters

Property Type	**Order of Kinetic Parameter Influence**
PSD	$k_{agg} > n_{agg} > k_g > n_g > k_{nuc} > n_{nuc}$
Yield	$n_g > k_g > n_{agg} > k_{agg} > k_{nuc} > n_{nuc}$

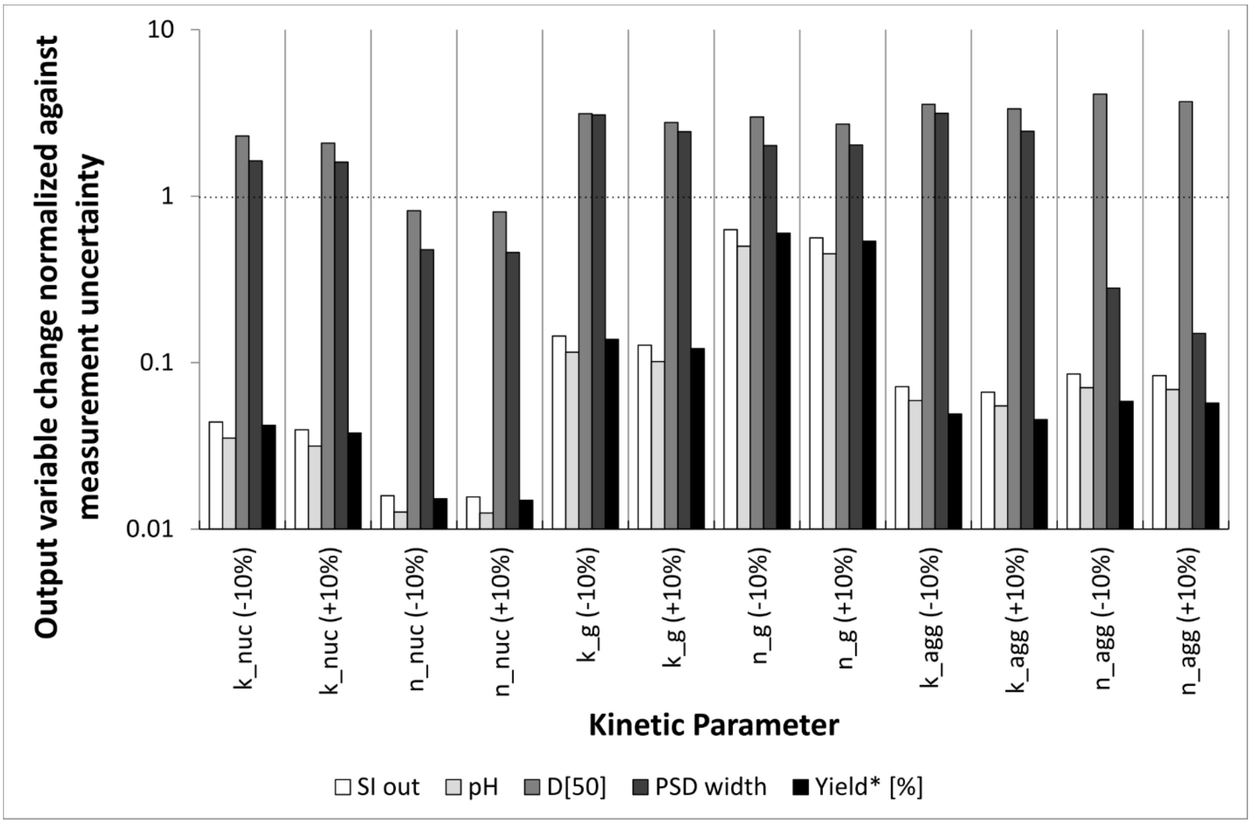

*Figure 6.5 - Galbraith et al. model sensitivity using ±10% uncertainty, showing normalised key output variable change resulting from kinetic parameters. Positive and negative sign (+/-) on kinetic parameter labels indicate increase and decrease respectively. *Yield is given as thermodynamic yield*

Generally, aggregation-related kinetic parameters have the greatest influence on PSD properties, growth-related parameters have the greatest influence on yield, and nucleation-related parameters are least influential. Assigning equal importance to yield and PSD indicates that aggregation and growth kinetic parameters are equally important. However, kinetic parameters have a greater influence on PSD properties than thermodynamic properties (relative to measurement uncertainties). Therefore the order of kinetic parameter influence on PSD should be used to identify the least important kinetic parameters which might be fixed during the parameter optimisation process. Results in Figure 6.5 also reinforce the linear nature of the process response to kinetic parameter changes.

6.5.2 Effect of kinetic parameters within solution space

This analysis serves to determine whether the range of kinetic parameter values considered by Galbraith *et al.* (Galbraith, 2011), presented in Table 6.4, can span the range of experimental data in this work. This range was adopted by Galbraith *et al.* using trial and error to ensure numerical stability while allowing a broad enough range of conditions to be examined.

Table 6.4 – Kinetic parameter range proposed by Galbraith *et al.* (Galbraith, 2011)

Parameter	Optimised Value	Lower Limit	Upper Limit
$\boldsymbol{k_{nuc}}\ [\mathbf{1/L.min}]$	8.5×10^{7}	1.0×10^{7}	9.0×10^{8}
$\boldsymbol{n_{nuc}}$	1.68	1	5
$\boldsymbol{k_g}\ [\mathbf{\mu m/min}]$	12.49	1	15
$\boldsymbol{n_g}$	5.06	1	6
$\boldsymbol{k_{agg}}\ [\mathbf{1/L.min}]$	3.72×10^{-7}	1×10^{-8}	9×10^{-6}
$\boldsymbol{n_{agg}}$	5.26	1	5

Table 6.5 compares output variable ranges resulting from the parameter ranges considered in Table 6.4 with those recorded during the experimental work from Chapter 5. The comparison is made with and

without particle aggregation considerations. The output variable boundaries in Table 6.5 are the minimum and maximum values based on uncertainties in individual kinetic parameters and worst case scenarios from combined kinetic parameter changes.

Table 6.5 – Limits of output variables using previously assumed nucleation and crystal growth kinetic parameter boundaries, compared to experimental results

		Mass and Population Balance Related Variables			**PSD Properties**	
		SI	pH	Yield [%]	D[50] [µm]	Width [µm]
Nucleation & Growth	Boundary Min	0	6.687	23	9	12.55
	Experimental Min	0.01	6.875	46	21.08	38.97
	Experimental Max	0.45	7.244	99	37.45	63.50
	Boundary Max	0.83	7.228*	100	35.44*	54.19*
Nucleation, Growth & Aggregation	Boundary Min	0	6.689	2	12.32	16.90
	Experimental Min	0.01	6.875	46	38.81	40.13
	Experimental Max	0.45	7.244	99	140.87	279.01
	Boundary Max	1.37	7.711	100	839.03	581.81

*Experimental measurement exceeds boundary maximum

In the nucleation and crystal growth-only scenario, the maximum experimental PSD properties exceed those achievable within the proposed parameter space. Therefore a broader nucleation and growth kinetic parameter space was utilised during parameter optimisations in this work. When aggregation is additionally considered, the PSD range achievable by the model significantly expands to include all measured PSD values, suggesting that the aggregation kinetic parameter range is suitable. The instance where measured pH exceeds its boundary is not considered significant as it still lies within experimental uncertainty.

6.5.3 Effect of existing struvite kinetic model parameter uncertainties

This analysis aimed to show whether output variables would be expected to vary significantly when adopting the kinetic parameter uncertainties determined by Galbraith *et al.* (Galbraith et al., 2014). The kinetic parameters optimised by Galbraith *et al.* were the most applicable to this work as they were estimated using DPB methods. The same kinetic parameters as section 6.4.2 are used here. The experimental uncertainties examined in that section were neglected here to show only the impacts of kinetic parameter uncertainties. Kinetic parameters were varied over their reported ranges (Table 6.6 below). The worst-case scenario of their combined uncertainties was examined by an increase in nucleation and growth rate constant and a decrease in both power law model orders. Decreasing orders resulted in an overall increase in nucleation and growth rate.

Table 6.6 – Kinetics parameter uncertainties

Parameter	Value	Uncertainty (95% CI)	Uncertainty (95% CI) [%]
$\boldsymbol{k_g}$ $[\mu \boldsymbol{m/min}]$	12.490	0.061	*0.49*
$\boldsymbol{n_g}$	5.060	0.005	*0.10*
$\boldsymbol{k_{nuc}}\ (\times \mathbf{10^{7}})$ $[\boldsymbol{L^{-1}}\mathbf{min^{-1}}]$	8.500	0.076	*0.89*
$\boldsymbol{n_{nuc}}$	1.680	0.014	*0.83*
$\boldsymbol{k_{agg}}\ (\times \mathbf{10^{-7}})$ $[\boldsymbol{L.min^{-1}}]$	3.72	0.014	*0.38*
$\boldsymbol{n_{agg}}$	5.260	0.004	0.08

Results presented in Figure 6.6 below show that no individual kinetic parameter uncertainty or their worst-case combination had a measurable effect on output uncertainty in the Poiseuille flow reactor model. Changes to the nucleation rate order had a minimal impact on output thermodynamic properties. Both nucleation and growth rate order had a smaller effect on output variables than nucleation and growth rate coefficients indicating that they are less important variables in parameter optimisations. Growth rate order did however have a more significant effect on phosphorus recovery than nucleation rate order but the magnitude of the change remains significantly lower than effects on PSD.

Interestingly, the combined effect of kinetic parameter uncertainties on PSD was less than the effect of uncertainties in individual parameters, while the effect on yield, pH and SI was greater. This is because, when nucleation and growth rates are simultaneously increased or decreased, the amount of crystallisation changes accordingly, but the fraction of de-supersaturation contributing to each mechanism is less affected. Put another way, kinetic parameters are positively correlated with respect to PSD properties and negatively correlated with respect to thermodynamic properties. This result is also shown in 6.5.1.

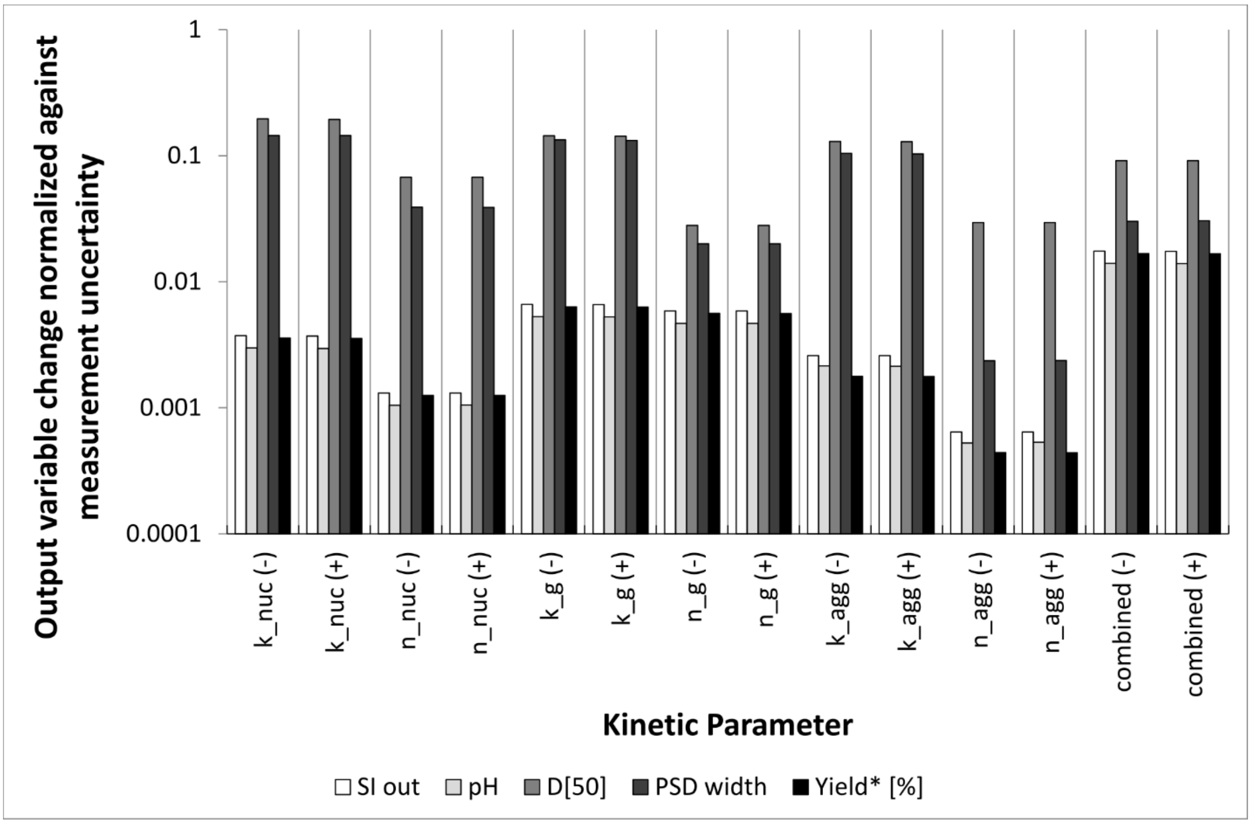

*Figure 6.6 – Galbraith et al. model sensitivity within optimisation uncertainty showing absolute normalised key output variable change resulting from kinetic parameters. Positive and negative sign (+/-) on labels indicates parameter increase and decrease, respectively. *Yield is given as thermodynamic yield*

6.5.4 Effect of generalised model kinetic parameter uncertainty

Since large variations exist between kinetic models within the literature (section 2.2), it is not unlikely that kinetics may be very different to those assumed earlier in this chapter. Figure 6.7 shows the effect of uncertainties in kinetic parameters which may be possible for a general model structure. In this general kinetic asnalysis, various growth rate investigations from the literature were averaged using a single model given by equation 6.4, where a reduced supersaturation was used, given by equation 6.5.

$$G_L = \frac{dL}{dt} = k_g S_r^{n_g} \tag{6.4}$$

$$S_r = \left(\frac{IAP}{K_{sp}}\right)^{1/3} - 1 \tag{6.5}$$

Where k_g $[\mu m. min^{-1}]$ and n_g are the growth rate constant and order; S_r is the reduced saturation; IAP is the ion activity product; and K_{sp} is the solubility product of struvite. Nearly all previous results were found to be represented by a first order model ($n_g = 1$) and k_g was found to vary between $0.06\,[\mu m. min^{-1}]$ and $[0.66\,\mu m. min^{-1}]$. For analysis purposes, a baseline value of $k_g = 0.36\,[\mu m. min^{-1}]$ was taken and given an uncertainty of ± 0.3 $[\mu m. min^{-1}]$. Nucleation rate was also investigated using a primary nucleation model, given by equation 6.6.

$$J = A_n \exp\left(-\frac{16\pi\gamma^3 v^2}{3k^3T^3(\ln\Omega)^2}\right) \tag{6.6}$$

Where A_n $[cm^{-3}s^{-1}]$ is a kinetic factor (/ pre-exponential factor/ collision factor), k is the Boltzmann constant ($1.38 \times 10^{-23} J. K^{-1}$), Ω is the saturation ratio, γ $[mJ. m^{-2}]$ is the interfacial tension between the crystal and the solution, v_m $[cm^3]$ is the molecular volume, and T $[K]$ is the absolute temperature ($298K$). Uncertainties in nucleation rate were examined based on interfacial tension reported in the literature ($15 < \gamma < 50$) and uncertainties in the pre-exponential factor, A_n. The pre-exponential factor for struvite is commonly assumed to be 10^{17} (Abbona & Boistelle, 1985; Bouropoulos & Koutsoukos, 2000), although for sparingly soluble salts is reported to be up to 10^{25} (Mullin, 2001; Alan D Randolph & Larson, 1988). Since no substantial information was available to suggest a reasonable variance for this value, it was given a baseline of 10^{17} and varied three orders of magnitude in either direction.

It should be noted that the primary nucleation model behaves significantly differently to the power law model, showing that model selection is important. When the nucleation rate constant estimated by Galbraith *et al.* was converted to the units of A_n, it became significantly smaller ($k_{nuc} = 1.42 \times 10^{-3}\ [cm^{-3}s^{-1}]$). This highlighted two things: first, that seeded secondary nucleation rate at low supersaturation (Galbraith *et al.* model) is significantly lower than primary nucleation rate (homo- or heterogeneous); and second, for the primary nucleation model to represent the same nucleation rate as the power law model, a judicious choice must be made in selecting an interfacial tension value as it determines the fraction of the pre-exponential maximum (A_n) achieved at a given supersaturation. This is troublesome as interfacial tension cannot be directly measured and is notoriously difficult to estimate. Most examinations of nucleation rate and interfacial tension occur around the transitional supersaturation where nucleation becomes significant, meaning that there likely exists a high correlation between the selection of pre-exponential factor and the estimated interfacial tension. It could be argued that the problem of estimating nucleation rates, especially using a primary nucleation model, is essentially guess-work. One might be tempted to increase complexity of the model, but without a sufficiently rich dataset, this only adds additional degrees of freedom to the problem. As such analysis was continued using this model, but results must be treated as estimates at best.

Figure 6.7 shows that when using the generalised nucleation and crystal growth model, individual kinetic parameter uncertainties caused significant uncertainties in output variables. Output variables maintained relatively similar ratios of uncertainty for all kinetic parameters, indicating that each kinetic parameter is equally important. Particle $D[50]$ was the most affected output variable, with uncertainties 50 to 80 times greater than measurement uncertainty for each individual kinetic parameter. Thermodynamic properties also appeared to be more significantly affected in this analysis than in the analysis presented in section 6.5.1. This is because the general model utilises a first order growth model, which does not slow growth as significantly at *SI* < 1, as higher order models do. The key conclusion drawn from this analysis is that, based on the literature, reactor outputs are highly uncertain. As such, stochastic simulations were used to estimate the expected variance of key output parameters based on the combined uncertainties of all kinetic parameters.

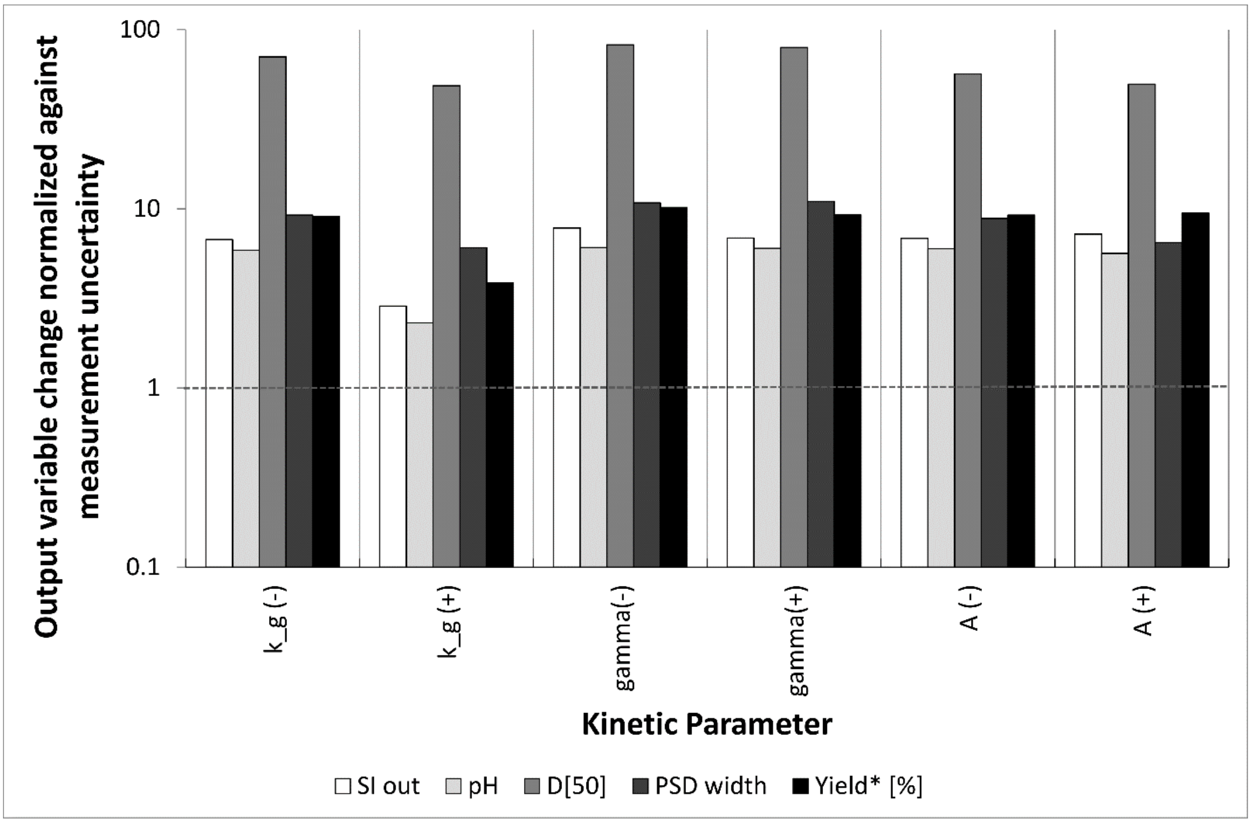

*Figure 6.7 – Generalised kinetic model sensitivity showing normalised key output variable change resulting from changes in kinetic parameters within the proposed solution space. Positive and negative sign (+/-) on kinetic parameter labels indicate variable increase and decrease respectively. *Yield is given as thermodynamic yield*

6.6 Stochastic simulations

In this section, stochastic simulations are used to examine the expected variance in reactor outputs using a generalised kinetic model using: 1) kinetic parameter uncertainties; and 2) feed concentration uncertainties.

6.6.1 General model

When assuming a kinetic model for design purposes, the variability of kinetic models available in the literature must be taken into consideration. This has been done here by estimating key output variable uncertainties using kinetic parameter uncertainties based on the literature. The uncertainties estimated here also provided reasonable upper limits to output variable uncertainties (PSD width, $D[50]$ and thermodynamic yield) which were found simultaneously with kinetic parameters (Chapter 7).[19] The stochastic simulation was performed applying the general kinetic model and associated variances given in section 6.5.3 and the input parameter uncertainties given in section 6.4.2. These uncertainties and the models used to describe them are shown below in Figure 6.7. A normal distribution was used where a parameter value was based on experimental data, while a uniform distribution was used if the distribution of a parameter was unknown.

---

[19] Using reasonable upper uncertainty limits is important as it constrains the solution space and associated execution times.

Table 6.7 – Variance models of kinetic parameters and experimental variables used in stochastic analysis of a general kinetic model

Parameters	Baseline	Notes	Distribution Type
Nucleation pre-exponential factor ($\boldsymbol{A}\ [\boldsymbol{cm^{-3}s^{-1}}]$)	$1 \times 10^{17\pm3}$	Assumed based on literature	Uniform
Nucleation interfacial tension ($\boldsymbol{\gamma}\ [\boldsymbol{mJ.m^{-2}}]$)	39.50 ± 16.66	Reported range = 15 to 50	Normal
Growth rate constant ($\boldsymbol{k_g}\ [\boldsymbol{min^{-1}}]$)	0.36 ± 0.30	Reported range = 0.06 to 0.66	Uniform
Total reactor outlet flow rate $[\boldsymbol{L.h^{-1}}]$	7.976 ± 0.1459	Measured	Normal
Nutrient feed flow rate $[\boldsymbol{L.h^{-1}}]$	4.00 ± 0.005	Assumed based on flow increment resolution	Uniform
NaOH feed flow rate $[\boldsymbol{L.h^{-1}}]$	4.00 ± 0.005	Assumed based on flow increment resolution	Uniform
Phosphorus concentration ($\boldsymbol{PO_4 - P}$) $[\boldsymbol{M}]$	$0.02 \pm 5.19 \times 10^{-6}$	Calculated using scale and glassware uncertainty	Normal
Ammonia concentration ($\boldsymbol{NH_4 - N}$) $[\boldsymbol{M}]$	$0.02 \pm 5.19 \times 10^{-6}$	Calculated using scale and glassware uncertainty	Normal

Stochastic simulations were conducted in batches of 100 until the mean and standard deviation of all output variables became independent of further simulations beyond an arbitrary tolerance of 1%. PSD width was used to identify the maximum number of simulations required, as it was found to fluctuate most (since it is calculated based on two properties $D[90]$ and $D[10]$). Figure 6.8 and Figure 6.9 show the normalised change of the PSD width average and standard deviation with increasing simulation number. It can be seen that the change in width average and standard deviation stabilised below 1% after 150 and 120 simulations, respectively. Therefore, 200 simulations was deemed sufficient to estimate all output variable uncertainties.

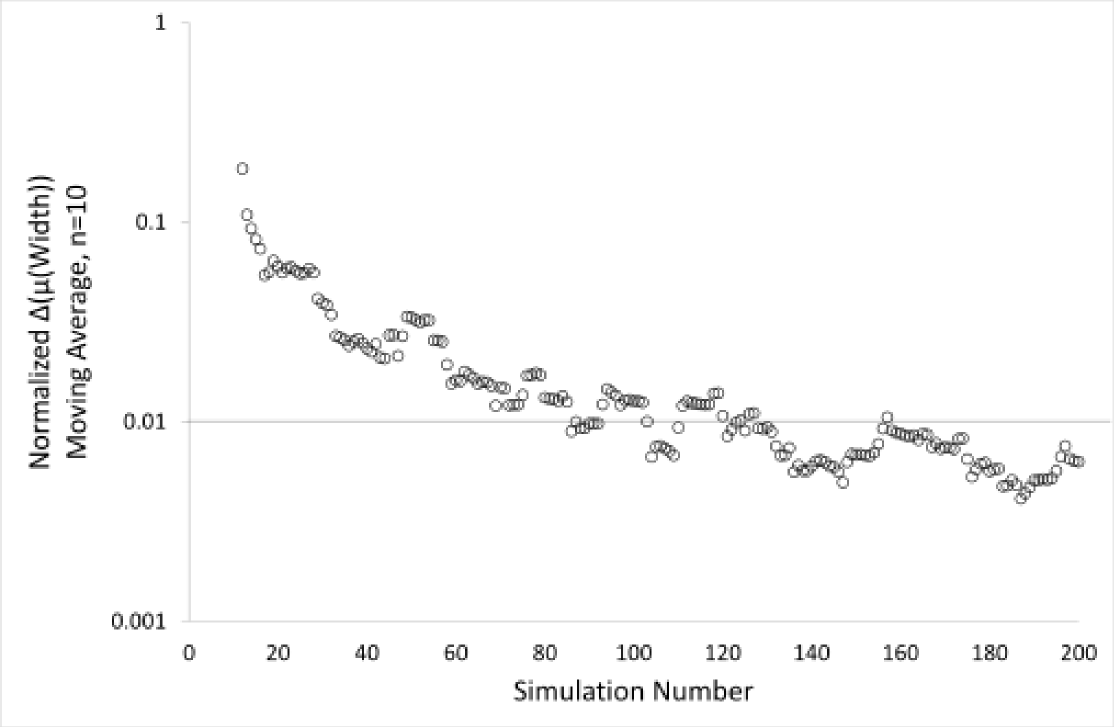

Figure 6.8 – PSD Width normalised change in average from generalised kinetic model shown as moving average over 10 data points

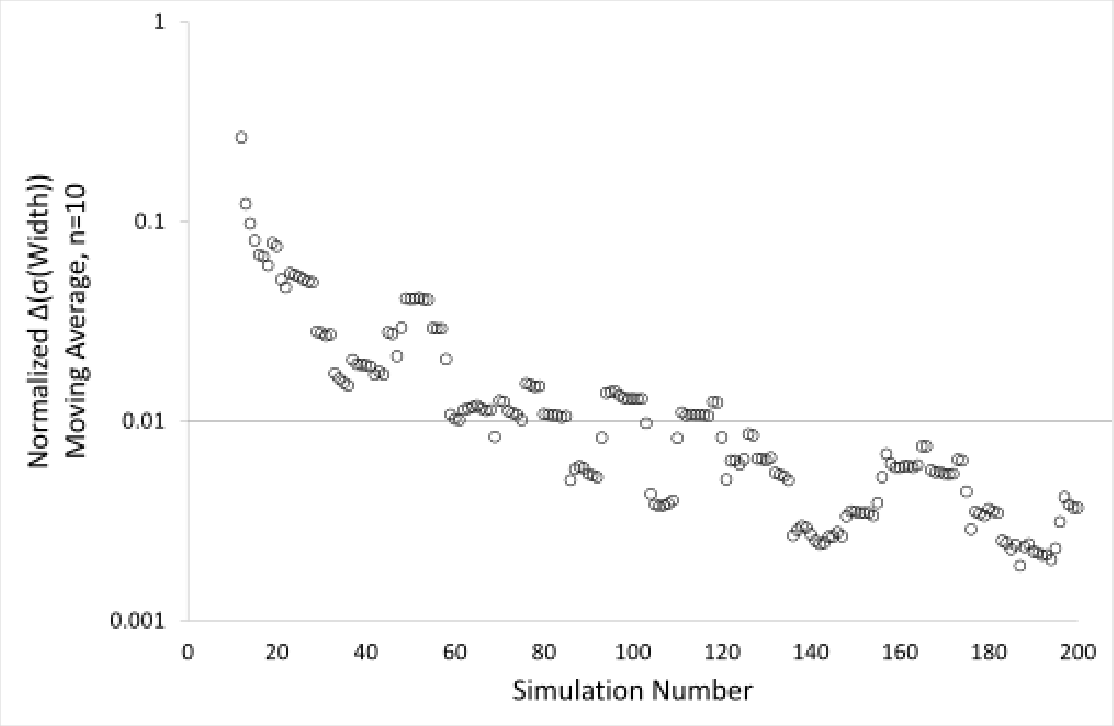

Figure 6.9 – PSD Width normalised change in standard deviation from generalised kinetic model shown as moving average over 10 points

The mean and standard deviation of each key output variable are shown below in Table 6.8. The PSD properties, thermodynamic yield and outlet SI exhibited standard deviations in the vicinity of 100%. This estimate provided an upper limit for estimations of output measurement uncertainties during parameter optimisation simulations, helping to constrain the problem and reduce solution time. This degree of uncertainty is not expected in any reactor because kinetic model uncertainty in the literature is likely systematic rather than random, having a strong dependence on differences in experimental conditions and parameter optimisation techniques. The wide variation in struvite kinetics available in the literature suggests that more rigorous experimental work and more detailed modelling is necessary. While it is tempting to avoid increased model complexity for fear of introducing too many unknown parameters (as mentioned earlier), it is evident that simplified models are unable to consistently represent struvite crystallisation. The power of a detailed model lies in its ability to show when operational parameters have a significant or insignificant impact on system outputs. This understanding is necessary for improved crystalliser designs. The process of improving understanding is iterative though. At this point, any number of more complex models could be proposed, but the ability to test them is limited by richness of datasets.

Table 6.8 – Key output variable average and standard deviation predicted by stochastic simulations using a generalised kinetic model

Output Variable	Mean ± Standard Deviation	Relative Error [%]
PSD D[50]	9.22 ± 11.36	123.21
PSD Width	13.33 ± 15.11	113.35
pH	6.955 ± 0.295	4.24
Thermodynamic Yield	0.593 ± 0.452	71.67
SI	0.392 ± 0.446	113.78

What these results did show, however, is that if a particular struvite crystallisation kinetic model is assumed to accurately represent a system and used for design purposes, the results must be taken with great caution. This assertion remains true even for scenarios where experimental conditions are similar. For example, kinetic investigations by both Glabraith *et al.* and Ali & Schneider were conducted using synthetic solutions under similar thermodynamic conditions (pH, SI, phosphorus concentration), but using batch and continuous reactors, respectively, and yielded very different results – their growth rate constants were an order of magnitude different and the growth rates were significantly greater at larger SI in the batch scenario (Ali & Schneider, 2008a; Galbraith et al., 2014). These results might be random but are most likely attributable to systematic differences in data collection and analysis methods. Similarly, one study showed that induction time model parameters vary with phosphorus concentration at constant SI, challenging traditional induction time theory (Galbraith & Schneider, 2009b), while other induction time models regressed under different SI and phosphorus concentrations are very similar (Mehta & Batstone, 2013; K. N. Ohlinger et al., 1999). Replication of studies may be useful in gaining better insight into this phenomenon, although very little attention is paid to repeating existing work. Replication (to some extent) is more frequent in industrial applications, since often similar technologies are used. It is however difficult to analyse differences in industrial results owing to variations in key nutrient, organics and competing and spectator ion concentrations.

6.6.2 Feed concentration variations

Feed concentration in experimental work conducted in this thesis was known to a high certainty, but in industrial applications can vary significantly and is difficult to measure in real time. As such, reactor sensitivity to industrial concentration variations was considered. Table 6.9 shows the baseline and variance models for feed phosphorus and ammonia concentrations, taken as the average and standard deviation of digester centrate based on data from the Cleveland Bay Purification Plant, Townsville QLD, Australia, and from various literature sources (Britton et al., 2005; Lahav et al., 2013; Lew et al., 2010; Musvoto, Wentzel, Loewenthal, & Ekama, 2000; Perera, Wu, Chen, & Han, 2009; Ueno & Fujii, 2001; van Rensburg, Musvoto, Wentzel, & Ekama, 2003). A triangular distribution was favoured over a normal distribution because a normal distribution enabled negative concentrations. Uncertainties in feed flow rates, sodium hydroxide concentration and magnesium concentration were the same as in section 6.4.2.

Flow and reagent concentration uncertainties were included to give an indication of 'real life' performance of the reactor. Diurnal patterns in flow were not considered of importance since they are buffered by upstream processes and can be accounted for with changes in feed flow rates.

For consistency with earlier analyses, simulations were performed using a fixed $NaOH$ flow and concentration necessary to achieve $SI = 1.0$ at the baseline phosphorus concentration. The spectator ion concentration (in this case Cl^{-}) was increased proportionally with ammonium concentration to maintain a similar reactor pH. Key output variables were monitored at steady state (80min). Using a fixed caustic dosing rate showed how a reactor without a control system would respond to natural variations. The kinetic model from section 6.5 was used for this analysis, incorporating kinetic parameter uncertainty. Finally, absolute yield was used instead of thermodynamic yield because the thermodynamic equilibrium point varied significantly with varying input nutrient concentrations.

Table 6.9 – Expected variations in phosphorus and ammonia concentration in anaerobic digester centrate

Variable	Baseline	Uncertainty (standard deviation)	Variance Model
Phosphorus concentration $(\boldsymbol{PO_4 - P})$ [M]	4.76×10^{-3}	2.80×10^{-3}	Triangular
Ammonia concentration $(\boldsymbol{NH_4 - N})$ [M]	3.86×10^{-2}	1.92×10^{-2}	Triangular

Table 6.10 shows that the final pH and SI vary relatively little, but the total yield varies significantly. For the purposes of removing phosphorus, yield is not considered important since it is assumed that the seeds produced by the PFR will be fed to a growth reactor where further phosphorus recovery will be achieved. For the purpose of using intentional continuous seeding to influence growth reactor operation though, the yield may be important as it is a direct measure of the seed loading rate. Reports on the effects of seed loading on final PSD vary in the literature, highlighting the need for further investigations. Increased

seed loading in a continuous tubular crystalliser has been shown to reduce final product size (Eder et al., 2011), which seems logical since the same mass deposition is distributed over a greater number of particles. Alternatively, growth and aggregation rates have been shown to increase with seed loading in other systems (Pitt, Mitchell, Ray, Heywood, & Hounslow, 2012). On this basis, it would be prudent to perform investigations into the effects of seed loading on final PSD in a struvite system before any conclusions are made. Unfortunately this is outside the scope of this work.

Table 6.10 – Key output variable average and standard deviation predicted by stochastic simulations using a generalised kinetic model

Output Variable	Average ± Standard Deviation	Relative Error [%]
PSD D[50]	18.72 ± 6.05	32.32
PSD Width	30.82 ± 10.73	34.82
pH	7.44 ± 0.17	2.28
Total Yield	0.21 ± 0.14	66.67
SI	0.35 ± 0.04	11.43

The D[50] and width variation (which are most important in a seed producing reactor) were approximately ±33%. The seed size range was comparable (both as an absolute and percentage) to seed PSDs used in previous struvite kinetic studies, where seeds have ranged in size from 5 - 20μm (Galbraith et al., 2014); 35±3μm (Mehta & Batstone, 2013); 45 – 63 μm (Ali et al., 2005). In industrial struvite crystallisation applications, larger seed particles in the size range of 100 to 1000 μm have been used (Le Corre et al., 2009). However, it is likely that to this point, researchers have used what they have on hand rather than designing and/or controlling seeds. This work aims to generate seeds intentionally to achieve better control of the crystal growth process. Unfortunately, no investigations could be found on the effects of struvite seed PSD on final PSD, making this a necessary investigation before any real conclusions can be made on the application of a Poiseuille flow seed reactor. Work on other crystallisation systems has however shown controlled seeding to be effective. Work on L-asparagine monohydrate has shown that continuous seeding of a growth reactor with a controlled PSD in the range of 10 – 20 µm can lead to tight control of output PSD (Jiang et al., 2012). Other work has used seeds in the size range of 40 – 106 µm to control a final PSD with a D[50] > 500 µm (Aamir et al., 2010), a comparable product size to struvite applications. Therefore, the PFR could likely produce a reasonable seed size range for the purposes of kinetic investigations and industrial PSD control.

6.7 Summary

- Sensitivity analysis determined diffusion effects to be negligible. Removing diffusion from the model halved simulation time
- Propagation of uncertainty in experimental variables was shown to cause significant variation in key output variables under low growth rate conditions. This was because low growth rate conditions increased the relative uncertainty in thermodynamic properties, due to the low level of phosphorus recovery
- Output variables were less sensitive to large variations in total flow rate than smaller variations in individual flow rates, since these caused changes in feed ratios
- PSD properties were more sensitive to kinetic parameter uncertainties than to thermodynamic properties were. However, if the kinetic model presented by Galbraith *et al.* was assumed, then kinetic uncertainties did not have a significant impact on reactor outputs
- Nucleation and growth kinetic boundaries used by Galbraith *et al.* were insufficient to cover the range of data observed in this work
- Nucleation rate order and constant had a smaller effect on thermodynamic and PSD properties than other kinetic parameters, suggesting that their accuracy is less important during parameter optimisation calculations
- Kinetic parameters are positively correlated with respect to PSD properties and negatively correlated with respect to thermodynamic properties

- If more liberal kinetic uncertainties or a more general kinetic model are assumed, a broad variation in reactor outputs may be possible for this reactor
- Stochastic simulations showed that selection of kinetic parameters for reactor simulation should be performed cautiously as expected model variations can produce PSD and thermodynamic property uncertainties of ±100%. This suggests that further investigations and replications of struvite crystallisation kinetic studies are necessary
- A Poiseuille seed reactor using industrial feeds is likely able to produce seeds for struvite kinetic studies and industrial applications
- Effects of seed PSD and seed loading rate on final PSD from a growth reactor require further investigation

6.8 Conclusions

Analysis in this chapter made a number of useful findings. It was shown that diffusion effects could be neglected from the model without significant recourse, resulting in valuable reductions in simulation time during subsequent parameter estimations. Simple delta analysis was able to show that it is possible (however unlikely) that propagated input variable uncertainty may exceed that of output variable measurements. Therefore, uncertainties need to be found during the parameter estimation process. It was shown that a broader kinetic parameter solution space is necessary in this work than what was used by Galbraith, ensuring that the estimation process is not constrained. Examining the primary nucleation model showed that interfacial tension is a very important parameter. Since this parameter is highly uncertain, a power law model will be used in the parameter estimation process. This also allows for comparison kinetic parameters found in this work to those found by Galbraith. Finally, it was shown that, expectedly, nucleation and growth kinetic parameters are correlated, meaning that some parameters may need to be fixed to obtain a reasonable degree of certainty in the parameter optimisation process. The least influential parameters were then identified as candidates to be fixed. Using equal percentage uncertainty for kinetic parameters showed that nucleation kinetic parameters were least influential.

However, using uncertainties regressed by Galbraith showed that nucleation and growth order were least influential. Since growth rate order is relatively well defined in the literature and nucleation rate order is not, the nucleation and growth rate orders are likely the best options for fixing.

Chapter 7 Kinetic parameter optimisation

As shown in Chapter 6, previously determined nucleation and crystal growth kinetic parameters did not produce PSDs or phosphorus recovery data fitting experimental data from this work. This chapter aims to improve this fit by conducting parameter optimisations for struvite nucleation, growth and aggregation power law model kinetic models. Kinetic parameters were tuned using the combined population balance and Poiseuille flow model. Each of these models was presented individually in Chapters 3 and 4. Sensitivity analysis of the combined model presented in Chapter 6 was used to inform uncertainties and kinetic parameter range boundaries in the parameter optimisation process. This chapter first presents information on parameter optimisation methods, including uncertainty models, parameter selection, parameter stability and solution techniques. The choice of datasets for the kinetic parameter optimisations are explained and justified, and the quality of the fit between the model and experimental datasets is discussed.

7.1 Methods

The parameter optimisation process works by iteratively varying kinetic parameters to minimise an objective function (section 7.1.3) incorporating differences between measured and simulated data. Since the objective function can incorporate measurements from different conditions of experiments, parameters can be regressed to simultaneously best fit all datasets. The parameter optimisations conducted in this work are visualised in Figure 7.1 below and described in detail in the following sections. Two separate parameter optimisations were conducted. The first used the sonicated data to estimate nucleation and crystal growth kinetic parameters, and the second used unsonicated data to estimate aggregation kinetic parameters. Parameter optimisations using batch data were also used to investigate alternative kinetic models.

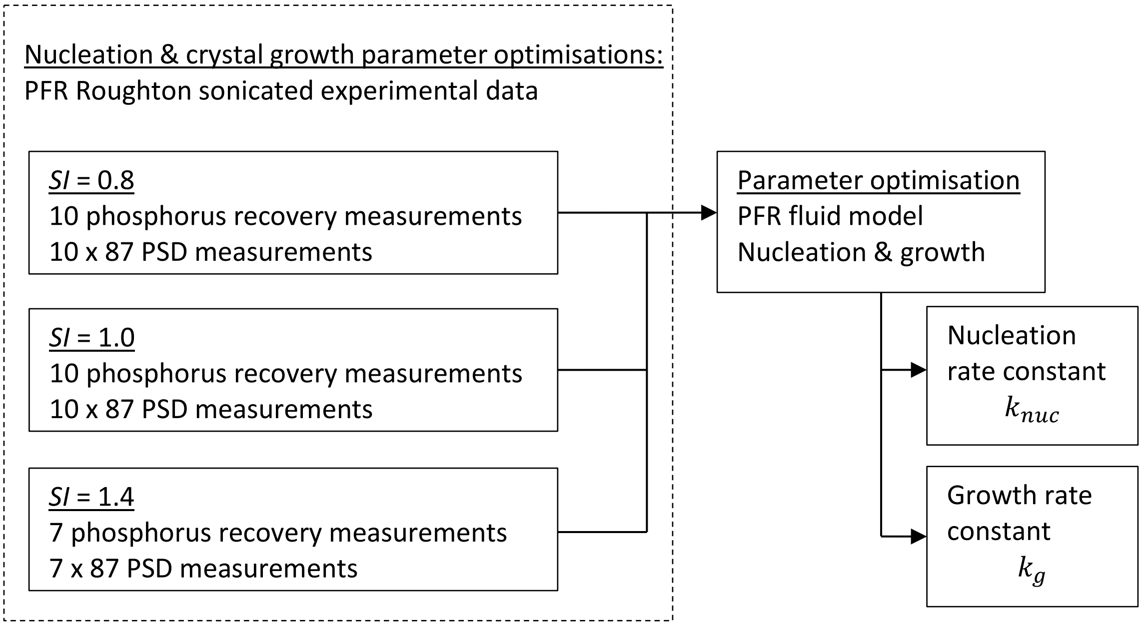

Figure 7.1 - Parameter optimisation flow chart for nucleation and crystal growth kinetic parameters

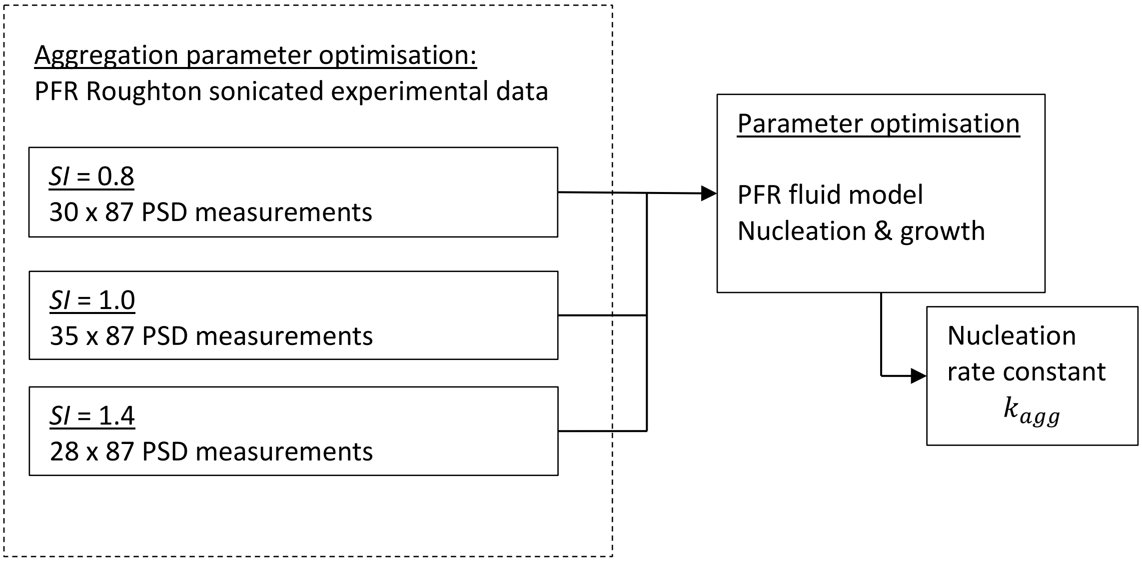

Figure 7.2 - Parameter optimisation flow chart for aggregation kinetic parameter

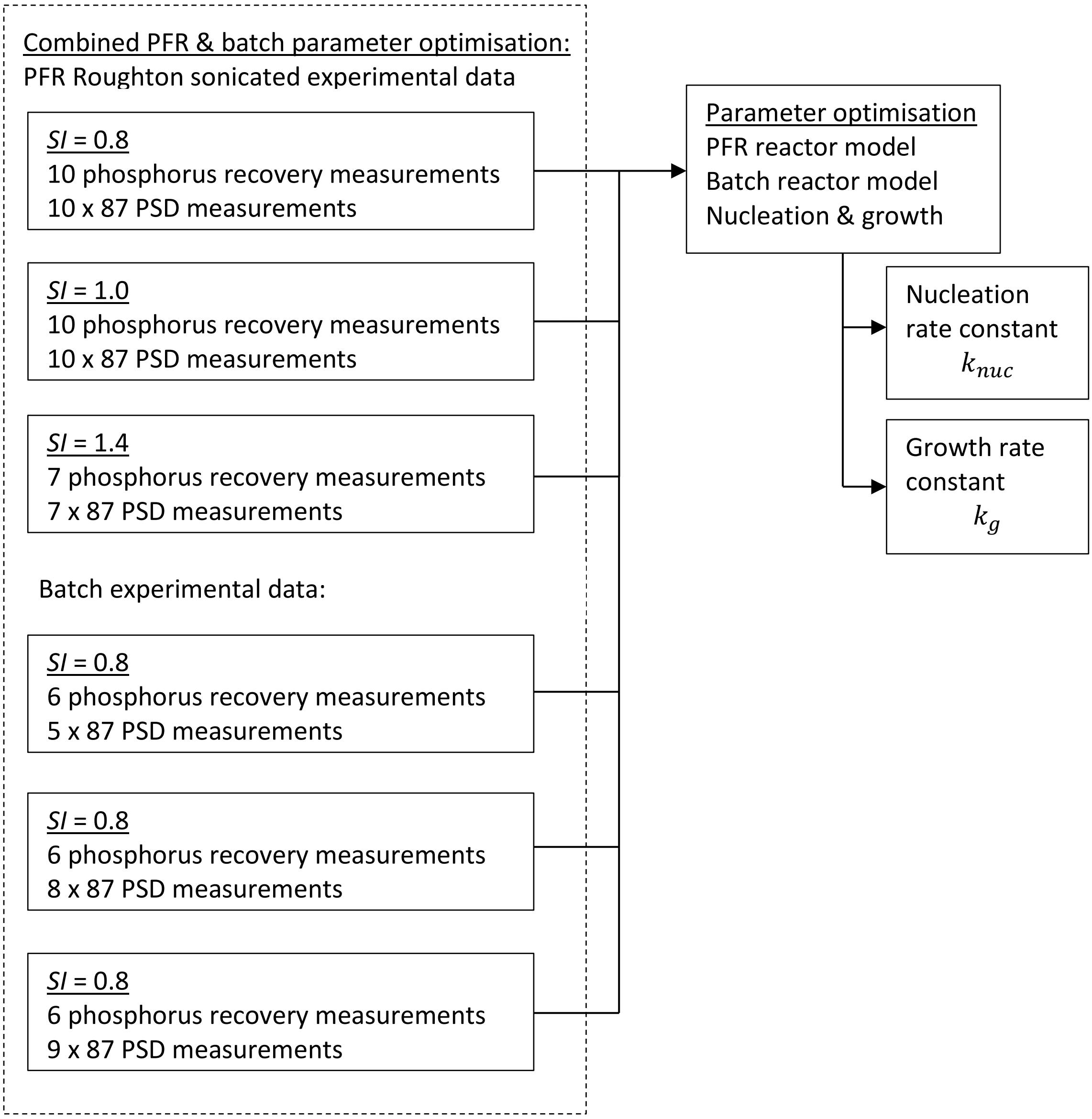

Figure 7.3 – Parameter optimisation flow chart for nucleation and crystal growth kinetic parameters

Before parameter optimisations could be conducted, it was important to ensure control of the process. Various factors influencing the parameter optimisation are discussed in this section including: measurement uncertainty models, parameter selection and solution techniques. First parameter uncertainty models were selected (section 7.1.1), then key kinetic parameters were selected for optimisation to reduce the probability of parameter correlation (section 7.1.2). Finally, solution techniques were investigated to identify a numerically stable parameter range, ensure an even contribution of experimental measurements to the optimisation process and identify solution local minima (section 7.1.3).

7.1.1 Uncertainty and variance model selection

The regressed parameter values depend on two key factors: 1) the validity of the model (assessed in earlier chapters), and 2) the experimental measurements and their uncertainties. Uncertainties and variance models can have a significant influence on the parameter optimisation process. Although measurement uncertainties were assumed[20] to refine the methods discussed herein, sensitivity analysis in Chapter 5 showed that PSD and yield uncertainties may exceed expected measurement uncertainties. Therefore the uncertainties were also estimated within the parameter optimisation process by using a feature of the optimisation tool which includes each measurement uncertainty as regressed parameter. Variance models used are shown in Table 7.1.

Table 7.1 – Variance models used for parameter optimisation

Measured Variable	Variance Model	Initially Assumed Variance	Calculated Variance
Phosphorus Concentration ($C_{PO_4^{3-}}$) [M]	Constant variance	8.88×10^{-5}	1.00×10^{-4}
PSD Volume [%]	Constant variance	0.01 – 2.73*	1.16
PSD Volume (zero measurement) *i.e.* volume fraction in cell = 0 [%]**	Constant variance	0.01	1.10×10^{-4}
PSD Median (D[50])* [µm]**	Constant variance	4.83	7.32
PSD Width* [µm]**	Constant variance	9.62	10.35

*Each PSD cell was given its own variance within this range based on experimental data variance
**A separate variance model must be specified for PSD volume fraction zero measurements to ensure that these terms do not dominate the objective function (discussed below) during parameter optimisations
***Calculated using the uncertainty in volume %

---

[20] Measurement uncertainties were initially assumed based on experimental work in Chapter 5

A constant variance model[21] was used for both outlet phosphorus concentration and PSD measurements. Constant variance is more appropriate to the collected PSD data as it avoids measurements with small absolute values exhibiting a small absolute variance, but large relative variance.

7.1.2 Selecting optimisation parameters

Previous work has shown that regressed parameters are not independent during the optimisation process (Galbraith, 2011). This means that a change in one parameter can be offset by a change in another, to achieve a similar fit to a dataset. Preliminary testing here found that similutaneously optimising for all parameters resulted in unacceptably long simulation times (~4 weeks) and parameter uncertainties in the range of 100%. Unfortunately, this meant that targeted parameter selection was necessary. Most influential parameters were kept in the optimisation, while least influential parameters were fixed. Section 6.5.1 showed that nucleation order was unequivocally the least influential kinetic parameter. This was followed by nucleation rate constant, however this parameter was maintained in the optimisation to allow nucleation rate to be varied during simulations. Results differed thereafter depending on whether PSD or yield were considered. PSD impacts were used to determine kinetic parameter importance though, since the magnitude of effect was far greater. On this basis, growth order was fixed. Similarly, in the aggregation parameter estimations, aggregation order was fixed. This method is supported by results in section 6.5.3, which use parameters and uncertainties optimised by Galbraith, to show that rate orders are less influential than their respective rate constants, on PSD and yield output variables. The nucleation and aggregation orders were set to 1.68 and 5.26, respectively, for comparison with previous estimations (Galbraith et al., 2014). A 2nd order growth rate model with respect to *SI* was assumed, aligning with the majority of previously determined struvite growth rate models (section 2.2.4) and traditional crystallisation theory (Mullin, 2001).[22] Additionally, the fifth order growth model used by Galbraith made

---

[21] Variance models available in the gPROMS software package include constant variance, constant relative variance, heteroscedastic (power law relative variance) and linear variance.

[22] When the traditional second order model using reduced saturation is converted to saturation index, the order becomes 2.2 as the logarithmic saturation index changes slower. This difference is not considered important considering the insensitivity of reactor outputs to growth rate order.

it very difficult to reach the near-equilibrium conditions observed in this work – an average of 99% thermodynamic phosphorus recovery in the Roughton mixer *SI* = 1.4 condition shown in section 5.5.3. This is because high order growth models cause the growth rate to rapidly decline as supersaturation approaches zero.

Parameter range upper boundaries were fixed to allow only solvable combinations (Table 7.2) and checks were made to ensure that the parameter ranges allowed prediction of the maximum PSD properties (D[50] and PSD width). Parameter range lower boundaries were arbitrarily set as they did not cause numerical instability and were not constrained during parameter optimisations. The lower boundary of the growth rate constant was based on the lowest observed in the literature and that of the nucleation rate constant was assigned a value which did not affect PSD within measurement uncertainty (determined in Chapter 6).

Table 7.2 – Numerically stable parameter range boundaries

Kinetic Parameter	Lower Boundary	Upper Boundary
Growth rate constant (k_g) [µm/min]	5	230
Nucleation rate constant (k_{nuc}) [1/L.min]	1×10^5	5×10^9
Aggregation rate constant (k_{agg}) [L/min]	1×10^{-8}	7.44×10^{-6}
Growth rate order (n_g)	2	2
Nucleation rate order (n_{nuc})	1.68	1.68
Aggregation rate order (n_{agg})	1	6

7.1.3 Solution techniques

The software package gPROMS was chosen in this work for parameter optimisation purposes for its ease of implementation with pre-existing models developed by Galbraith *et al.* (Galbraith, 2011) and because it allows the simultaneous estimation of multiple parameters using ensemble data sets (dynamic and steady state data sets from a variety of experimental conditions). The estimation technique also allows sensor variance to be quantified, as per the above discussion.

The objective function (equation 7.1) used by the gPROMS software for all parameter optimisations, determines optimum kinetic parameters based on experimental data. It is a global, normalised, weighted objective function and is statistically robust. Optimisation was conducted using a nonlinear optimisation solver built into the gPROMS software. The solver employs a sequential quadratic programming method for the solution of a nonlinear programming problem.

$$\Phi = \frac{N}{2}\ln(2\pi) + \frac{1}{2}\min_{\theta}\left\{\sum_{i=1}^{NE}\sum_{j=1}^{NV_i}\sum_{k=1}^{NM_{ij}}\left[\ln\left(\sigma_{ijk}^2\right) + \frac{\left(\tilde{z}_{ijk} - z_{ijk}\right)}{\sigma_{ijk}^2}\right]\right\} \tag{7.1}$$

Where N is the total number of measurements; θ is the set of estimated model parameters, subject to upper and lower bounds; NE is the number of experiments performed; NV_i is the number of variables measured in the i^{th} experiment; NM_{ij} is the number of measurements of the j^{th} variable in the i^{th} experiment; σ_{ijk}^2 is the variance of the k^{th} measurement of variable j in experiment i; $\tilde{z}_{ijk}$ is the k^{th} measured value of variable j in experiment i; and z_{ijk} is the k^{th} (model-) predicted value of variable j in experiment i.

In each iteration of the optimisation procedure, parameters are varied, the model is solved and results are evaluated. The following criteria must be met before an optimal solution is accepted: 1) No parameter or variable boundary conditions are exceeded; 2) The rate of change of the objective function is zero; 3) An optimisation tolerance (calculated by normalising a Lagrange function incorporating the objective function), is less than a given uncertainty (default 0.001). If these criteria are not met, parameters are varied to achieve a solution closer to an optimum. Since the optimisation tolerance is somewhat arbitrary, a solution can also be accepted if the absolute objective function change is less than 1E-12 between iterations.

Using volume based PSD measurements increases simulation time by a factor of two, but produces a lower objective function value, indicating a better fit to data and more accurate parameter optimisations. As such, volume fraction PSD measurements were used in this work.

PSD measurements consist of volume fractions at discrete representative sizes called cells. Cells in which all experimental measurements were zero were deemed unnecessary in the parameter optimisation model and were eliminated to improve solution times and focus parameter optimisations on meaningful data. This is important since the optimisation objective function is contributed to by all measurements and can be unnecessarily weighted by 'zero' measurements away from the main PSD. Often the smallest detected particle size is significantly larger than the assumed nuclei size and the intermittent cells created by the geometric distribution are not used. Some of the cells between the nuclei size and the first measured particle size can be lumped together without sacrificing accuracy[23] or numerical stability. This variable discretisation capability is one advantage of the cell average technique. The geometric distribution must be maintained in higher cells ($i \geq 2$) to minimise numerical diffusion. Figure 7.4 below shows how this was achieved and Figure 7.5 and Figure 7.6 show that moments and number density were not significantly affected. When applied to the measurement discretisation used by the Malvern Mastersizer3000, a 26% simulation time reduction was achieved by extending the second cell to 115% of the first cell size (whereas in the original distribution it was only 14% larger). Further lumping of smaller cells created numerical instability.

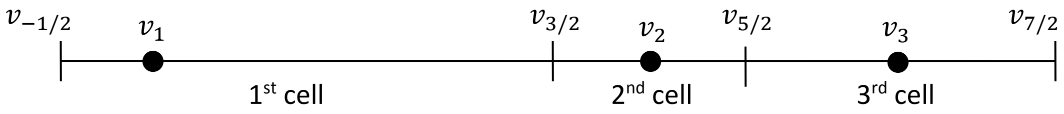

Figure 7.4 – large lower cell created by combining smaller geometrically distributed cells

---

[23] When combining lower cells, the first representative size must still be defined at a sufficiently low size relative to growth rate to ensure the DPB represents nucleation properly (as discussed earlier).

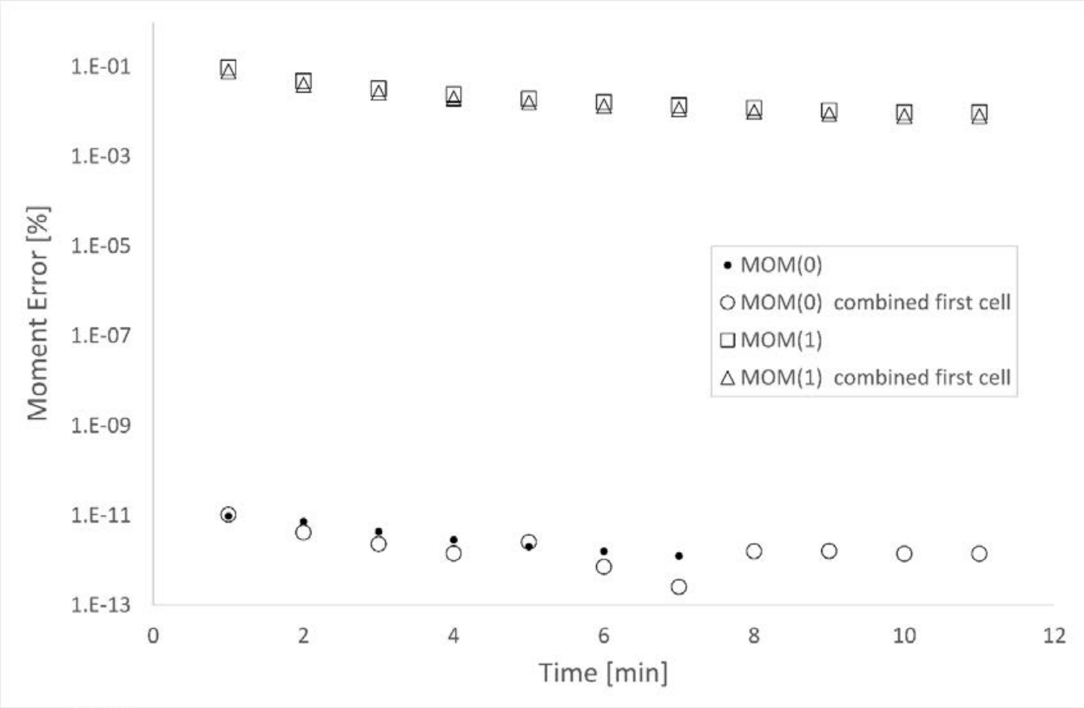

Figure 7.5 – Error in PSD moments caused by combining smaller cells

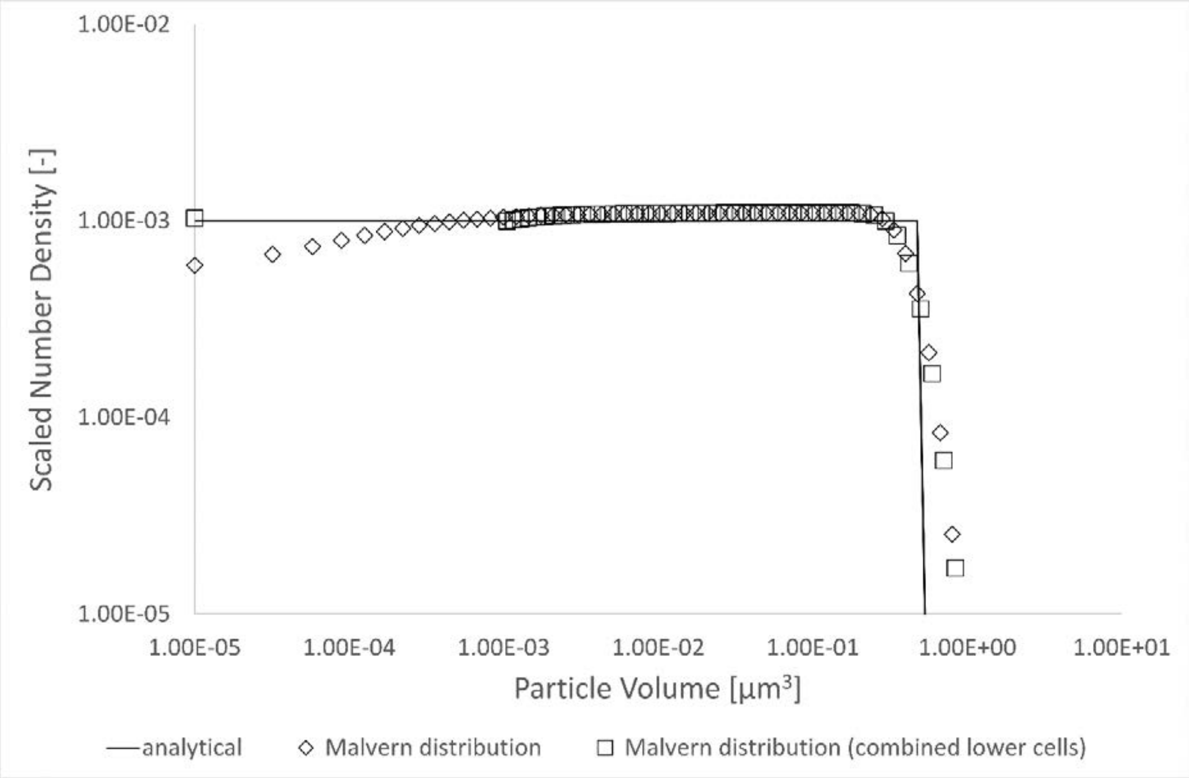

Figure 7.6 – PSD Number density difference caused by combining lower cells

Since there are 87 discrete particle size ranges (cells) in each PSD measurement[24], the PSD measurements hold 87 times the weighting of phosphorus recovery measurements in the objective function. To evenly weight PSD and phosphorus recovery measurements in the objective function, a weighting factor of 87 was added to phosphorus recovery measurements. This was achieved by multiplying the objective function term $\left(\tilde{z}_{ijk} - z_{ijk}\right)$ by a weighting factor of 87. Addition of a weighting factor gave a significantly better fit to phosphorus recovery measurements, without noticeable changes to PSD fit or solution time.

The Cell Average Technique (CAT) was used for all nucleation and crystal growth parameter optimisations. The Galbraith Modified Hounslow (GMH) technique was favoured for aggregation parameter optimisations because of its superior aggregation simulation, despite carrying a 4.15% particle volume uncertainty. This is an unfortunate result of the iterative nature of parameter optimisations. In future, steps must be taken to obtain more efficient solutions to the CAT aggregation model and to develop steady state model solutions for parameter optimisation purposes.

A multi-start analysis was conducted to ensure that initial guesses did not influence parameter optimisation results. For consistency with the optimisations shown later in this chapter, nucleation and crystal growth parameter optimisations were conducted separate to those for aggregation. Table 7.3 shows that kinetic parameters were estimated to be the same irrespective of starting condition, suggesting that no local minima existed for this problem.

---

[24] While the Mastersizer3000 uses 101 cells, only 87 were necessary to cover all measurement data. Reducing the total number of cells considered reduces simulation time.

Table 7.3 – Multi-start analysis results

		Low	**Medium**	**High**
Initial Guess	k_g $[\mu m.min^{-1}]$	6	12.5	25
	k_{nuc} $[L^{-1}min^{-1}]$ $(\times 10^7)$	0.1	8.5	100
	k_{agg} $[L.min^{-1}]$ $(\times 10^{-7})$	0.1	1	10
Weighted residual/Chi squared (<1 represents good fit)		0.45	0.45	0.46
Number of iterations		8	14	9
Regressed Value (CI=95%)	k_g $[\mu m.min^{-1}]$	9.12 ± 0.30	9.09 ± 0.30	9.00 ± 0.28
	k_{nuc} $[L^{-1}min^{-1}]$ $(\times 10^7)$	1.00 ± 0.05	1.00 ± 0.05	1.00 ± 0.05
	k_{agg} $[L.min^{-1}]$ $(\times 10^{-7})$	0.771 ± 0.114	0.770 ± 0.113	0.771 ± 0.114

7.1.4 Experimental datasets used for optimisation

PFR kinetic parameter optimisations used steady state data from the Roughton mixer because of its better mixing performance (Chapter 5). In addition, supplementary unseeded batch experiments (detailed in Appendix G) were conducted to provide temporal PSD and phosphorus recovery data not achievable by the PFR and reduce parameter optimisation uncertainty. This is possible since each dataset can be combined with its associated process model to feed into the parameter optimisation process.

Early samples in the batch experiments contained insufficient crystal concentration to achieve the laser obscuration necessary for reliable PSD measurements, specifically, samples taken at 17.97min, 14.12min and 12.83min for *SI* = 0.8, 1.0 and 1.4, respectively. Therefore, data used for kinetic parameter optimisation included: steady state PFR phosphorus recovery and PSD data; temporal batch phosphorus recovery data; and the later segments of batch PSD data. The lack of reliable PSD information available early in the crystallisation process casts some doubt upon estimated kinetic parameters, as it is during this time that significant changes occur. Measurement techniques capable of accurately detecting small particles (>0.01μm) at low concentrations (<1%) are highly recommended for future studies of crystallisation kinetics. Such techniques may include single particle optical sizing or quenching and concentrating large samples.

7.2 Results and discussion

The following sections show the optimisation fits to PSD and phosphorus recovery datasets and independent datasets. PSD data is displayed as an average of the multiple PSD measurements taken, with their variability described by the standard deviation.[25] The regressed kinetic parameters are shown in Table 7.4.

Table 7.4 – Estimated Kinetic Parameters for Poiseuille flow reactor using Roughton mixer. Uncertainties given as 95% confidence intervals

Mechanism (i)	Rate Constant	Parameter Correlation (R)	95% CI [%]	Rate Order (fixed)
Nucleation $(\times \mathbf{10^7})$ $\boldsymbol{k_{nuc}}\ [\boldsymbol{L^{-1}min^{-1}}]$	7.509 ± 0.257	-0.91	3.42%	*1.68*
Growth $\boldsymbol{k_g}\ [\boldsymbol{\mu m.min^{-1}}]$	16.72 ± 0.195		1.17%	*2*
Aggregation $(\times \mathbf{10^{-6}})$ $\boldsymbol{k_{agg}}\ [\boldsymbol{L.min^{-1}}]$	2.09 ± 0.01	*N/A*	*0.5%*	*5.26*

Kinetic parameter uncertainties shown in Table 7.4 were up to 5 times larger than those found in optimisations by Galbraith *et al.* [ref]. However, they are still deemed acceptable for future design purposes, as it is unlikely that they would have a measureable impact on key reactor output parameters. This is demonstrated by results from Chapter 6, which showed that: 1) kinetic parameter uncertainties (±10%) which propagated to measurable changes in output variables were 3 times larger than the maximum uncertainty regressed here (±3.42%); and 2) Galbraith *et al.*'s kinetic parameter uncertainties caused maximum key output parameter variations approximately 10 fold lower than measurement uncertainties.

---

[25] Error was presented as the standard deviation of all measurement values to show how the shapes of the curves varied.

Outlet phosphorus concentration uncertainty predicted during the parameter optimisation process (Table 7.1) was 12.6 % higher than what was estimated experimentally (8.88×10^{-5}) because of the variation between individual data points. It is unknown whether this variation stems from reactor operation or measurement technique, but this increased level of uncertainty is not considered of significance to overall results considering that it equates to a maximum relative uncertainty of 1.32% (for *SI* = 1.4 phosphorus concentration measurements). Average PSD volume percentage measurement variance was estimated to be 1.16 % (absolute); significantly larger than if the recommended 1% relative uncertainty were used (PSD measurement device manufacturer specification). This shows that the combination of input uncertainties (flow rate, concentration and kinetics) was sufficient to increase the reactor output PSD variance beyond expected measurement variance. When PSD uncertainty was propagated to D[50] and PSD width, their respective uncertainties were 7.32% and 10.35%. This is lower than previously used struvite median diameter uncertainty of 20% (Galbraith et al., 2014), and is deemed to be a realistic estimation useful for future work. Quantifying kinetic parameter uncertainty allows for informed comparison of results to the literature and quantification of propagated uncertainty in any subsequent reactor designs.

7.2.1 Nucleation & crystal growth

Figure 7.7 and Figure 7.8 show nucleation and growth kinetic parameter optimisation results, comparing experimental and simulated PSDs and phosphorus recovery, respectively.

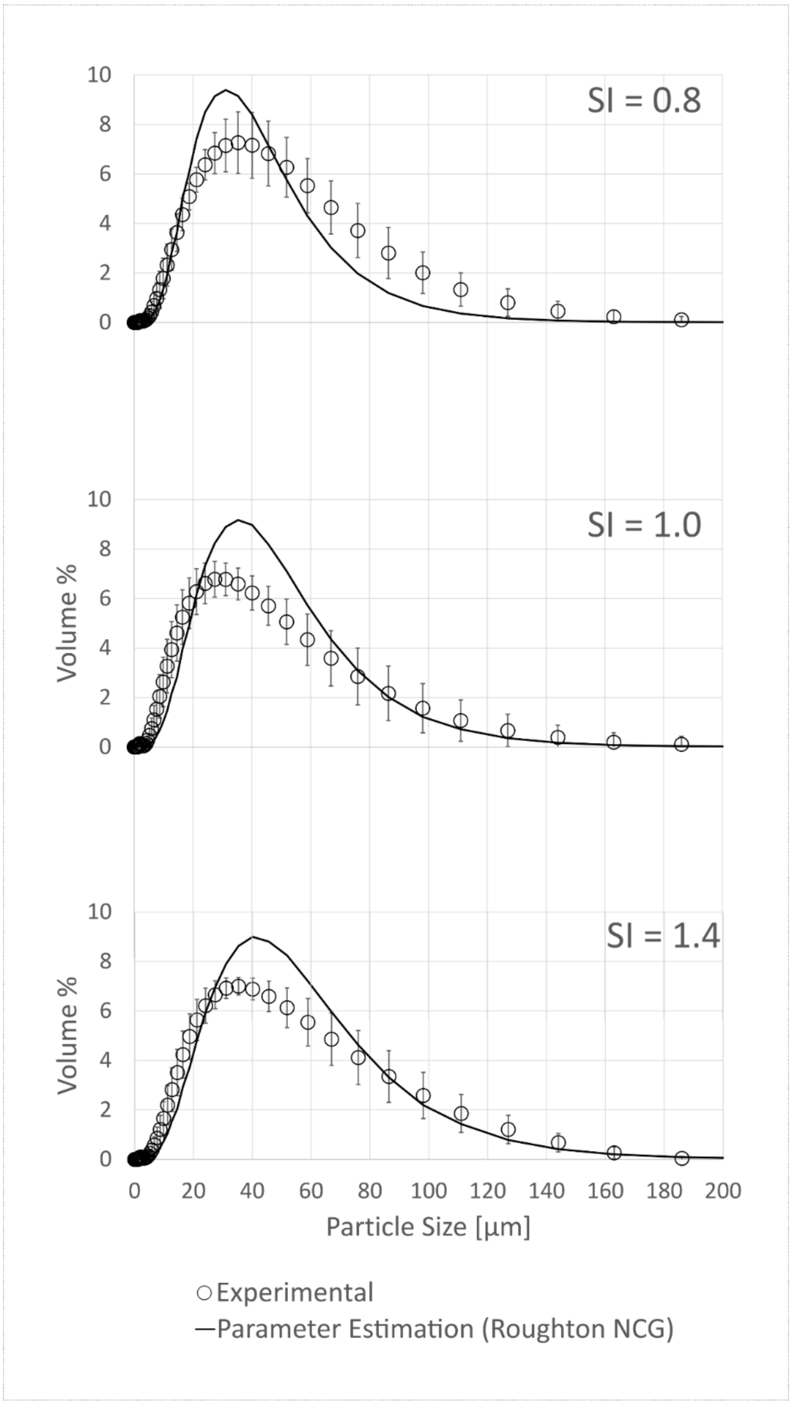

Figure 7.7 – PSDs for nucleation and crystal growth parameter optimisation using the Roughton mixer

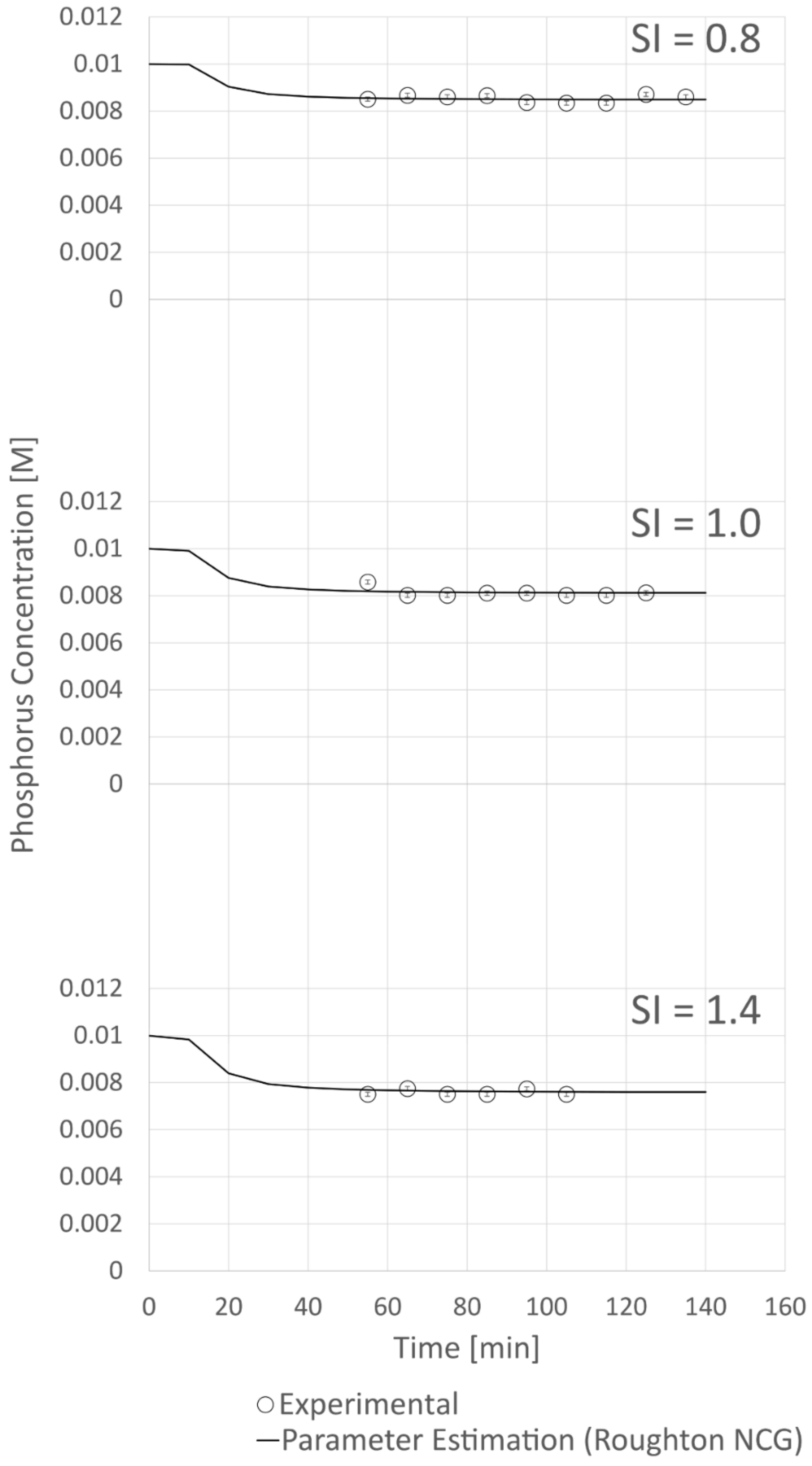

Figure 7.8 – Phosphorus recovery for nucleation and crystal growth parameter optimisation using the Roughton mixer

The contributions of different measurements to different terms are shown for the readers information below in Table 7.5. The absolute value of the objective function is dominated by the residual term ($(\tilde{z}_{ijk} - z_{ijk})/\sigma_{ijk}^2$) pertaining to the phosphorus concentration measurements. This is because the already low uncertainty in the phosphorus measurement is amplified by the weighting factor implemented. However, the large magnitude does not indicate that the optimisation is most sensitive to phosphorus concentration. A more detailed examination of the hessian would be necessary to determine this.

Table 7.5 – Nucleation and crystal growth parameter estimation objective function contributions

SI	Measurement	Constant Term	Variance Term	Residual Term
0.8	P conc.	8.3	-124.2	85989.9
	PSD	719.5	-2231.8	524.1
1.0	P conc.	7.4	-110.4	105500.0
	PSD	639.6	-1903.2	719.7
1.4	P conc.	5.5	-82.8	46673.7
	PSD	479.7	-1437.0	196.7

Figure 7.7 shows that the under-shoot of larger particles for *SI* = 0.8 is more pronounced than the under-shoot of small particles for *SI* = 1.0 and 1.4. This is because the geometric discretisation creates a larger concentration of data points in lower size ranges, unevenly weighting the fit towards the smaller particles in the distribution. Future parameter optimisations could be improved by incorporating a particle size weighting into the objective function to account for the geometric discretisation.

The PSDs in Figure 7.7 are slightly narrower, compared to the experimental data, in all scenarios. This indicates minor formation of agglomerates (strong aggregates) unable to be disrupted by sonication. The transition between weak aggregate and fully formed agglomerate can be modelled by incorporating aggregate density and bond strength parameters although this is outside the scope of this work.

The correlation coefficient (R) between k_g and k_{nuc} was -0.91, showing an inverse relationship between these parameters. Although the correlation value was large, it is not high considering the that the model is non-linear, and was not considered high enough by gPROMS (>0.95) to be of concern. Additionally, since the correlation coefficient is based on linear regression theory, the meaning of this result is uncertain in such a non-linear model. The correlation between k_g and k_{nuc} observed in this work was higher than that presented in Galbraith's PhD thsesis (Galbraith, 2011). It was however lower than the correlation observed between the rate constants and orders in his work. Increasing dataset breadth and resolution would reduce correlation, but it is an effect of parameter optimisation which cannot be avoided.

Correlation may also have been influenced by the weighting factor applied to phosphorus recovery data to give it an even objective function contribution to PSD data. Results in section 6.5.1 and 6.5.3 showed that kinetic parameters are positively correlated with respect to PSD data and negatively correlated with respect to phosphorus recovery data. This was reinforced by positive correlations observed in preliminary parameter optimisations which did not use objective function weighting, and were therefore more strongly influenced by PSD data.

The negative correlation observed shows that an increase in nucleation rate results in a reduction in growth rate and vice versa. This is because if k_{nuc} is low, fewer particles are born and a high growth rate is necessary to consume feed reagents to the same extent. If k_{nuc} is high, more particles are born and a lower growth rate is necessary to consume feed reagents to the same extent. Therefore the parameter correlation was dominated by the phosphorus recovery data contributions, although they were scaled to make a more evenly weighted contribution. Geometric discretisation would have contributed to this effect by placing disproportionate focus on low particle size measurements in PSD data. This results in an accurate fit around these small particle data points which do not contribute significantly to the mass balance, and a looser fit around larger particle measurements which do. The result is that the PSD measurements are not able to influence the mass balance in the model as easily as the phosphorus recovery data. This conclusion highlights the influence of measurement weighting on regressed kinetic parameters.

Figure 7.9 below compares nucleation and crystal growth optimisation predicted PSDs (Figure 7.7) to an independent dataset (sonicated impinging jet scenario) for validation purposes. Only *SI* = 1.0 and 1.4 conditions were considered as it had already been established in Chapter 5 that sonicated impinging jet phosphorus recovery at *SI* = 0.8 was significantly different to that of the Roughton mixer.

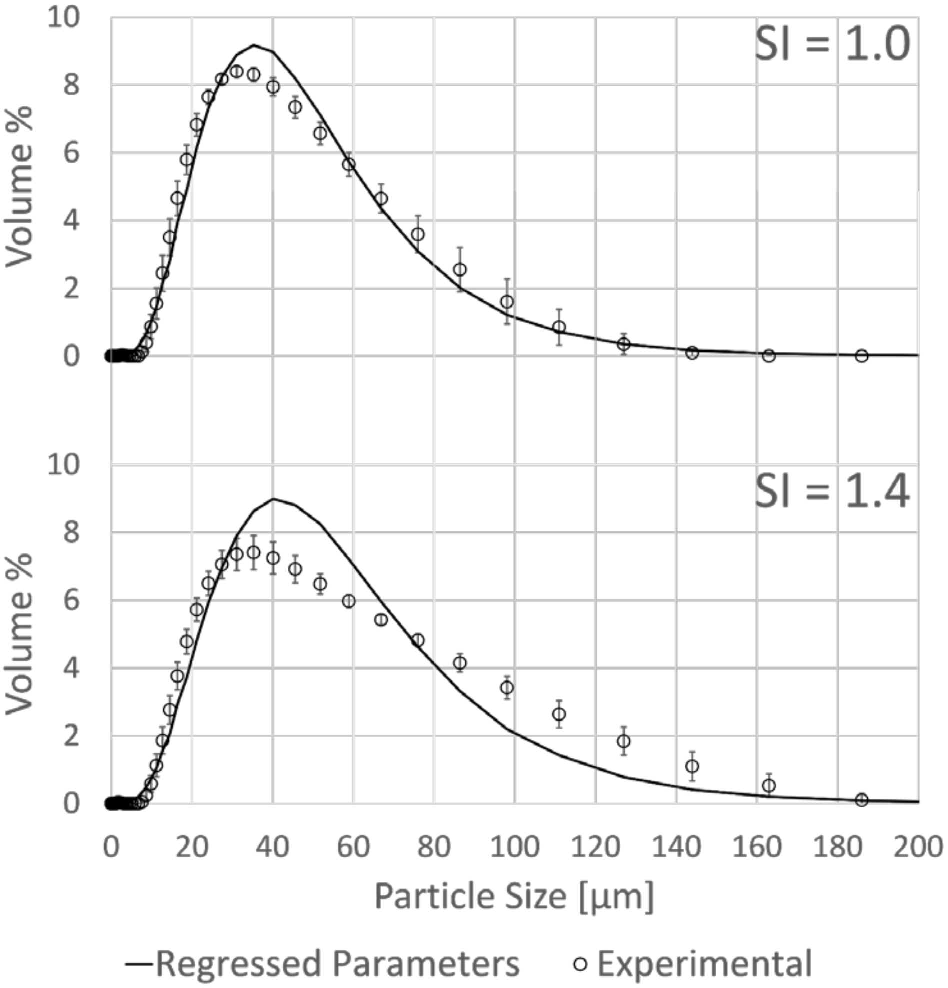

Figure 7.9 – Validation of regressed nucleation and growth kinetic parameters by comparison of predicted PSDs to data from sonicated IJ mixer experiments not used in optimisations

Figure 7.9 shows that nucleation and growth kinetic predicted PSDs fit independent experimental data well although large particles present in experimental datasets showed that the impinging jet samples contained more aggregates unable to be disrupted by sonication. The reasonable fit adds confidence to the predictive capability of the calibrated model, within the operating condition range examined.

7.2.2 Aggregation

Figure 7.10 and Figure 7.11 show aggregation kinetic parameter optimisation results, comparing unsonicated experimental with simulated PSDs and measured with simulated phosphorus recovery, respectively. Table 7.6 below shows, for the readers information, the objective function contributions. The residual term for *SI* = 1.4 correspond to the differences seen between simulation and experimental results in Figure 7.10.

Table 7.6 – Nucleation and crystal growth parameter estimation objective function contributions

SI	Measurement	Constant Term	Variance Term	Residual Term
0.8	PSD	2109.0	-7294.8	7507.8
1.0	PSD	1640.3	-5779.3	6711.3
1.4	PSD	1312.2	-4269.5	86767.1

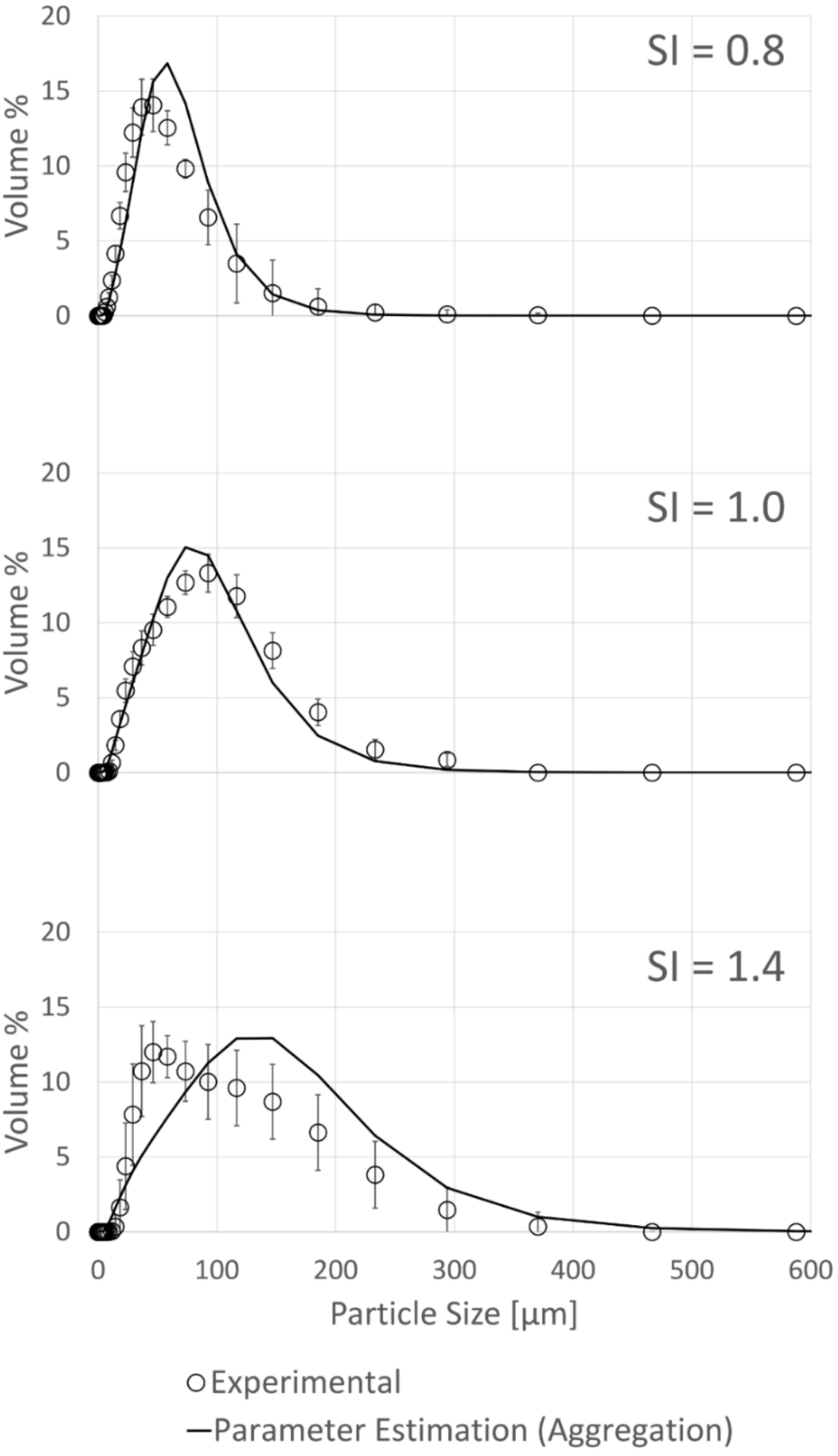

Figure 7.10 – PSDs for aggregation parameter optimisation using the Roughton mixer

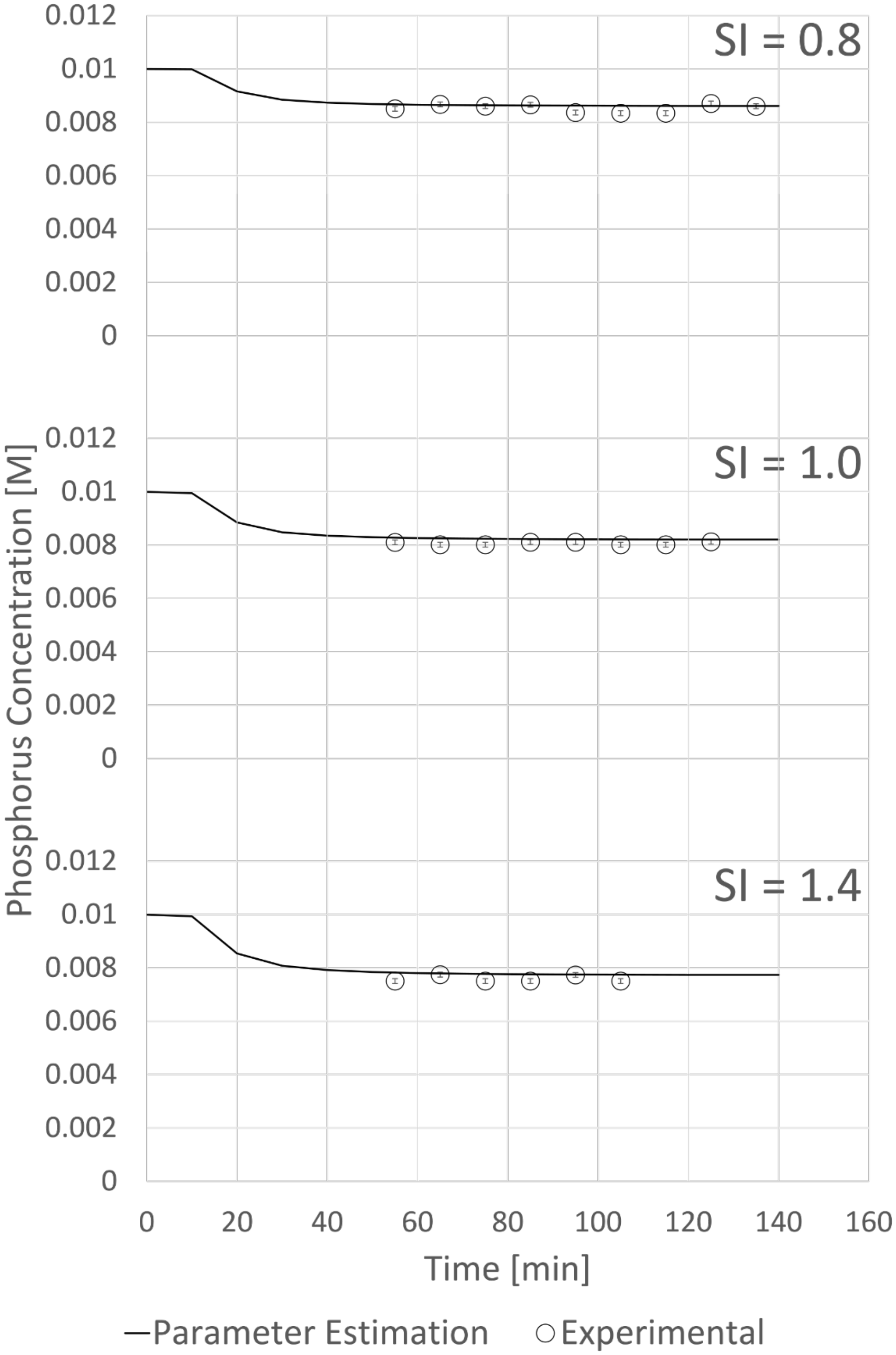

Figure 7.11 - Phosphorus recovery for aggregation parameter optimisation using the Roughton mixer

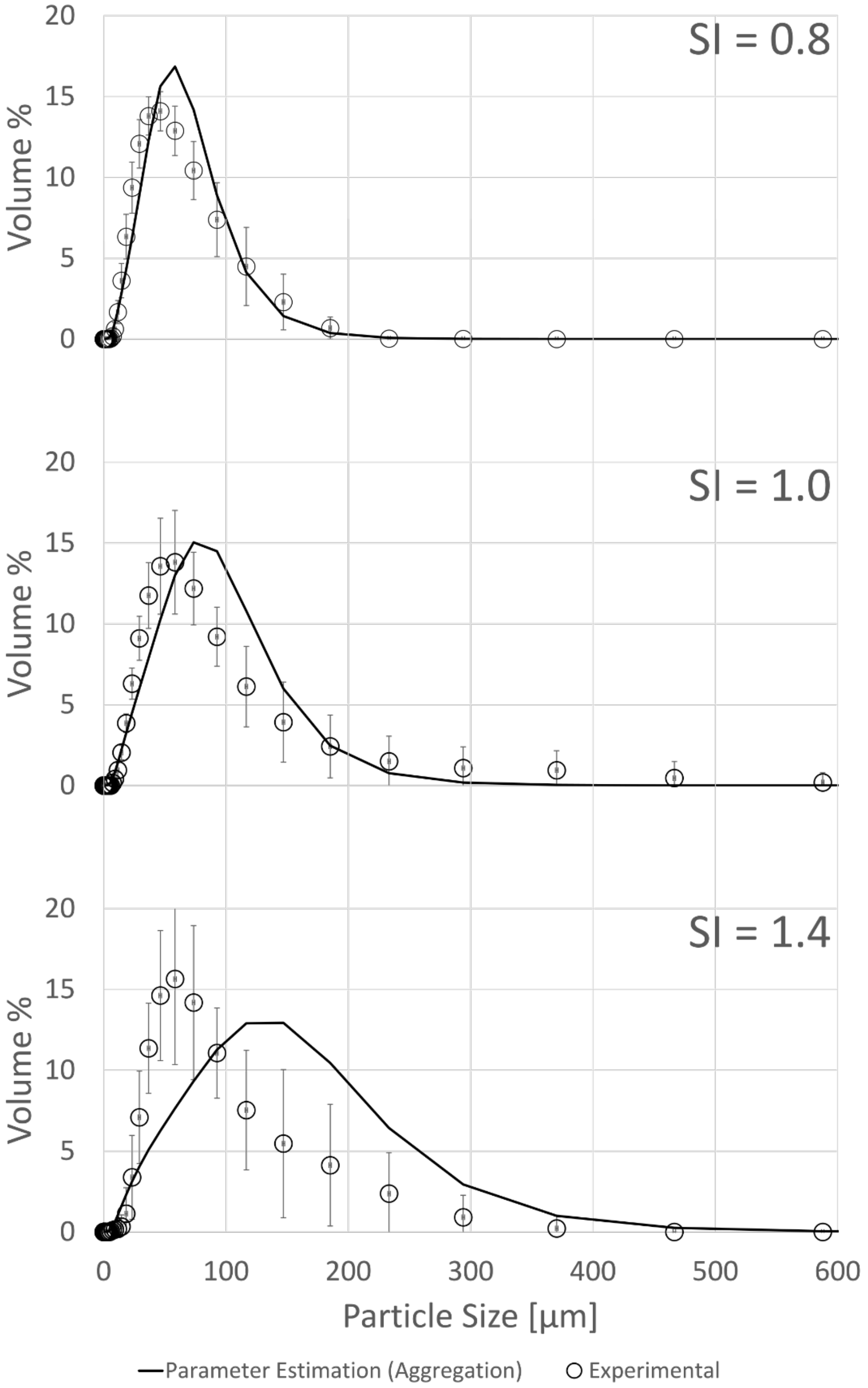

Figure 7.12 – Validation of regressed nucleation, growth and aggregation kinetic parameters by comparison of predicted PSDs to data from unsonicated R mixer experimental data not used in optimisations

Aggregation predicted PSDs (Figure 7.10 and Figure 7.12) showed reasonable fits for *SI* = 0.8 and *SI* = 1.0. At *SI* = 1.4 though, the optimisation PSDs include more large particles than the experimental PSDs. This may be an indicator that aggregation in this system is size dependent. Aggregation is theoretically a size dependent process, but has been best modelled in previous work as size independent (section 2.2.5). A size dependent aggregation kernel would allow smaller particles to remain in the system while larger particles continued to aggregate. The *SI* = 1.4 aggregation data also exhibited more nuclei than predicted by the model, both for optimisation (Figure 7.10) and validation datasets (Figure 7.12). This indicates that the model was unable to properly describe the nucleation rate. This suggests that nucleation rate may have been higher than predicted, using regressed nucleation and crystal growth parameters, at *SI* = 1.4. Therefore, a higher nucleation order may be more suitable as it would increase nucleation rate at *SI* = 1.4 while having a lesser effect on nucleation rate at lower *SI* levels where the PSD fit is better. Unfortunately, increasing the number of parameters regressed is not possible with the dataset used here because of correlation issues. In any event the PSD fit is relatively good for *SI* = 0.8 and 1.0, and acceptable for *SI* = 1.4.

Insignificant differences in simulated phosphorus recovery between aggregation (Figure 7.11) and nucleation-growth optimisations (Figure 7.8) show that aggregate formation does not significantly affect the mass balance. This is to be expected and supports conclusions made in Chapter 5 that aggregate bonds are weak. In contrast, aggregation significantly affects PSD results, increasing $D[50]$ by 39%, 62% and 102% for *SI* = 0.8, 1.0 and 1.4, respectively.

7.2.3 Batch experiments

Batch experiments were conducted in an attempt to gather temporal data not attainable using the PFR. To identify whether the aggregation model was necessary for modelling batch experiments, PSD was measured for final batch samples before and after sonication. Figure 7.13 confirms that aggregation was minimal, since the sonicated and unsonicated PSDs overlap within uncertainty ranges. As such, batch data was analysed using the nucleation and crystal growth kinetic model.

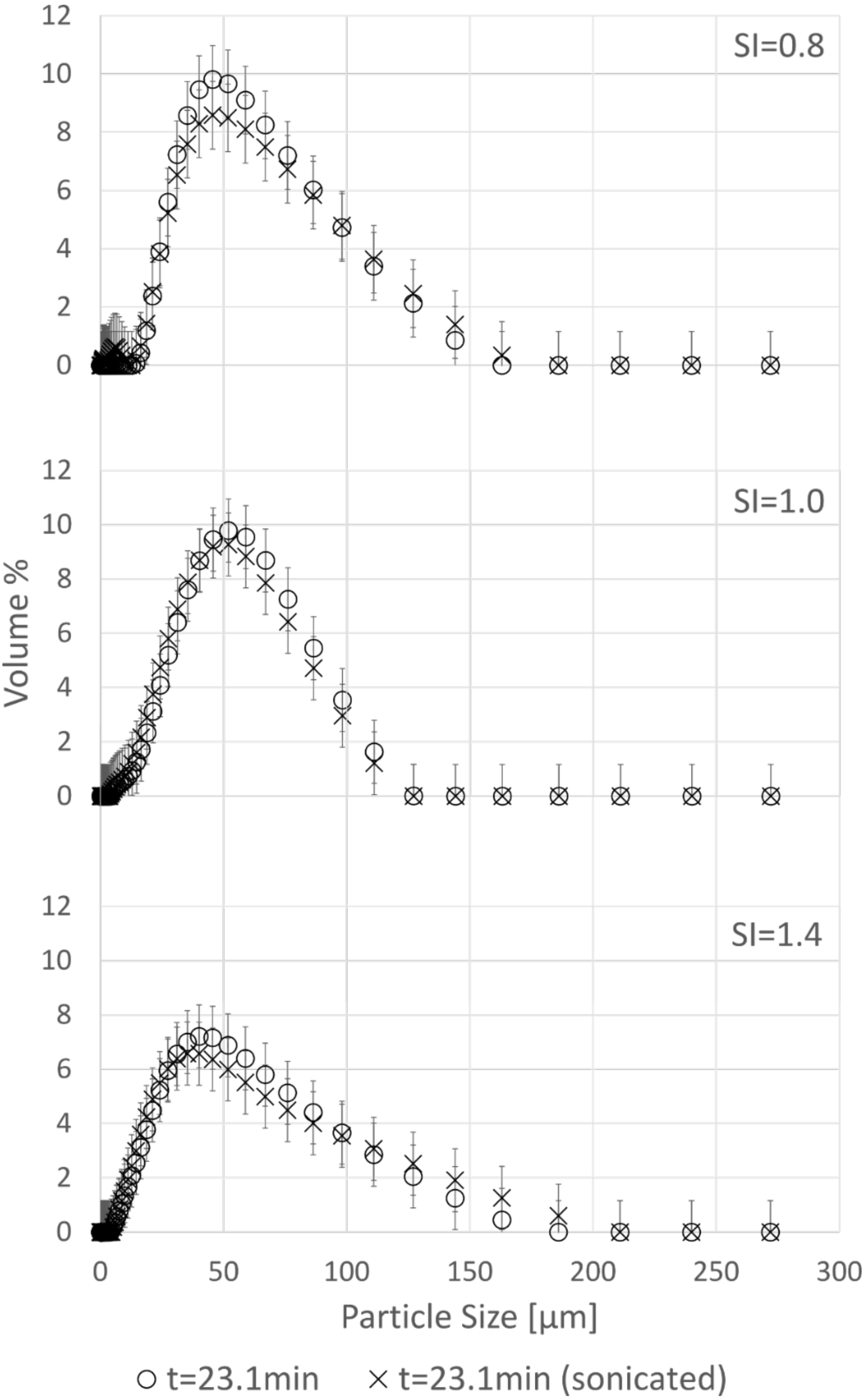

Figure 7.13 – Final PSDs for batch tests before and after 5 minutes of sonication

Temporal data collection from batch experiments was partially successful, although particle concentrations remained too low to make PSD measurements early in the crystallisation process. Nonetheless, the acceptable results were implemented in a novel parameter optimisation process which identified a single set of kinetic parameters to represent both reactors simultaneously. PFR data was examined using the PFR model while batch data was examined using a batch model. Both models fed results to a single objective function during parameter optimisation. Table 7.7 shows the resulting nucleation and growth kinetic parameters. Figure 7.14 and Figure 7.15 compare optimisation and experimental PSD and phosphorus recovery data.

Table 7.7 – Kinetic parameters regressed using both batch and Roughton PFR data at SI = 0.8, 1.0 and 1.4

Mechanism (i)	Rate Constant	Rate Order (fixed)
Nucleation$(\times 10^7)$ $k_{nuc}\ [L^{-1}min^{-1}]$	4.47*	*1.68*
Growth $k_g\ [\mu m.min^{-1}]$	15.97*	*2*

* Kinetic parameter uncertainty could not be calculated since a satisfactory fit could not be achieved.

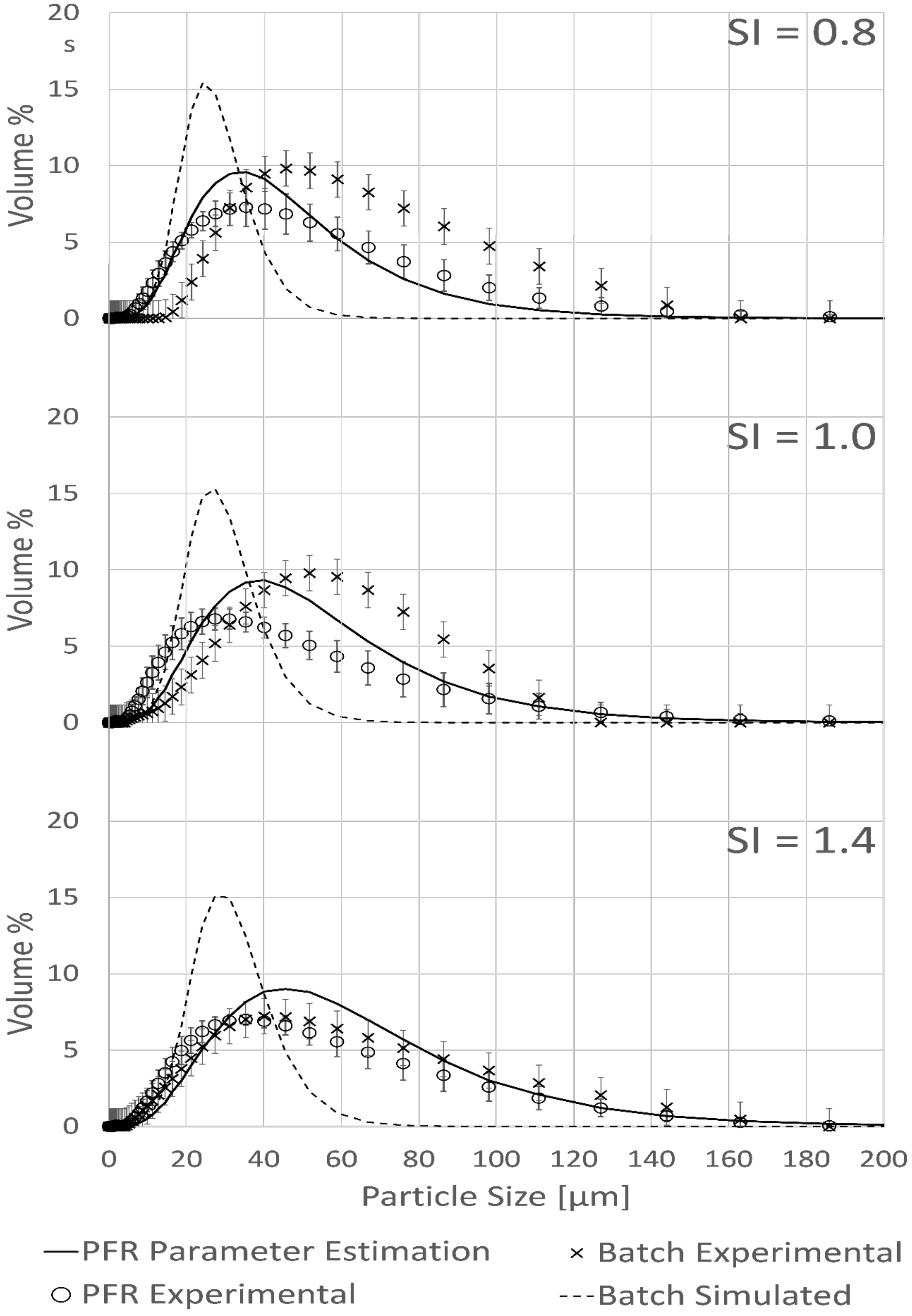

Figure 7.14 – PSDs from parameter optimisation combining Roughton PFR and batch data

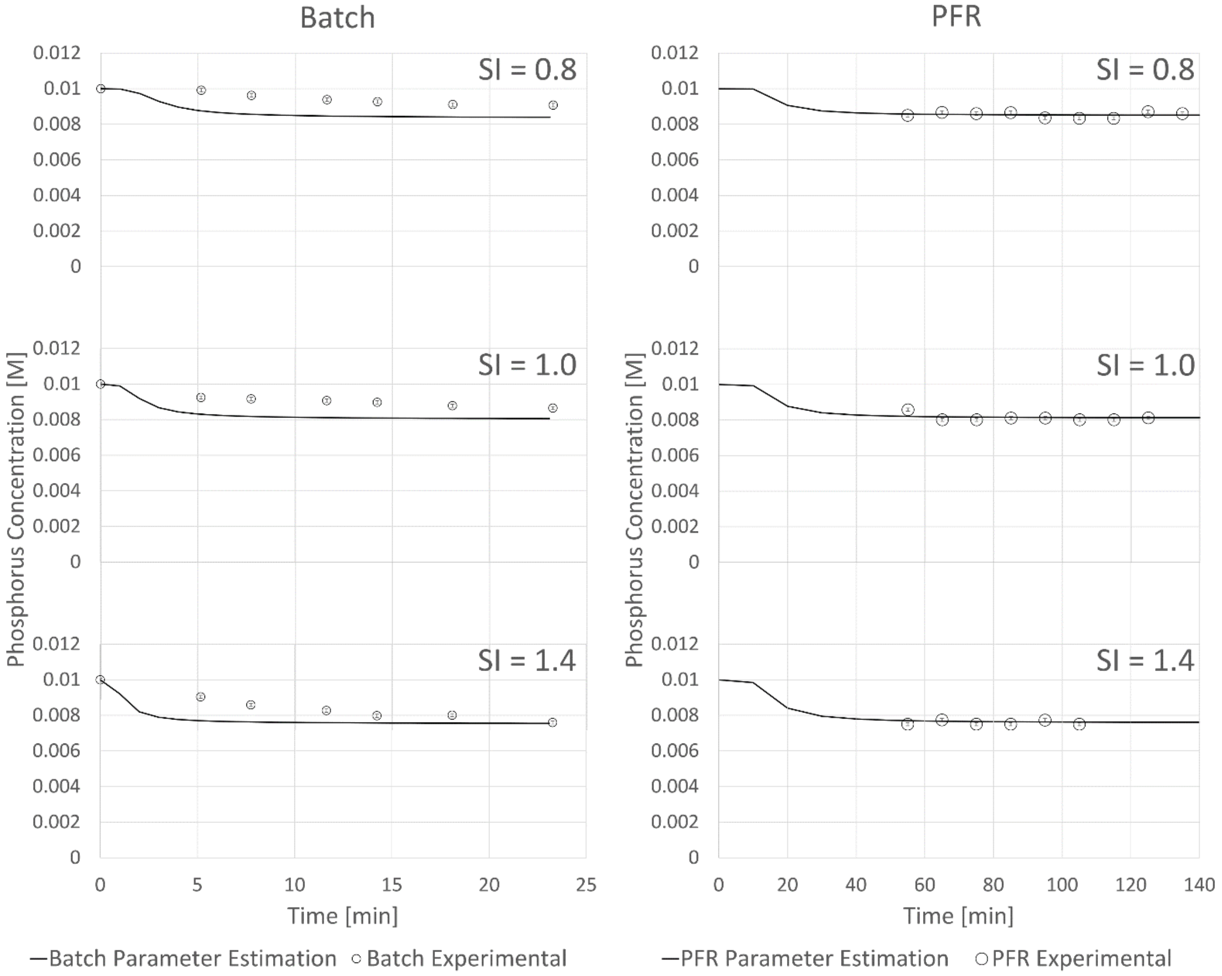

Figure 7.15 – Phosphorus recoveries from parameter optimisation combining PFR and batch data

Figure 7.14 shows that sonicated PSDs at the batch experiment conclusion were larger and wider than those observed in PFR experiments. This confirms (as suspected from tracer studies shown in section 5.2.4) that the de-aggregated crystals from the Poiseuille flow reactor have a narrower PSD than those produced in a batch reactor.

A set of kinetic parameters which provided a satisfactory fit to batch and continuous datasets simultaneously could not be found. PFR PSDs were overestimated for *SI* = 1.0 and 1.4, while batch PSDs were underestimated for all scenarios and did not match experimental PSD shape. Batch phosphorus recovery data was also overestimated in each scenario. The inability of the kinetic model to fit both PFR and batch datasets simultaneously can be explained by a combination of two things. First, differences in experimental conditions (*e.g.* hydrodynamics) were not accounted for by the model. Second, an alternative kinetic model form may better represent struvite kinetics. Various alternative kinetic model combinations were examined to identify whether a better fit to batch data could be achieved. Alternative kinetic model optimisation PSD and phosphorus recovery data are compared in Figure 7.16 and Figure 7.17 below. The models detailed in the legend of Figure 7.16 are discussed in detail in section 2.2.4.

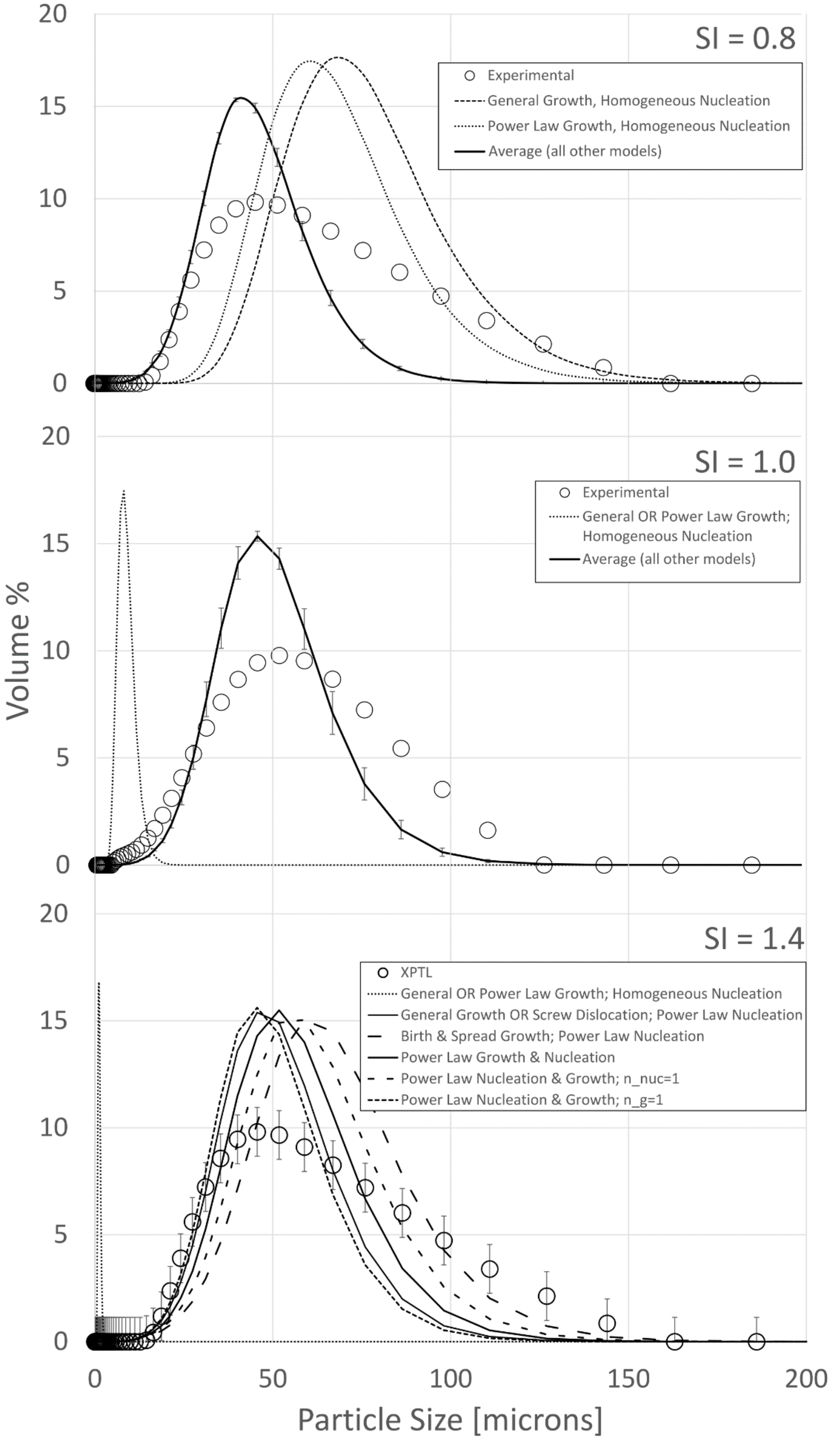

Figure 7.16 – PSDs from batch alternative kinetic model parameter optimisations

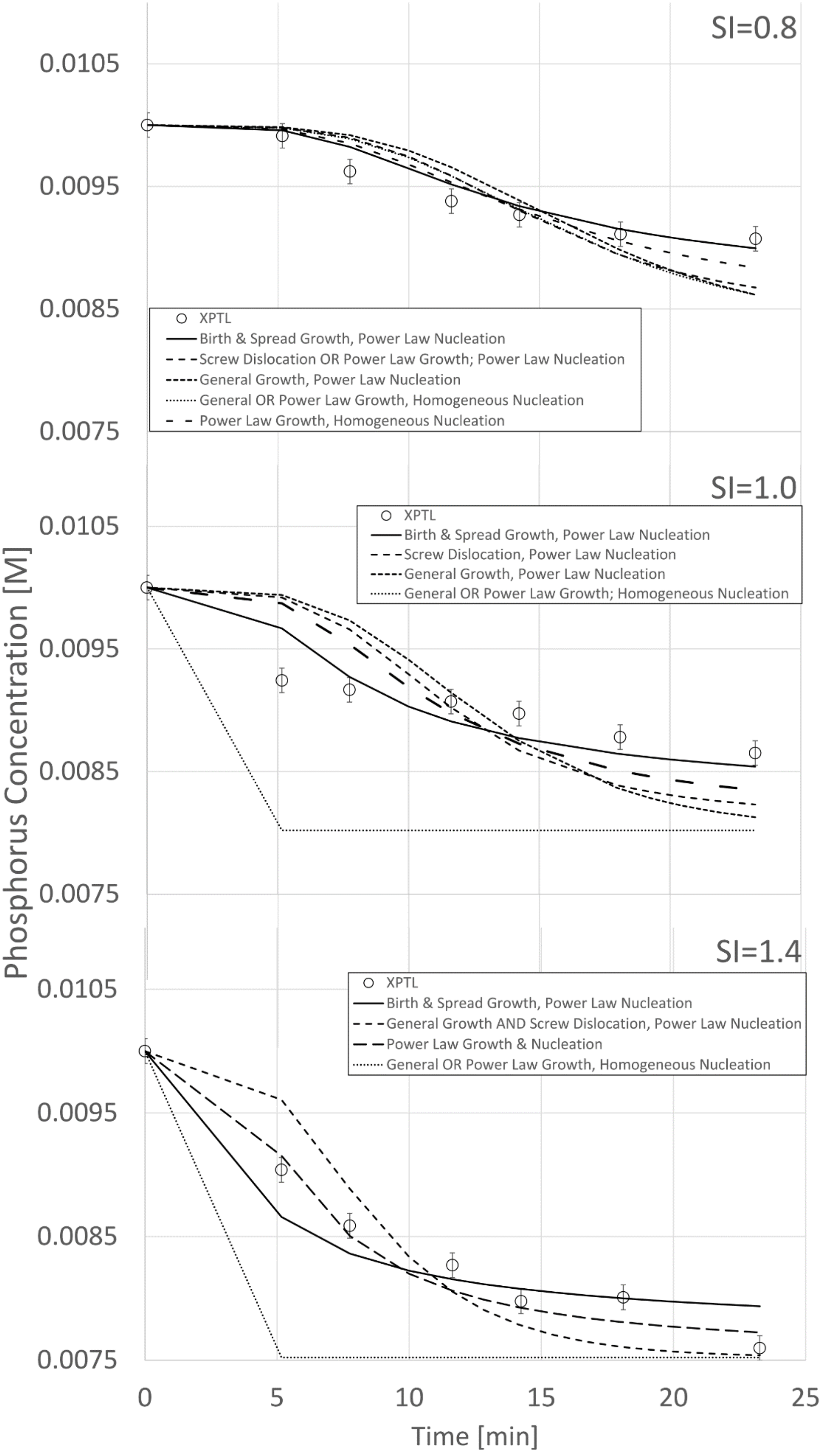

Figure 7.17 – Phosphorus recoveries from batch alternative kinetic model parameter optimisations

The birth and spread growth model (equation 7.2) provided the best fit to batch phosphorus recovery data (Figure 7.17) and produced a PSD indistinguishable from other growth models (Figure 7.16).

$$G = A'' S_r^2 \exp\left(-\frac{B'}{S_r}\right) \tag{7.2}$$

Where $A''[\mu m/min]$ is the growth rate constant and B' represents a value of S_r above which which growth becomes significant, which was selected to be equivalent to $SI = 0.3$ based on previous work (Galbraith et al., 2014). On this basis, the nucleation and crystal growth parameter optimisations simultaneously assessing batch and PFR data were repeated, substituting the new growth model. This generated kinetic parameters shown in Table 7.8, which correspond to the PSD and phosphorus recovery data shown by Figure 7.18 and Figure 7.19, respectively.

Table 7.8 – Birth and spread growth model and power law nucleation model regressed kinetic parameters

Mechanism	Rate Constant	Rate Order (fixed)
Nucleation $\boldsymbol{B_{nuc}\ L^{-1}min^{-1}}$	$(1.791 \pm 0.002) \times 10^7$	*1.68*
Growth $\boldsymbol{A''[\mu m/min]}$	64.63 ± 0.16	*2*

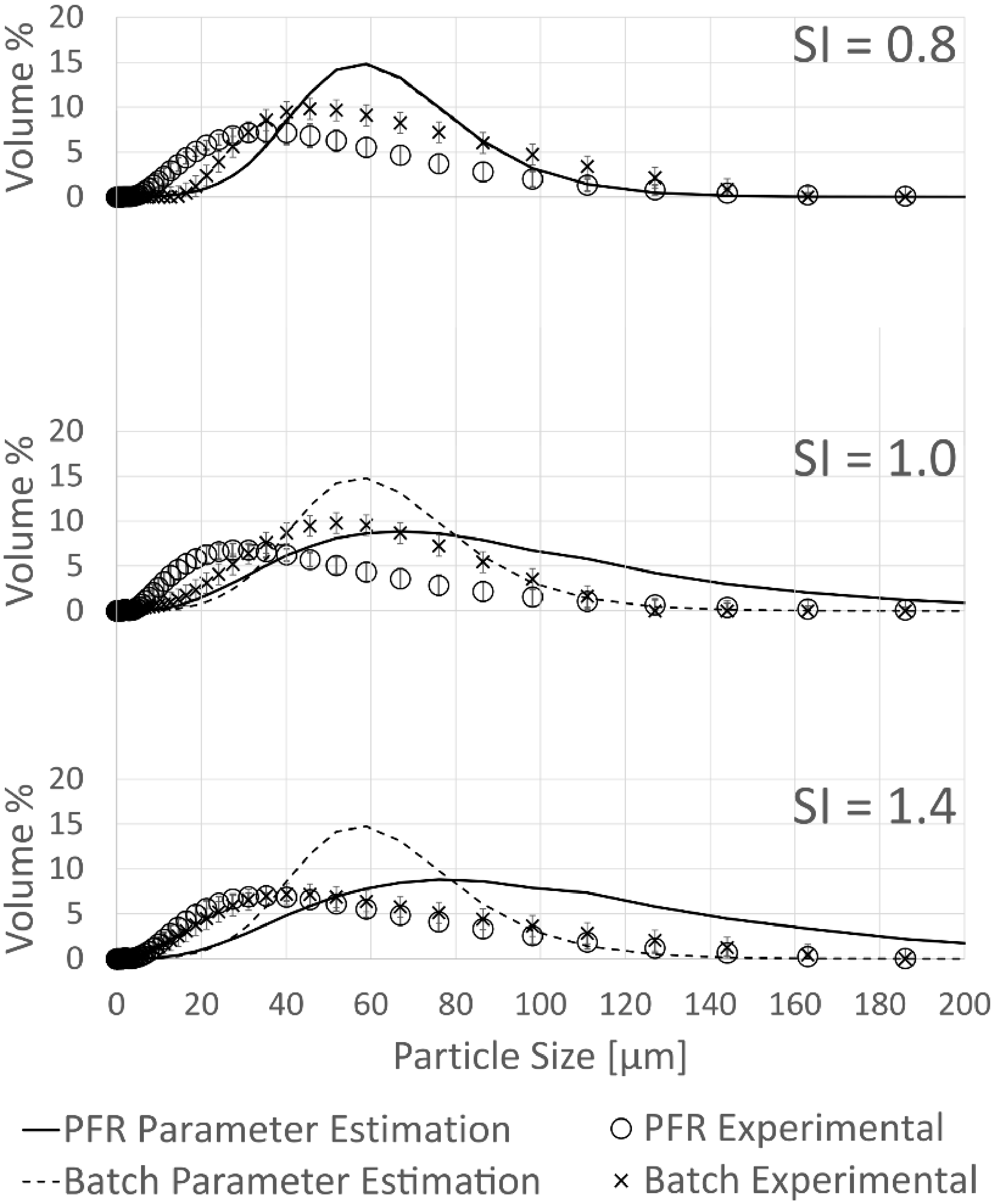

Figure 7.18 – PSDs from combined PFR and batch parameter optimisation using birth and spread crystal growth model

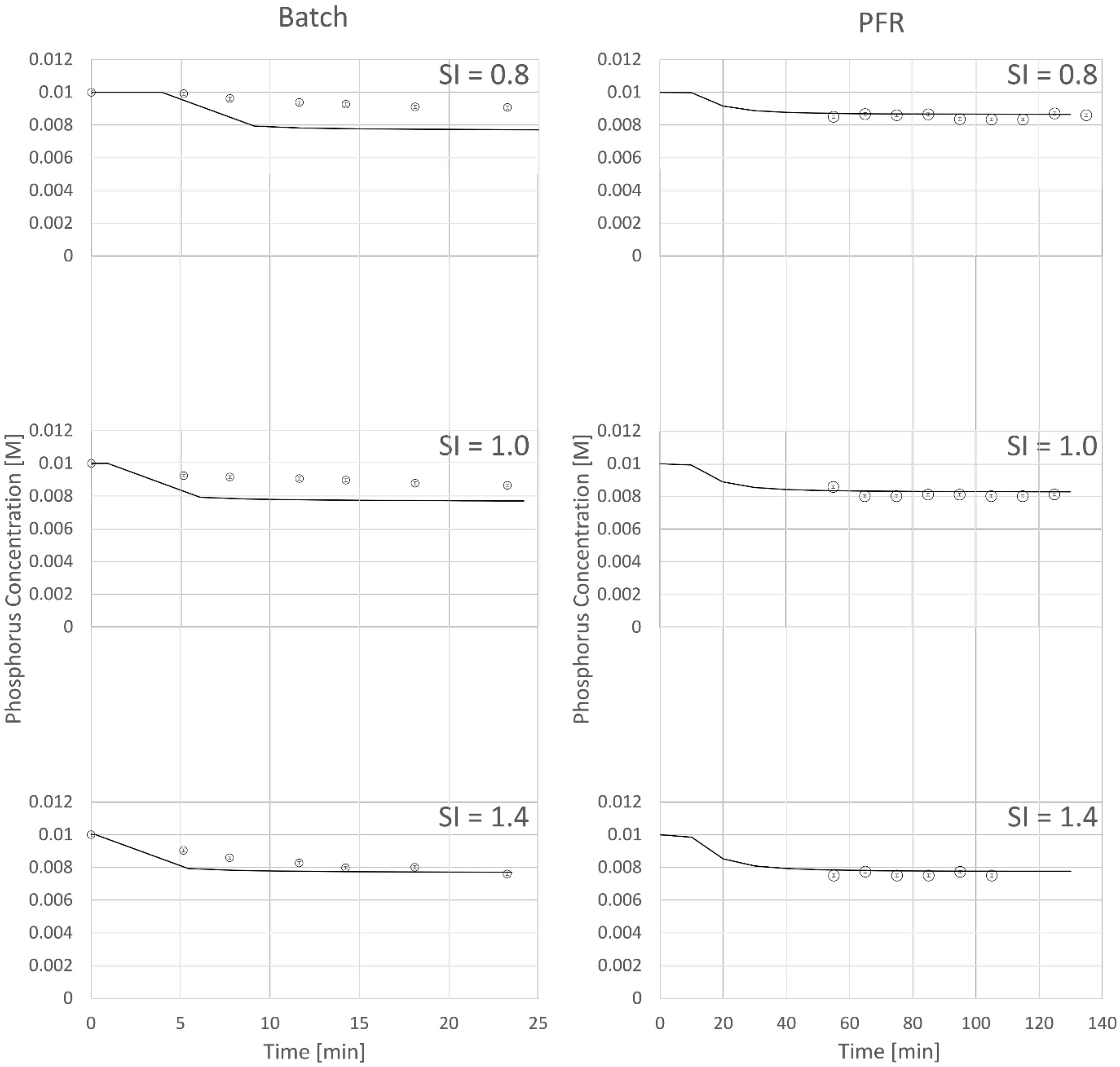

Figure 7.19 – Phosphorus recoveries from parameter optimisation combining PFR and batch data using birth and spread growth model

Repeating the combined batch and PFR parameter optimisation with the birth and spread model provided a better batch PSD fit and a worse PFR PSD fit (Figure 7.18). It also gave a marginally better fit to batch phosphorus recovery data at *SI* = 1.4, a poorer fit at lower supersaturations, and an unchanged fit to PFR phosphorus recovery (Figure 7.19). The fact that PSDs were underestimated in batch experiments and overestimated in PFR experiments suggests that aggregation might be playing a role in batch experiments. However, sonication showed aggregation effects to be minimal (Figure 7.13). The remaining explanation is that physical differences (like hydrodynamics) between batch and PFR experiments must be examined in detail and incorporated into kinetic models to fit both datasets simultaneously.

7.2.4 Nucleation rate

The estimated nucleation rate constant is 12% lower than that found by Galbraith (Galbraith et al., 2014). This difference is not large and is likely a result of scatter in experimental data. However, this result is interesting, since it was expected that the higher supersaturation in this work would generate a higher (primary) nucleation rate (section 2.2.3), compared to the secondary nucleation rate examined in Galbraith's work (Figure 7.20). This shows that, in the PFTR, after some initial primary nucleation, secondary nucleation may dominate.

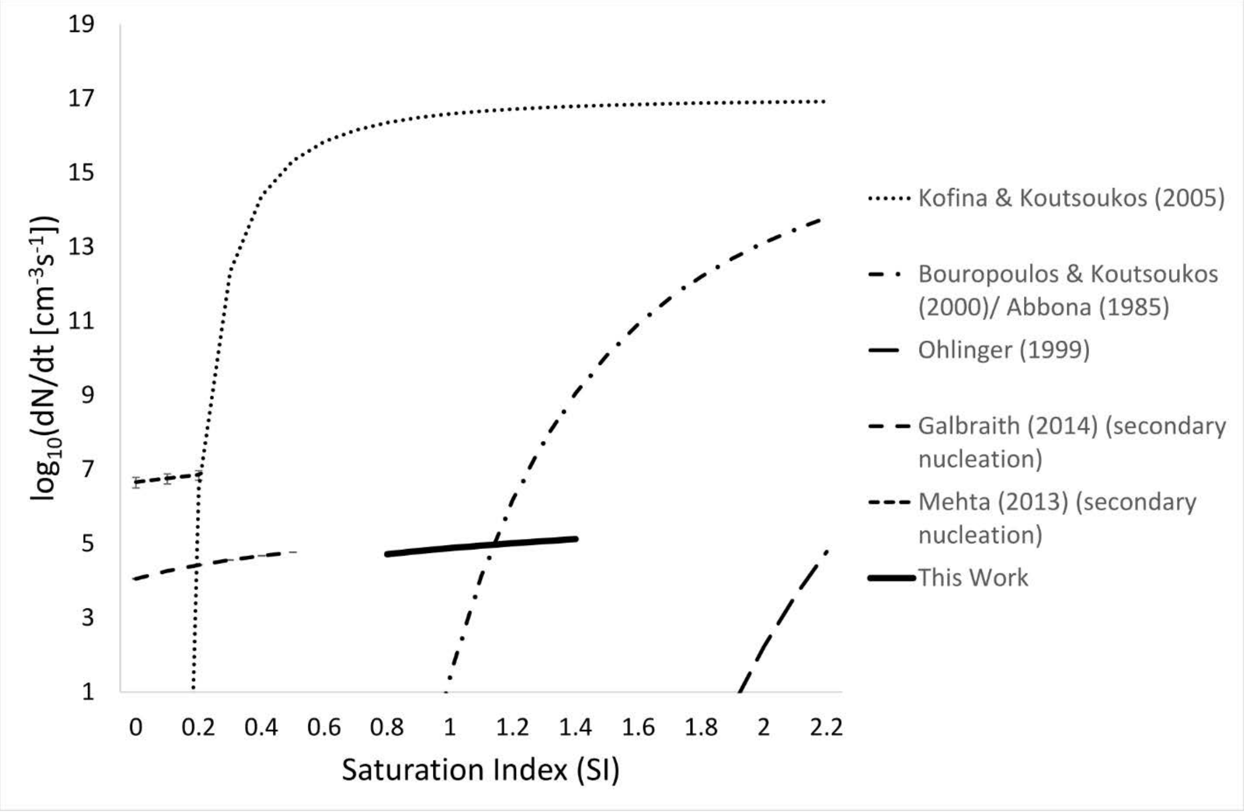

Figure 7.20 – Nucleation rate estimation comparison to models available in the literature

Further, parameter optimisations from batch data using a number of different nucleation and growth models (Figure 7.16 and Figure 7.17) showed that a primary homogeneous nucleation model was unable to fit PSDs for all *SI* values. A sharp drop in nucleation rate with decreasing *SI* is a property exhibited by the primary homogeneous nucleation models, as discussed in section 6.5.4. This means that when this model is used for parameter optimisations, there is an insufficient nucleation rate at *SI* = 0.8 and an excessive nucleation rate at higher *SI* values, resulting in over- and underestimated PSDs and severely overestimated recoveries. This result reinforces that primary homogeneous nucleation is not a dominant mechanism, and that for the supersaturation range examined, secondary nucleation can be achieved by relatively low shear rates.

7.2.5 Growth rate

Phosphorus recovery curves (Figure 7.8) are matched accurately in each case, implying that the 2nd order growth model is better than 5th order model (Figure 7.21), which was unable to achieve the required desupersaturation.

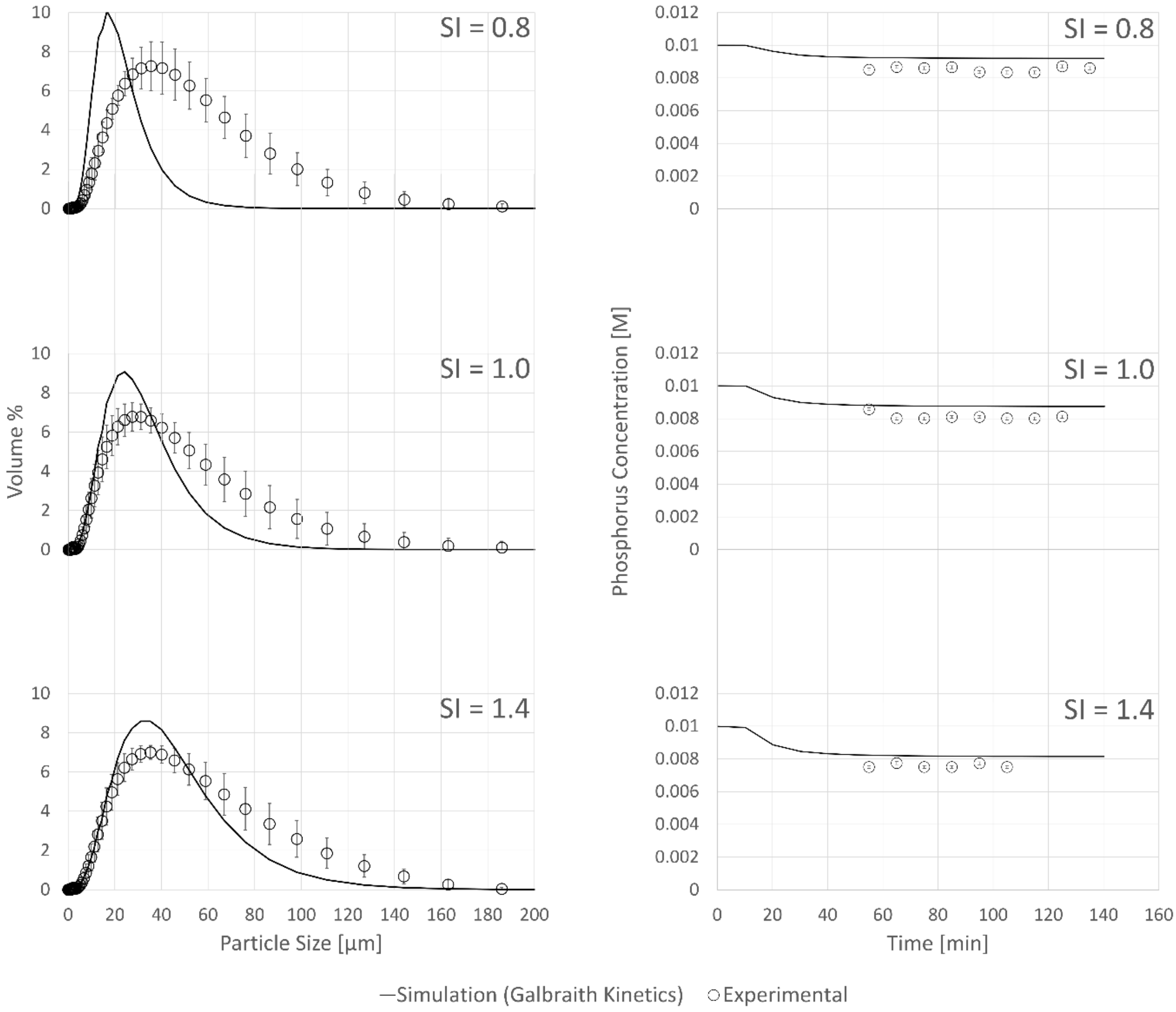

Figure 7.21 – Roughton mixer PFR PSD and outlet phosphorus concentration compared to those predicted by kinetics estimated by Galbraith (Galbraith et al., 2014), which used a 5th order growth model

The regressed growth rate constant (Table 7.4) was higher than that predicted by Galbraith *et al.* (Galbraith et al., 2014). This means that growth rate itself is also higher (than Galbraith's), which is especially evident when considering that a second order growth model was used in this work, compared to a fifth order growth model in the work by Galbraith. This is because the second order model enables higher growth rates below *SI* = 1.0 than the 5th order model.

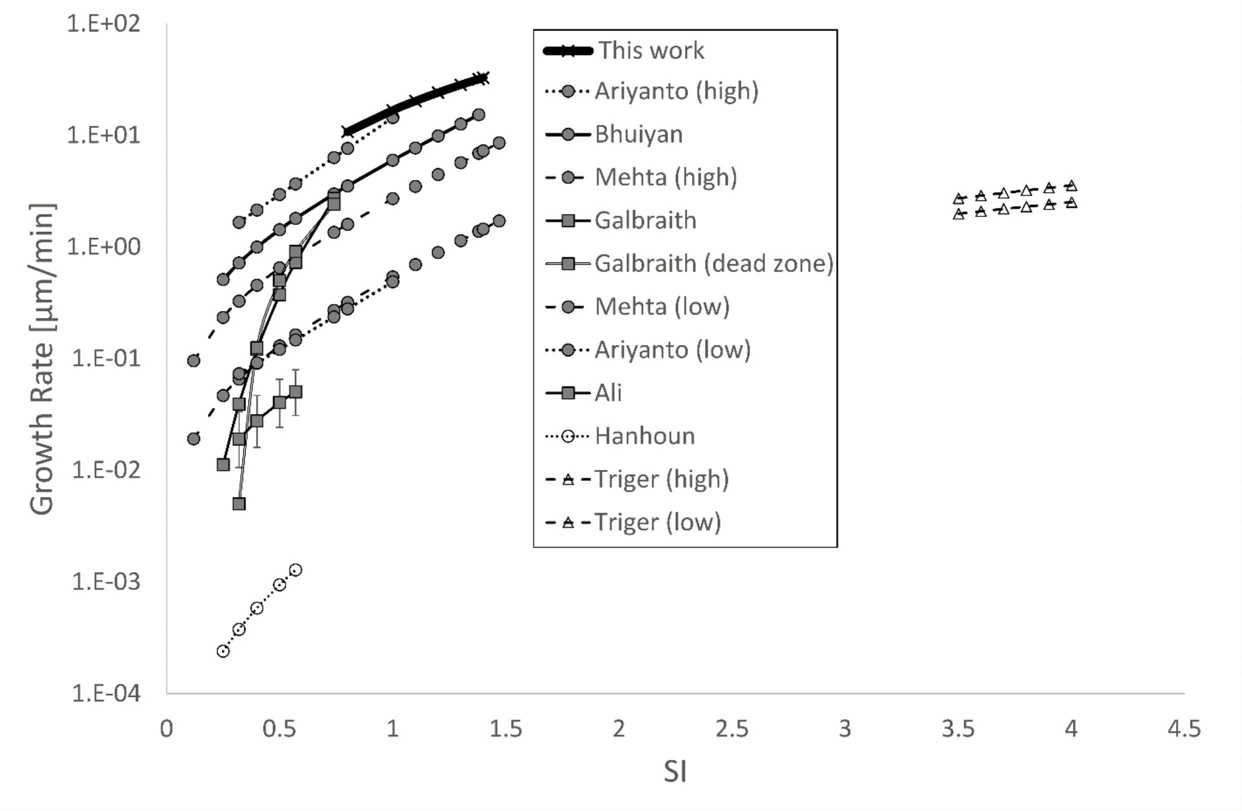

Figure 7.22 - Growth rate estimation comparison to models available in the literature. Dashed and solid lines represent batch and continuous reactors, respectively. Circles indicate $C_{PO_4} < 5$ *mM, squares indicate* $5 \leq C_{PO_4} < 10$ *mM and triangles indicate* $C_{PO_4} \geq 10$ *mM. Filled and unfilled markers represent seeded and unseeded scenarios, respectively. Uncertainties in kinetic parameters were incorporated where available and significant enough to be visible.*

Figure 7.22 compares the estimated growth rates, over the range examined, to pre-existing struvite growth rate models. It shows that the overall growth rate generated by parameters regressed in this work is higher than most other models. This is because other models ignore aggregation, which can be construed as lumping it with growth. When aggregation and growth are lumped together, and growth is regressed from phosphorus recovery data (a common practice), the apparent overall growth rate is lower because aggregation causes a decrease in particle surface area available for growth. This shows that the true growth rate is higher and that agglomeration plays a significant role in struvite particle size enlargement (a result supported by the unsonicated/ aggregation data). Therefore, aggregation, agglomeration and the variables affecting these processes must be accounted for to properly model crystallisation kinetics.

As mentioned earlier, including operating variables which influence aggregation and agglomeration, like fluid shear, into a kinetic model may provide a means of consolidating batch and Poiseuille data. More generally it may also help to consolidate differences seen the many kinetic models available in the literature. Struvite growth rate dependency on fluid shear has been suggested before (Le Corre, Valsami-Jones, et al., 2007b), but no research has been made into the effects. To properly incorporate this effect, a fluid-particle drag or energy transfer model is necessary. Such a model could be adapted from existing work modelling collision probability as a function of fluid shear (H. Mumtaz et al., 1997).

7.2.6 Aggregation rate

Table 7.9 shows that the size-independent aggregation kernel found in this work is larger than those found in other works on sparingly soluble salts.

Table 7.9 – Aggregation kernel comparison between this work and previous works

Reference	Compound	SSR	Aggregation Kernel
This work	Struvite	6.3-23.1	$6.46 \times 10^{-7} - 1.23 \times 10^{-5}$
(Galbraith et al., 2014)*	Struvite	6.3-23.1	$1.15 \times 10^{-7} - 2.18 \times 10^{-6}$
(Livk & Ilievski, 2007)	Gibbsite	1.5-2.9	$4.8 \times 10^{-10} - 6.0 \times 10^{-11}$
(D Ilievski, 2001)	Gibbsite	1.67-1.86	$4.2 \times 10^{-12} - 1.5 \times 10^{-11}$
(H. S. Mumtaz & Hounslow, 2000)	Calcium oxalate monohydrate (COM)	3.61	$2.0 \times 10^{-9} - 6.0 \times 10^{-11}$

*Model applied to the same supersaturation measure (*SI*) as this work

Aggregation rate constant was 5.6 times larger than that found by Galbraith. Greater confidence is held in this aggregation rate constant, since it was calculated independent of crystal growth rate, eliminating possible parameter confounding. Factors contributing to the higher aggregation rate are: 1) reduced probability of aggregate breakup at low shear rate, and 2) larger apparent aggregate size caused by LD measurement inaccuracies. Using equation 7.3 (derived from equation 4.8) the maximum shear rate in the PFR was found to be $0.181\ [s^{-1}]$.

$$\dot{\gamma}_{max} = \frac{\partial v}{\partial r}_{r=R} = \frac{4\bar{v}}{R} \tag{7.3}$$

Various works on the Calcium Oxalate Monohydrate (COM), a crystal system similar to struvite, suggest that this shear rate, in combination with the relatively high growth rate observed in this work, can cause high aggregation rates. Firstly, in Poiseuille flow experiments on COM an aggregation efficiency of >50% was observed at a shear rate[26] of $10\ [s^{-1}]$, linearly decreasing to 15% at $500\ [s^{-1}]$ (H. S. Mumtaz & Hounslow, 2000). The lower shear rate in this work suggests that aggregation efficiency should also be >50%. Secondly, for the same COM system, the critical aggregate size (the point where aggregation disruptive and bonding forces balance) was approximately 8µm for the same shear rate as used here (Pitt & Hounslow, 2015). This suggests that for particles greater than 8µm, aggregation effects become more significant. For reference, in this work an average of 3% (by number) or 5% (by mass) of particles exiting the reactor were less than 8µm in size. Finally, inferences can be made on aggregation efficiency by applying a dimensionless variable M (equation 7.4), which describes the ratio of particle bond strength to hydrodynamic forces (Pitt & Hounslow, 2015).

$$M = \frac{\sigma_Y L^* G}{\dot{\gamma}^2 \mu d_{eq}^2} \tag{7.4}$$

Where $\sigma_Y\ [Pa]$ is the yield strength at the aggregate cementing site, $L^*\ [m]$ is a geometric factor combining collision geometry and contact length, $\mu\ [Pa.s]$ is dynamic viscosity and $d_{eq}\ [m]$ is an equivalent diameter. For the purpose of analysis, d_{eq} is assumed here as the $D[50]$ and the term $\sigma_Y L^*$ is assumed to be the same as in the COM system (*i.e.* 1.35), based on work by (Pitt & Hounslow, 2015). A Mumtaz number significantly greater than 1 represents a system with high aggregation efficiency. The Mumtaz number calculated for this work ranged between 6.2 and 12.8, which indicates an aggregation efficiency $\sim 100\%$ (M.J. Hounslow, Wynn, Kubo, & Pitt, 2013).

---

[26] Shear rate calculated by $\dot{\gamma} = \frac{8}{15}\dot{\gamma}_{max}$

When compared to the experimental system used by Galbraith, the lower shear rate and high growth rate in this work create ideal conditions for aggregate formation as colliding particles are less likely to be disrupted and can bond more quickly. Additionally, settling effects in this reactor (examined in section 6.3.1), would have been more significant than in Galbraith's reactor which was mixed[27] and contained smaller particles (less than 35µm). It is expected that this contributed to an increase in particle collision rate in this reactor, as faster moving particles collide with slower ones. The relative impact of settling on aggregation may not have been large however, due to the low particle concentration (0.2 – 0.3 g/L). In any case, these factors may explain the larger struvite aggregation rate in this work.

While aggregation rates appear to be very high, strong confidence cannot be held in aggregate measurements using PSD. Laser diffraction accuracy decreases as particle shape deviates from spherical (Kelly & Kazanjian, 2006). Additionally, loosely bound aggregates may contain a significant degree of voids not accounted for by the model – examples of such a particles are shown below in Figure 7.23

---

[27] Mixing rate was not reported by Galbraith

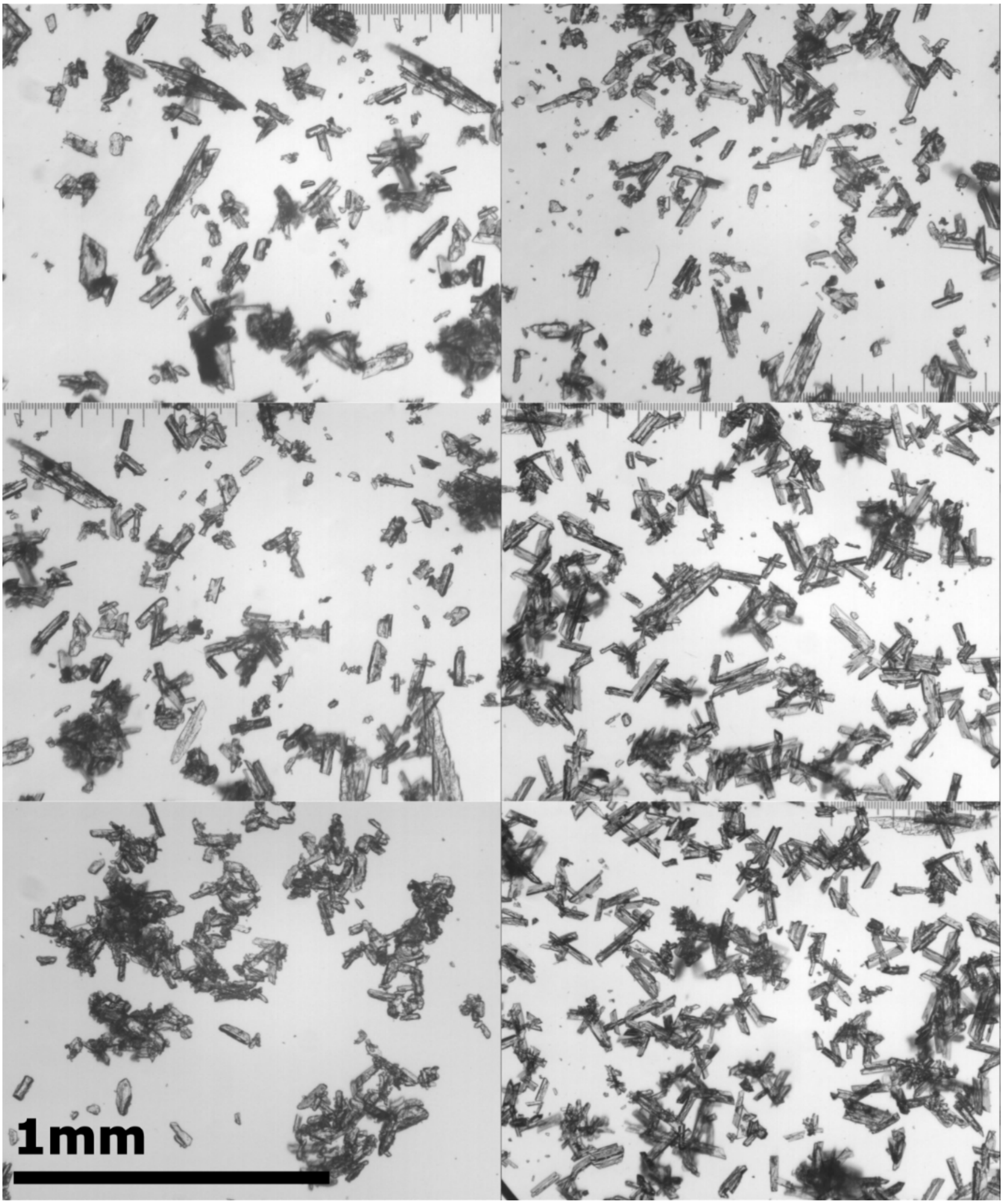

Figure 7.23 – Unsonicated struvite crystals created in Poiseuille flow at SI = 1.4

7.3 Conclusions & recommendations

This chapter investigated parameter optimisation methods including multi-start analysis, objective function weighting and parameter correlation reduction. Multi-start analysis observed no local minima.

Objective function weighting was used to balance PSD and phosphorus recovery contributions and successfully improved fit without significantly increasing computation times. Reducing parameter correlation effects by reducing the number of estimated parameters successfully reduced simulation time, although kinetic parameter correlation remained. The negative correlation between nucleation and growth rate constants showed that the optimisation was weighted towards phosphorus recovery data. Future analysis might counter this by including a volume weighting factor to account for the concentration of PSD data at lower particle sizes, which is caused by geometric discretisation. Parameter correlation may also be reduced by using a richer data set. This was attempted by conducting batch experiments to examine PSDs early in the crystallisation process, however particle concentration remained too low for accurate PSD measurements. Future work should examine alternative sampling and/or measurement techniques for samples with low particle concentrations. This could be achieved by concentrating large samples or using an alternative PSD measurement technique like single particle optical sizing (Pitt & Hounslow, 2015). In addition, a simultaneous fit could not be achieved between batch and PFR data, indicating that the kinetic model needed to incorporate physical properties like hydrodynamics to achieve this.

Estimated kinetic parameters, using the power law model, were similar to previous estimations for struvite using population balance methods and showed similar agreement to experimental data not used in optimisations, giving confidence to results. Low nucleation rate in the PFR, combined with poor primary nucleation model fits to batch data, indicated that secondary nucleation was a dominant mechanism. Results from aggregation investigations showed that a higher nucleation order than that assumed in this work (1.68) is appropriate for future struvite kinetic investigations. A second order growth model better fitted phosphorus recovery data than a previously used fifth order model, indicating that a ‘growth dead zone’ was unlikely. Alternatively, batch investigations showed that a ‘birth and spread’ growth model provided a quality fit to phosphorus recovery data by using an exponential decaying rate at low supersaturation. This shows that the birth and spread growth model is a good candidate for future investigations. Aggregation rate was successfully decoupled from nucleation and crystal growth rates by examining data from experiments with and without sonication separately. The estimated aggregation rate constant was higher than prior estimates. This was because of high aggregation efficiency in Poiseuille flow, although the rate may have been overestimated since laser diffraction becomes inaccurate when applied to irregular shapes and the model used here did not describe aggregate porosity. These issues could be addressed, to a point, by using optical particle sizing techniques mentioned above.

When considering alternative models, it is clear that the power law model provides the best description of the PFR system. It is also currently the best option for modelling struvite crystallisation over a wide supersaturation range, based on the agreement between this work and work by Galbraith using very different experimental systems. This work has also shown that the homogeneous nucleation model is not suitable for modelling struvite.

The kinetic parameters found in this work suggest that a struvite crystalliser could be operated at high supersaturation, maximising aggregation rate. This is because high supersaturation and low shear rates created an ideal scenario for aggregation. Additionally, since secondary nucleation appeared to be dominant, large nucleation rates (predicted by primary nucleation models) are less likely to be an issue. As such, this possibility warrants further investigation as it may offer a means of significantly reducing crystal residence time necessary to achieve a given particle size.

Chapter 8 Conclusions & recommendations

This chapter provides an overarching summary and draws conclusions about Poiseuille flow struvite seed production and population balance based kinetic parameter optimisation. Recommendations are made on future improvements and directions for research in this field.

8.1 Summary of work carried out

This study investigated the production of struvite seed crystals in a Poiseuille flow reactor via experimentation and numerical modelling and analysis. This included design and operation of a bench-scale reactor and the development a process model suitable for sensitivity analysis and, using data from the bench-scale reactor, kinetic parameter optimisations.

Experimental investigations carried out across a range of feed supersaturations using two different mixers provided insight into the effects of mixing and the data necessary for kinetic parameter optimisations. This work successfully met the aims and objectives outlined in section 1.4 as detailed below.

Objective 1 – to develop a dynamic reactor model capable of accurately predicting Poiseuille flow seed reactor operation. Throughout the thesis, a dynamic reactor model was developed incorporating a non-ideal thermodynamic model; Poiseuille fluid flow including advection, diffusion and reaction effects; and a discretised population balance (DPB) model representing nucleation, growth and aggregation mechanisms. The reactor model and the DPB were validated via a grid convergence study and comparison to analytic solutions, respectively.

Objective 2 – perform a sensitivity analysis to determine key input variables and kinetic parameters as they impacted on key model outputs. Chapter 6 investigated the sensitivity of the reactor to diffusion and settling effects, uncertainties in experimental independent variables, and the uncertainty in kinetic parameters. It also examined reactor operation via stochastic simulations.

Objective 3 – investigate continuous struvite seed production in a lab-scale Poiseuille flow crystalliser. Based on available literature, the reactor developed was the first to combine vortex mixing with Poiseuille flow, underlining its novelty. It also utilised sonication to disrupt weakly bound aggregates and better understand the crystallisation process in a fashion not performed elsewhere. Various operational issues were identified for improvement in future work.

Objective 4 was to regress nucleation, growth and aggregation kinetic parameters using experimental data from the bench-scale reactor. Parameter optimisation methods were developed based on the available literature, sensitivity analysis, and optimisation model testing. This process accounted for parameter uncertainties, parameter boundaries and correlation; optimisation data selection; and objective function local minima and application of weighting factors to experimental data. Nucleation and crystal growth rates were regressed with the more accurate CAT model, while the aggregation rate was regressed using the GMH nucleation, growth and aggregation model since it delivered faster simulation times.

Great effort was taken to reduce and, failing that, quantify uncertainties and identify areas of improvement for future work. This work has extended the field of struvite crystallisation, mixing and Poiseuille flow crystallisation modelling and laid down a framework for future studies on any crystallisation system.

8.2 Conclusions

The Poiseuille flow crystalliser experimentally examined in this work produced struvite seed crystals of a similar quality to those used in previous investigations. This work has shown that vortex mixing is superior to impinging jet mixing, producing higher phosphorus recovery than an impinging jet mixer at all SI levels tested and negligible aggregation at the lowest supersaturation level tested ($SI = 0.8$).

Examining the feed concentration variance expected in an industrial application showed struvite seeds, acceptable by current industrial standards, can be achieved without a control system in place. These results show the potential of this model to be utilised for process interrogation and design, and provides grounds for further investigation into continuous struvite seeding.

Sonication was an effective means of disrupting aggregates without damaging individual crystals. Two key conclusions arose from this practice. First, sonicated PSDs were indistinguishable between the feed supersaturation levels studied, for both mixers (exception in the IJ mixer between *SI* = 0.8 and 1.0). This suggests that the constituent particles making up porous aggregates continued to grow after aggregation. Second, sonicated data offered a novel approach to separate the aggregation mechanism from nucleation and growth. Sonicated samples were assumed to be an acceptable proxy measurement of nucleation and growth mechanisms only, while unsonicated samples represented all three mechanisms of particle size enlargement. This assumption was considered reasonable based on microscopy and the relative ease of aggregate disruption by sonication, which indicated that the contact area of particles forming weak aggregates was small.

The resulting nucleation and growth rate coefficients (k_{nuc} and k_g) were 12% lower and 34% higher, respectively, than those from previous struvite kinetic investigations using DPBs. This is an important result as these are relatively small differences compared to the much larger variations in previously-estimated struvite nucleation and growth rate kinetics discussed in section 2.2. Adding to the significance of this result is the fact that the earlier DPB studies on struvite varied in a number of key ways: they were seeded while these were not; they used a stirred batch system while these were continuous Poiseuille flow; they operated at lower supersaturation levels (SI = 0.37 - 0.74) than used here (SI = 0.8 – 1.4); and they used a numerical model with a 5% higher uncertainty in mass conservation than that used here. Achieving similar results, despite these differences and in light of the large variations seen in the literature, is a step forward in struvite modelling and gives confidence that DPB techniques are a valid modelling platform for further crystallisation kinetic modelling.

Examining the kinetic models regressed in this work revealed multiple insights. The nucleation rate was significantly lower than those predicted by existing struvite primary nucleation models, despite the high supersaturation used in this work. Further, attempts to fit a primary nucleation model to the data were unsuccessful, resulting in insufficient nucleation at low ($SI = 0.8$) and excessive nucleation at high ($SI = 1.4$) supersaturations. Together, these results revealed that, over the course of crystallisation, secondary nucleation was dominant over primary nucleation. Analysis using alternative growth models identified that the exponentially decaying 'birth and spread' crystal growth model was superior, providing an improved fit to experimental data. Finally, the aggregation rate was five times larger than previous estimates for struvite. This was likely influenced by laser diffraction measurement techniques, which have inherent problems measuring irregular and loosely aggregated particles.

In addition to experimental determinations, the process model was used to identify the relative influence of system variables and kinetic parameters. Diffusion effects and uncertainties in reagent concentration and flow rate were found to have an insignificant effect on the reactor model output. Sensitivity analysis found that nucleation kinetic parameters had the least influence on both PSD and yield, growth kinetic parameters had the greatest influence on yield, and aggregation kinetic parameters had the greatest influence on PSD. These results were important for minimising parameter correlation impacts on the optimisation process by allowing less influential parameters to be fixed. This improved optimisation simulation time and stability.

A correlation between regressed parameters was still observed although it was lower than those from previous works. Based on sensitivity analysis results, this negative correlation indicated that the optimisation process was more significantly influenced by phosphorus recovery data than PSD data. The geometric discretisation is expected to have caused this by magnifying the contribution of small particles which do not contribute significantly to the mass balance. This extension on previous correlation analysis serves as a stepping stone for future parameter optimisations by highlighting that good parameter optimisation is multifaceted and difficult.

8.3 Implications for nutrient recovery and crystallisation modelling

The conclusions discussed above describe the *outputs* of the work, which significantly add to the body of research within the struvite community. The real value of this work though is in the *outcome* of developing a new experimental and modelling framework which can be adapted and applied to analyse any crystallisation system. The care taken to quantify uncertainty and identify areas for improvement paves the way for future research of the same fashion to be conducted with far greater ease. This has ramifications in a number of areas.

The state of the art in industrial struvite crystallisation modelling is significantly less complex than that shown here. However, DPB modelling is not uncommon in the pharmaceuticals industry and its broader application is the next logical step in nutrient recovery kinetic modelling. As most nutrient recovery systems operate as fluidised beds, discretised Poiseuille flow could be replaced with a simpler and faster tanks in series model, where each tank represents a relatively constant region of supersaturation. Some representation of fluid mixing/turbulence in each tank could then be incorporated into the power law rate expressions for secondary nucleation and aggregation, while growth could remain independent of mixing assuming that it is reaction controlled. Kinetic parameter optimization could be achieved by sampling PSD and concentration data over a range of feed concentrations and flow rates. Once kinetic parameters capable of representing the operating conditions are found, the model could be used for PSD and recovery optimization and crystalliser design. Integration of such a model into existing frameworks may prove to be the most difficult step as it would need to be developed in a new software environment where numerical solution methods must be manually specified.

There are multiple implications for future experimental studies. Firstly, identification of a superior mixing technique (*i.e.* the vortex mixer) is important on industrial and lab scales since complete reactant mixing is necessary to achieve uniform supersaturation and resulting uniform crystal nucleation, growth and aggregation. Secondly, continuous struvite seed production, within the PSD range used for lab-scale studies, showed that methods applied here are worthy of crystalliser feasibility studies. Further work in this area would draw together existing industrial struvite seeding studies with continuous seeding work applied to other crystallisation systems where PSD control is a key objective.

A key aim in crystallisation design is to produce a PSD with desirable filterability and storage properties. Designing reactors to achieve a desired PSD requires an accurately calibrated model capable of predicting PSD as a function of process variables. This work has shown that DPB models are capable in this regard.

One major disadvantage of introducing kinetic models for nucleation, growth and aggregation is the commensurate increase in the number of unknown parameters. As discussed in Chapter 7, this results in parameter correlation where, during the optimisation process, changes in one parameter can be offset by changes in another. This reduces confidence in the applicability of regressed kinetic parameters to different experimental conditions, despite how well they may fit datasets used for their optimisation. This work highlighted that this phenomenon is very difficult to avoid and should not be ignored, lest the high variability between regressed kinetic parameters in the literature continue. Additionally, sensitivity analysis validated a logical interpretation of what nucleation and growth coefficient correlation means, which will help future interpretation of results.

The sonication method used in this work successfully separated aggregation from nucleation and growth, removing the potential correlation expected between growth and aggregation kinetic parameters, during their optimisation. This provides a precedent for future crystallisation kinetic investigations. Applying experimental and modelling techniques developed in this work to future struvite investigations may reduce some of the large range encountered in kinetics reported in the literature review.

Nucleation and growth kinetics predicted in this work were similar to those from other DPB based work on struvite when compared to the large variations observed in other kinetic modelling studies in the literature. This showed that modelling of nucleation, growth and agglomeration processes is necessary for improved accuracy in struvite crystalliser modelling. Any future simulation of the struvite system would be wise to implement at least a nucleation and crystal growth DPB.

Traditionally, primary nucleation has been assumed and high supersaturation levels avoided to limit excessive nucleation. In this work however, the estimated nucleation rate was much lower and less dependent on supersaturation than previously employed primary nucleation models. The Poiseuille flow reactor was also found to be less sensitive to nucleation kinetic parameters than those of aggregation and growth. Combining these result with the relatively high aggregation rate observed highlights the potential for reactor operation at high supersaturation to achieve fast particle size enlargement without the risk of excessive nucleation.

8.4 Recommendations for future research

It is important to continue the iterative process of improving, calibrating and validating crystallisation models. This will lead to improved understanding of crystallisation processes and better, more cost effective reactor designs. In addition, investigation of alternative reactor types is essential to achieving optimum designs. The implications discussed in 8.3 could be further realised by addressing a number of key areas discussed in detail below, namely: 1) Experimental improvements to the current work; 2) Choice of larger dataset ranges with respect to supersaturation and mixing regimes; 3) Experimental investigations of Poiseuille flow reactors and combined continuous seeding and growth reactors; and 4) advancement in modelling techniques.

<u>Experimental improvements:</u>

1. Many PSD measurements in this work were deemed unacceptable because of insufficient particle concentrations. This can be dealt with by either concentrating particles in samples or using PSD measurement techniques that better accommodate low particle concentration, for example single particle optical sizing (SPOS). One advantage of SPOS is that is quantifies particle number concentrations, the property directly predicted by PBMs. This enables a more direct method of model calibration. Another advantage (of SPOS) is its ability to provide more information about properties of non-spherical particles, enabling improved aggregation modelling.

2. Flow restriction due to crystal scaling around the orifice separating the mixer from the main reactor was observed in this work. Future work should utilise a constant diameter from mixer to reactor outlet to avoid this issue. Alternatively, plug flow could be as it could achieve reactor scouring velocities.
3. Probe encrustation caused pH measurement response times to become unacceptably large (>5min), rendering pH measurements essentially useless. Future work can improve *in-situ* pH measurement by using a flow cell or shroud to reduce the impact of probe encrustation on response time and accuracy. Alternatively, a process type probe suitable for crystallisation systems should be sought, although care must be taken to ensure probe accuracy.

Data Collection/ Validation:

4. Nucleation and growth rate coefficients regressed in this work showed a correlation coefficient of$R = -0.91$, coming very close to being classified as highly correlated (>0.95). This can be countered by collecting a wider range of PSD and phosphorus recovery data. It is suggested that data be collected for supersaturations between *SI* = 0.1 and 1.4 to capture the ‘null supersaturation’ range proposed by various authors (section 2.2.4.5), while not creating needle-like crystals. Data should be collected throughout the entire course of reaction, to show distinctly different aspects of kinetic mechanisms. This will require techniques suitable for low particle concentration PSD measurement, as discussed above. It may also be worth considering seeded experiments that measure only a secondary nucleation rate as this appears to become dominant over primary nucleation anyway.

Further experimental investigations:

5. The literature presented very little work investigating the effects of struvite seed PSD and seed loading rate on final PSD from a growth reactor (Chapter 2). This information is pre-requisite to seed reactor designs and investigations of combined seeding and growth reactors. As such tests

should be conducted examining the effects of seed PSD variations on crystal output variations at a variety of *SI* levels (ideally *SI* = 0.8, 1.0 and 1.4 for comparison to this work). These results would also be useful for kinetic parameter optimisations.

6. This research has shown that a Poiseuille flow crystalliser is able to produce struvite with a PSD suitable for seeding. Subject to studies mentioned in point 5 above, the Poiseuille flow reactor should be examined to identify its suitability as a control actuator for PSD in a subsequent growth reactor. This could be achieved by operating at steady state and introducing a step change in seed reactor feed conditions.
7. Fluid sheer was identified as a key variable likely to account for the inability to regress kinetic parameters which fit data from two different reactor types (discussed throughout Chapter 7). Further work must be done to investigate the impact of fluid shear on each kinetic mechanism so it can be incorporated into kinetic models. This can be achieved utilising any reactor with a well-defined fluid shear rate (*e.g.* Poiseuille flow or Taylor-Couette flow).
8. As discussed in section 8.3, nucleation rates were lower than expected from primary nucleation models and the PFR outputs were less sensitive to nucleation parameters than aggregation parameters, even at high supersaturation levels. Therefore, at high supersaturation, nuclei may be able to be incorporated into aggregates and fast formation of enlarged particles may be possible. This warrants investigations of struvite crystallisation at supersaturation levels exceeding those examined in this work (SI>1.4), and up to the maximum supersaturation level examined in other work (SI<4).

Modelling:

9. Model Structure: The reactor model developed in Chapter 4 assumed that no nucleation occurred within the entry length, although scaling evident in the mixer (section 5.5) suggests otherwise. Particulate processes can be modelled in this region provided some description of fluid flow is

developed. This could be achieved simply (though roughly) by modelling the transition zone, where Poiseuille flow is developing, as a well-mixed volume.

10. Model Assumptions:
    i. The literature review reveals that the majority of struvite kinetic investigations have utilised solutions containing only the species necessary for struvite crystallisation. To enable kinetic modelling of real-life systems, the thermodynamic model must include species encountered in real waste streams, such as urine. These included carbonate, potassium and calcium. Inclusion of these species would also require the inclusion of the potential solid phases and their associated kinetic models (which may not exist).
    ii. Settling was shown to play a significant role in the Poiseuille flow reactor, both experimentally and in modelling. The settling model used in this work assumed spherical particles. However, individual particles were not spherical and aggregate particles were irregular and porous. As such, future work should extend the settling model to represent non-spherical particles.
    iii. This work showed that secondary nucleation was likely dominant. Primary nucleation however, still plays a significant role. Future modelling work should consider implementing parallel primary and secondary nucleation mechanisms. Note though that introducing another level of complexity to the model would lead to over-parameterisation.
    iv. Extend particle aggregation description to include porosity, fractal dimension, collision efficiency and bond strength. This work identified growth of aggregate constituent particles after aggregation and regressed an aggregation rate significantly higher than expected as a result of overestimation of aggregate mass. Together these results suggest that porosity must be accounted for to accurately model aggregation and subsequent agglomeration.
11. Numerical Improvements:

i. A steady state numerical solution for the PFR process (algebraic) model could not be achieved in this work. Instead, the dynamic model had to be solved to a steady state. Achieving a steady state solution would significantly reduce simulation times, making the parameter optimisation process much faster and easier to troubleshoot. This must be done by obtaining steady state solutions for each model sub-section (mass balance, population balance, thermodynamics) and progressively combining these models.
ii. A limitation of this work was the significant time required to solve the CAT DPB incorporating aggregation. It is anticipated that simulation times could be vastly reduced with increased control over numerical solution methods. This can be achieved by implementing the solution in an alternative software package, for example MATLAB. Take note, though, that this would require the development of new parameter optimisation techniques.

Bibliography

Aage, H., Andersen, B. L., Blom, A., & Jensen, I. (1997). The solubility of struvite in urine. *Journal of Radioanalytical and Nuclear Chemistry*, *223*(1–2), 213–215.

Aamir, E., Nagy, Z. K., & Rielly, C. D. (2010). Optimal seed recipe design for crystal size distribution control for batch cooling crystallisation processes. *Chemical Engineering Science*, *65*(11), 3602–3614. http://doi.org/10.1016/j.ces.2010.02.051

Abbona, F., & Boistelle, R. (1985). Nucleation of Struvite (MgNH4PO4.6H2O) Single Crystals and Aggregates. *Crystal Research and Technology*. http://doi.org/10.1007/s00251-011-0563-3

Adamson, A. W., & Gast, A. P. (1997). *Physical Chemistry of Surfaces* (6th ed.). John Wiley & Sons, Inc.

Adnan, A., Mavinic, D. S., & Koch, F. A. (2003). Pilot-scale study of phosphorus recovery through struvite crystallisation examining the process feasibility. *Journal of Environmental Engineering and Science*, *2*(5), 315–324. http://doi.org/10.1139/s03-040

Ahmed, S., Klassen, T. N., Keyes, S., Daly, M., Jones, D. L., Mavrogordato, M., … Roose, T. (2015). Imaging the interaction of roots and phosphate fertiliser granules using 4D X-ray tomography. *Plant and Soil*. http://doi.org/10.1007/s11104-015-2425-5

Alexopoulos, A. H., & Kiparissides, C. A. (2005). Part II : Dynamic evolution of the particle size distribution in particulate processes undergoing simultaneous particle nucleation , growth and aggregation. *Chemical Engineering Science*, *60*, 4157–4169. http://doi.org/10.1016/j.ces.2005.02.052

Ali, M. I., & Schneider, P. A. (2008a). An approach of estimating struvite growth kinetic incorporating thermodynamic and solution chemistry, kinetic and process description. *Chemical Engineering*

Science.

Ali, M. I., Schneider, P. A., & Hudson, N. (2005). Thermodynamics and solution chemistry of struvite. *Journal of the Indian Institute of Science*, *85*(May-June), 141–149.

Ali, & Schneider, P. A. (2008b). An approach of estimating struvite growth kinetic incorporating thermodynamic and solution chemistry , kinetic and process description. *Chemical Engineering Science*, *63*, 3514–3525.

Alison, H. G., Davey, R. J., Garside, J., Quayle, M. J., Tiddy, G. J. T., Clarke, D. T., & Jones, G. R. (2003). Using a novel plug flow reactor for the in situ, simultaneous, monitoring of SAXS and WAXD during crystallisation from solution. *Physical Chemistry Chemical Physics*, *5*(22), 4998. http://doi.org/10.1039/b309309c

Alvarez, A. J., & Myerson, A. S. (2010). Continuous Plug Flow Crystallisation of Pharmaceutical Compounds. *Crystal Growth & Design*, *10*(5), 2219–2228. http://doi.org/10.1021/cg901496s

APHA, AWWA, & WEF. (1999). *Standard Methods for the Examination of Water and Wastewater*.

Ariyanto, E., Sen, T. K., & Ang, H. M. (2014). The influence of various physico-chemical process parameters on kinetics and growth mechanism of struvite crystallisation. *Advanced Powder Technology*, *25*(2), 682–694. http://doi.org/10.1016/j.apt.2013.10.014

Ashley, K., Cordell, D., & Mavinic, D. (2011). A brief history of phosphorus: from the philosopher's stone to nutrient recovery and reuse. *Chemosphere*, *84*(6), 737–46. http://doi.org/10.1016/j.chemosphere.2011.03.001

Babler, M. U. (2008). A Collision Efficiency Model for Flow-Induced Coagulation of Fractal Aggregates. *AIChE*, *54*(7), 1748–1760. http://doi.org/10.1002/aic

Balakin, B. V, Hoffmann, A. C., & Kosinski, P. (2010). Population Balance Model for Nucleation, Growth, Aggregation, and Breakage of Hydrate Particles in Turbulent Flow, *56*(8).

http://doi.org/10.1002/aic

Band, L. R., Cummings, L. J., Waters, S. L., & Wattis, J. a D. (2009). Modelling crystal aggregation and deposition in the catheterised lower urinary tract. *Journal of Mathematical Biology*, *59*(6), 809–40. http://doi.org/10.1007/s00285-009-0253-z

Battistoni, P., De Angelis, A., Prisciandaro, M., Boccadoro, R., & Bolzonella, D. (2002). P removal from anaerobic supernatants by struvite crystallisation: long term validation and process modelling. *Water Research*, *36*(8), 1927–1938. Retrieved from http://www.sciencedirect.com/science/article/B6V73-443K08H-2/2/cfdcd64ec5b26fe4145c2d8174171bf2

Battistoni, P., Paci, B., Fatone, F., & Pavan, P. (2005). Phosphorus Removal from Supernatants at Low Concentration Using Packed and Fluidised-Bed Reactors. *American Chemical Society*, 6701–6707.

Battistoni, P., Paci, B., Fatone, F., & Pavan, P. (2006). Phosphorus Removal from Anaerobic Supernatants: Start-Up and Steady-State Conditions of a Fluidised Bed Reactor Full-Scale Plant. *American Chemical Society*, (1), 663–669.

BBC News Africa. (2014). Western Sahara Profile. Retrieved September 1, 2015, from http://www.bbc.com/news/world-africa-14115273

Berazneva, J., & Lee, D. R. (2013). Explaining the African food riots of 2007–2008: An empirical analysis. *Food Policy*, *39*, 28–39. http://doi.org/10.1016/j.foodpol.2012.12.007

Bhuiyan, M. I. H., & Mavinic, D. S. (2008). Assessing struvite precipitation in a pilot-scale fluidised bed crystalliser. *Environmental Technology*, *29*(11), 1157–67. http://doi.org/10.1080/09593330802075452

Bhuiyan, M. I. H., Mavinic, D. S., & Beckie, R. D. (2007). A solubility and thermodynamic study of struvite. *Environmental Technology*, *28*(9), 1015–26. http://doi.org/10.1080/09593332808618857

Bhuiyan, M. I. H., Mavinic, D. S., & Beckie, R. D. (2008). Nucleation and growth kinetics of struvite in a fluidised bed reactor. *Journal of Crystal Growth*, *310*(6), 1187–1194. Retrieved from http://www.sciencedirect.com/science/article/B6TJ6-4RGFN28-4/2/5e57338f3b77517e38cf45a8c7587c93

Bhuiyan, M. I. H., Mavinic, D. S., & Beckie, R. D. (2009). Dissolution kinetics of struvite pellets grown in a pilot-scale struvite crystalliser. *Canadian Journal of Civil Engineering*, *36*, 550–558.

Binev, D., Seidel-Morgenstern, a., & Lorenz, H. (2015). Study of crystal size distributions in a fluidised bed crystalliser. *Chemical Engineering Science*, *133*, 116–124. http://doi.org/10.1016/j.ces.2014.12.041

Bouropoulos, N. C., & Koutsoukos, P. G. (2000). Spontaneous precipitation of struvite from aqueous solutions. *Journal of Crystal Growth*, *213*(3–4), 381–388. Retrieved from http://www.sciencedirect.com/science/article/B6TJ6-40BPPFH-S/2/0d57e58db7c73c587ceb47a48155f204

Bramley, A., Hounslow, M., & Ryall, R. (1997). Aggregation during precipitation from solution. Kinetics for calcium oxalate monohydrate. *Chemical Engineering Science*, *52*(5), 747–757. Retrieved from http://www.sciencedirect.com/science/article/pii/S0009250996004472

Bramley, A. S. (1994). *A Study of the Growth and Aggregation of Calcium Oxalate Monohydrate*. University of Adelaide.

Bramley, A. S., Hounslow, M. J., Newman, R., & Paterson, W. R. (1997). THE ROLE OF SOLUTION COMPOSITION ON AGGREGATION DURING PRECIPITATION. *Institution of Chemical Engineers*, *75*(A), 119–124.

Britton, A., Koch, F., Mavinic, D., Adnan, A., Oldham, W., & Udala, B. (2005). Pilot-scale struvite recovery from anaerobic digester supernatant at an enhanced biological phosphorus removal wastewater treatment plant. *Journal of Environmental Engineering and Science*, *4*(4), 265–277. http://doi.org/10.1139/s04-059

Buchanan, J. R., Mote, C. R., & Robinson, R. B. (1994). Thermodynamics of struvite formation. *Society*, *3*(1), 617–621.

Burns, J. R., & Finlayson, B. (1982). Solubility product of magnesium ammonium phosphate hexahydrate at various temperatures. *Journal of Urology*, *128*(2), 426–428. Retrieved from http://www.scopus.com/inward/record.url?eid=2-s2.0-0019959398&partnerID=40&md5=df02d055b4204b9ae2c8221a86d81c39

Burton, W. K., Cabrera, N., & Frank, N. C. (1951). The Growth of Crystals and the Equilibrium Structure of their Surfaces. *Philosophical Transactions*, *A243*, 299–358.

Celen, I., Buchanan, J. R., Burns, R. T., Bruce Robinson, R., & Raj Raman, D. (2007). Using a chemical equilibrium model to predict amendments required to precipitate phosphorus as struvite in liquid swine manure. *Water Research*, *41*(8), 1689–1696. Retrieved from http://www.sciencedirect.com/science/article/B6V73-4N6FNS8-2/2/bfd50c429b7376ec6cd498f3e44ceddc

Chauhan, C. K., Joseph, K. C., Parekh, B. B., & Joshi, M. J. (2008). Growth and characterisation of struvite crystals. *Indian Journal of Pure & Applied Physics*, *46*(July), 507–512.

Cooper, J., Lombardi, R., Boardman, D., & Carliell-Marquet, C. (2011). The future distribution and production of global phosphate rock reserves. *Resources, Conservation and Recycling*, *57*(January), 78–86. http://doi.org/10.1016/j.resconrec.2011.09.009

Cordell, D., Drangert, J.-O., & White, S. (2009). The story of phosphorus: Global food security and food for thought. *Global Environmental Change*, *19*(2), 292–305. http://doi.org/10.1016/j.gloenvcha.2008.10.009

Cordell, D., Neset, T.-S. S., & Prior, T. (2012). The phosphorus mass balance: identifying “hotspots” in the food system as a roadmap to phosphorus security. *Current Opinion in Biotechnology*, *23*(6), 839–45. http://doi.org/10.1016/j.copbio.2012.03.010

Corell, H. (2002). *United Nations Security Council - Letter dated 29 January 2002 from the Under-Secretary-General for Legal Affairs, the Legal Counsel, addressed to the President of the Security Council* (Vol. 24987).

Costanza, R., de Groot, R., Sutton, P., van der Ploeg, S., Anderson, S. J., Kubiszewski, I., … Turner, R. K. (2014). Changes in the global value of ecosystem services. *Global Environmental Change*, *26*, 152–158. http://doi.org/10.1016/j.gloenvcha.2014.04.002

David, R., Paulaime, A., Espitalier, F., & Rouleau, L. (2003). Modelling of multiple-mechanism agglomeration in a crystallisation process. *Powder Technology*, *130*, 338–344.

Davies. (1932). The Constant a in the DeBye-Huckel Limiting Equation, *54*, 1698–1699.

Dumas, M., Frossard, E., & Scholz, R. W. (2011). Modeling biogeochemical processes of phosphorus for global food supply. *Chemosphere*, *84*(6), 798–805. http://doi.org/10.1016/j.chemosphere.2011.02.039

Eder, R. J. P., Schmitt, E. K., Grill, J., Radl, S., Gruber-Woelfler, H., & Khinast, J. G. (2011). Seed loading effects on the mean crystal size of acetylsalicylic acid in a continuous-flow crystallisation device. *Crystal Research and Technology*, *46*(3), 227–237. http://doi.org/10.1002/crat.201000634

Fattah, K. P., Mavinic, D. S., Koch, F. A., & Jacob, C. (2008). Determining the feasibility of phosphorus recovery as struvite from filter press centrate in a secondary wastewater treatment plant, (907464858). http://doi.org/10.1080/10934520801960052

Ferguson, S., Morris, G., Hao, H., Barrett, M., & Glennon, B. (2012). In-situ monitoring and characterisation of plug flow crystallisers. *Chemical Engineering Science*, *77*, 105–111.

http://doi.org/10.1016/j.ces.2012.02.013

Forrest, a. L., Fattah, K. P., Mavinic, D. S., & Koch, F. a. (2008). Optimising Struvite Production for Phosphate Recovery in WWTP. *Journal of Environmental Engineering*, *134*(5), 395–402. http://doi.org/10.1061/(ASCE)0733-9372(2008)134:5(395)

Galbraith, S. C. (2011). A Study of Struvite Nucleation , Crystal Growth and Aggregation, (November).

Galbraith, S. C., & Schneider, P. A. (2009a). A review of struvite nucleation studies. In *International Conference on Nutrient Recovery* (pp. 69–78).

Galbraith, S. C., & Schneider, P. A. (2014). Modelling and simulation of inorganic precipitation with nucleation, crystal growth and aggregation: A new approach to an old method. *Chemical Engineering Journal*, *240*, 124–132. http://doi.org/10.1016/j.cej.2013.11.070

Galbraith, S. C., Schneider, P. A., & Flood, A. E. (2014). Model-driven experimental evaluation of struvite nucleation, growth and aggregation kinetics. *Water Research*, *56C*, 122–132. http://doi.org/10.1016/j.watres.2014.03.002

Galbraith, & Schneider. (2009b). A review of struvite nucleation studies. *International Conference on Nutrient Recovery from Wastewater Streams. Vancouver, Canada: IWA Publishing*, (1), 69–78.

Garside, J., Rusli, I. T., & Larson, M. A. (1979). Origin and size distribution of secondary nuclei. *AIChE Journal*, *25*(1), 57–64. http://doi.org/10.1002/aic.690250107

Gillian, J. M., & Kirwan, D. J. (2008). Identification and Correlation of Mixing Times in Opposed-Jet Mixers. *Chemical Engineering Communications*, *195*(12), 1553–1574. http://doi.org/10.1080/00986440802115614

Golubev, S. V., Pokrovsky, O. S., & Savenko, V. S. (2001). Homogeneous precipitation of magnesium phosphates from seawater solutions. *Journal of Crystal Growth*, *223*(4), 550–556. http://doi.org/10.1016/S0022-0248(01)00681-9

Hacherl, J. M., Paul, E. L., & Buettner, H. M. (2003). Investigation of impinging-jet crystallisation with a calcium oxalate model system. *AIChE Journal*, *49*(9), 2352–2362. http://doi.org/10.1002/aic.690490911

Hanhoun, M., Montastruc, L., Azzaro-pantel, C., Biscans, B., Frèche, M., & Pibouleau, L. (2011). Temperature impact assessment on struvite solubility product : A thermodynamic modeling approach. *Chemical Engineering Journal*, *167*(1), 50–58. http://doi.org/10.1016/j.cej.2010.12.001

Hanhoun, M., Montastruc, L., Azzaro-Pantel, C., Biscans, B., Frèche, M., & Pibouleau, L. (2013). Simultaneous determination of nucleation and crystal growth kinetics of struvite using a thermodynamic modeling approach. *Chemical Engineering Journal*, *215–216*, 903–912. http://doi.org/10.1016/j.cej.2012.10.038

Harada, H., Shimizu, Y., Miyagoshi, Y., Matsui, S., Matsuda, T., & Nagasaka, T. (2006). Predicting struvite formation for phosphorus recovery from human urine using an equilibrium model. *Water Science and Technology*, *54*(8), 247–255. http://doi.org/10.2166/wst.2006.720

Harrison, M. L., Johns, M. R., White, E. T., & Mehta, C. M. (2011). Growth rate kinetics for struvite crystallisation. *Chemical Engineering Transactions*, *25*, 309–314. http://doi.org/10.3303/CET1125052

Henderson, R., Sharp, E., Jarvis, P., Parsons, S., & Jefferson, B. (2006). Identifying the linkage between particle characteristics and understanding coagulation performance. *Water Science and Technology: Water Supply*. Retrieved from http://www.scopus.com/inward/record.url?eid=2-s2.0-33744489650&partnerID=40&md5=9d2e8566355c1a17a7a50621ce20f0ed

Hiemenz, P. C., & Rajagopalan, R. (1997). *Principles of Colloid and Surface Chemistry* (3rd ed.). CRC Press.

Hounslow, M. J. (1990a). *A Discretised Population Balance for Nucleation, Growth and Aggregation*. University of Adelaide.

Hounslow, M. J. (1990b). *A discretised population balance for simultaneous nucleation, growth and aggregation*. University of Adelaide, South Australia.

Hounslow, M. J., Bramley, A. S., & Paterson, W. R. (1998). Aggregation During Precipitation from Solution . A Pore Diffusion – Reaction Model for Calcium Oxalate Monohydrate. *Water*, *391*(203), 383–391.

Hounslow, M. J., Wynn, E. J. W., Kubo, M., & Pitt, K. (2013). Aggregation of growing crystals in suspension: I. Mumtaz revisited. *Chemical Engineering Science*, *101*, 731–743. http://doi.org/10.1016/j.ces.2013.06.058

Hounslow, M., Mumtaz, H., Collier, A., Barrick, J., & Bramley, A. (2001). A micro-mechanical model for the rate of aggregation during precipitation from solution. *Chemical Engineering Science*, *56*(7), 2543–2552. Retrieved from http://www.sciencedirect.com/science/article/pii/S000925090000436X

Huang, H., Mavinic, D. S., Lo, K. V, & Koch, F. A. (2005). Production and Basic Morphology of Struvite Crystals from a Pilot-Scale Crystallisation Process. *Environmental Technology*, *27*, 233–245.

Hunter, R. J. (2001). *Foundations of Colloid Science*. Oxford University Press Inc., New York.

Hutnik, N., Piotrowski, K., Wierzbowska, B., & Matynia, A. (2011). Continuous reaction crystallisation of struvite from phosphate (V) solutions containing calcium ions. *Evolution*, *449*(5), 443–449. http://doi.org/10.1002/crat.201100049

Ilievski, D. (1991). *Modelling Al(OH)3 Agglomeration during Batch and Continuous Precipitation in Supersaturated Caustic Aluminate Solutions*. University of Queensland.

Ilievski, D. (2001). Development and application of a constant supersaturation, semi-batch crystalliser for investigating gibbsite agglomeration. *Journal of Crystal Growth*, *233*(4), 846–862. http://doi.org/10.1016/S0022-0248(01)01640-2

Jaffer, Y., Clark, T. A., Pearce, P., & Parsons, S. A. (2002). Potential phosphorus recovery by struvite formation. *Water Research*, *36*(7), 1834–1842. Retrieved from http://www.sciencedirect.com/science/article/B6V73-45J85RK-M/2/ce8f2e8e58b53e28c2f70f6b2a1038b7

Jiang, M., Wong, M. H., Zhu, Z., Zhang, J., Zhou, L., Wang, K., … Braatz, R. D. (2012). Towards achieving a flattop crystal size distribution by continuous seeding and controlled growth. *Chemical Engineering Science*, *77*, 2–9. http://doi.org/10.1016/j.ces.2011.12.033

Jones, A. G. (2002). *Crystallisation Process Systems*. Butterworth Heinemann.

Kabdasli, I., Parsons, S. A., & Tunay, O. (2006). Effect of Major Ions on Induction Time of Struvite Precipitation. *Croatia Chemica ACTA*, *79*(2), 243–251.

Kataki, S., West, H., Clarke, M., & Baruah, D. C. (2016a). Phosphorus recovery as struvite: Recent concerns for use of seed, alternative Mg source, nitrogen conservation and fertiliser potential. *Resources, Conservation and Recycling*, *107*, 142–156. http://doi.org/10.1016/j.resconrec.2015.12.009

Kataki, S., West, H., Clarke, M., & Baruah, D. C. (2016b). Phosphorus recovery as struvite from farm, municipal and industrial waste: Feedstock suitability, methods and pre-treatments. *Waste Management*, *49*, 437–454. http://doi.org/10.1016/j.wasman.2016.01.003

Kelly, R. N., & Kazanjian, J. (2006). Commercial reference shape standards use in the study of particle shape effect on laser diffraction particle size analysis. *AAPS PharmSciTech*, *7*(2), E49. http://doi.org/10.1208/pt070249

Kim, D., Ryu, H.-D., Kim, M.-S., Kim, J., & Lee, S.-I. (2007). Enhancing struvite precipitation potential for ammonia nitrogen removal in municipal landfill leachate. *Journal of Hazardous Materials*, *146*(1–2), 81–85. Retrieved from http://www.sciencedirect.com/science/article/B6TGF-4MGDYX6-

1/2/1eac2fa9c6cebb8dbf112dbf2a1ecdb1

Klare, M. (2012). *The Race For What's Left: The Global Scramble for the World's Last Resources*.

Kofina, A. N., & Koutsoukos, P. G. (2005). Spontaneous precipitation of struvite from synthetic wastewater solutions. *Crystal Growth and Design*, *5*(2), 489–496. http://doi.org/10.1021/cg049803e

Kofina, a. N., & Koutsoukos, P. G. (2005). Spontaneous Precipitation of Struvite from Synthetic Wastewater Solutions. *Crystal Growth & Design*, *5*(2), 489–496. http://doi.org/10.1021/cg049803e

Kohonen, J., Reinikainen, S.-P., & Höskuldsson, A. (2009). Block-based approach to modelling of granulated fertilisers' quality. *Chemometrics and Intelligent Laboratory Systems*, *97*(1), 18–24. http://doi.org/10.1016/j.chemolab.2008.06.015

Koralewska, J., Piotrowski, K., Wierzbowska, B., & Matynia, A. (2007). Reaction-Crystallisation of Struvite in a Continuous Liquid Jet-Pump DTM MSMPR Crystalliser with Upward Circulation of Suspension in a Mixing Chamber – an SDG Kinetic Approach. *Chemical Engineering & Technology*, *30*(11), 1576–1583. http://doi.org/10.1002/ceat.200700229

Koralewska, J., Piotrowski, K., Wierzbowska, B., & Matynia, A. (2009). Kinetics of Reaction-Crystallisation of Struvite in the Continuous Draft Tube Magma Type Crystallisers—Influence of Different Internal Hydrodynamics. *Chinese Journal of Chemical Engineering*, *17*(2), 330–339. http://doi.org/10.1016/S1004-9541(08)60212-8

Korchef, A., Saidou, H., & Ben Amor, M. (2011). Phosphate recovery through struvite precipitation by CO2 removal: effect of magnesium, phosphate and ammonium concentrations. *Journal of Hazardous Materials*, *186*(1), 602–13. http://doi.org/10.1016/j.jhazmat.2010.11.045

Kozik, A., Hutnik, N., Piotrowski, K., & Matynia, A. (2014). Continuous reaction crystallisation of struvite from diluted aqueous solution of phosphate(V) ions in the presence of magnesium ions excess.

Chemical Engineering Research and Design, *92*(3), 481–490. http://doi.org/10.1016/j.cherd.2013.08.032

Kumar, J. (2006). *Numerical approximations of population balance equations in particulate systems*. Otto-von-Guericke-Universitat Magdeburg.

Kumar, J., Peglow, M., Warnecke, G., & Heinrich, S. (2008). An efficient numerical technique for solving population balance equation involving aggregation , breakage , growth and nucleation. *Powder Technology*, *182*, 81–104. http://doi.org/10.1016/j.powtec.2007.05.028

Kumar, R., & Pal, P. (2015). Assessing the feasibility of N and P recovery by struvite precipitation from nutrient-rich wastewater: a review. *Environmental Science and Pollution Research*, 17453–17464. http://doi.org/10.1007/s11356-015-5450-2

Kumar, S., & Ramkrishna, D. (1996a). On The Solution of Population Balance Equations by Discretisation - A Fixed Pivot Technique. *Chemical Engineering*, *51*(8), 1311–1332.

Kumar, S., & Ramkrishna, D. (1996b). On the Solution of Population Balance Equations by Discretisation - II. A Moving Pivot Technique. *Chemical Engineering Science*, *51*(8), 1333–1342.

Kumar, S., & Ramkrishna, D. (1997). On the solution of population balance equations by discretisation--lll. Nucleation, growth and aggregation of particles. *Chemical Engineering Science*, *52*(24), 4659–4679.

Kusters, K. a., Wijers, J. G., & Thoenes, D. (1997). Aggregation kinetics of small particles in agitated vessels. *Chemical Engineering Science*, *52*(1), 107–121. http://doi.org/10.1016/S0009-2509(96)00375-2

Lahav, O., Telzhensky, M., Zewuhn, A., Gendel, Y., Gerth, J., Calmano, W., & Birnhack, L. (2013). Struvite recovery from municipal-wastewater sludge centrifuge supernatant using seawater NF concentrate as a cheap Mg(II) source. *Separation and Purification Technology*, *108*, 103–110.

http://doi.org/10.1016/j.seppur.2013.02.002

Larson, M. A., & Bendig, L. L. (1976). NUCLEI GENERATION FROM REPETITIVE CONTACTING. *AIChE Symposium Series*, *72*(153), 21–27. Retrieved from http://www.scopus.com/inward/record.url?eid=2-s2.0-0016890876&partnerID=40&md5=0826c8f90044f9fba157dc080e2625da

Le Corre, K. S., Hobbs, P., & Parsons, S. A. (2007a). Kinetics of Struvite Precipitation: Effect of the Magnesium Dose on Induction Times and Precipitation Rates. *Environmental Technology*, (September 2011), 37–41.

Le Corre, K. S., Hobbs, P., & Parsons, S. A. (2007b). Kinetics of Struvite Precipitation: Effect of the Magnesium Dose on Induction Times and Precipitation Rates. *Environmental Technology*, (September 2011), 37–41. http://doi.org/10.1080/09593332808618891

Le Corre, K. S., Valsami-Jones, E., Hobbs, P., Jefferson, B., & Parsons, S. A. (2007a). Agglomeration of struvite crystals. *Water Research*, *41*(2), 419–425. Retrieved from http://www.sciencedirect.com/science/article/B6V73-4MG1NT3-2/2/83c28b381e2aa1c9375ec933bd0f8cf8

Le Corre, K. S., Valsami-Jones, E., Hobbs, P., & Parsons, S. A. (2007b). Kinetics of struvite precipitation: Effect of the Magnesium Dose on Induction Times and Precipitation Rates. *Environmental Technology*, *28*(12), 1317–1324. http://doi.org/10.1080/09593332808618891

Le Corre, K. S., Valsami-Jones, E., Hobbs, P., & Parsons, S. A. (2009). Phosphorus Recovery from Wastewater by Struvite Crystallisation : A Review. *Environmental Science & Technology*, (907464858). http://doi.org/10.1080/10643380701640573

Levenspiel, O. (1999). *Chemical Reaction Engineering* (3rd ed.). Wiley.

Lew, B., Phalah, S., Sheindorf, C., Kummel, M., Rebhun, M., & Lahav, O. (2010). Favorable Operating

Conditions for Obtaining High-Value Struvite Product from Sludge Dewatering Filtrate. *Environmental Engineering Science*, *27*(9), 733–741. http://doi.org/10.1089/ees.2009.0279

Lewis, A. H. (1906). The Day of Discontent. *Cosmopolitan Magazine*, 603.

Liew, B. T. L., Barrick, J. P., & Hounslow, M. J. (2003). A Micro-Mechanical Model for the Rate of Aggregation during Precipitation from Solution. *Chemical Engineering & Technology*, *26*(3), 282–285.

Lindenberg, C., & Mazzotti, M. (2009). Experimental characterisation and multi-scale modeling of mixing in static mixers. Part 2. Effect of viscosity and scale-up. *Chemical Engineering Science*, *64*(20), 4286–4294. http://doi.org/10.1016/j.ces.2009.06.067

Lindenberg, C., Schöll, J., Vicum, L., Mazzotti, M., & Brozio, J. (2008). Experimental characterisation and multi-scale modeling of mixing in static mixers. *Chemical Engineering Science*, *63*(16), 4135–4149. http://doi.org/10.1016/j.ces.2008.05.026

Liu, Y., Cheng, C., Prud’homme, R. K., & Fox, R. O. (2008). Mixing in a multi-inlet vortex mixer (MIVM) for flash nano-precipitation. *Chemical Engineering Science*, *63*(11), 2829–2842. http://doi.org/10.1016/j.ces.2007.10.020

Livk, I., & Ilievski, D. (2007). A macroscopic agglomeration kernel model for gibbsite precipitation in turbulent and laminar flows. *Chemical Engineering Science*, *62*, 3787–3797. http://doi.org/10.1016/j.ces.2007.03.030

Lizarralde, I., Fernández-Arévalo, T., Brouckaert, C., Vanrolleghem, P., Ikumi, D. S., Ekama, G. A., … Grau, P. (2015). A new general methodology for incorporating physico-chemical transformations into multi-phase wastewater treatment process models. *Water Research*, *74*, 239–256. http://doi.org/10.1016/j.watres.2015.01.031

Lobanov, S. (2009). Struvite Reaction-Crystallisation as Applied to Wastewater Treatment Technology to

Remove Ammonium Ions. In *International Conference on Nutrient Recovery from Wastewater Streams*.

Matynia, A., Koralewska, J., & Wierzbowska, B. (2006). The Influence of Process Parameters on Struvite Continuous Crystallisation Kinetics. *Chemical Engineering Communications*, *193*(2001), 160–176. http://doi.org/10.1080/009864490949008

Maurer, M., Pronk, W., & Larsen, T. a. (2006). Treatment processes for source-separated urine. *Water Research*, *40*(17), 3151–66. http://doi.org/10.1016/j.watres.2006.07.012

Mazienczuk, A., Matynia, A., Piotrowski, K., & Wierzbowska, B. (2012). Reaction crystallisation of struvite in a continuous draft tube magma (DTM) crystalliser with a jet pump driven by recirculated mother solution. *Procedia Engineering*, *42*(August), 1540–1551. http://doi.org/10.1016/j.proeng.2012.07.547

Mehta, C. M., & Batstone, D. J. (2013). Nucleation and growth kinetics of struvite crystallisation. *Water Research*, *47*(8), 2890–900. http://doi.org/10.1016/j.watres.2013.03.007

Mehta, C. M., Khunjar, W. O., Nguyen, V., Tait, S., & Batstone, D. J. (2014). Technologies to Recover Nutrients from Waste Streams: A Critical Review. *Critical Reviews in Environmental Science and Technology*, *45*(4), 385–427. http://doi.org/10.1080/10643389.2013.866621

Melis, S., Verduyn, M., Storti, G., Morbidelli, M., & Baldyga, J. (1999). Effect of fluid motion on the aggregation of small particles subject to interaction forces. *AIChE Journal*, *45*(7), 1383–1393. Retrieved from http://onlinelibrary.wiley.com/doi/10.1002/aic.690450703/abstract

Mersmann, A., Braun, B., & Löffelmann, M. (2002). Prediction of crystallisation coefficients of the population balance. *Chemical Engineering Science*, *57*(20), 4267–4275. http://doi.org/10.1016/S0009-2509(02)00343-3

Mitrović, M. M., Žekić, A. a., & Baroš, Z. Z. (2008). Growth rate changes of sodium chlorate crystals independent of growth conditions. *Chemical Physics Letters*, *464*(1–3), 38–41. http://doi.org/10.1016/j.cplett.2008.08.104

Mitrovic, M. M., Zekic, A. A., & Iiic, Z. Z. (2002). Connection between the growth rate distribution and the size dependent crystal growth, *361*(July), 312–316.

Mittal, A. (2009). The 2008 Food Price Crisis: Rethinking Food Security Policies, (56).

Morales, N., Boehler, M. A., Buettner, S., Liebi, C., & Siegrist, H. (2013). Recovery of N and P from Urine by Struvite Precipitation Followed by Combined Stripping with Digester Sludge Liquid at Full Scale. *Water*, *5*, 1262–1278.

Mullin, J. W. (2001). *Crystallisation* (Fourth Edi). Butterworth-Heinemann.

Mumtaz, H., Hounslow, M., Seaton, N., & Paterson, W. (1997). Orthokinetic aggregation during precipitation: A computational model for calcium oxalate monohydrate. *Chemical Engineering Research and Design*, *75*(2), 152–159. Retrieved from http://www.sciencedirect.com/science/article/pii/S0263876297715119

Mumtaz, H. S., & Hounslow, M. J. (2000). Aggregation during precipitation from solution : an experimental investigation using Poiseuille flow, *55*, 5671–5681.

Munson, B. R., Young, D. F., & Okiishi, T. H. (2006). *Fundamentals of Fluid Mechanics* (Fifth). John Wiley & Sons, Inc.

Musvoto, E. V, Wentzel, M. C. M., Loewenthal, R. E., & Ekama, G. A. M. (2000). INTEGRATED CHEMICAL ± PHYSICAL PROCESSES MODELLING - I. DEVELOPMENT OF A KINETIC-BASED MODEL FOR MIXED WEAK ACID / BASE SYSTEMS, *34*(6).

Nagy, Z. K., & Aamir, E. (2012). Systematic design of supersaturation controlled crystallisation processes for shaping the crystal size distribution using an analytical estimator. *Chemical Engineering Science*, *84*, 656–670. http://doi.org/10.1016/j.ces.2012.08.048

Nelson, N. O., Mikkelsen, R. L., & Hesterberg, D. L. (2003). Struvite precipitation in anaerobic swine lagoon liquid: effect of pH and Mg:P ratio and determination of rate constant. *Bioresource Technology*, *89*(3), 229–236. Retrieved from http://www.sciencedirect.com/science/article/B6V24-48PM2D5-7/2/acaef02a547f1ca89d8cb4136056f726

Neset, T.-S. S., & Cordell, D. (2012). Global phosphorus scarcity: identifying synergies for a sustainable future. *Journal of the Science of Food and Agriculture*, *92*(1), 2–6. http://doi.org/10.1002/jsfa.4650

New Internationalist Magazine. (1997). Web Page Of Facts About The Western Sahara Including Landuse, Health, Population, Economy And Human Rights. Retrieved September 1, 2014, from http://newint.org/features/1997/12/05/facts/

Nillesen, E., & Bulte, E. (2014). Natural Resources and Violent Conflict. *Annual Review of Resource Economics*, *6*(1), 69–83. http://doi.org/10.1146/annurev-resource-091912-151910

Ochsenbein, D. R., Schorsch, S., Salvatori, F., Vetter, T., Morari, M., & Mazzotti, M. (2015). Modeling the facet growth rate dispersion of β l-glutamic acid—Combining single crystal experiments with nD particle size distribution data. *Chemical Engineering Science*, *133*, 30–43. http://doi.org/10.1016/j.ces.2015.02.026

Ohara, M., & Reid, R. C. (1973). *Modeling crystal growth rates from solution*. Englewood Cliffs, N.J.: Prentice-Hall.

Ohlinger, B. K. N., Young, T. M., & Schroeder, E. D. (2000). POSTDIGESTION STRUVITE PRECIPITATION USING A FLUIDISED BED REACTOR. *Journal of Environmental Engineering*, (April), 361–368.

Ohlinger, B. N., Young, T. M., & Schroeder, E. D. (2000). Postdigestion struvite precipitation using a fluidised bed reactor. *Journal of Environmental Engineering*, *126*(4), 361–368.

Ohlinger, K. N., Young, T. M., & Schroeder, E. D. (1998). Predicting struvite formation in digestion. *Water Research*, *32*(12), 3607–3614. Retrieved from http://www.sciencedirect.com/science/article/B6V73-3VW2KW6-D/2/a1e3c4e98bc01eb71a7feb1eccbbf4fa

Ohlinger, K. N., Young, T. M., & Schroeder, E. D. (1999). Kinetics Effects on Preferential Struvite Accumulation in Wastewater. *Journal of Environmental Engineering*, (August).

Pastor, L., Mangin, D., Barat, R., & Seco, A. (2008). A pilot-scale study of struvite precipitation in a stirred tank reactor: Conditions influencing the process. *Bioresource Technology*, *99*(14), 6285–6291. Retrieved from http://www.sciencedirect.com/science/article/B6V24-4RKDPK0-3/2/e07aa817eb2947134818020ebdb1c243

Perera, P. W. A., Wu, W.-X., Chen, Y.-X., & Han, Z.-Y. (2009). Struvite Recovery from Swine Waste Biogas Digester Effluent through a Stainless Steel Device under Constant pH Conditions. *Biomedical and Environmental Sciences*, *22*(3), 201–209. Retrieved from http://www.sciencedirect.com/science/article/B8JH5-4WW9HGP-4/2/755f1c62d42989abe1939b16bfd2a588

Perry, R. H., Green, D. W., & Maloney, J. O. (Eds.). (1999). *Perry's Chemical Engineers' Handbook* (7th ed.). McGraw Hill.

Persona, A. (2014). A half-policy announcement - The implications of China's new export tariffs on phosphates. Retrieved from http://www.crugroup.com/about-cru/cruinsight/The_implications_of_a_Chinas_new_export_tariffs_on_phosphates

Pitt, K., & Hounslow, M. J. (2015). Aggregation of growing crystals in suspension: II. Poiseuille flow crystalliser. *Chemical Engineering Science*, *133*(0), 148–156. http://doi.org/http://dx.doi.org/10.1016/j.ces.2014.12.055

Pitt, K., Mitchell, G. P., Ray, A., Heywood, B. R., & Hounslow, M. J. (2012). Micro-mechanical model of calcium oxalate monohydrate aggregation in supersaturated solutions : Effect of crystal form and seed concentration. *Journal of Crystal Growth*, *361*, 176–188. http://doi.org/10.1016/j.jcrysgro.2012.09.020

Qu, X. (2003). *BENCH-SCALE TWO-DIMENSIONAL FLUIDISED BED HYDRODYNAMICS AND STRUVITE GROWTH STUDIES*. University of British Columbia.

Quintana, M., Colmenarejo, M. F., Barrera, J., Garc, G., S�nchez, E., Garc�a, G., & Borja, R. (2005). Kinetics of phosphorus removal and struvite formation by the utilization of by-product of magnesium oxide production. *Chemical Engineering Journal*, *111*(1), 45–52. http://doi.org/10.1016/j.cej.2005.05.005

Quintana, M., Sánchez, E., Colmenarejo, M. F., Barrera, J., García, G., & Borja, R. (2005). Kinetics of phosphorus removal and struvite formation by the utilization of by-product of magnesium oxide production. *Chemical Engineering Journal*, *111*(1), 45–52. http://doi.org/10.1016/j.cej.2005.05.005

Rahaman, M. S., Ellis, N., & Mavinic, D. S. (2008). Effects of Various Process Parameters on Struvite Precipitation Kinetics and Subsequent Determination of Rate Constants. *Water Science and Technology*, *57*(1999), 647–654. http://doi.org/10.2166/wst.2008.022

Rahaman, M. S., & Mavinic, D. S. (2009). Recovering nutrients from wastewater treatment plants through struvite crystallisation: CFD modelling of the hydrodynamics of UBC MAP fluidised-bed crystalliser. *Water Science and Technology*, *59*(10), 1887–1892. http://doi.org/10.2166/wst.2009.214

Rahaman, M. S., Mavinic, D. S., & Ellis, N. (2008). Phosphorus recovery from anaerobic digester supernatant by struvite crystallisation: Model-based evaluation of a fluidised bed reactor. *Water Science and Technology*, *58*(6), 1321–1327. http://doi.org/10.2166/wst.2008.721

Rahaman, M. S., Mavinic, D. S., Meikleham, A., & Ellis, N. (2014). Modeling phosphorus removal and recovery from anaerobic digester supernatant through struvite crystallisation in a fluidised bed reactor. *Water Research*, *51*, 1–10. http://doi.org/10.1016/j.watres.2013.11.048

Rahman, M. M., Liu, Y., Kwag, J.-H., & Ra, C. (2011). Recovery of struvite from animal wastewater and its nutrient leaching loss in soil. *Journal of Hazardous Materials*, *186*(2–3), 2026–30. http://doi.org/10.1016/j.jhazmat.2010.12.103

Rahman, M. M., Salleh, M. A. M., Rashid, U., Ahsan, A., Hossain, M. M., & Ra, C. S. (2014). Production of slow release crystal fertiliser from wastewaters through struvite crystallisation – A review. *Arabian Journal of Chemistry*, *7*(1), 139–155. http://doi.org/10.1016/j.arabjc.2013.10.007

Ramabhadran, T. E. (1976). Dynamics of aerosol coagulation and condensation. *AIChE Journal*, *22*(5), 840–851. http://doi.org/10.1002/aic.690220505

Randolph, A. D., & Larson, M. a. (1988). *Theory of Particulate Processes*. http://doi.org/10.1016/B978-0-12-579650-7.50008-7

Randolph, A. D., & White, E. T. (1977). Modeling size dispersion in the prediction of crystal-size distribution. *Chemical Engineering Science*, *32*(9), 1067–1076. http://doi.org/10.1016/0009-2509(77)80144-9

Randolph, A., & Larson, M. (1988). *Theory of particulate processes: analysis and techniques of continuous crystallisation*. *Information Storage and Retrieval* (Second). Academic Press, Inc. Retrieved from http://www.getcited.org/pub/102617560

Regy, S., Mangin, D., Klein, J. P., & Lieto, J. (2001). *PHOSPHATE RECOVERY BY STUVITE PRECIPITATION IN A STIRRED REACTOR*. *Ceep* (Vol. 2).

Rice, R. G., & Do, D. D. (1995). *Applied Mathematics and Modeling for Chemical Engineers*. John Wiley & Sons, Inc.

Roache, P. J. (1998). *Fundamentals of Computational Fluid Dynamics*. Albuquerque, New Mexico: Hermosa Publishers.

Rojkowski, Z. (1978). New hyperbolic empirical model of size dependent crystal growth. *Bull. Acad. Pol. Sci. Ser. Sci. Chim.*, *26*, 265–270.

Ronteltap, M., Maurer, M., & Gujer, W. (2007a). Struvite precipitation thermodynamics in source-separated urine. *Water Research*, *41*(5), 977–984. Retrieved from http://www.sciencedirect.com/science/article/B6V73-4MWXT4X-1/2/030a9fc1ba1b33c1348a0a401a0fe3b5

Ronteltap, M., Maurer, M., & Gujer, W. (2007b). The behaviour of pharmaceuticals and heavy metals during struvite precipitation in urine. *Water Research*, *41*(9), 1859–1868. Retrieved from http://www.sciencedirect.com/science/article/B6V73-4NBY8KF-3/2/15f8a64c088479f879a400dfac1f938c

Ronteltap, M., Maurer, M., Hausherr, R., & Gujer, W. (2010). Struvite precipitation from urine - Influencing factors on particle size. *Water Research*, *44*(6), 2038–46. http://doi.org/10.1016/j.watres.2009.12.015

Saidou, H., Ben Moussa, S., & Ben Amor, M. (2009). Influence of airflow rate and substrate nature on heterogeneous struvite precipitation. *Environmental Technology*, *30*(1), 75–83. http://doi.org/10.1080/09593330802505029

Sakthivel, S. R., Tilley, E., & Udert, K. M. (2012). Wood ash as a magnesium source for phosphorus recovery from source-separated urine. *The Science of the Total Environment*, *419*, 68–75.

Schneider, P. A., Wallace, J. W., & Tickle, J. C. (2013). Modelling and dynamic simulation of struvite precipitation from source-separated urine. *Water Science and Technology*, *67*(12), 2724–2732. http://doi.org/10.2166/wst.2013.184

Shepherd, T. A., Burns, R. T., Raman, D. R., Moody, L. B., & Stalder, K. J. (2009). Performance of a pilot-scale air sparged continuous flow reactor and hydrocyclone for struvite precipitation and removal from liquid swine manure. *Applied Engineering in Agriculture*, *25*(2), 257–267.

Shimamura, K., Ishikawa, H., Tanaka, T., & Hirasawa, I. (2007). Use of a seeder reactor to manage crystal growth in the fluidised bed reactor for phosphorus recovery. *Water Environment Research : A Research Publication of the Water Environment Federation*, *79*(4), 406–13. Retrieved from http://www.ncbi.nlm.nih.gov/pubmed/17489275

Shimamura, K., Tanaka, T., Miura, Y., & Ishikawa, H. (2003). Development of a high-efficiency phosphorus recovery method using a fluidised-bed crystallised phosphorus removal system. *Water Science and Technology*, *48*(1), 163–170.

Shu, L., Schneider, P., Jegatheesan, V., & Johnson, J. (2006). An economic evaluation of phosphorus recovery as struvite from digester supernatant. *Bioresource Technology*, *97*(17), 2211–2216. Retrieved from http://dx.doi.org/10.1016/j.biortech.2005.11.005

Sigurnjak, I., Crappé, S., Michels, E., & Meers, E. (2015). Utilization of derivatives from nutrient recovery processes as alternatives for fossil-based mineral fertilisers in commercial greenhouse production of Lactuca sativa L. *Scientia Horticulturae*, *198*, 267–276. http://doi.org/10.1016/j.scienta.2015.11.038

Singh, M. R., & Ramkrishna, D. (2014). Dispersions in crystal nucleation and growth rates: Implications of fluctuation in supersaturation. *Chemical Engineering Science*, *107*(0), 102–113. http://doi.org/http://dx.doi.org/10.1016/j.ces.2013.11.047

Smil, V. (2000). Phosphorus in the Environment: Natural Flows and Human Interferences. *Annual Review of Energy Environment*, (25), 53–88.

Sohnel, O., & Garside, J. (1992). *Precipitation: Basic principles and industrial applications*. *Science And Technology*. Butterworth Heinemann.

Steffen, W., Richardson, K., Rockstrom, J., Cornell, S. E., Fetzer, I., Bennett, E. M., … Sorlin, S. (2015).

Planetary boundaries: Guiding human development on a changing planet. *Science*, *347*(6223), 1259855-. http://doi.org/10.1126/science.1259855

Stratful, I., Scrimshaw, M. D., & Lester, J. N. (2001a). Conditions influencing the precipitation of magnesium ammonium phosphate. *Water Research*, *35*(17), 4191–4199. Retrieved from http://cat.inist.fr/?aModele=afficheN&cpsidt=14066391

Stratful, I., Scrimshaw, M. D., & Lester, J. N. (2001b). CONDITIONS INFLUENCING THE PRECIPITATION OF MAGNESIUM AMMONIUM PHOSPHATE. *Water Research*, *35*(17), 4191–4199.

Stumm, W., & Morgan, J. J. (1996). *Aquatic chemistry*. John Wiley & Sons, Inc.

Sutugin, A., & Fuchs, N. (1970). Formation of condensation aerosols under rapidly changing environmental conditions:: Theory and method of calculation. *Journal of Aerosol Science*, *1*(4), 287–293. Retrieved from http://www.sciencedirect.com/science/article/pii/0021850270900029

Tai, C. (1999). Crystal growth kinetics of two-step growth process in liquid fluidised-bed crystallisers. *Journal of Crystal Growth*, *206*(1–2), 109–118. http://doi.org/10.1016/S0022-0248(99)00300-0

Talboys, P. J., Heppell, J., Roose, T., Healey, J. R., Jones, D. L., & Withers, P. J. A. (2015). Struvite: a slow-release fertiliser for sustainable phosphorus management? *Plant and Soil*. http://doi.org/10.1007/s11104-015-2747-3

Tao, W., Fattah, K. P., & Huchzermeier, M. P. (2016). Struvite recovery from anaerobically digested dairy manure: A review of application potential and hindrances. *Journal of Environmental Management*, *169*, 46–57. http://doi.org/10.1016/j.jenvman.2015.12.006

Taylor, B. N., & Kuyatt, C. E. (1994). *Guidelines for Evaluating and Expressing the Uncertainty of NIST Measurement Results*. *Technical Note*. Retrieved from http://books.google.com/books?hl=en&lr=&id=xgJeJzsbhoAC&oi=fnd&pg=PA10&dq=Guidelines+for+Evaluating+and+Expressing+the+Uncertainty+of+NIST+Measurement

+Results&ots=0nN8XOBf1X&sig=zz3STNxWVQJExIOlisM-GjhKMUg

Tilley, E., Gantenbein, B., Khadka, R., Zurbrügg, C., & Udert, K. M. (2009). *International Conference on Nutrient Recovery from Wastewater Streams*. *Social and economic feasibility of struvite recovery from urine at the community level in Nepal*.

Tolfo, F. (1977). A simplified model of aerosol coagulation. *Journal of Aerosol Science*, *8*(1), 9–19. http://doi.org/10.1016/0021-8502(77)90058-1

Triger, A., Pic, J.-S., & Cabassud, C. (2012). Determination of struvite crystallisation mechanisms in urine using turbidity measurement. *Water Research*, *46*(18), 6084–94. http://doi.org/10.1016/j.watres.2012.08.030

Türker, M., & Celen, I. (2007). Removal of ammonia as struvite from anaerobic digester effluents and recycling of magnesium and phosphate. *Bioresource Technology*, *98*(8), 1529–34. http://doi.org/10.1016/j.biortech.2006.06.026

Udert, K. M., Larsen, T. a, Biebow, M., & Gujer, W. (2003). Urea hydrolysis and precipitation dynamics in a urine-collecting system. *Water Research*, *37*(11), 2571–82. http://doi.org/10.1016/S0043-1354(03)00065-4

Ueno, Y., & Fujii, M. (2001). Three years experience of operating and selling recovered struvite from full-scale plant. *Environmental Technology*, *22*(11), 1373–81. http://doi.org/10.1080/09593332208618196

Van Kauwenbergh, S. (2010). *World Phosphate Rock*. Retrieved from www.ifdc.org

van Rensburg, P., Musvoto, E. V, Wentzel, M. C., & Ekama, G. A. (2003). Modelling multiple mineral precipitation in anaerobic digester liquor. *Water Research*, *37*, 3087–3097. http://doi.org/10.1016/S0043-1354(03)00173-8

Van Vuuren, D. P., Bouwman, a. F., & Beusen, a. H. W. (2010). Phosphorus demand for the 1970–2100 period: A scenario analysis of resource depletion. *Global Environmental Change*, *20*(3), 428–439. http://doi.org/10.1016/j.gloenvcha.2010.04.004

Wang, J., Burken, J. G., & Zhang, X. J. (2006). Effect of Seeding Materials and Mixing Strength on Struvite Precipitation. *Water Environment Research*, *78*, 125–132.

Wang, J., Song, Y., Yuan, P., Peng, J., & Fan, M. (2006). Modeling the crystallisation of magnesium ammonium phosphate for phosphorus recovery. *Chemosphere*, *65*(7), 1182–7. http://doi.org/10.1016/j.chemosphere.2006.03.062

Warmadewanthi, & Liu, J. C. (2009). Recovery of phosphate and ammonium as struvite from semiconductor wastewater. *Separation and Purification Technology*, *64*(3), 368–373. Retrieved from http://www.sciencedirect.com/science/article/B6THJ-4TVSFMH-2/2/47a59193dfd2053e3977c85e9ec3ab8e

Wauters, P. A., Liu, L. X., & Meesters, G. M. H. (2001). A Population Balance Model for High Shear Granulation. *Chemical Engineering Communications*, 1309–1334. http://doi.org/10.1080/00986440302147

Woo, X. Y., Tan, R. B. H., & Braatz, R. D. (2011). Precise tailoring of the crystal size distribution by controlled growth and continuous seeding from impinging jet crystallisers. *CrystEngComm*, *13*, 2006. http://doi.org/10.1039/c0ce00637h

Wynn, E. J. W. (1996). Improved Accuracy and Convergence of Discretised Population Balance of Lister et al. *AIChE Journal*, *42*(7), 2084–2086.

Ye, Z., Shen, Y., Ye, X., Zhang, Z., Chen, S., & Shi, J. (2014). Phosphorus recovery from wastewater by struvite crystallisation: Property of aggregates. *Journal of Environmental Sciences*, *26*(5), 991–1000. http://doi.org/10.1016/S1001-0742(13)60536-7

Youngquist, G. R., & Randolph, A. D. (1972). Secondary nucleation in a class II system. Ammonium sulfate- water. *AIChE Journal*, *18*(2), 421–429. Retrieved from http://www.scopus.com/inward/record.url?eid=2-s2.0-0015316264&partnerID=40&md5=9073261d8bfa5d764855f99badb9064b

Zekic, A. A., Mitrovic, M. M., Elezovic-Hadzic, S. M., & Malivuk, D. A. (2011). Long-Time Growth Rate Changes of Sodium Chlorate , Potassium Dihydrogen Phosphate , and Rochelle Salt Crystals Independent of Growth Conditions eki. *Industrial & Engineering Chemistry Research*, *50*, 8726–8733. http://doi.org/10.1021/ie102425z

Zeng, L., & Li, X. (2006). Nutrient removal from anaerobically digested cattle manure by struvite precip ... *Journal of Environmental Engineering*, *5*(4), 285–294.

Appendix A Photomicrographs

A.1. Photomicrographs

Microscopy is presented using two experimental runs for the Roughton mixer and one for the impinging jet mixer. For each experimental run, two images of are given before and after sonication for each supersaturation level.

A.1.1. SI = 0.8 A unsonicated

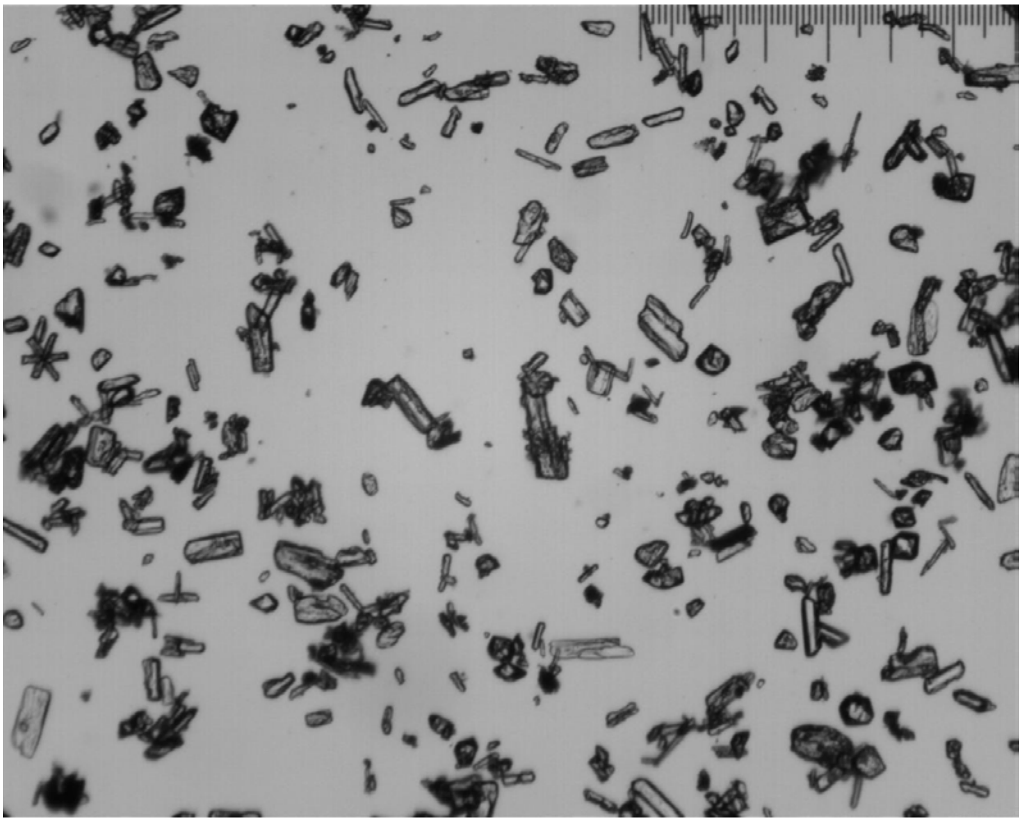

A.1.2. SI = 0.8 A sonicated

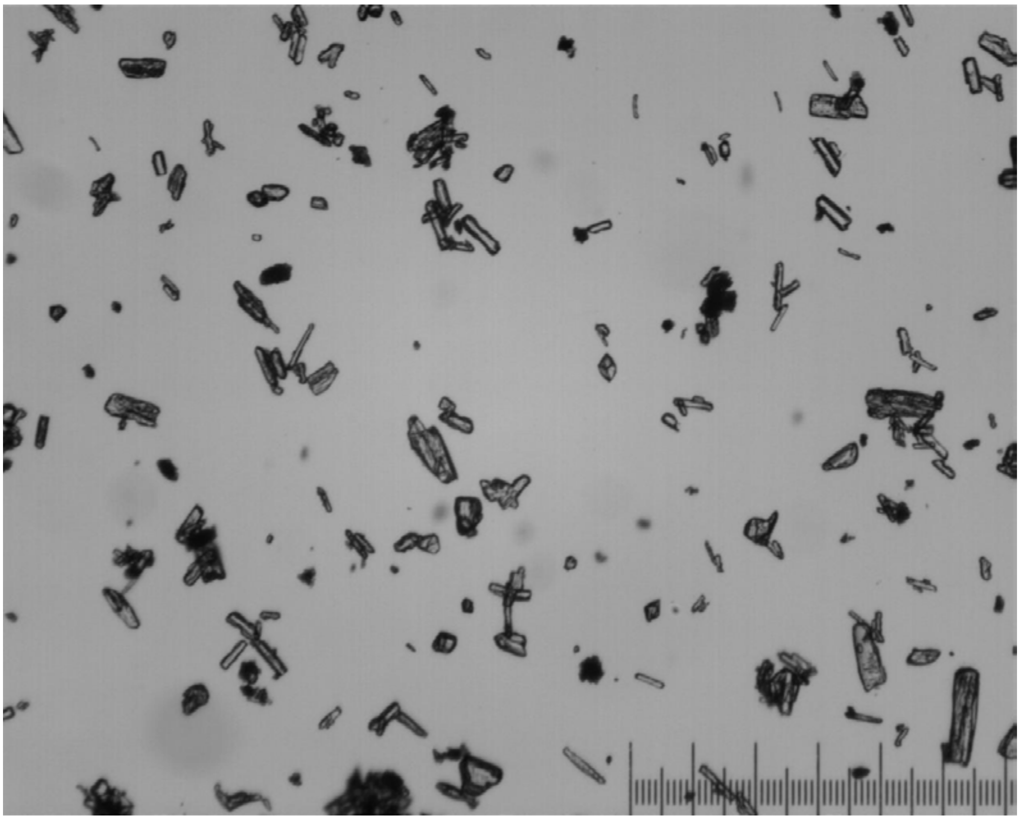

A.1.3. SI = 0.8 B unsonicated

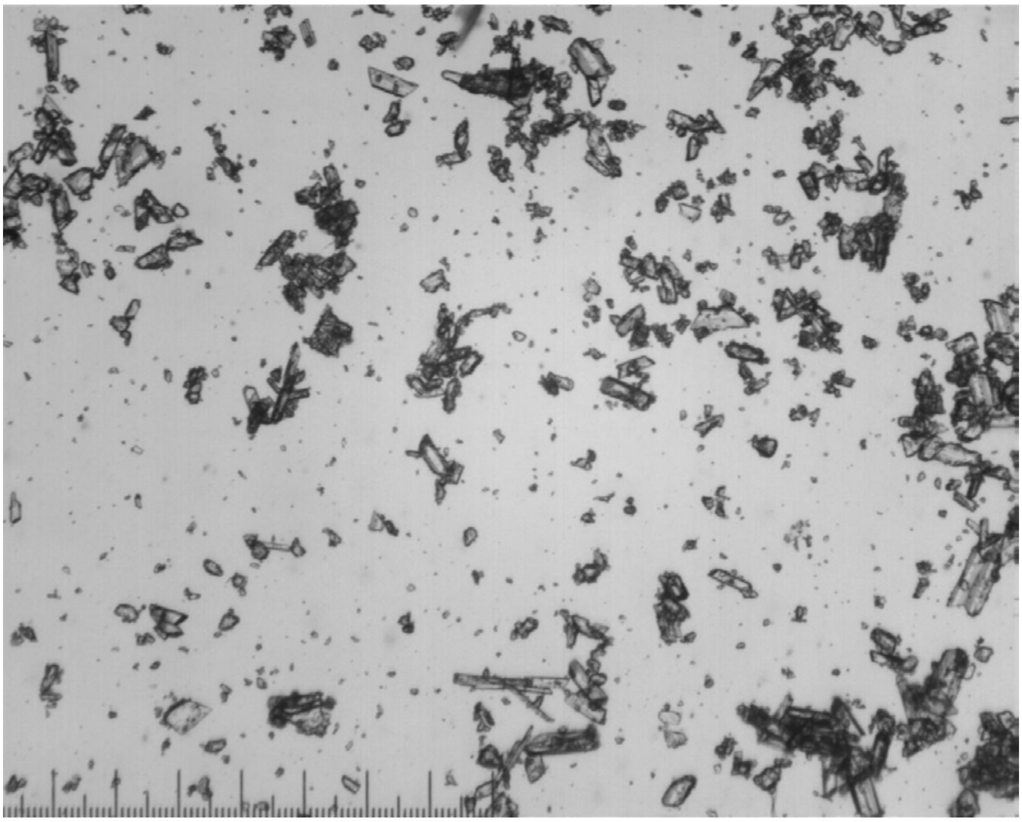

A.1.4. SI = 0.8 B sonicated

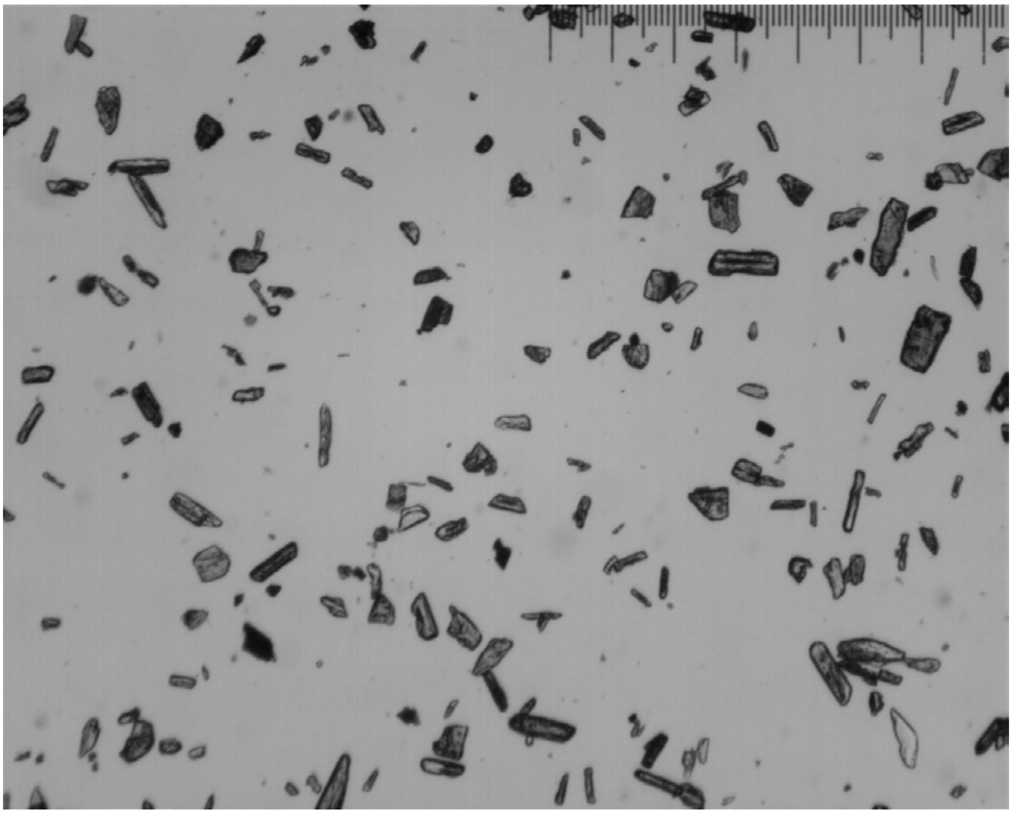

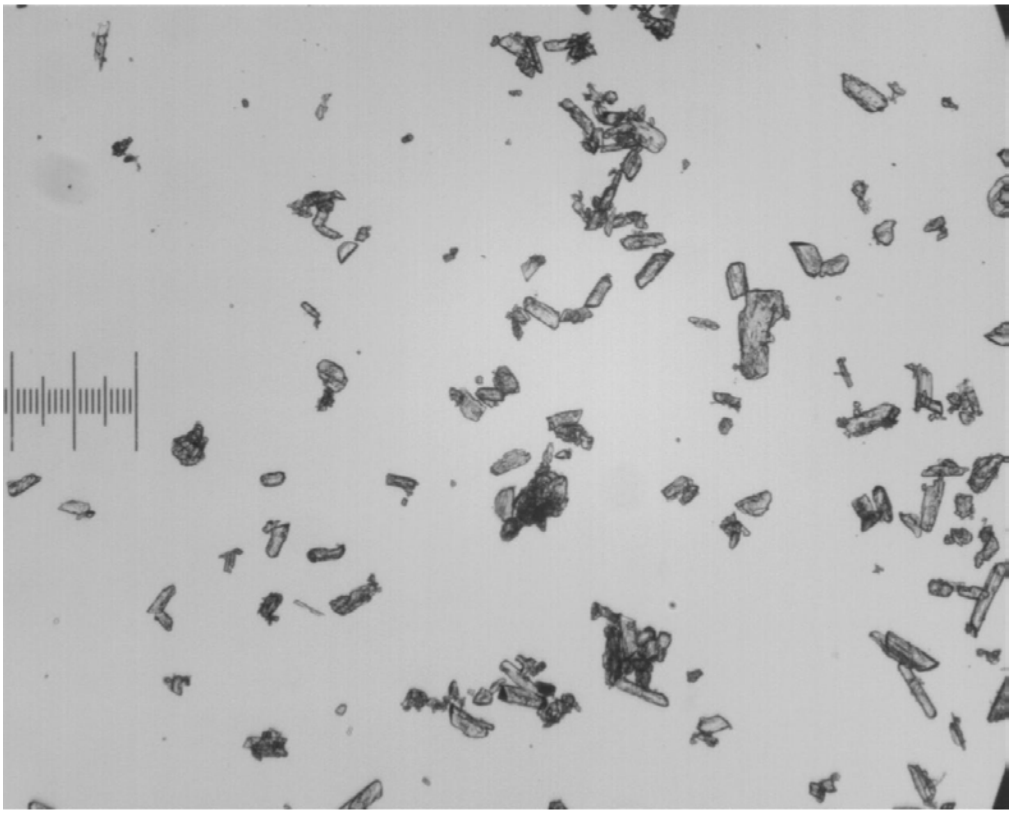

A.1.5. SI = 1.0 A unsonicated

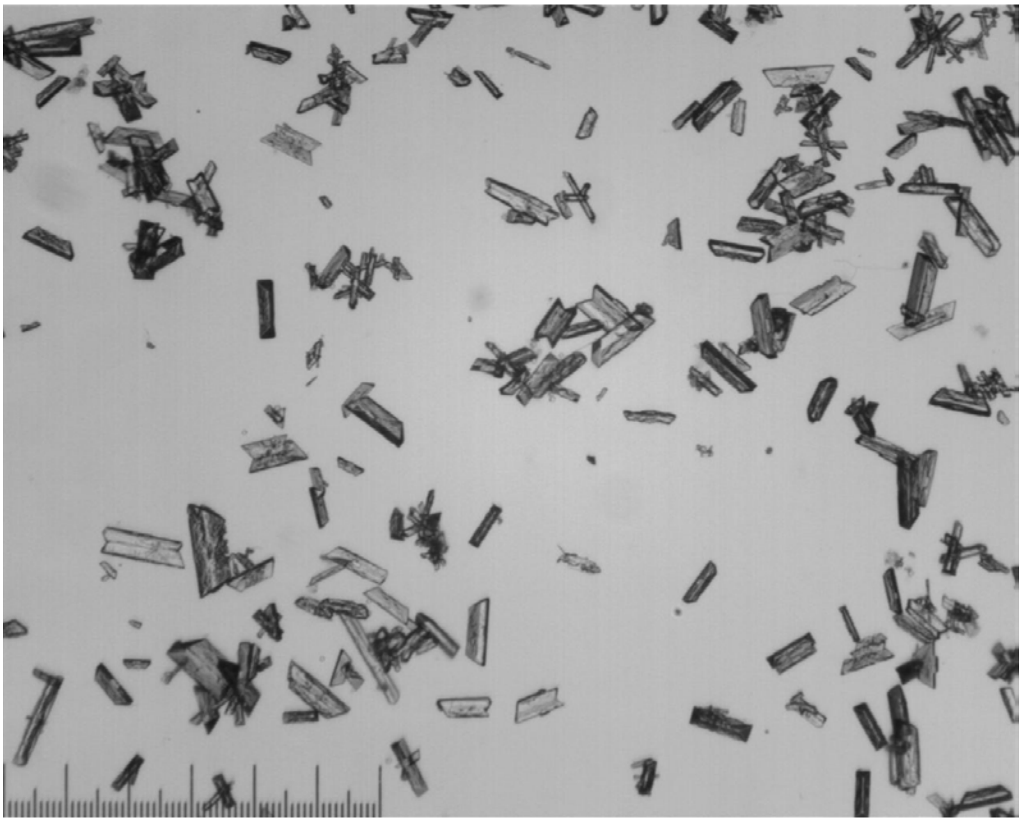

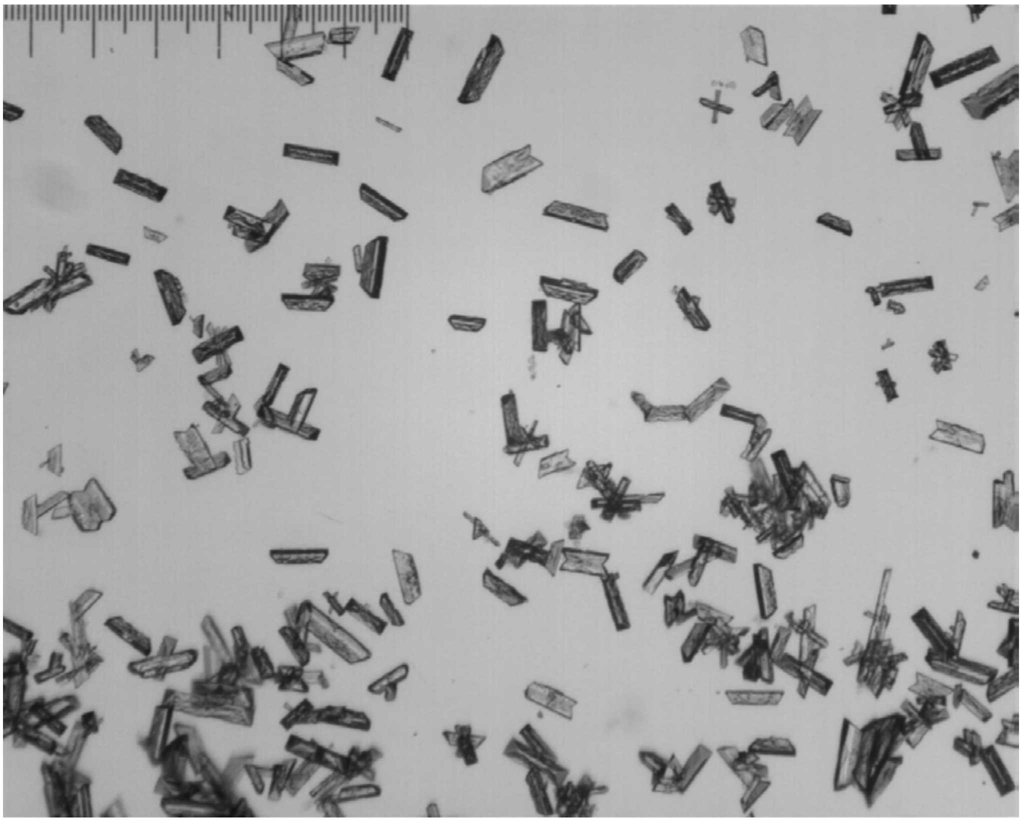

A.1.6. SI = 1.0 A sonicated

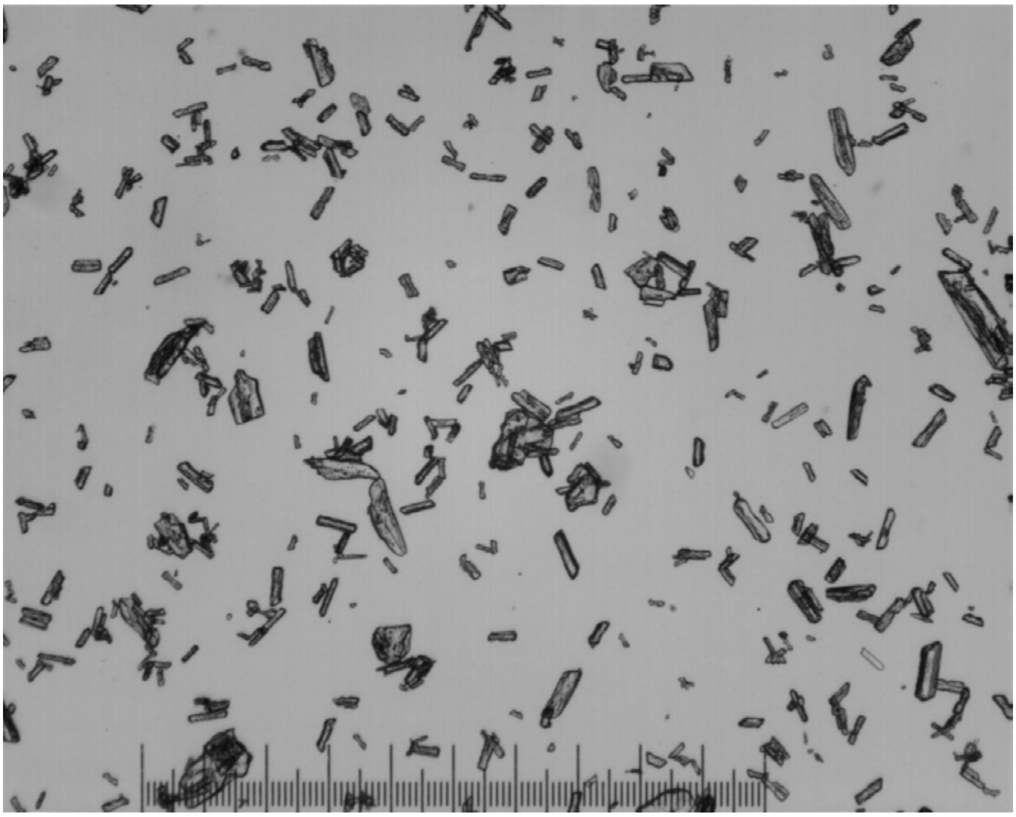

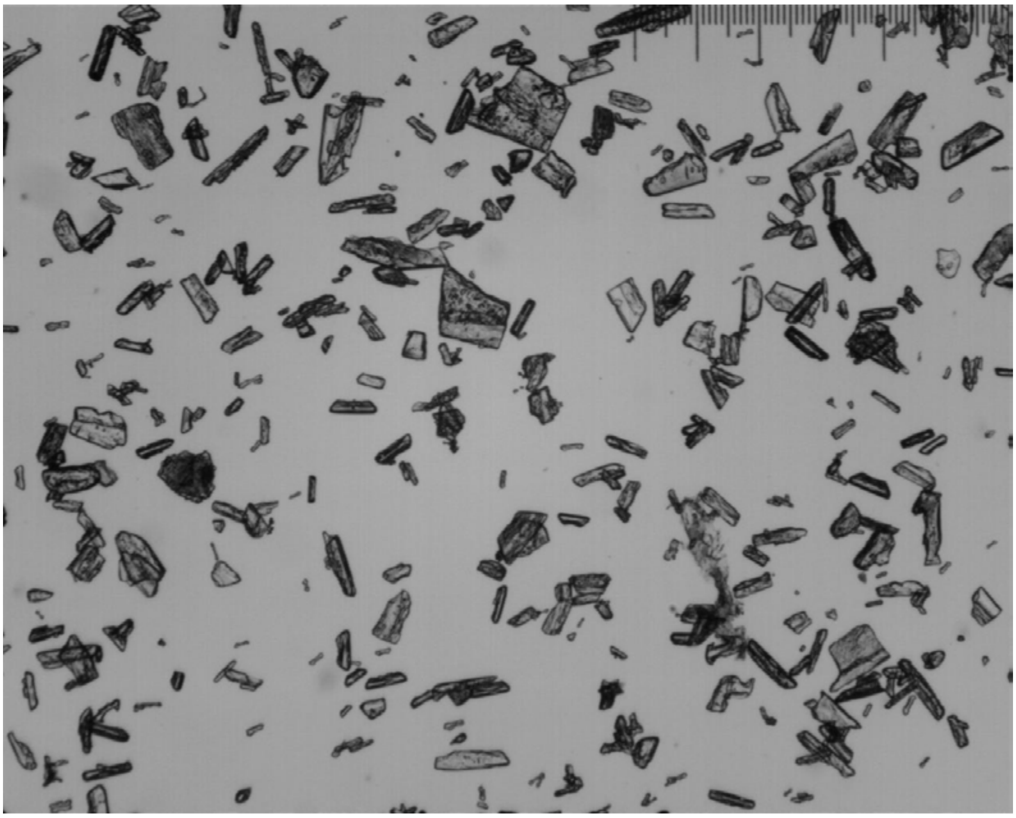

A.1.7. SI = 1.0 B unsonicated

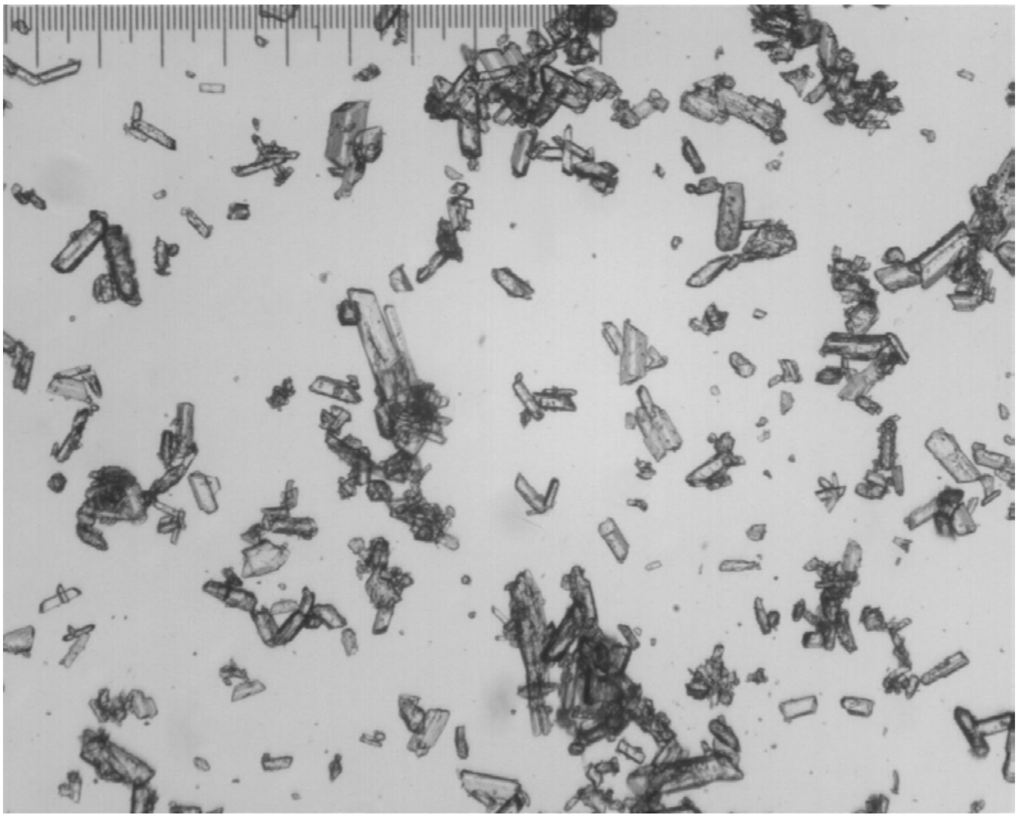

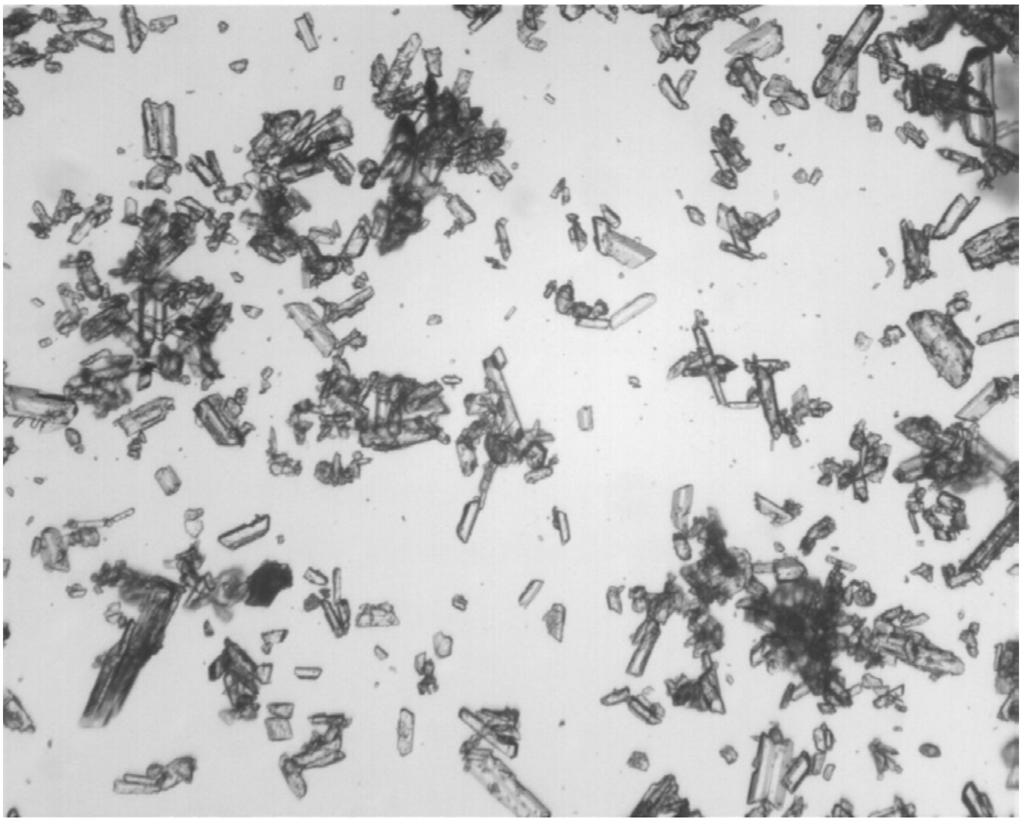

A.1.8. SI = 1.0 B sonicated

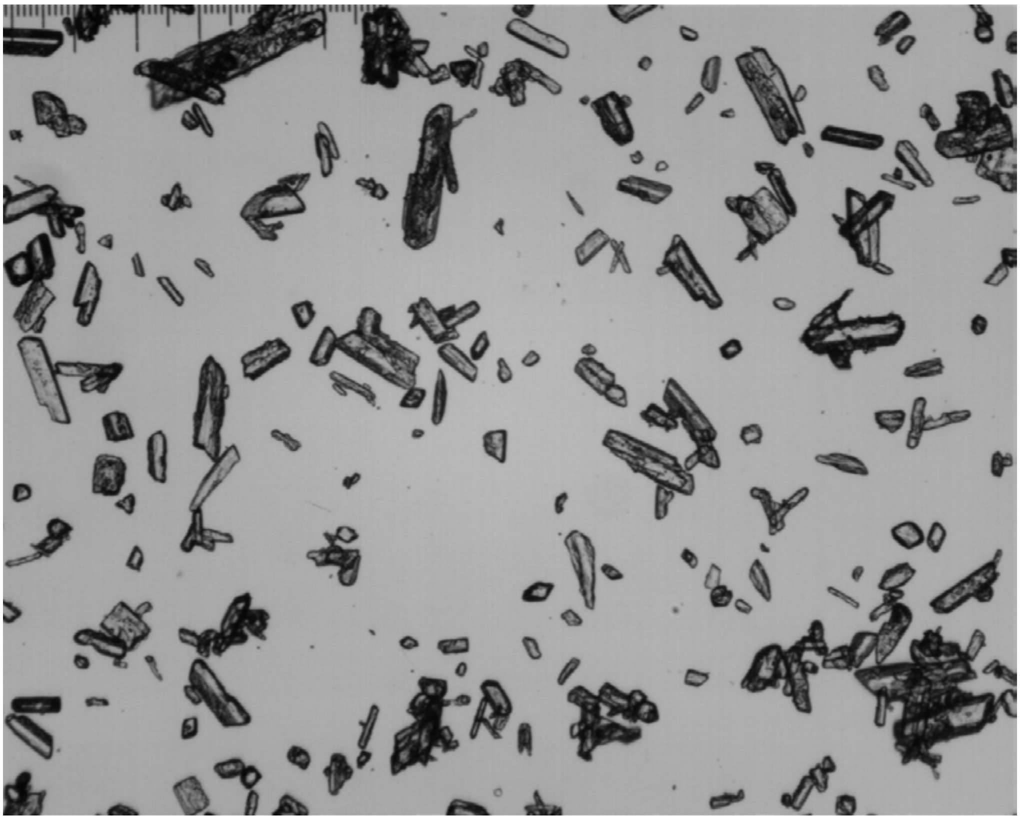

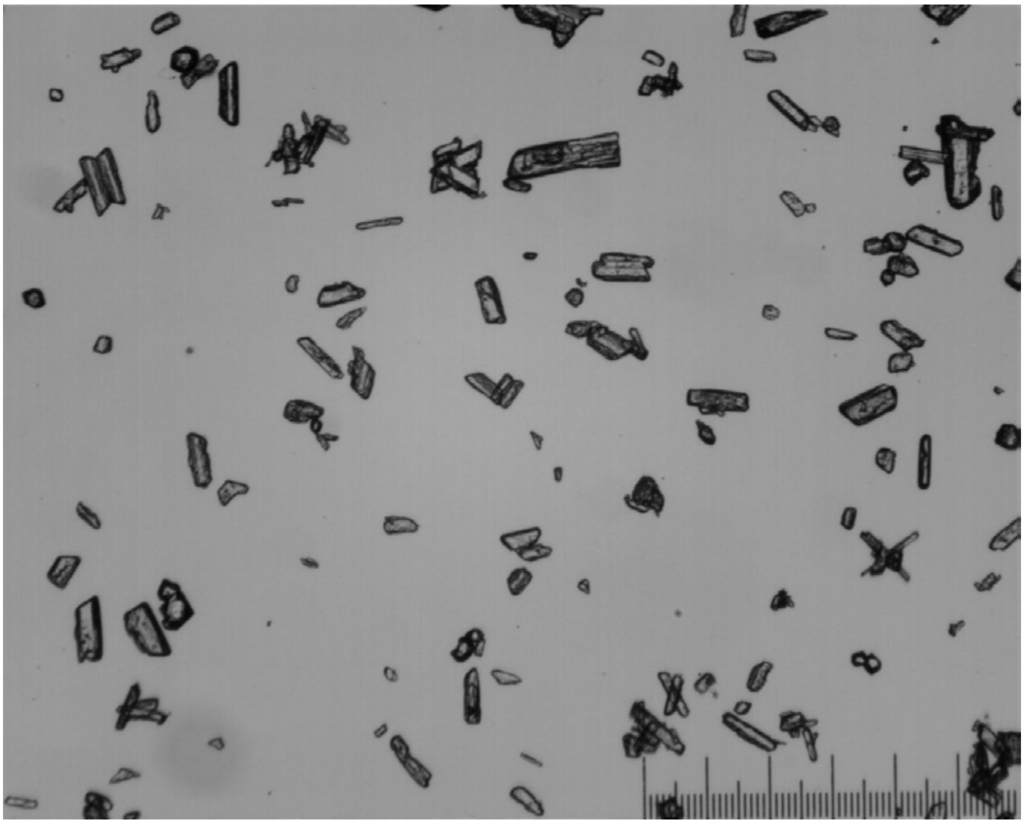

A.1.9. SI = 1.4 A unsonicated

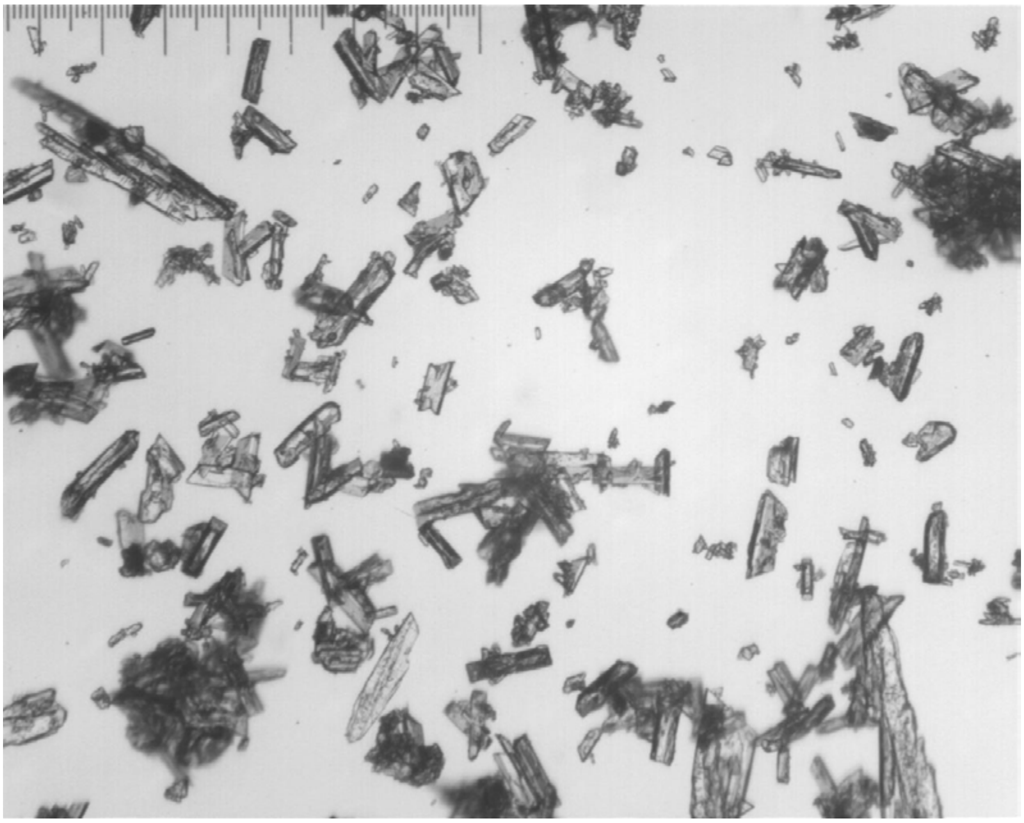

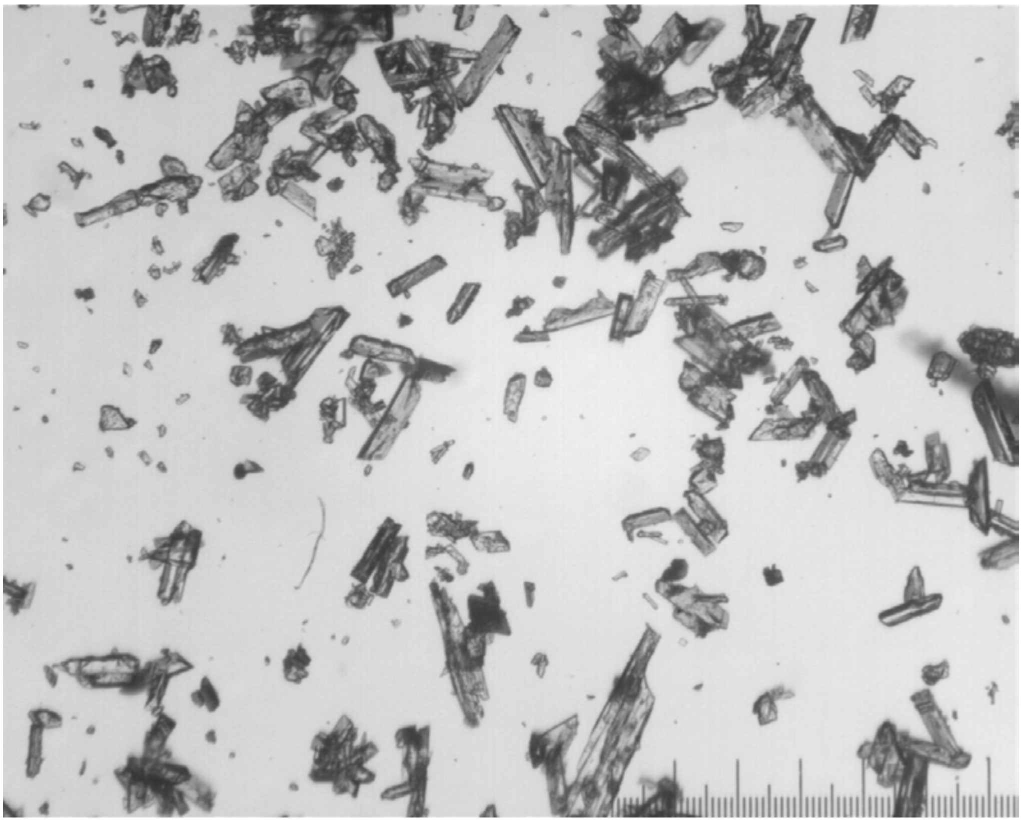

A.1.10. SI = 1.4 A sonicated

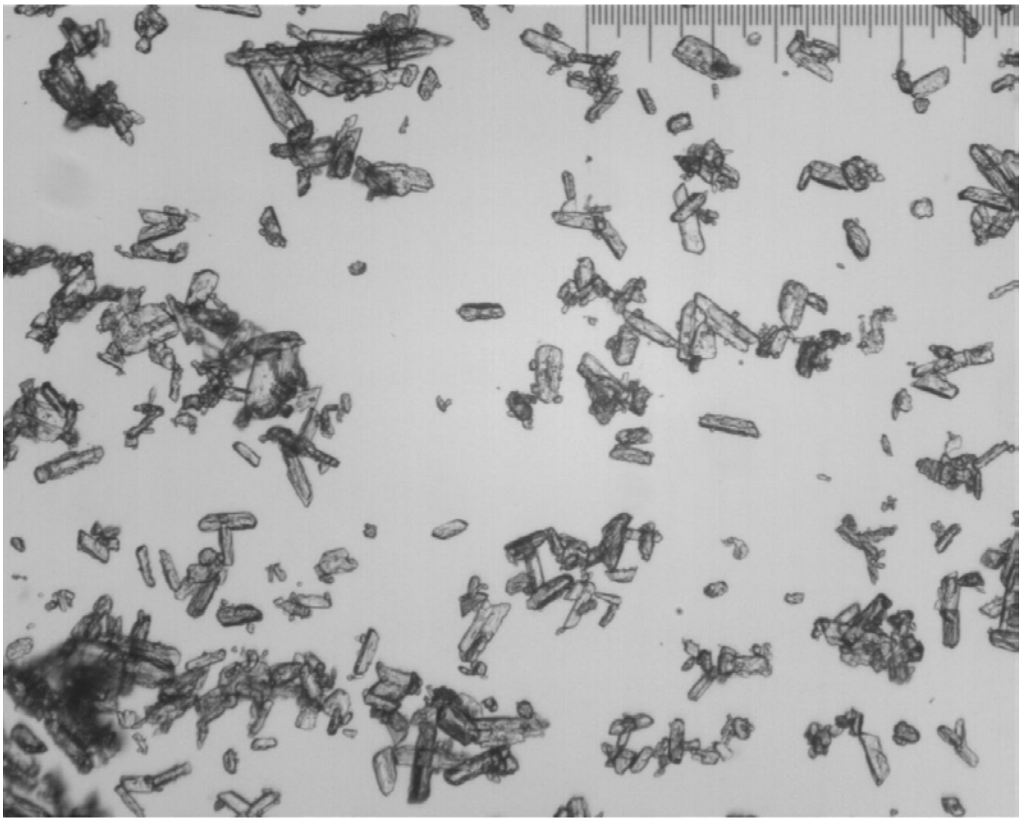

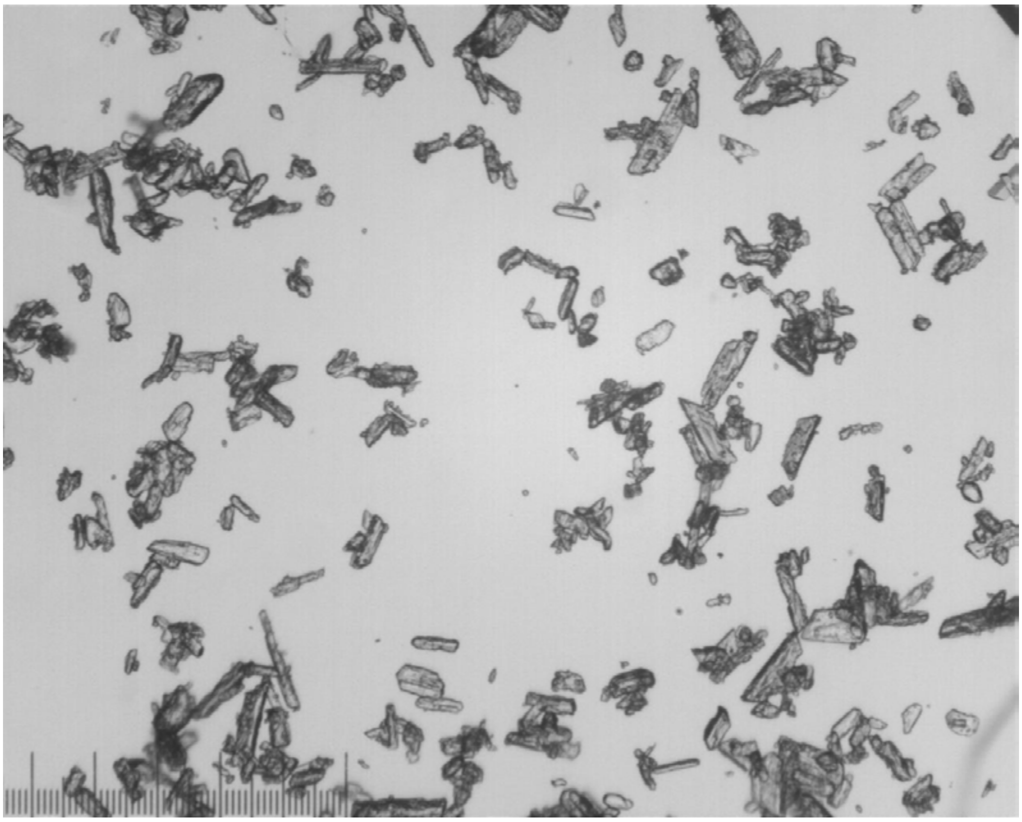

A.1.11. SI = 1.4 B unsonicated

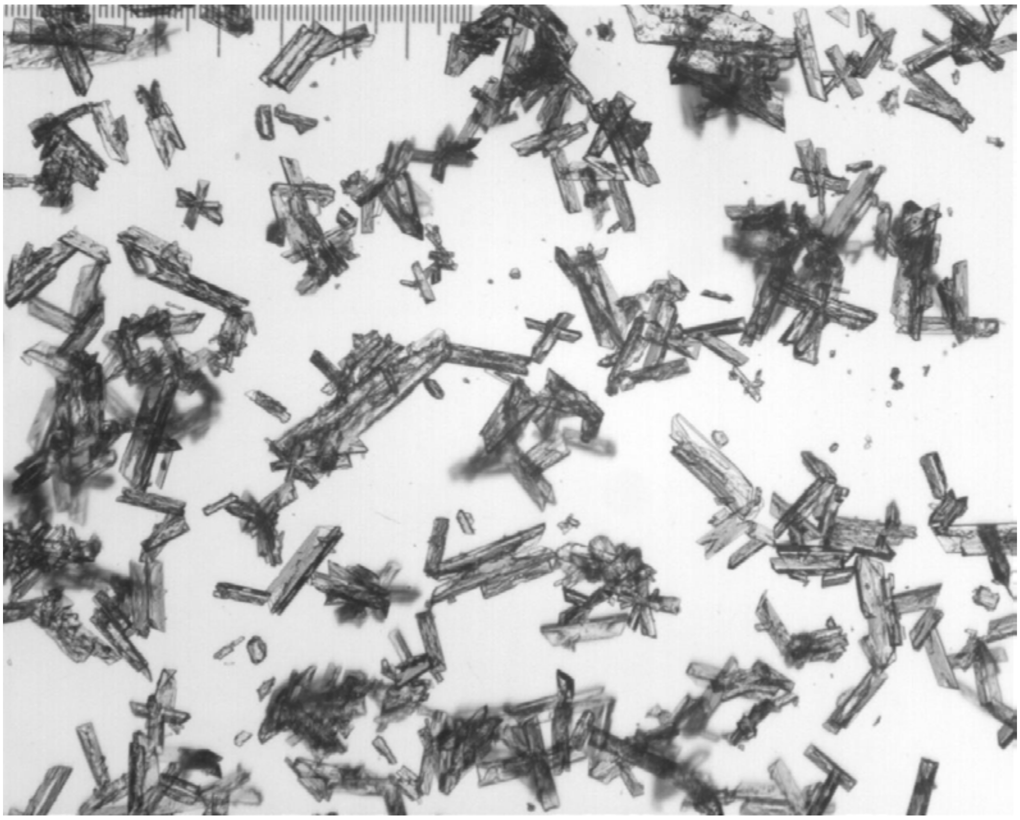

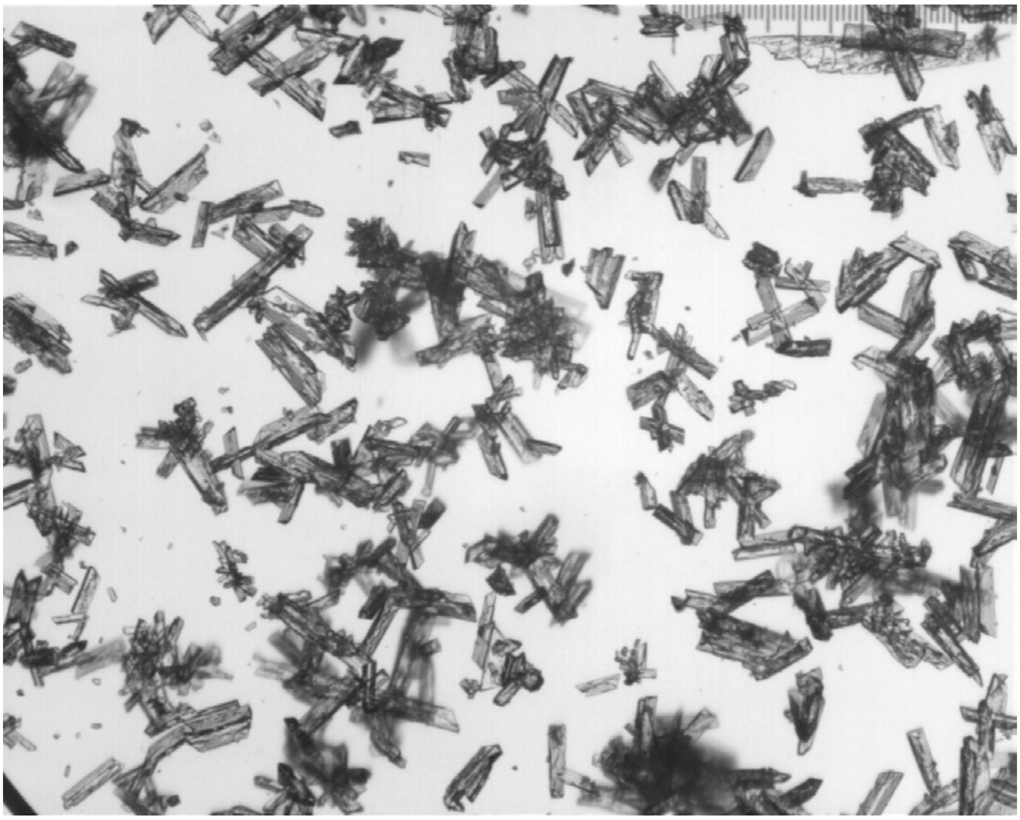

A.1.12. SI = 1.4 B sonicated

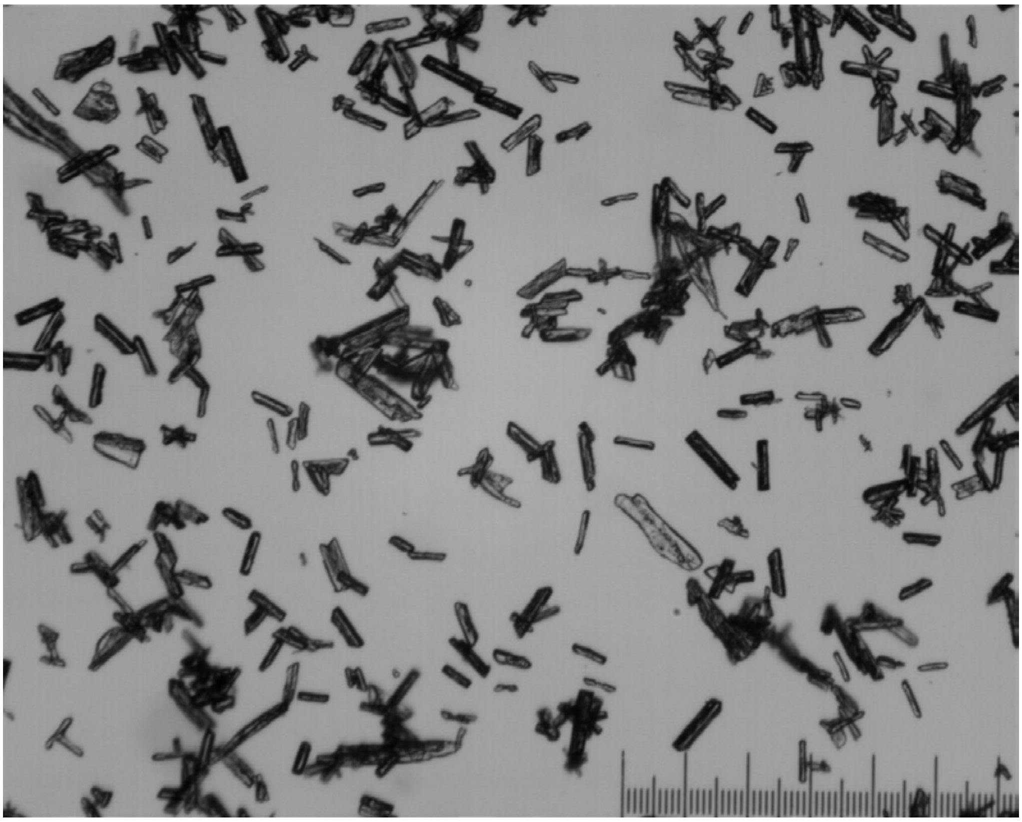

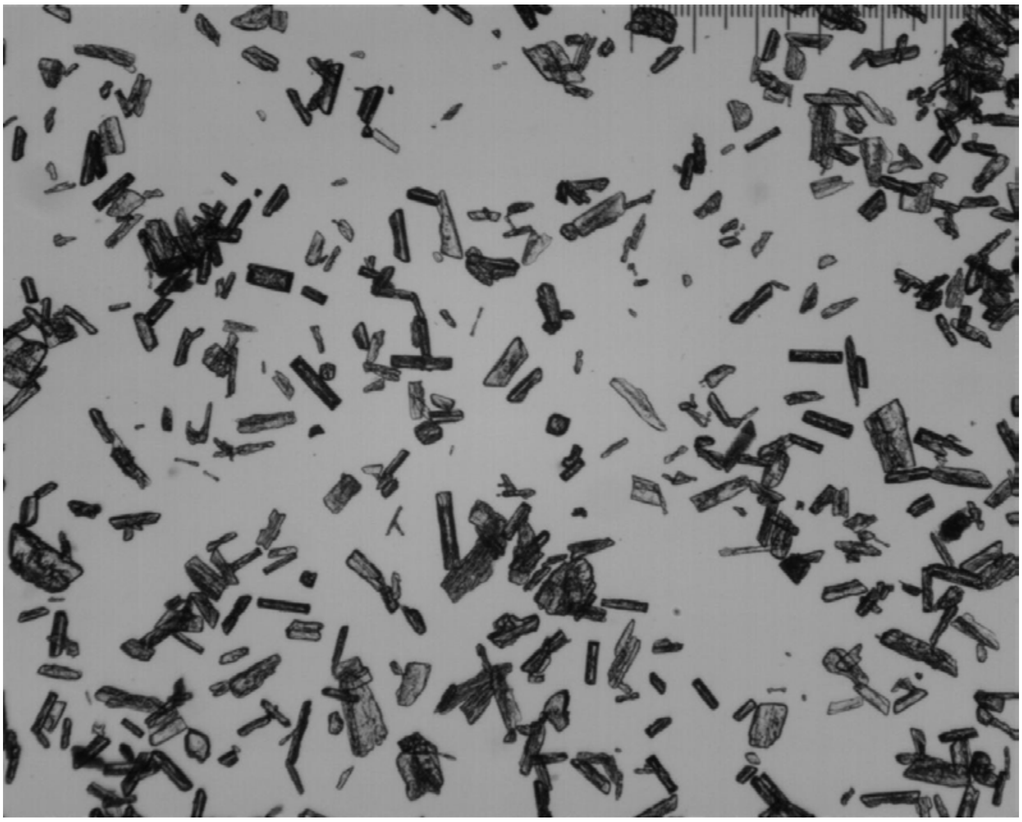

Appendix B – DPB formulations

All formulations shown here are adapted from work by (J. Kumar et al., 2008) and are displayed in this thesis for the convenience of the reader only.

B.1. CAT Growth only

In the cell average approach, growth is modelled as the formation and subsequent adherence of infinitely small nuclei onto particles. This approach makes combination of growth with other processes quite simple. In the below section, the agglomeration based growth model is related to a standard growth rate expression ($G(t,v)$), and the CA technique is used to create a set of ODEs. First the population balance for agglomeration (equation 0.1) is applied to the scenario of particles of volume v_0 aggregating with particles of size v. This expression does not include the integral terms usually seen in an agglomeration population balance because the size of the agglomerating particle, v_0, is fixed.

$$\frac{\partial n(t,v)}{\partial t} = \beta(v - v_0, v_0)n(v - v_0)n(v_0) - \beta(v, v_0)n(v)n(v_0) \qquad 0.1$$

factoring out $v_0 n(v_0)$ gives:

$$\frac{\partial n(t,v)}{\partial t} = -v_0 n(v_0)\left(\frac{\beta(v, v_0)n(v) - \beta(v - v_0, v_0)n(v - v_0)}{v_0}\right) \qquad 0.2$$

Assuming that $m_0 = v_0 n(v_0)$ and taking the limit of $v_0 \rightarrow 0$:

$$\frac{\partial n(t,v)}{\partial t} = -m_0 \frac{\partial}{\partial v}\big(\beta(v, v_0)n(v)\big) \qquad 0.3$$

given the classical growth equation:

$$\frac{\partial n(t,v)}{\partial t} = -\frac{\partial}{\partial v}\big(G(t,v)n(v)\big) \qquad 0.4$$

the following equivalency is evident:

$$G(t,v) = m_0 \beta(v, v_0) \qquad 0.5$$

Now that a relationship has been developed between this new formulation and the classical definition of growth, the cell average technique can be applied to develop ODEs.

Step 1 - Birth and death rates:

The discrete birth and death rates within any cell can be described by integrating the birth and death terms of equation 0.1 over cell i. Equation 0.6 describes the agglomeration of a nuclei of size v_0 and a particle of size $(v - v_0)$ to form a particle of size v, while equation 0.7 describes the agglomeration of a particle of size v_0 with a particle of size v resulting in the particle moving out of that size range.

$$B_{growth,i} = \int_{x_{i-\frac{1}{2}}}^{x_{i+\frac{1}{2}}} \beta(v - v_0, v_0) n(v - v_0) n(v_0) dv \tag{0.6}$$

$$D_{growth,i} = \int_{x_{i-\frac{1}{2}}}^{x_{i+\frac{1}{2}}} \beta(v, v_0) n(v) n(v_0) dv \tag{0.7}$$

Where $\beta(v - v_0, v_0)$ is the agglomeration kernel for particles of size $v - v_0$ and v_0; $n(v - v)$ and $n(v_0)$ are the particle number densities of size $v - v_0$ and v_0 respectively. The integral term is removed by substituting the number density $n(t, v) = \sum_{j=1}^{I} N_j \delta(v - v_j)$. As v_0 has zero size, this function uses a Dirac delta function to concentrate the number densities to points $v = v_j$.

$$B_{growth,i} = \int_{v_{i-\frac{1}{2}}}^{v_{i+\frac{1}{2}}} \beta(v - v_0, v_0) \sum\nolimits_{j=1}^{I} N_j \delta(v - v_0 - v_j)\, n(v_0) dv \tag{0.8}$$

$$B_{growth,i} = \beta(v_i, v_0) N_i n(v_0)$$

Similarly:

$$D_{growth,i} = \int_{v_{i-\frac{1}{2}}}^{v_{i+\frac{1}{2}}} \beta(v, v_0) \sum\nolimits_{j=1}^{I} N_j \delta(v - v_j)\, n(v_0) dv \tag{0.9}$$

$$D_{growth,i} = \beta(v_i, v_0) N_i n(v_0)$$

The equality of birth and death rates is expected as the total number of particles must remain constant in a pure growth scenario.

Step 2 - Average volume of particles born into cell i:

All particles increase by the volume of the nuclei during the growth process. As a result, the average volume of particles resulting from growth can be expressed quite simply:

$$\bar{v}_i = \frac{V_{growth,i}}{B_{growth,i}} = \frac{B_{growth,i}(v_i + v_0)}{B_{growth,i}} = (v_i + v_0) \quad 0.10$$

Step 3 - Birth modification:

$$\begin{aligned} B_i^{CA} = {} & B_{growth,i-1}\lambda_i^-(\bar{v}_{i-1})H(\bar{v}_{i-1} - v_{i-1}) \\ & + B_{growth,i}\lambda_i^-(\bar{v}_i)H(v_i - \bar{v}_i) \\ & + B_{growth,i}\lambda_i^+(\bar{v}_i)H(\bar{v}_i - v_i) \\ & + B_{growth,i+1}\lambda_i^+(\bar{v}_{i+1})H(v_{i+1} - \bar{v}_{i+1}) \end{aligned} \quad 0.11$$

Since $\bar{v}_i > v_i$ the Heaviside step function will always be equal to zero in the second and fourth term and always equal to one in the first and third term.

$$B_{i,growth}^{CA} = B_{growth,i-1}\lambda_i^-(\bar{v}_{i-1}) + B_{growth,i}\lambda_i^+(\bar{v}_i) \quad 0.12$$

Step 4 - Development of ODEs describing change in total particle number:

$$\frac{dN_i}{dt} = B_{i,growth}^{CA} - D_{i,growth} \quad 0.13$$

Substituting equation 0.12 into equation 0.13:

$$\frac{dN_i}{dt} = B_{growth,i-1}\lambda_i^-(\bar{v}_{i-1}) + \ B_{growth,i}\lambda_i^+(\bar{v}_i) - D_{i,growth} \quad 0.14$$

Applying the definition of the lambda function and substituting equations 0.8 and 0.9 gives:

$$\frac{dN_i}{dt} = \beta(v_{i-1}, v_0)N_{i-1}n(v_0)\left(\frac{\bar{v}_{i-1} - v_{i-1}}{v_i - v_{i-1}}\right) \\ + \beta(v_i, v_0)N_i n(v_0)\left(\frac{\bar{v}_i - v_{i+1}}{v_i - v_{i+1}}\right) \\ - \beta(v_i, v_0)N_i n(v_0) \tag{0.15}$$

$$\frac{dN_i}{dt} = \beta(v_{i-1}, v_0)N_{i-1}n(v_0)\left(\frac{\bar{v}_{i-1} - v_{i-1}}{v_i - v_{i-1}}\right) \\ + \beta(v_i, v_0)N_i n(v_0)\left(\frac{\bar{v}_i - v_{i+1}}{v_i - v_{i+1}} - \frac{v_i - v_{i+1}}{v_i - v_{i+1}}\right) \tag{0.16}$$

$$\frac{dN_i}{dt} = \beta(v_{i-1}, v_0)N_{i-1}n(v_0)\left(\frac{\bar{v}_{i-1} - v_{i-1}}{v_i - v_{i-1}}\right) + \beta(v_i, v_0)N_i n(v_0)\left(\frac{\bar{v}_i - v_i}{v_i - v_{i+1}}\right) \tag{0.17}$$

substituting $\bar{v}_i = v_i + v_0$ (equation 0.10) gives:

$$\frac{dN_i}{dt} = \beta(v_{i-1}, v_0)N_{i-1}n(v_0)\left(\frac{v_{i-1} + v_0 - v_{i-1}}{v_i - v_{i-1}}\right) + \beta(v_i, v_0)N_i n(v_0)\left(\frac{v_i + v_0 - v_i}{v_i - v_{i+1}}\right) \tag{0.18}$$

Recalling equation 0.5, $G(t, v) = m_0\beta(v, v_0)$ and $m_0 = v_0 n(v_0)$:

$$\frac{dN_i}{dt} = G(v_{i-1})N_{i-1}\left(\frac{1}{v_i - v_{i-1}}\right) + G(v_i)N_i\left(\frac{1}{v_i - v_{i+1}}\right) \tag{0.19}$$

rearranging:

$$\frac{dN_i}{dt} = G(v_{i-1})\frac{N_{i-1}}{v_i - v_{i-1}} - G(v_i)\frac{N_i}{v_{i+1} - v_i} \tag{0.20}$$

For equidistant grids and constant volumetric growth rate, equation 0.20 reduces to the first order upwind discretisation. Equation 0.20 holds for $i = 2$ to I. In the first cell, $i = 1$, the first term doesn't exist, reducing the expression to:

$$\frac{dN_1}{dt} = -G(v_1)\frac{N_1}{v_2 - v_1} \tag{0.21}$$

B.2. CAT Nucleation and crystal growth

The general formulation of the ODE is given by equation 0.22

$$\frac{dN_i}{dt} = B^{CA}_{nuc+grwoth,i} - D_{growth,i} \tag{0.22}$$

Where:

$$\begin{aligned} B^{CA}_i = {} & B_{nuc+growth,i-1}\lambda^-_i(\bar{v}_{i-1})H(\bar{v}_{i-1} - v_{i-1}) \\ & + B_{nuc+growth,i}\lambda^-_i(\bar{v}_i)H(v_i - \bar{v}_i) \\ & + B_{nuc+growth,i}\lambda^+_i(\bar{v}_i)H(\bar{v}_i - v_i) \\ & + B_{nuc+growth,i+1}\lambda^+_i(\bar{v}_{i+1})H(v_{i+1} - \bar{v}_{i+1}) \end{aligned} \tag{0.23}$$

<u>Step 1 - Birth and death rates:</u>

$$B_{nuc+growth,i} = B_{nuc,i} + B_{growth,i} \tag{0.24}$$

Nucleation can be introduced in a few manners. If nucleation is mono-disperse it can be defined as a boundary condition at particle size zero, as a source located near particle size zero or appearance of particles at the representative size of the first cell. In this work the latter will be implemented for simplicity. The implications of using this technique are discussed in section xx. Birth and death rates associated with growth are the same as those in equations 0.8 and 0.9 respectively. If nucleation is mono-disperse at the representative size of the first cell:

for $i = 1$:

$$B_{nuc+growth,1} = B_{nuc,1} + B_{growth,1} \tag{0.25}$$

$$B_{nuc+growth,1} = B_{nuc,1} + \beta(v_i, v_0)N_i n(v_0) \tag{0.26}$$

and for $i = 2 \rightarrow I$:

$$B_{nuc+growth,i} = B_{growth,i} = \beta(v_i, v_0)N_i n(v_0) \qquad 0.27$$

for all i

$$D_{growth,i} = \beta(v_i, v_0)N_i n(v_0) \qquad 0.28$$

Step 2 - Average volume of particles born into cell i:

$$\bar{v}_i = \frac{V_{nuc+growth,i}}{B_{nuc+growth,i}} \qquad 0.29$$

$$\bar{v}_i = \frac{V_{nuc,i} + V_{growth,i}}{B_{nuc,i} + B_{growth,i}}$$

for $i = 1$:

$$\bar{v}_1 = \frac{B_{nuc,1}v_1 + (v_1 + v_0)\beta(v_1, v_0)N_1 n(v_0)}{B_{nuc,1} + \beta(v_1, v_0)N_1 n(v_0)} \qquad 0.30$$

for $i = 2 \rightarrow I$, nucleation doesn't occur and the standard growth formulation can be applied:

$$\bar{v}_i = \frac{V_{growth,i}}{B_{growth,i}} = \frac{B_{growth,i}(v_i + v_0)}{B_{growth,i}} = (v_i + v_0) \qquad 0.31$$

Step 3 - Birth modification:

$$\begin{aligned} B_i^{CA} = {} & B_{nuc+growth,i-1}\lambda_i^-(\bar{v}_{i-1})H(\bar{v}_{i-1} - v_{i-1}) \\ & + B_{nuc+growth,i}\lambda_i^-(\bar{v}_i)H(v_i - \bar{v}_i) \\ & + B_{nuc+growth,i}\lambda_i^+(\bar{v}_i)H(\bar{v}_i - v_i) \\ & + B_{nuc+growth,i+1}\lambda_i^+(\bar{v}_{i+1})H(v_{i+1} - \bar{v}_{i+1}) \end{aligned} \qquad 0.32$$

As in the pure growth scenario, since $\bar{v}_i > x_i$, the Heaviside step function will always be equal to zero in the second and fourth term and always equal to one in the first and third term. This also holds for the first cell as the nuclei are born exactly at the representative size. Equation 0.32 is reduced to equation 0.33.

$$B^{CA}_{nuc+growth,i} = B_{nuc+growth,i-1}\lambda_i^-(\bar{v}_{i-1}) + B_{nuc+growth,i}\lambda_i^+(\bar{v}_i) \qquad 0.33$$

Step 4 - Development of ODEs describing change in total particle number:

Substituting equation 0.33 into equation 0.22 gives

$$\frac{dN_i}{dt} = B_{nuc+growth,i-1}\lambda_i^-(\bar{v}_{i-1}) + B_{nuc+growth,i}\lambda_i^+(\bar{v}_i) - D_{growth,i} \qquad 0.34$$

Cell $i = 1$:

Nucleation is defined to occur only in cell $i = 1$. In this cell, the term $\lambda_i^-(\bar{v}_{i-1})$ doesn't exist, reducing the expression to:

$$\frac{dN_i}{dt} = B_{nuc+growth,1}\left(\frac{\bar{v}_1 - v_2}{v_1 - v_2}\right) - D_{growth,1} \qquad 0.35$$

Substituting the expression for the average volume ($\bar{v}_1$) in cell 1 (equation 0.30), the expression for birth due to nucleation and growth in cell 1 (equation xx) and the expression for death due to growth in cell 1 (equation xx) gives:

$$\frac{dN_1}{dt} = \left(B_{nuc,1} + \beta(v_1, v_0)N_1 n(v_0)\right)\left(\frac{\frac{B_{nuc,1}v_1 + (v_1 + v_0)\beta(v_1, v_0)N_1 n(v_0)}{B_{nuc,1} + \beta(v_1, v_0)N_1 n(v_0)} - v_2}{v_1 - v_2}\right) \qquad 0.36$$

$$- \beta(v \quad , v_0)N_1 n(v_0)$$

The equality $G(t, x_i) = x_0 n(x_0)\beta(x_i, x_0)$ can be rearranged and substituted into equation 0.36 to give:

$$\frac{dN_1}{dt} = \left(B_{nuc,1} + \frac{N_1 G(t, v_1)}{v_0}\right)\left(\frac{\dfrac{B_{nuc,1} v_1 + (v_1 + v_0)\dfrac{N_i G(t, v_1)}{v_0}}{B_{nuc,1} + \dfrac{N_i G(t, v_1)}{v_0}} - v_2}{v_1 - v_2}\right) - \frac{N_1 G(t, v_1)}{v_0} \tag{0.37}$$

$$\frac{dN_1}{dt} = \left(B_{nuc,1} + \frac{N_1 G(t, v_1)}{v_0}\right)\left(\frac{B_{nuc,1} v_1 + (v_1 + v_0)\dfrac{N_1 G(t, v_1)}{x_0} - v_2\left(B_{nuc,1} + \dfrac{N_1 G(t, v_1)}{v_0}\right)}{\left(B_{nuc,1} + \dfrac{N_1 G(t, v_1)}{v_0}\right)(v_i - v_2)}\right) - \frac{N_1 G(t, v_1)}{v_0} \tag{0.38}$$

$$\frac{dN_1}{dt} = \left(\frac{B_{nuc,1} v_1 + (v_1 + v_0)\dfrac{N_i G(t, v_1)}{v_0} - v_2\left(B_{nuc,1} + \dfrac{N_i G(t, v_1)}{v_0}\right)}{(v_1 - v_2)}\right) - \frac{N_1 G(t, v_1)}{v_0} \tag{0.39}$$

$$\frac{dN_1}{dt} = \left(\frac{B_{nuc,1}(v_1 - v_2) + (v_1 - v_2)\dfrac{N_i G(t, v_i)}{v_0} + N_i G(t, v_i)}{(v_1 - v_2)}\right) - \frac{N_i G(t, v_i)}{v_0} \tag{0.40}$$

$$\frac{dN_1}{dt} = B_{nuc,1} + \frac{N_i G(t, v_i)}{v_0} + \frac{N_i G(t, v_i)}{(v_1 - v_2)} - \frac{N_i G(t, v_i)}{v_0} \tag{0.41}$$

$$\frac{dN_1}{dt} = B_{nuc,1} + \frac{N_i G(t, v_i)}{(v_1 - v_2)} \tag{0.42}$$

B.3. CAT Aggregation and crystal growth

The general formulation of the ODE is given by equation 0.22

$$\frac{dN_i}{dt} = B^{CA}_{agg+grwoth,i} - D_{agg+growth,i} \qquad 0.43$$

Where:

$$\begin{aligned} B^{CA}_i = {} & B_{agg+growth,i-1}\lambda^-_i(\bar{v}_{i-1})H(\bar{v}_{i-1} - v_{i-1}) \\ & + B_{agg+growth,i}\lambda^-_i(\bar{v}_i)H(v_i - \bar{v}_i) \\ & + B_{agg+growth,i}\lambda^+_i(\bar{v}_i)H(\bar{v}_i - v_i) \\ & + B_{agg+growth,i+1}\lambda^+_i(\bar{v}_{i+1})H(v_{i+1} - \bar{v}_{i+1}) \end{aligned} \qquad 0.44$$

Step 1 - Birth and death rates:

$$B_{agg+growth,i} = B_{agg,i} + B_{growth,i} \qquad 0.45$$

for all i

$$D_{agg+growth,i} = D_{agg,i} + D_{growth,i} \qquad 0.46$$

Step 2 - Average volume of particles born into cell i:

$$\bar{v}_i = \frac{V_{agg+growth,i}}{B_{agg+growth,i}} \qquad 0.47$$

$$\bar{v}_i = \frac{V_{agg,i} + V_{growth,i}}{B_{agg,i} + B_{growth,i}}$$

Steps 3 & 4 - Birth modification & development of ODEs describing change in total particle number:

Inclusion of aggregation means that the equations presented in steps 1 and 2 cannot be analytically reduced as was done in sections B.1 and B.2. Because of this, equations 0.43 to 0.47 are implemented directly to obtain the aggregation and growth numerical solution.

Appendix C – Population balance analytic solutions

C.1. Agglomeration and growth analytic solution

This analytic solution of the scenario of constant agglomeration and linear growth is based on work by (Ramabhadran, 1976). Assuming an exponential distribution initial condition (equation 0.48), the PSD evolution is given by equation 0.49.

$$n(v,0) = \frac{N_0}{v_0}\exp\left(-\frac{v}{v_0}\right) \tag{0.48}$$

$$n(v,t) = \frac{N_0}{v_0}(1-T)^2\exp\left(-\frac{2\Lambda T}{1-T}\right)\exp\left(-\frac{v}{v_0}(1-T)\exp\left(-\frac{2\Lambda T}{1-T}\right)\right) \tag{0.49}$$

Where:

$$\Lambda = \frac{G_0}{v_0\beta_0 N_0} \tag{0.50}$$

$$G_v = G_0 v \tag{0.51}$$

$$T = 1 - \frac{\mu_0}{N_0} \tag{0.52}$$

The zeroth and first moments are given by equations 0.53 and 0.54.

$$\mu_0 = \frac{2N_0}{2+\beta_0 N_0 t} \tag{0.53}$$

$$\mu_1 = \mu_0 v_0 \exp(\sigma_1 t) \tag{0.54}$$

The dimensionless aggregation time and dimensionless growth time are defined by equations 0.55 and 0.56, respectively.

$$T_a = \beta_0 N_0 t \tag{0.55}$$

$$T_g = \frac{G_v(v_0)t}{v_0} \tag{0.56}$$

C.2. Nucleation and growth analytical solution

C.2.1. Constant volumetric growth rate

The population balance for nucleation and crystal growth can be written in terms of particle volume as:

$$\frac{\partial n(t,v)}{\partial t} = S(v) - \frac{\partial [G(t,v)n(t,v)]}{\partial v} \tag{0.57}$$

Where $S(v)$ is the nucleation term. Hounslow (Michael J Hounslow, 1990b) gave the **analytic solution for a constant growth rate** ($G(t,v) = G_v$) and mono-disperse nuclei of zero volume ($S(v) = B_{nuc}\delta(v - v_0)$), starting with no particles ($n(0,v) = 0$) as:

$$n(t,v) = \frac{B_{nuc}}{G_v} H\left(t - \frac{v}{G_v}\right) \tag{0.58}$$

The general analytical solution for the moments of the population balance are obtained by substituting equation 0.58 into the general definition for the j^{th} moment of a distribution.

$$\mu_j = \int_0^\infty v^j \frac{B_0}{G_v} H\left(t - \frac{v}{G_v}\right) dv \tag{0.59}$$

The unit step function causes the limits of the integral to be changed. The unit step function is unity at $v < G_v t$, causing the function to only exist when this condition is satisfied. As such the upper limit on the integration becomes $G_v t$.

$$\mu_j = \frac{B_0}{G_v} \int_0^{G_v t} v^j dv \tag{0.60}$$

solving gives:

$$\mu_j = \frac{B_0}{(j+1)G_v} (G_v t)^{j+1} \tag{0.61}$$

where C is a constant, the value of which is unimportant when the derivative is taken with respect to time

$$\frac{\partial \mu_j}{\partial t} = B_0 G_v^j t^j \tag{0.62}$$

substituting $j = 0$, and $j = 1$ gives

$$\frac{\partial \mu_0}{\partial t} = B_0 \tag{0.63}$$

And

$$\frac{\partial \mu_1}{\partial t} = B_0 G_v t \tag{0.64}$$

respectively.

C.2.2. Constant length growth rate

The population balance for nucleation and crystal growth can be written in terms of particle length as:

$$\frac{\partial n(t,L)}{\partial t} = S(L) - \frac{\partial [G(t,L) n(t,L)]}{\partial L} \tag{0.65}$$

Where $S(L)$ is the nucleation term. Hounslow (Michael J Hounslow, 1990b) gave the **analytical solution for a constant growth rate** ($G(t,L) = G_L$) and mono-disperse nuclei of zero volume ($S(L) = B_{nuc}\delta(L - L_0)$), starting with no particles ($n(0,L) = 0$) as:

$$n(t,L) = \frac{B_{nuc}}{G_L} H\left(t - \frac{L}{G_L}\right) \qquad 0.66$$

To express this solution in terms of a volumetric distribution ($n(t,v)$), $n(t,v)$ must be related to $n(t,L)$ and length must be expressed in terms of volume. Using a spherical particle volume and the differential relationship between volume and length based distributions gives an analytical solution for a volume distributed population balance, starting with no particles, undergoing nucleation and constant particle length growth.

$$n(t,v) = \frac{B_{nuc}}{G_L} H\left(t - \frac{\left(\frac{6v}{\pi}\right)^{1/3}}{G_L}\right)\left(\frac{2}{9\pi}\right)^{1/3} v^{-2/3} \qquad 0.67$$

Equation 0.67 can be substituted into the general moment definition to give an expression for the moments for the distribution in terms of a volume discretisation.

$$\mu_j = \int_0^\infty v^j \frac{B_{nuc}}{G_L} H\left(t - \frac{\left(\frac{6v}{\pi}\right)^{1/3}}{G_L}\right)\left(\frac{2}{9\pi}\right)^{1/3} v^{-2/3} dv \qquad 0.68$$

The term $\frac{B_{nuc}}{G_L}\left(\frac{2}{9\pi}\right)^{1/3}$ is absorbed in to a constant k^* for simplicity in this derivation giving:

$$\mu_j = k^* \int_0^\infty v^j\, H\left(t - \frac{\left(\frac{6v}{\pi}\right)^{1/3}}{G_L}\right) v^{-2/3} dv \qquad 0.69$$

As in equation 0.60, the limits of the unit step function alters the limits of the integration. In this case the upper limit becomes $\frac{G_L^3 t^3 \pi}{6}$

$$\mu_j = k^* \int_0^{\frac{G_L^3 t^3 \pi}{6}} v^{j-2/3} dv \qquad 0.70$$

solving yields:

$$\mu_j = \frac{3k^*\left(\frac{G_L^3 t^3 \pi}{6}\right)^{j+\frac{1}{3}}}{j+1} + C \qquad 0.71$$

substituting $j = 0$:

$$\mu_0 = 3k^* G_L t \left(\frac{\pi}{6}\right)^{1/3} + C \qquad 0.72$$

therefore:

$$\frac{\partial \mu_0}{\partial t} = 3k^* G_L \left(\frac{\pi}{6}\right)^{1/3} \qquad 0.73$$

similarly for $j = 1$:

$$\mu_1 = \frac{3k^* G_L^4 t^4 \left(\frac{\pi}{6}\right)^{\frac{4}{3}}}{2} + C \qquad 0.74$$

and

$$\frac{\partial \mu_1}{\partial t} = 6k^* G_L^4 t^3 \left(\frac{\pi}{6}\right)^{\frac{4}{3}} \qquad 0.75$$

Appendix D – Derivation of advection, diffusion & reaction model and key process parameters

This appendix provides a first principles derivation of the advection diffusion reaction model. It also includes methods used to calculate key process variables, namely: reactor outlet concentration; concentration over a sampling period not at steady state; and reactor outlet PSD percentiles (D[10], D[50] & D[90]).

D.1. Advection, diffusion and reaction model derivation

To construct a differential mole balance on an arbitrary species i we consider a differential volume within the reactor:

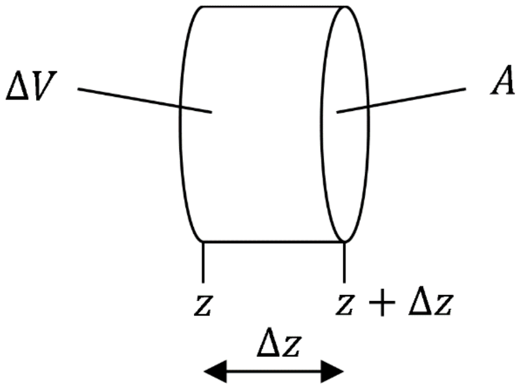

Where ΔV is differential control volume, A is reactor cross sectional area and Δz is differential length. If we write a general mass balance equation as follows:

$$Accumulation = In - Out + Generation \qquad 0.76$$

Accumulation can be described by:

$$Accumulation = \Delta V \frac{\partial C_i}{\partial t} \qquad 0.77$$

Component i can enter and exit the differential volume by convection and diffusion:

$$Convection\ In = (vAC_i)_z \qquad 0.78$$

$$Convection\ Out = (vAC_i)_{z+\Delta z}$$

$$Diffusion\ In = (AJ_i)_z$$

$$Diffusion\ Out = (AJ_i)_{z+\Delta z}$$

Where v is bulk fluid velocity in the axial direction, J_i is the molar flux of species i and Fick's Law defines J_i as:

$$J_i = D\frac{\partial C_i}{\partial z} \qquad 0.79$$

Generation (also accounting for consumption if negative) is given by:

$$Generation = v_i \cdot \Delta V \cdot rate_i \qquad 0.80$$

Where v_i is the stoichiometric coefficient of species i and $rate_i$ is the rate of formation of species i (given by a kinetic model). Substituting these equations into the original mass balance gives:

$$\Delta V\frac{\partial C_i}{\partial t} = (vAC_i)_z - (vAC_i)_{z+\Delta z} + (AJ_i)_z - (AJ_i)_{z+\Delta z} + v_i \cdot \Delta V \cdot rate_i \qquad 0.81$$

Assuming cross-sectional area of the reactor is constant we can substitute $\Delta V = A \cdot \Delta z$ to get:

$$A \cdot \Delta z\frac{\partial C_i}{\partial t} = (vAC_i)_z - (vAC_i)_{z+\Delta z} + (AJ_i)_z - (AJ_i)_{z+\Delta z} + v_i \cdot A \cdot \Delta z \cdot rate_i \qquad 0.82$$

Dividing by $A \cdot \Delta z$ and taking $\lim\limits_{\Delta z \to 0}$ gives:

$$\frac{\partial C_i}{\partial t} = -\frac{\partial(vC_i)}{\partial z} - \frac{\partial J_i}{\partial z} + v_i \cdot rate_i \qquad 0.83$$

using the product rule:

$$\frac{\partial C_i}{\partial t} = -C_i\frac{\partial v}{\partial z} - v\frac{\partial C_i}{\partial z} - \frac{\partial J_i}{\partial z} + v_i \cdot rate_i \qquad 0.84$$

As cross-sectional area was assumed constant, fluid bulk velocity does not vary axially. Therefore:

$$\frac{\partial C_i}{\partial t} = -v\frac{\partial C_i}{\partial z} - \frac{\partial J_i}{\partial z} + v_i \cdot rate_i \qquad 0.85$$

Substituting Fick's Law gives:

$$\frac{\partial C_i}{\partial t} = -v\frac{\partial C_i}{\partial z} + D\frac{\partial^2 C_i}{\partial z^2} + \upsilon_i \cdot rate_i \qquad 0.86$$

This equation can be solved numerically if boundary conditions, initial conditions and a kinetics are defined.

D.1.1. Poiseuille flow

Equation 0.86 can be easily extended into the radial dimension since the reactor radius only affects the velocity term. Poiseuille flow can be derived from the Navier-Stokes equations by assuming fully developed axisymmetric steady state flow with zero radial velocity. Under these assumptions, velocity profile can be written as a function of pipe radius ($v_z(r)$).

$$v_z(r) = 2\bar{v}\left(1 - \left(\frac{r}{R}\right)^2\right) \qquad 0.87$$

Where $\bar{v}$ is the mean fluid velocity and R is the pipe radius.

D.2. Outlet concentrations

D.2.1. Instantaneous outlet concentration

The concentrations of compounds exiting the reactor are key process variables as they can be measured and used to assess reactor performance. These concentrations are not intrinsically calculated by the distributed model and as such must be calculated manually. This is done by integrating over the reactor radius. The differential expression flow in the pipe is then given by:

$$dQ = v_z(r)dA \qquad 0.88$$

where,

$$dA = 2\pi r dr \qquad 0.89$$

Number of moles of component i (N_i) can then be expressed by multiplying concentration of component i ($C_i(r)$) by flow:

$$dN_i = C_i(r)dQ \qquad 0.90$$

Combining equations 0.88 to 0.90 gives an expression for the total concentration of a component exiting the pipe:

$$C_i = \frac{N_{i,T}}{Q_T} = \frac{\int_0^R C(r) v_z(r) 2\pi r \, dr}{\int_0^R v_z(r) 2\pi r \, dr} \tag{0.91}$$

D.2.2. Average outlet concentration over a sampling period

The outlet concentration of component i (C_i) taken during a period of transient operation must be integrated through time. The following construct was used to achieve this:

$$\frac{d\overline{C_{\iota,J}}}{dt} = \frac{1}{S_j} \cdot \frac{dS_j}{dt} \cdot C_i \tag{0.92}$$

$$\frac{dS_j}{dt} = \left(\tanh\left(1 \times 10^{10}(t - t_s(j-1))\right) + 1\right)\left(\tanh\left(-1 \times 10^{10}(t - t_s j)\right) + 1\right)/2 \tag{0.93}$$

Where $\overline{C_{\iota,J}}$ is the average concentration of species i over the sampling period j and S is a continuous variable used to describe discrete sampling, where t_s is the duration of each sample (in this case 10min). For example, for the second sample: $j = 2$, $C_{i,2}$is integrated (by 0.97) only for the period described by equation 0.94 *i.e.*

$$\frac{dS_2}{dt} = \begin{array}{c} 0; t < 10 \\ 1; 10 < t < 20 \\ 0; t > 20 \end{array} \tag{0.94}$$

D.2.3. Particle size distribution percentiles

The 10th, 50th and 90th percentiles of the particle volume distribution are commonly used to describe particulates. The 50th percentile is also known as the volume median diameter (VMD) and represents the diameter which 50% of the total crystal volume resides under. These properties are not immediately available from the moments of the PSD and must be calculated using cumulative volume percent. Note that the equations provided are applied to the exit of the reactor for all modelling conducted in this work but can be applied at any axial coordinate. The volume percentage is given by:

$$f_V = \frac{v_i \int_0^R N_i \, dr}{\int_0^R \mu_1 \, dr} \tag{0.95}$$

Where f_V is the volume fraction, v_i and N_i are the representative particle volume and number in the DPB cell i, and μ_1 is the first moment or total particle volume. The volume fraction is converted to a cumulative form f_{Vc} and the following mechanism is used to describe the percentiles using a single expression without logical terms. Frequently changing logical terms can increase simulation time.

$$D[10] = \sum_i \begin{matrix} \left[\frac{\left(0.1 - f_{Vc,i}\right)(D_{i+1} - D_i)}{\left(f_{Vc,i+1} - f_{Vc,i}\right)} + D_i\right] \times \\ \left[\tanh\left(1 \times 10^{10}\left(0.1 - f_{Vc,i}\right)\right) + 1\right] \times \\ \left[\tanh\left(1 \times 10^{10}\left(f_{Vc,i+1} - 0.1\right)\right) + 1\right] \end{matrix} \tag{0.96}$$

The first term is an iterator is used to interpolate the exact diameter corresponding to a given volume weighted percentile. The following terms ensure that the interpolation is performed between the correct particle sizes. The second term is equal to 1 for all particle sizes where $f_{Vc} < 50\%$ and the third term is equal to 1 for all particle sizes where $f_{Vc} > 50\%$. Multiplying these terms for all cell sizes provides a binary indicator of the lower cell to be used in an interpolation. While the TANH function is used in this example, the same effect can be achieved in various ways.

Appendix E – Thermodynamic model code

This section gives examples of raw code for each simulation described in this thesis. The processes used to call each model are given first, followed by the individual models and sub-models. This code will not solve if copy pasted into gPROMS without the associated initialisation files, parameter boundaries and other specifications, which are not provided here. Please contact the authors if you would like a working version of a model presented here.

E.1. Processes

Processes are used in the simulation package gPROMS to instantiate generic models by providing specifications for undefined model parameters and variables and to define operating procedures for these models. Below are examples of processes used for reactor simulations (including for parameter regressions) and stochastic simulations.

E.1.1. Reactor simulation

```
{Struvite_Growth_Batch_1
The process contains the following nested models:
   - PFR mass balance
      - kinetics & 2D DPB
         - thermodynamic model

Strict variable limits and high order growth rate made it difficult for gPROMS
to initialise. This issue was overcome by removing H3PO4 from thermo model.
Reducing the order of the growth model also allows for full de-supersaturation
to occur.
}


UNIT
   MB AS PFR_Mass_Balance

PARAMETER
   ReactorLength   AS  REAL
   ReactorRadius   AS  REAL
   NoSamples       AS  INTEGER # 10min per sample - gives sample time
   number_scaling  AS  REAL

VARIABLE
```

```
   # Stored_values is an array containing: SI, pH, VMD, PSD_width and N at outlet
   # for min/max values of: NaOH flow, feed flow, NaOH conc., Feed P conc.,
   # k_nuc, n_nuc, k_g, n_g
   RunTime        AS  NOTYPE # simulation time
   PSD_width      AS  NOTYPE
   Yield_thermo   AS  NOTYPE
   SI_out         AS  NOTYPE
   pH_out         AS  NOTYPE
   VMD_out        AS  NOTYPE
   particulate_num AS  NOTYPE # initial number of particles (for numerical stability)

SET
   # -----  SAMPLES NUMBER  -----
   NoSamples          :=  12; #120min covers all steady state simulations

   # If a parameter is set in the process, its value is known in sub models.
   ReactorLength      :=  1.58; # [m]
   ReactorRadius      :=  0.025; # [m]

   number_scaling     :=  1E-9; # 1E-6 minimum required. Can go up to 1E-9 without affecting solution.

EQUATION
   # Link key process variables to sub-models
   PSD_width      =   MB.Kinetics.PSD_width_out;
   Yield_thermo   =   MB.Yield_thermo;
   SI_out         =   MB.SI_out;
   pH_out         =   MB.pH_out;
   VMD_out        =   MB.Kinetics.VMD_out;
   MB.Kinetics.particulate_num = particulate_num;
   particulate_num = 1;

ASSIGN
# Comment in scenario of interest
   # SI=0.8:
#   MB.C_NaOH_batch        := 0.008249*2; # [mol/L]; SI=0.8
#   MB.C_T_P_satd          := 0.008335; # SI=0.8
#   MB.Kinetics.t_ind      := 3.942; # 0.8

   # SI=1.0:
#  MB.C_NaOH_batch      := 0.008803*2; # + 1.067E-5; # [mol/L]; SI=1.0 from EES uncertainty propagation
#   MB.C_T_P_satd          := 0.008013; # SI=1.0
#   MB.Kinetics.t_ind      := 0.908; # 1.0

   # SI=1.4
   MB.C_NaOH_batch        := 0.00965*2; # [mol/L]; SI=1.4
   MB.C_T_P_satd          := 0.007515; # SI=1.4
   MB.Kinetics.t_ind      := 0.253; # 1.4

   RunTime           :=  10*NoSamples; # [min]

# Add kinetics of interest
```

```
   # Growth Rate - Galbraith 2014
   # @ SI=1, this growth rate varies from 12 to 0.1
   MB.Kinetics.k_g := 16.72; # growth rate constant
   MB.Kinetics.n_g := 2; # growth rate order
   # Nucleation kinetic parameters - Galbraith 2014
   MB.Kinetics.k_nuc := 1.195E7; # nucleation rate constant
   MB.Kinetics.n_nuc := 1.68; # nucleation rate order
   # Aggregation kinetic mechanisms:
   MB.Kinetics.k_agg := 2.09E-6; # aggregation rate constant
   MB.Kinetics.n_agg := 5.26; # aggregation rate order

   # General fundamental nucleation kinetics:
   MB.Kinetics.k_g_avg := 0.36; #0.06, 0.66
   MB.Kinetics.n_g_avg := 1; #0.06, 0.66
   MB.Kinetics.tension  := 39.5; #-16.66; #(+/-16.66); #+.061;
   MB.Kinetics.A_factor  := 1E17; #UNIFORM(1E14, 1E20); #+.061;

   # Total concentrations entering PFTR:
   # NOTE: C_MAP is set implicitly by the initial number of particles present (below)
   MB.C_MgCl26H2O_batch    :=  0.03; #-6.019E-6; #(uncertainty) # [mol/L]
   MB.C_NH4_batch         :=  0.02; #-5.195E-6; # [mol/L] # C_NH4 and C_PO4 were made using NH4H2PO4
in experiments.
   MB.C_PO4_batch         :=  0.02; #-5.195E-6; # [mol/L] # They have been split up here to analyse varying
N:P
   MB.C_NaCl_batch        :=  0; # [mol/L]
   MB.C_HCl_batch         := 0; # mol/L

   # Diffusivity
   MB.D    :=  4.5E-9*60; #[m^2/x]*[60s/min] - KCl=2.47E-9m2/s; NH4=1.64E-9m2/s; Cl=1.25E-9m2/s;

   # Flow rates of streams entering PFR
   MB.Flow_Reagent_Batch       :=  4; # [L/h]
   MB.Flow_NaOH_Batch          :=  4; # [L/h]
   MB.Flow_T                   :=  7.976; # + 0.1459; # [L/h]

   # Volume of batch containers - determines mass of reagents.
   MB.Vol_Reagent_Batch       := 10; # [L]
   MB.Vol_NaOH_Batch          := 10; # [L]

#PRESET
#    RESTORE "Base_solution_industrial"


INITIAL
   WITHIN MB.Kinetics DO
      FOR z := 0|+ TO ReactorLength|- DO
         FOR r := 0|+ TO ReactorRadius|- DO
            N(1,z,r) = particulate_num*number_scaling;
            FOR i := 2 TO NEQ DO
               n_density(i,z,r) = 0;
            END #FOR
```

```
         END #FOR
      END #FOR
   END #DO

   # for distributed model, every point in distribution (apart from the boundaries)
   # needs an initial condition:

   # REAL DIGESTER CENTRATE - Start with reactor full of saturated solution from previous run
#    WITHIN MB DO
#       FOR z := 0|+ TO ReactorLength|- DO
#          FOR r := 0|+ TO ReactorRadius|- DO
#             # give non-zero values to get initial solution
#             # start with saturated solution based on "saturated solution calculation.EES"
#             C_T_Mg(z,r)   =   0.003567; # [moles/L]
#             C_T_NH4(z,r)  =   0.01932; # [moles/L]
#             C_T_PO4(z,r)  =   0.002378; # [moles/L]
#                C_Na(z,r)      =    0.001599;   # [moles/L] # Modelled for SI = 0 using gPROMS Thermo in file
"Volume_Average_DPB_G_L_analytical_moments
#             C_Cl(z,r)     =   0.02408; # [moles/L]
#             C_MAP(z,r)    =   0; # [moles/L]
#          END #FOR
#       END #FOR
#    END #WITHIN

   WITHIN MB DO
      FOR z := 0|+ TO ReactorLength|- DO
         FOR r := 0|+ TO ReactorRadius|- DO
            # give non-zero values to get initial solution
            # start with saturated solution based on "saturated solution calculation.EES"
            C_T_Mg(z,r)   =   0.015; # [moles/L]
            C_T_NH4(z,r)  =   0.01; # [moles/L]
            C_T_PO4(z,r)  =   0.01; # [moles/L]
            C_Na(z,r)    =   0.005378; #0.005351916;  # [moles/L] # Modelled for SI = 0 using gPROMS Thermo
in file "Volume_Average_DPB_G_L_analytical_moments
            C_Cl(z,r)     =   0.03; # [moles/L]
            C_MAP(z,r)    =   0; # [moles/L]
         END #FOR
      END #FOR
   END #WITHIN


SOLUTIONPARAMETERS
REPORTINGINTERVAL := 10;

IndexReduction := ON
#IdentityElimination := OFF

DASolver := "DASOLV" [
"LASolver" := "MA48" [
"FullSwitchFactor" := 0.01,
"PivotStabilityFactor" := 0.99
```

```
],
"AbsoluteTolerance" := 1.0E-9,
"OutputLevel" := 0,
"RelativeTolerance" := 1.0E-9,
"VariablesWithLargestCorrectorSteps" := 2
]


SCHEDULE
      CONTINUE FOR RunTime
```

E.1.2. Stochastic simulation

```
{ ------------ PROCESS - Stochastic Simulation ----------------
THIS STOCHASTIC PROCESS IS USED TO SIMULATE THE EFFECT OF VARIATIONS IN
P CONCENTRATION, REACTOR EQUIPMENT AND CAUSTIC DOSING CONCENTRATION,
IN AN INDUSTRIAL APPLICATION.

This process calls on the model 'Stochastic_industrial2' and gives it the
stochastic simulation inputs. It also defines all parameters and variables in
sub models necessary for them to run. The definitions are taken from the process
'Struvite_Growth_Batch_solved'.
}

PARAMETER
  NoSamples      AS  INTEGER #
  # Define common parameters in the process so that their values can be propagated
  # to sub-models:
  ReactorLength   AS  REAL
  ReactorRadius   AS  REAL
  number_scaling  AS  REAL

VARIABLE
  RunTime        AS  NOTYPE
  particulate_num AS  NOTYPE

UNIT
  # Call an instance of the stocastic simulation model
    MonteCarlo   AS  Stochastic_industrial2

SET
# Number of samples gives run time (10 min per sample)
  NoSamples          :=  18; # simulation goes for 180 min per run

# Set the number of scenarios to be included in the stochastic simulation.
# This is limited by the RAM of the machine running the simulation. The 32GB RAM machine can run 20
simulations simultaneously
# Repeat blocks of scenarios can be run back to back using the 'schedule' below to gather more data.
  MonteCarlo.NoScenarios := 20 ; # simulation has 20 scenarios per run, then run is repeaded in schedule

# Set the reactor dimensions to be used by all sub-models:
  ReactorLength      :=  1.58; # [m]
  ReactorRadius      :=  0.025; # [m]

# Scale total particle number by this fraction:
  number_scaling      :=  1E-9;


EQUATION
  particulate_num = 1E3; # Number of initial particles in first cell for every scenario
  WITHIN MonteCarlo DO
    FOR i := 1 TO NoScenarios DO
      ScenarioMB(i).Kinetics.particulate_num = particulate_num;
```

```
      END # WITHIN
    END # FOR


ASSIGN
    RunTime            :=  10*NoSamples; # [min]

# Variable assignments remain the same as the deterministic simulation accept
# for the following variables which are being analysed:

# DISTRIBUTED INPUT VARIABLES:
    WITHIN MonteCarlo DO
#       VMD_out_stddev              := 0;
#       PSD_width_out_stddev     := 0;
#       SI_out_stddev                 := 0;
#       Yield_thermo_stddev       := 0;
#       pH_out_stddev                := 0;

      FOR i := 1 TO NoScenarios DO
        ScenarioMB(i).Flow_NaOH_Batch        := UNIFORM(3.995, 4.005) ; # uniformly assign as standard
deviation is unknown and there is no evidence to suggest any particular distribution

        ScenarioMB(i).Flow_Reagent_Batch    := UNIFORM(3.995, 4.005) ;

        ScenarioMB(i).C_NaOH_batch             :=  NORMAL(0.005753,  1.067E-5)  ;  #  +/-  0.002g  based  on
measurements = +/- 5E-5M, was less for lower SI but 0.0036g/L(9E-5) for SI=1.4

        ScenarioMB(i).C_MgCl26H2O_batch     := NORMAL(0.004756*1.5, 6.019E-6) ;

        ScenarioMB(i).C_NH4_batch          := TRIANGULAR(0.019446,0.038643,0.05784);

        ScenarioMB(i).Kinetics.k_g := NORMAL(12.49,0.061);

        ScenarioMB(i).Kinetics.n_g := NORMAL(5.06,0.005); #5.06;

        ScenarioMB(i).Kinetics.k_nuc := NORMAL(8.5E7,0.076E7);

        ScenarioMB(i).Kinetics.n_nuc := NORMAL(1.68,0.014);

# NON-VARIANT PROCESS VARIABLES:
    # for every simulation, use the following FEED CONDITIONS:
        WITHIN ScenarioMB(i) DO
#             Kinetics.k_g := 12.49;
#             Kinetics.n_g := 5.06; #5.06;
#             Kinetics.k_nuc := 8.5E7;
#             Kinetics.n_nuc := 1.68;
            Kinetics.tension  := 39.5; #-16.66; #(+/-16.66); #+.061;
            Kinetics.A_factor  := 1E17; #UNIFORM(1E14, 1E20); #+.061;
            Kinetics.k_g_avg := 0.36; #0.06, 0.66
            Kinetics.n_g_avg := 1; #0.06, 0.66
            # Total concentrations entering PFTR to achieve SI=1.0
```

```
#              C_MgCl26H2O_batch    :=  0.03; # [mol/L]
            C_NaCl_batch        :=  0; # [mol/L]
            C_HCl_batch         := 0; # mol/L
            D    :=  1E-7; #[m^2/s]
            Vol_Reagent_Batch       := 10; # [L]
            Vol_NaOH_Batch          := 10; # [L]
            Flow_T                  := 7.976 ; # [L/h]
         END # WITHIN
      END # FOR
   END # WITHIN


PRESET
   # An initialisation condition created using experimental conditions from this work
   RESTORE "Base_solution_stoch_industrial"


INITIAL
# for every simulation, use the following INITIAL CONDITIONS:
   WITHIN MonteCarlo DO
   # for each scenario:
      FOR x := 1 TO NoScenarios DO
      # set the particle number:
         WITHIN ScenarioMB(x).Kinetics DO
            FOR z := 0|+ TO ReactorLength|- DO
               FOR r := 0|+ TO ReactorRadius|- DO
                  N(1,z,r) = particulate_num*number_scaling;
                  FOR i := 2 TO NEQ DO
                     n_density(i,z,r) = 0;
                  END #FOR
               END #FOR
            END #FOR
         END #DO

      # for distributed model, every point in distribution (apart from the boundaries)
      # needs an initial condition:
      # Start with reactor full of filtered saturated solution from previous run
         WITHIN ScenarioMB(x) DO
            FOR z := 0|+ TO ReactorLength|- DO
               FOR r := 0|+ TO ReactorRadius|- DO
                  # give non-zero values to get initial solution
                  # start with saturated solution based on "saturated solution calculation.EES"
                  C_T_Mg(z,r)   =   0.015; # [moles/L]
                  C_T_NH4(z,r)  =   0.01; # [moles/L]
                  C_T_PO4(z,r)  =   0.01; # [moles/L]
                  C_Na(z,r)     =   0.005351916;  # [moles/L] # Modelled for SI = 0 using gPROMS Thermo in file
"Volume_Average_DPB_G_L_analytical_moments
                  C_Cl(z,r)     =   0.03; # [moles/L]
                  C_MAP(z,r)    =   0; # [moles/L]
               END #FOR
            END #FOR
```

```
         END #WITHIN
      END #FOR
   END # WITHIN


SOLUTIONPARAMETERS
REPORTINGINTERVAL := 80;
IndexReduction:= ON
DASolver := "DASOLV" [
"LASolver" := "MA48" [
"FullSwitchFactor" := 0.01,
"PivotStabilityFactor" := 0.99
],
"AbsoluteTolerance" := 1.0E-9,
"OutputLevel" := 0,
"RelativeTolerance" := 1.0E-9,
"VariablesWithLargestCorrectorSteps" := 2
]


SCHEDULE # the order of model execution
   SEQUENCE
   # run the first batch of simulations
      CONTINUE FOR RunTime; # RunTime # [min] ; Steady State
```

(Note: The following piece of code was repeated 6 times during stochastic simulations:

```
#################################################

   # restore a common start point from which initialisation is gauranteed
         RESTORE "Base_solution_stoch_industrial"
   # generate new distributions of the stochastic varaibles
      RESET
         WITHIN MonteCarlo DO
            FOR i := 1 TO NoScenarios DO
               ScenarioMB(i).Flow_NaOH_Batch         := UNIFORM(3.995, 4.005) ; # uniformly assign as
standard deviation is unknown and there is no evidence to suggest any particular distribution
               ScenarioMB(i).Flow_Reagent_Batch    := UNIFORM(3.995, 4.005) ;
               ScenarioMB(i).C_NaOH_batch          := NORMAL(0.005753, 1.067E-5) ;
               ScenarioMB(i).C_MgCl26H2O_batch     := NORMAL(0.004756*1.5, 6.019E-6) ;
               ScenarioMB(i).C_NH4_batch          := TRIANGULAR(0.019446,0.038643,0.05784);
               ScenarioMB(i).C_PO4_batch          := TRIANGULAR(0.001956,0.004756,0.007556) ;
               ScenarioMB(i).Kinetics.k_g := NORMAL(12.49,0.061);
               ScenarioMB(i).Kinetics.n_g := NORMAL(5.06,0.005); #5.06;
               ScenarioMB(i).Kinetics.k_nuc := NORMAL(8.5E7,0.076E7);
               ScenarioMB(i).Kinetics.n_nuc := NORMAL(1.68,0.014);
            END # FOR
         END # WITHIN
      END # RESET
      CONTINUE FOR RunTime # [min] ; Steady State
#################################################
```

E.2. Models

E.2.1. PFR mass balance

```
# This model describes the MB over a Poiseuille flow reactor. The model has the
# following traits:
# - It is distributed over PFR length and radius.
# - solved using 1st order BFDM
# - Boundary conditions are used to represent mixing point
# - Instant mixing is assumed

PARAMETER
   NoSamples         AS  INTEGER
   PI                AS  REAL DEFAULT 3.14159265  #Pi
   {Molecular masses}
   # reagents are used to make up batch solution. These MM's are needed to
   # calculate the masses required
   MM_MgCl26H2O    AS REAL
   MM_NH4H2PO4     AS REAL
   MM_NaOH         AS REAL
   MM_NaCl         AS REAL

   # Reactor length - must be parameter for distribution domain to work
   ReactorLength   AS REAL
   ReactorRadius   AS  REAL

   # coefficient to indicate consumption. Uused for distributed test on Mg
   v_Mg    AS REAL
   v_NH4   AS REAL
   v_PO4   AS REAL
   v_MAP   AS REAL

DISTRIBUTION_DOMAIN
# Note: distribution domain can't be variable therefore reactor length must be a parameter
   Axial   AS  [ 0 : ReactorLength ] # [m]
   Radial  AS  [ 0 : ReactorRadius ] # [m]


UNIT
   # An instance of the kinetics model is called kinetics.
#    Kinetics AS Cell_Avg_Nuc_Growth_GL
   Kinetics    AS Kinetics_Poiseiulle_NCG_DPB_scaled_Malvern #_no_props
   Thermo_out  AS Thermodynamics


VARIABLE
   #variables for trial PDE using Mg based on PFR example
   C_T_Mg        AS  Distribution(Axial,Radial)  OF Concentration
   C_T_NH4       AS  Distribution(Axial,Radial)  OF Concentration
   C_T_PO4       AS  Distribution(Axial,Radial)  OF Concentration
   C_Na          AS  Distribution(Axial,Radial)  OF Concentration
   C_Cl          AS  Distribution(Axial,Radial)  OF Concentration
```

```
C_MAP          AS  Distribution(Axial,Radial)  OF Concentration
v_z            AS  Distribution(Radial)        OF Velocity # [m/min]
C_MAP_int      AS  Distribution(Axial)         OF Concentration
v_bar          AS  Velocity
D              AS  Diffusivity
ReactorVol     AS  Volume
C_PO4_out      AS  moles   # [mol/min]
C_T_P_satd     AS  moles
C_NH4_out      AS  moles   # [mol/min]
C_Mg_out       AS  moles   # [mol/min]
C_Mg_out_2     AS  NOTYPE   # [mol/min]
C_Na_out       AS  moles   # [mol/min]
C_Cl_out       AS  moles   # [mol/min]
C_MAP_out      AS  moles   # [mol/min]
C_MAP_out_g    AS  Concentration   # [g/L]
C_MAP_out_g_bar AS  ARRAY(NoSamples)   OF  Concentration   # [g/L]
t_bar          AS  NOTYPE  # [min]
tau            AS  NOTYPE  # [dimensionless]
SI_out         AS  NOTYPE
my_time        AS  NOTYPE  # [min]
SampleTime     AS  ARRAY(NoSamples)   OF   NOTYPE  # [min]
integrating    AS  ARRAY(NoSamples)   OF   NOTYPE  # [min]
first_term     AS  ARRAY(NoSamples)   OF   NOTYPE  # [min]
second_term    AS  ARRAY(NoSamples)   OF   NOTYPE  # [min]
Yield_thermo   AS  NOTYPE
pH_out         AS  NOTYPE

{Flowrates}
# Overall volumetric flow rates around the mixing point between the batch
# solution and the NaOH
Flow_T                 AS     FlowRate    # [L/h]
Flow_T_out             AS     FlowRate    # [L/h]
Flow_Reagent_Batch     AS     FlowRate    # [L/h]
Flow_NaOH_Batch        AS     FlowRate    # [L/h]

{moles of reagents}
# initial amount of reagents in the batch solution i.e. remains same.
moles_MgCl26H2O        AS  moles
moles_NH4H2PO4         AS  moles
moles_NaOH             AS  moles
moles_NaCl             AS  moles
moles_HCl              AS  moles

{Volume}
# Volumes of the batch containers feeding the PFR
Vol_Reagent_Batch      AS  Volume
Vol_NaOH_Batch         AS  Volume

{mass of solid reagents to be mixed up in batch solution}
mass_MgCl26H2O         AS  mass
mass_NH4H2PO4          AS  mass
```

```
   mass_NaOH              AS  mass
   mass_NaCl              AS  mass

   {concentration of of compounds in their batch solutions}
   C_NaOH_batch           AS Concentration
   C_HCl_batch            AS Concentration
   C_NaCl_batch           AS Concentration
   C_MgCl26H2O_batch      AS Concentration
   C_NH4_batch            AS Concentration
   C_PO4_batch            AS Concentration

   {concentrations of compounds after the mixing point}
   # these values change due to dilution but they do not vary over reactor length
   C_T_Mg_in              AS Concentration    # [mol/L];  removed for distribution test
   C_T_NH4_in             AS Concentration    # [mol/L]
   C_T_PO4_in             AS Concentration    # [mol/L]
   C_Na_in                AS Concentration    # [mol/L]
   C_Cl_in                AS Concentration    # [mol/L]

   # Checking for mass balance conservation via two different calculation methods:
   MAP_MB_percent_overshoot    AS  NOTYPE

SET
   # Test at setting distribution solution parameters in model rather than process:
   Axial    := [ BFDM, 1, 18 ] ; # determined by grid independence study
   Radial   := [ BFDM, 1, 41 ] ; # determined by grid independence study
#    Axial    := [ CFDM, 2, 18 ] ; # determined by grid independence study
#    Radial   := [ CFDM, 2, 41 ] ; # determined by grid independence study



   # Molecular masses
   MM_MgCl26H2O    :=  203.30; # [g/mole]
   MM_NH4H2PO4     :=  115.03; # [g/mole]
   MM_NaOH         :=  40.00; # [g/mole]
   MM_NaCl         :=  58.44; # [g/mole]

   # Stoicheometry (-ve means consumed, +ve means produced)
   v_Mg    :=  -1;
   v_NH4   :=  -1;
   v_PO4   :=  -1;
   v_MAP   :=  1;



BOUNDARY
   # @ z = 0, for all r (inlet)
   FOR r := 0 TO ReactorRadius DO
      C_T_Mg(0,r)         =      C_MgCl26H2O_batch*Flow_Reagent_Batch/(Flow_Reagent_Batch      +
Flow_NaOH_Batch);
      C_T_NH4(0,r)  = C_NH4_batch*Flow_Reagent_Batch/(Flow_Reagent_Batch + Flow_NaOH_Batch);
      C_T_PO4(0,r)  = C_PO4_batch*Flow_Reagent_Batch/(Flow_Reagent_Batch + Flow_NaOH_Batch);
```

```
    C_Na(0,r) = (C_NaOH_batch*Flow_NaOH_Batch +
C_NaCl_batch*Flow_Reagent_Batch)/(Flow_Reagent_Batch + Flow_NaOH_Batch);
    C_Cl(0,r)      = (C_HCl_batch*Flow_Reagent_Batch + C_NaCl_batch*Flow_Reagent_Batch +
C_MgCl26H2O_batch*2*Flow_Reagent_Batch + (C_NH4_batch-
C_PO4_batch)*Flow_Reagent_Batch)/(Flow_Reagent_Batch + Flow_NaOH_Batch);
    C_MAP(0,r)   = 0; # this model is for a reactor making seeds, doesn't need any initial MAP
  END #FOR

  # @ z = L, for all r (outlet) - outlet concentration change in axial direction is 0
  # this means that the last two axial grid points are the same but can change
  FOR r := 0 TO ReactorRadius DO
    PARTIAL(C_T_Mg(ReactorLength,r),Axial)     = 0;
    PARTIAL(C_T_NH4(ReactorLength,r),Axial)    = 0;
    PARTIAL(C_T_PO4(ReactorLength,r),Axial)    = 0;
    PARTIAL(C_Na(ReactorLength,r),Axial)       = 0;
    PARTIAL(C_Cl(ReactorLength,r),Axial)       = 0;
    PARTIAL(C_MAP(ReactorLength,r),Axial)      = 0;
  END #FOR

  # @ r = 0, for all L (centreline) - dC/dr = 0 - change in concentration radially at r=0 is 0
  # this means that radial grid points at r=0 are same as those next door. Ensures symetry.
  FOR z := 0|+ TO ReactorLength|- DO
    PARTIAL(C_T_Mg(z,0),Radial)     = 0;
    PARTIAL(C_T_NH4(z,0),Radial)    = 0;
    PARTIAL(C_T_PO4(z,0),Radial)    = 0;
    PARTIAL(C_Na(z,0),Radial)       = 0;
    PARTIAL(C_Cl(z,0),Radial)       = 0;
    PARTIAL(C_MAP(z,0),Radial)      = 0;
  END #FOR

  # @ r = R, for all L (reactor wall) - change in concentration radially at r=R is 0
  # this means that radial grid points at r=R are same as those next door. Ensures symetry.
  FOR z := 0|+ TO ReactorLength|- DO
    PARTIAL(C_T_Mg(z,ReactorRadius),Radial)     = 0;
    PARTIAL(C_T_NH4(z,ReactorRadius),Radial)    = 0;
    PARTIAL(C_T_PO4(z,ReactorRadius),Radial)    = 0;
    PARTIAL(C_Na(z,ReactorRadius),Radial)       = 0;
    PARTIAL(C_Cl(z,ReactorRadius),Radial)       = 0;
    PARTIAL(C_MAP(z,ReactorRadius),Radial)      = 0;
  END #FOR


EQUATION
#-------------------          MODEL LINKING          -------------------
  # C_MAP isn't defined in thermo - MB occurs here. It's presence is implicit
  # by the loss of ions in solutions from the MB.
  C_T_Mg     =  Kinetics.Thermo.C_T_Mg;
  C_T_NH4    =  Kinetics.Thermo.C_T_NH4;
  C_T_PO4    =  Kinetics.Thermo.C_T_PO4;
  C_Na       =  Kinetics.Thermo.C_Na;
  C_Cl       =  Kinetics.Thermo.C_Cl;
```

```
   Kinetics.v_z = v_z; # [m/min]

#-------------------          FEED CONDITIONS          -------------------
   # elemental MB over the mixing point - these variables just give C_T_Mg @ z=0
   C_T_Mg_in          =     C_MgCl26H2O_batch*Flow_Reagent_Batch/(Flow_Reagent_Batch  +
Flow_NaOH_Batch); # [mol/L]*[L/h]*[h/L] = [mol/L]
   C_T_NH4_in   =  C_NH4_batch*Flow_Reagent_Batch/(Flow_Reagent_Batch + Flow_NaOH_Batch);
   C_T_PO4_in   =  C_PO4_batch*Flow_Reagent_Batch/(Flow_Reagent_Batch + Flow_NaOH_Batch);
   C_Na_in                          =          (C_NaOH_batch*Flow_NaOH_Batch     +
C_NaCl_batch*Flow_Reagent_Batch)/(Flow_Reagent_Batch + Flow_NaOH_Batch);
   C_Cl_in          =    (C_HCl_batch*Flow_Reagent_Batch  +  C_NaCl_batch*Flow_Reagent_Batch  +
C_MgCl26H2O_batch*2*Flow_Reagent_Batch)/(Flow_Reagent_Batch + Flow_NaOH_Batch);

   # Calculate the mass of reagent required:
   {moles of reagents in batch containers}
   moles_NaOH     =  C_NaOH_batch*Vol_NaOH_batch;
   moles_HCl      =  C_HCl_batch*Vol_reagent_batch;
   moles_NaCl     =  C_NaCl_batch*Vol_reagent_batch;
   moles_MgCl26H2O =  C_MgCl26H2O_batch*Vol_reagent_batch;
   moles_NH4H2PO4  =  C_PO4_batch*Vol_reagent_batch; # only applicable if N:P=1:1

   {masses of reagents in batch containers}
   mass_MgCl26H2O  =  moles_MgCl26H2O * MM_MgCl26H2O;
   mass_NH4H2PO4   =  moles_NH4H2PO4 * MM_NH4H2PO4;
   mass_NaOH      =  moles_NaOH * MM_NaOH;
   mass_NaCl      =  moles_NaCl * MM_NaCl;

#-------------------          HYDRODYNAMICS          -------------------
   # Actual residence time:
#   t_bar   = 23.11; # [min]
   # Simplified geometry residence time
   t_bar = ReactorVol/Flow_T*60; # [min] = [L]/[L/h]*[60min/h]
   # residence time count:
   $tau    = 1/t_bar; # [dimensionless]
   # Velocity Profile:
   # Average flow velocity v_z
   v_bar = ReactorLength/(ReactorVol/Flow_T)/60; # [m/min] = [m]/([L]/[L/h])/60[min/h]
   #v_bar = 0.01;
   # Actual reactor volume
#   ReactorVol = 2.93; # [L]
   # Simplified geometry reactor volume
   ReactorVol = ReactorLength*pi*ReactorRadius^2*1000; # 2.93; # [L]=[m^3]*1000L/m^3

   # v_z is only used in differential equations not defined at boundaries
   # v_z is the same for any point in L
   FOR r := 0 TO ReactorRadius DO
      v_z(r) = 2*v_bar*(1-(r/ReactorRadius)^2); # [m/min]
   END #FOR

   {Flow rates}
#   Flow_T      =  Flow_Reagent_Batch + Flow_NaOH_Batch;
```

```
#   Flow_Reagent_Batch = Flow_NaOH_Batch;

#-------------------          MASS BALANCE          -------------------
   # The diffusion term has negligable effect on the results so it was removed
   FOR z := 0|+ TO ReactorLength|- DO
      FOR r := 0|+ TO ReactorRadius|- DO
         # Diffusion term not included
         # [Molar/min]   = [m/min]*[Molar/m]              + [Molar/min]
         $C_T_Mg(z,r)    = -v_z(r)*PARTIAL(C_T_Mg(z,r),Axial) + v_Mg*Kinetics.rate(z,r);
         $C_T_NH4(z,r)   = -v_z(r)*PARTIAL(C_T_NH4(z,r),Axial) + v_NH4*Kinetics.rate(z,r);
         $C_T_PO4(z,r)   = -v_z(r)*PARTIAL(C_T_PO4(z,r),Axial) + v_PO4*Kinetics.rate(z,r);
         $C_Na(z,r)      = -v_z(r)*PARTIAL(C_Na(z,r), Axial);
         $C_Cl(z,r)      = -v_z(r)*PARTIAL(C_Cl(z,r), Axial);
         $C_MAP(z,r)     = -v_z(r)*PARTIAL(C_MAP(z,r), Axial) + v_MAP*Kinetics.rate(z,r);

         # Axial Diffusion term included:
#            $C_T_Mg(z,r)     = -v_z(r)*PARTIAL(C_T_Mg(z,r),Axial) + D*PARTIAL(C_T_Mg(z,r),Axial,Axial) +
v_Mg*Kinetics.rate(z,r); # [Molar/min] = [m/min]*[Molar/m] + [m^2/s]*[Molar/m^2]*[60s/min]
#          $C_T_NH4(z,r)   = -v_z(r)*PARTIAL(C_T_NH4(z,r),Axial) + D*PARTIAL(C_T_NH4(z,r),Axial,Axial) +
v_NH4*Kinetics.rate(z,r);
#           $C_T_PO4(z,r)   = -v_z(r)*PARTIAL(C_T_PO4(z,r),Axial) + D*PARTIAL(C_T_PO4(z,r),Axial,Axial) +
v_PO4*Kinetics.rate(z,r);
#         $C_Na(z,r)      = -v_z(r)*PARTIAL(C_Na(z,r), Axial) + D*PARTIAL(C_Na(z,r),Axial,Axial);
#         $C_Cl(z,r)      = -v_z(r)*PARTIAL(C_Cl(z,r), Axial) + D*PARTIAL(C_Cl(z,r),Axial,Axial);
#             $C_MAP(z,r)      = -v_z(r)*PARTIAL(C_MAP(z,r), Axial) + D*PARTIAL(C_MAP(z,r),Axial,Axial) +
v_MAP*Kinetics.rate(z,r);

         # Axial and Radial Diffusion term included:
#            $C_T_Mg(z,r)     = -v_z(r)*PARTIAL(C_T_Mg(z,r),Axial) + D*PARTIAL(C_T_Mg(z,r),Axial,Axial) +
D*PARTIAL(C_T_Mg(z,r),Radial,Radial) + v_Mg*Kinetics.rate(z,r); # [Molar/min] = [m/min]*[Molar/m] +
[m^2/s]*[Molar/m^2]*[60s/min]
#          $C_T_NH4(z,r)   = -v_z(r)*PARTIAL(C_T_NH4(z,r),Axial) + D*PARTIAL(C_T_NH4(z,r),Axial,Axial) +
D*PARTIAL(C_T_NH4(z,r),Radial,Radial) + v_NH4*Kinetics.rate(z,r);
#           $C_T_PO4(z,r)   = -v_z(r)*PARTIAL(C_T_PO4(z,r),Axial) + D*PARTIAL(C_T_PO4(z,r),Axial,Axial) +
D*PARTIAL(C_T_PO4(z,r),Radial,Radial) + v_PO4*Kinetics.rate(z,r);
#                $C_Na(z,r)         = -v_z(r)*PARTIAL(C_Na(z,r),  Axial)  + D*PARTIAL(C_Na(z,r),Axial,Axial) +
D*PARTIAL(C_Na(z,r),Radial,Radial);
#                 $C_Cl(z,r)          =  -v_z(r)*PARTIAL(C_Cl(z,r),  Axial)  +  D*PARTIAL(C_Cl(z,r),Axial,Axial)  +
D*PARTIAL(C_Cl(z,r),Radial,Radial);
#             $C_MAP(z,r)      = -v_z(r)*PARTIAL(C_MAP(z,r), Axial) + D*PARTIAL(C_MAP(z,r),Axial,Axial) +
D*PARTIAL(C_MAP(z,r),Radial,Radial) + v_MAP*Kinetics.rate(z,r);
      END #FOR
   END #FOR

#-------------------          OUTLET CONDITIONS          -------------------
   {Average molar flow rates of each component exiting the reactor (integrated over the radius)}
   C_NH4_out          =          INTEGRAL(     r     :=     0:ReactorRadius     ;
v_z(r)*2*pi*r*C_T_NH4(ReactorLength,r))*1000*1/Flow_T*60;                                          #
[m/min]*[m]*[mol/L]*[m]*[L/m^3]*[h/L]*[min/h] = [mol/L]
```

```
   C_Mg_out = INTEGRAL( r := 0:ReactorRadius ;
v_z(r)*2*pi*r*C_T_Mg(ReactorLength,r))*1000*1/Flow_T*60; #
[m/min]*[m]*[mol/L]*[m]*[L/m^3]*[h/L]*[min/h] = [mol/L]
   C_PO4_out = INTEGRAL( r := 0:ReactorRadius ;
v_z(r)*2*pi*r*C_T_PO4(ReactorLength,r))*1000*1/Flow_T*60; #
[m/min]*[m]*[mol/L]*[m]*[L/m^3]*[h/L]*[min/h] = [mol/L]
   C_Na_out = INTEGRAL( r := 0:ReactorRadius ;
v_z(r)*2*pi*r*C_Na(ReactorLength,r))*1000*1/Flow_T*60; #
[m/min]*[m]*[mol/L]*[m]*[L/m^3]*[h/L]*[min/h] = [mol/L]
   C_Cl_out = INTEGRAL( r := 0:ReactorRadius ;
v_z(r)*2*pi*r*C_Cl(ReactorLength,r))*1000*1/Flow_T*60; #
[m/min]*[m]*[mol/L]*[m]*[L/m^3]*[h/L]*[min/h] = [mol/L]
   C_MAP_out = INTEGRAL( r := 0:ReactorRadius ;
v_z(r)*2*pi*r*C_MAP(ReactorLength,r))*1000*1/Flow_T*60; #
[m/min]*[m]*[mol/L]*[m]*[L/m^3]*[h/L]*[min/h] = [mol/L]

   # MAP concentration profile
   FOR z := 0 TO ReactorLength DO
      C_MAP_int(z)   =   INTEGRAL( r := 0:ReactorRadius ; v_z(r)*2*pi*r*C_MAP(z,r))*1000*1/Flow_T*60;
# [m/min]*[m]*[mol/L]*[m]*[L/m^3]*[h/L]*[min/h] = [mol/L]
   END # FOR


   # Instantaneous mass conc. (not time averaged over the interval)
   C_MAP_out_g        =   C_MAP_out*245.41; # [mol/min]*[h/L]*[min/h]*[g/mol] = [g/L]

   {Integrated flow term at the exit to check conservation of volume}
   # This may be the cause of outlet concentration integration not giving the correct result
   Flow_T_out   =   INTEGRAL( r := 0:ReactorRadius ; v_z(r)*2*pi*r ) * 1000 * 60; # [m/min]*[m]*[m] =
[m^3/min];[m^3/min]*[1000L/m^3]*[60min/h]=[L/h]
   C_Mg_out_2 = INTEGRAL( r := 0:ReactorRadius ;
v_z(r)*2*pi*r*C_T_Mg(ReactorLength,r))*1000*1/Flow_T_out*60; #
[m/min]*[m]*[mol/L]*[m]*[L/m^3]*[h/L]*[min/h] = [mol/L]

   {Saturation Index at the outlet}
   Thermo_out.C_T_Mg   =   C_Mg_out; # [mol/min]*[1min] assume a 1min basis
   Thermo_out.C_T_PO4  =   C_PO4_out; # [mol/min]*[1min] assume a 1min basis
   Thermo_out.C_T_NH4  =   C_NH4_out; # [mol/min]*[1min] assume a 1min basis
   Thermo_out.C_Na     =   C_Na_out; # [mol/min]*[1min] assume a 1min basis
   Thermo_out.C_Cl     =   C_Cl_out; # [mol/min]*[1min] assume a 1min basis
   Thermo_out.SI       =   SI_out;
   Thermo_out.pH       =   pH_out;

   {Thermodynamic yield - needs adjustment for each initial concentration}
   Yield_thermo       =   (C_T_PO4(0,0) - C_PO4_out)/(C_T_PO4(0,0)-C_T_P_satd);   #from EES for SI=1.0.
0.008335 for SI=0.8; 0.007515 for SI=1.4;

   {Percentage overshoot of the crystal relative to the PO4 removal.}
   C_MAP_out          = MAP_MB_percent_overshoot   * (C_T_PO4_in - C_PO4_out); # Rearrange to avoid
div0 error during simulation
```

```
# TIME INTEGRATED MASS CONCENTRATION OF STRUVITE EXITING THE REACTOR - Only necessary for parameter regression
  {Average concentration of MAP exiting the reactor between 10min samples}
  # internal time variable to continuously calculate integrating variable:
  $my_time = 1;
{
  FOR i := 1 TO NoSamples DO
#      # WHY IS integrating not = 0? break up the terms:
#      # for i=2: 0 until t=10, 1 after.
#      first_term(i) = MAX(0, SGN(my_time-10*(i-1)) );
#      # for i=2: 1 before t=20, 0 after
#      second_term(i) = MAX(0, SGN(10*i-my_time) );
#      integrating(i) = first_term(i) * second_term(i);

    # integrating original:
    integrating(i)        =   MAX(0, SGN(my_time-10*(i-1)) ) * MAX(0, SGN(10*i-my_time) );
#      integrating(i) = (TANH(1E10*(my_time-10*(i-1)))+1)/2 * (TANH( -1E10*(my_time-10*i) )+1)/2;

#      # integrating ALTERNATIVE 1:
#        IF my_time < 10*i AND my_time >= 10*(i - 1) THEN
#          integrating(i) = 1 ;
#          ELSE
#          integrating(i) = 0 ;
#        END

    # Samples time of sample i starts counting when integrating = 1
    $SampleTime(i)        =   integrating(i);
    # The average concentration over sample i is given by:
    SampleTime(i) * $C_MAP_out_g_bar(i)     =   integrating(i)*C_MAP_out_g;

  END # FOR
}

# Eliminate time integrated sampling:
    first_term      = 0;
    second_term     = 0;
    integrating     = 0;
    SampleTime      = 0;
    C_MAP_out_g_bar  = 0;


INITIAL
  tau = 0;
  my_time = 0;
#   C_MAP_out_g_bar = 0;
#   SampleTime = 0;
```

E.2.2. CAT implicit nucleation growth kinetics

```
{ This model uses the implicit numerical NCG model only.
Solution description:
 - Within the reactor:
   - particle number changes are described by an advection and reaction (DPB) model
   - molar rate of MAP production/ species consumption is the sum of particle number changes
   - liquid species concentrations are described by an advection and reaction model
 - At the boundaries (as advised by all texts including Rice & Do):
   - inlets are defined using type 1/ dirichlet boundary conditions i.e. the feeds
   - others are defined using type 2/ Neumann boundary condition (dC/dz=0), which gives
homogeneous problem definition (only one solution)
   - symetry condition is applied to the centreline dC/dr=0
      - From what i can tell from Rice & Do, dC/dr @ R is linked to this symetry condition
         Nick also said that this is physically correct due to no slip condition
   - outlet boundary dC/dz=0 stops numerical accumulation upstream (especially relevant when
diffusion is included)
   - rate terms defined within the model are set to zero at all boundaries as they are not used in the
problem description
      and N & C are defined by the boundary conditions. This is confirmed by running the boundary
rate at different values.
}

UNIT
   Thermo AS Thermodynamics_dist       # Axially and radially distributed thermo model

PARAMETER
   PI               AS  REAL DEFAULT 3.14159265  #Pi
   # NEQ selected such that particles do not grow to the last cell size
   NEQ              AS  INTEGER #The number of discrete size domains
   rho_struvite       AS  REAL    # kg/m^3
   rho_water          AS  REAL    # kg/m^3
   mu_water           AS  REAL    # Pa.s
   ReactorLength      AS  REAL    # [m]
   ReactorRadius      AS  REAL    # [m]
   number_scaling     AS  REAL


DISTRIBUTION_DOMAIN
Axial      AS  [ 0 : ReactorLength ]
Radial     AS  [ 0 : ReactorRadius ]


VARIABLE
   N_out              AS  Distribution(NEQ)                 OF NDENSITY # [1E6 xtl/L];       Total number of
particles exiting the reactor
   N                AS  Distribution(NEQ,Axial,Radial)      OF NDENSITY # [1E6 xtl/L];       Total number of
particles at each node. Use NDENSITY variable type - same bounds
   n_density          AS  Distribution(NEQ,Axial,Radial)      OF NDENSITY # [1E6 xtl/um^3.L];   Number
density of particles for each node
   n_density_length    AS  Distribution(NEQ,Axial,Radial)      OF NDENSITY # [1E6 xtl/um.L];     length
based discretisation number density
```

```
  v              AS  Distribution(NEQ)              OF Volume   # [um^3];      representative volume of
each node
  L              AS  Distribution(NEQ)              OF Length   # [um];        representative length of each
node
  W              AS  Distribution(NEQ+1)            OF NOTYPE   # [um^3];      width of volume distributed
cells
  W_L            AS  Distribution(NEQ+1)            OF NOTYPE   # [um];        width of length distributed
cells
  G              AS  Distribution(NEQ,Axial,Radial)     OF NOTYPE   # [um^3/min];   constant volume
growth rate
  G_L            AS  Distribution(Axial,Radial)         OF NOTYPE   # [um/min];    constant length based
growth rate - size independent growth
  LOWER          AS  Distribution(NEQ+2)            OF NOTYPE   # [um^3];      Lower bound on cell i.
  LOWER_L        AS  Distribution(NEQ+2)            OF NOTYPE   # [um];        Lower length bound on
cell i.
  q              AS  NOTYPE                                     #          geometric progression coarseness factor
  MOM            AS  Distribution(2,Axial,Radial)       OF NOTYPE   # [1E6 xtl/L]; [um^3/L]; Moments of
the particle size distribution
  B_nuc          AS  Distribution(Axial,Radial)         OF NOTYPE   # [1E6 xtl/L.min];   Nucleation rate
varies through reactor but only exists in the first size range.
  D_4_3          AS  Distribution(Axial,Radial)         OF Length   # [um]        Volume weighted median
diameter
  D_3_0          AS  Distribution(Axial,Radial)         OF Length   # [um]        Number weighted median
diameter
  v_z            AS  Distribution(Radial)           OF Velocity # [m/min];     discrete fluid velocity at a
given radius
  rate           AS  Distribution(Axial,Radial)         OF rate     # [Molar/min];  refers to the molar
production rate of struvite
  rate_g         AS  Distribution(Axial,Radial)         OF rate     # [Molar/min];
  NDASH_xtl      AS  Distribution(NEQ,Axial,Radial)     OF rate     # [1E6 xtl/L.min];   change in particle
number in a size due to crystallisation
  NDASH_tot      AS  Distribution(NEQ,Axial,Radial)     OF rate     # [1E6 xtl/L.min];   total change in
particle number including advection
  VP_out         AS ARRAY(NEQ)                  OF Dimensionless    # [%];        volume % exiting the
reactor
  VPC_out        AS ARRAY(NEQ)                  OF Dimensionless    # [%];        cumulative volume %
exiting the reactor
  VMD_out        AS                                 Length      # [um];        the VMD exiting the reactor =
SIGMA(VMD_out)
  VMD_cell_out   AS ARRAY(NEQ-1)                OF Length       # [um];        an array of particle sizes
where all elements are zero accept that where the VMD lies
  D10_cell_out   AS ARRAY(NEQ-1)                OF Length       # [um];        an array of particle sizes
where all elements are zero accept that where the D10 lies
  D90_cell_out   AS ARRAY(NEQ-1)                OF Length       # [um];        an array of particle sizes
where all elements are zero accept that where the D90 lies
  PSD_width_out  AS                                 Length      # [um];        the PSD width exiting the reactor
  particulate_num   AS  NOTYPE
  induction_fcn  AS  Distribution(Axial,Radial)  OF  NOTYPE
  t_ind          AS  NOTYPE

  # PARAMETERS TO BE ESTIMATED
```

```
   k_g              AS  NOTYPE
   n_g              AS  NOTYPE
   k_nuc            AS  NOTYPE
   n_nuc            AS  NOTYPE

   # ALTERNATIVE GROWTH KINETICS
   k_g_avg          AS  NOTYPE
   n_g_avg          AS  NOTYPE
   S_r              AS  Distribution(Axial,Radial) OF Dimensionless

   # ALTERNATIVE NUCLEATION KINETICS
   tension          AS  NOTYPE
   A_factor         AS  NOTYPE
   omega            AS  Distribution(Axial,Radial) OF Dimensionless
   G_L_2            AS  Distribution(Axial,Radial)      OF NOTYPE   # [um/min];     constant length based growth rate - size independent growth
   B_nuc_2          AS  Distribution(Axial,Radial)      OF NOTYPE   # [1E6 xtl/L.min];    Nucleation rate varies through reactor but only exists in the first size range.
   Null_Sat         AS                    NOTYPE


#SELECTOR
   # Use a selector to turn off the growth and nucleation rate at saturation. Make sure saturation is positive initially first
#    Saturation AS (Oversat, Undersat) DEFAULT Oversat

SET
   rho_struvite       :=  1740; #kg/m^3
   rho_water          :=  998; #kg/m^3
   mu_water           :=  0.001002; #Pa.s
#    k_d              :=  0; #12.49; # set as the same as growth rate via galbraith model
#    n_d              :=  5.06; # set as the same as growth rate via galbraith model
   NEQ                :=  87; #87; #101; #35 was previously 35 but PFC only achieves 24, simulation will fail if bound is hit
#    number_scaling     :=  1E-6; # [Mxtl/1E6xtl] - scale particle number to avoid integration errors

BOUNDARY
# ALL POSSIBLE BOUNDARIES:
   # rate_g @ r=R for 0|+ - L|-
FOR z := 0|+ TO ReactorLength|- DO
   rate_g(z,ReactorRadius) = 1;
   # rate_g @ r=0 for 0|+ - L|-
   rate_g(z,0) = 1;
END #FOR
   # rate_g @ z=0 for 0 - R
   rate_g(0,) = 1;
   # rate_g @ z=L for 0 - R
   rate_g(ReactorLength,) = 1;

FOR z := 0|+ TO ReactorLength|- DO
   # rate @ r for 0|+ - L|-
```

```
   rate(z,ReactorRadius) = 0;
   # rate @ r=0 for 0|+ - L|-
   rate(z,0) = 0;
END #FOR
   # rate @ z=0 for 0 - R
   rate(0,) = 0;
   # rate @ z=L for 0 - R
   rate(ReactorLength,) = 0;

FOR z := 0|+ TO ReactorLength|- DO
   # NDASH_tot @ r for 0|+ - L|-
   NDASH_tot(,z,ReactorRadius) = 0;
   # NDASH_tot @ r=0 for 0|+ - L|-
   NDASH_tot(,z,0) = 0;
   # NDASH_xtl @ r for 0|+ - L|-
   NDASH_xtl(,z,ReactorRadius) = 0;
   # NDASH_xtl @ r=0 for 0|+ - L|-
   NDASH_xtl(,z,0) = 0;
END #FOR
   # NDASH_tot @ z=0 for 0 - R
   NDASH_tot(,0,) = 0;
   # NDASH_tot @ z=L for 0 - R
   NDASH_tot(,ReactorLength,) = 0;
   # NDASH_xtl @ z=0 for 0 - R
   NDASH_xtl(,0,) = 0;
   # NDASH_xtl @ z=L for 0 - R
   NDASH_xtl(,ReactorLength,) = 0;

   # @ z=0, for all r, @ NEQ = 1, N = 1 - one particle of the smallest size enters the reactor at all radii
   # INLET
   # @ z=0, for all r:
      FOR r := 0 TO ReactorRadius DO
         N(1,0,r) = number_scaling*particulate_num; # always 1E6 particles coming in in the first size
bracket - avoids div0 errors
         N(2:NEQ,0,r) = 0;
      END

   # OUTLET
   # @ z = ReactorLength, for all r, for all NEQ, dN/dz = 0 - number of particles does not change axially
at the exit
      FOR r := 0 TO ReactorRadius DO
         PARTIAL(N(,ReactorLength,r),Axial)   =   0;
      END

   # CENTRELINE
   # @ r = 0, for all z (except the ends), for all NEQ, dN/dr = 0 - number of particles does not vary
radially at the centreline
      FOR z := 0|+ TO ReactorLength|- DO
         PARTIAL(N(,z,0),Radial)        =   0;
      END #FOR
   # WALL
```

```
  # @ r = ReactorRadius, for all z (except the ends), for all NEQ, dN/dr = 0 - number of particles does
not vary radially at the boundary
      FOR z := 0|+ TO ReactorLength|- DO
        PARTIAL(N(,z,ReactorRadius),Radial)        =   0;
      END #FOR


EQUATION
#--------------          PSD DISCRETISATION (Malvern)          ---------------
   # Discretisation factor - define just to make the model work:
   q = 4;
   # Length-Volume relationship
   v = pi/6*L^3;

   # Lower bounds:
   LOWER(1) = 0;
   LOWER_L(1) = 0;
   # lower bound of 2nd to NEQ+1 cell (determined by width discretisation)
   FOR i := 2 TO NEQ+2 DO
   # Both of these can be defined at the same time as they are independent
      LOWER(i) = LOWER(i-1) + W(i-1); # (4)
      LOWER_L(i) = LOWER_L(i-1) + W_L(i-1); # (2)
   END
   # Widths:
   W(1) = 2*v(1);
   W_L(1) = 2*L(1); #know L(1) from the v/L relationship above
   # Width of 2nd to NEQ cell determined by geo discretisation
   FOR i := 2 TO NEQ+1 DO
      W_L(i) = LOWER_L(i+1) - LOWER_L(i); # (1)
      W(i) = LOWER(i+1) - LOWER(i); # (3)
   END

   # Malvern cell sizes (Particle diameter)
   L(1)= 0.01      ;
   L(2)= 0.0114  ;
   L(3)= 0.0129  ;
   L(4)= 0.0147  ;
   L(5)= 0.0167  ;
   L(6)= 0.0189  ;
   L(7)= 0.0215  ;
   L(8)= 0.0244  ;
   L(9)= 0.0278  ;
   L(10)=          0.0315  ;
   L(11)=          0.0358  ;
   L(12)=          0.0407  ;
   L(13)=          0.0463  ;
   L(14)=          0.0526  ;
   L(15)=          0.0597  ;
   L(16)=          0.0679  ;
   L(17)=          0.0771  ;
   L(18)=          0.0876  ;
```

L(19)= 0.0995 ;
L(20)= 0.113 ;
L(21)= 0.128 ;
L(22)= 0.146 ;
L(23)= 0.166 ;
L(24)= 0.188 ;
L(25)= 0.214 ;
L(26)= 0.243 ;
L(27)= 0.276 ;
L(28)= 0.314 ;
L(29)= 0.357 ;
L(30)= 0.405 ;
L(31)= 0.46 ;
L(32)= 0.523 ;
L(33)= 0.594 ;
L(34)= 0.675 ;
L(35)= 0.767 ;
L(36)= 0.872 ;
L(37)= 0.991 ;
L(38)= 1.13 ;
L(39)= 1.28 ;
L(40)= 1.45 ;
L(41)= 1.65 ;
L(42)= 1.88 ;
L(43)= 2.13 ;
L(44)= 2.42 ;
L(45)= 2.75 ;
L(46)= 3.12 ;
L(47)= 3.55 ;
L(48)= 4.03 ;
L(49)= 4.58 ;
L(50)= 5.21 ;
L(51)= 5.92 ;
L(52)= 6.72 ;
L(53)= 7.64 ;
L(54)= 8.68 ;
L(55)= 9.86 ;
L(56)= 11.2 ;
L(57)= 12.7 ;
L(58)= 14.5 ;
L(59)= 16.4 ;
L(60)= 18.7 ;
L(61)= 21.2 ;
L(62)= 24.1 ;
L(63)= 27.4 ;
L(64)= 31.1 ;
L(65)= 35.3 ;
L(66)= 40.1 ;
L(67)= 45.6 ;
L(68)= 51.8 ;
L(69)= 58.9 ;

```
   L(70)=       66.9    ;
   L(71)=       76      ;
   L(72)=       86.4    ;
   L(73)=       98.1    ;
   L(74)=       111     ;
   L(75)=       127     ;
   L(76)=       144     ;
   L(77)=       163     ;
   L(78)=       186     ;
   L(79)=       211     ;
   L(80)=       240     ;
   L(81)=       272     ;
   L(82)=       310     ;
   L(83)=       352     ;
   L(84)=       400     ;
   L(85)=       454     ;
   L(86)=       516     ;
   L(87)=       586     ;


#-------------------          KINETICS          -------------------
   # Kinetics can be defined over the whole reactor and not used at the boundaries
   # Nucleation kinetics
   FOR z := 0 TO ReactorLength DO
      FOR r := 0 TO ReactorRadius DO
         induction_fcn(z,r) = (tanh(1E10*(z - v_z(r)*t_ind))+1)/2; # zero when length is less than
induction length
      END
   END

   B_nuc = number_scaling*induction_fcn*(k_nuc*(Thermo.SI* ( (tanh(1E20*Thermo.SI)+1) / 2)
)^n_nuc); # [Mxtl/L/min]=[Mxtl/1E6 xtl][xtl/L.min]
   G_L = induction_fcn*k_g*(Thermo.SI*(tanh(1E20*Thermo.SI)+1)/2)^n_g; # [um/min]

   # ALTERNATIVE GROWTH KINETICS (comment in and change to G_L as required):
      # Screw dislocation model:
      omega = 10^Thermo.SI ;
      S_r = (omega)^(1/3)-1;
   #   G_L_2 = induction_fcn*k_g_avg*(S_r*(tanh(1E20*Thermo.SI)+1)/2)^n_g_avg;

      # Birth and spread model:
      G_L_2 = induction_fcn*k_g_avg*(S_r*(tanh(1E20*Thermo.SI)+1)/2)^2 * exp(-
((10^Null_Sat)^(1/3)-1)/(S_r*(tanh(1E20*Thermo.SI)+1)/2));
      Null_Sat = 0.3;

      # Theoretical nucleation rate - should be in the range of 1E7 at inlet to 1E-4 at outlet
      B_nuc_2 = induction_fcn*number_scaling*A_factor*exp(-16.75*(tension/1000)^3*(7.94655E-
23/1E6)^2/(1.38E-23^3*298^3*(log(omega))^2));

   # Converting to volumetric growth rate:
   FOR z := 0 TO ReactorLength DO
```

```
    FOR r := 0 TO ReactorRadius DO
      # Number/ number density relation for all cells
      FOR i := 1 TO NEQ DO
        # GROWTH RATE - Define the growth rate in the DPB in terms of the SI
        # ignore rate constants for purposes of model validation
        G(i,z,r) = pi/2*(6*v(i)/pi)^(2/3)*G_L(z,r); # [um^3/min] = [um^3]^(2/3) * [um/min]
      END #FOR
    END #FOR
  END #FOR

#-------------------          NCG DPB          -------------------
# DPB exists to give rate
# Definition of rate terms through reactor volume:
FOR z := 0|+ TO ReactorLength|- DO
    FOR r := 0|+ TO ReactorRadius|- DO
      # SEPARATE POP BAL AND PARTICLE ADVECTION:
        # NDASH is the rate of change of particles due to particle interactions:
      # ODE for first cell - derived assuming N(i-1)=0 as i-1 cell does not exist
      NDASH_xtl(1,z,r) = B_nuc(z,r) - G(1,z,r)*N(1,z,r)/(v(2)-v(1)) ; # [Mxtl/L.min] = [Mxtl/L.min] -
[um^3/min]*[Mxtl/L]/[um^3]
      # ODE for 2nd to NEQ-1 cell
      FOR i := 2 TO NEQ-1 DO
        NDASH_xtl(i,z,r) = G(i-1,z,r)*N(i-1,z,r)/(v(i)-v(i-1)) - G(i,z,r)*N(i,z,r)/(v(i+1)-v(i)); # [Mxtl/L.min]
= [um^3/min]*[Mxtl/L]/[um^3] - [um^3/min]*[Mxtl/L]/[um^3]
      END
      # ODE for last cell - derived to include a calculation for average cell volume
      NDASH_xtl(NEQ,z,r) = G(NEQ,z,r)*(N(NEQ-1,z,r)/(v(NEQ)-v(NEQ-1)) -
N(NEQ,z,r)/((pi/6)*((2*LOWER(NEQ+1)+W(NEQ+1))/2)^3-v(NEQ))); # [Mxtl/L.min] =
[um^3/min]*[Mxtl/L]/[um^3] - [um^3/min]*[Mxtl/L]/[um^3]

      #ADVECTION TERM
      FOR i := 1 TO NEQ DO
        NDASH_tot(i,z,r) = -v_z(r)*PARTIAL(N(i,z,r),Axial) + NDASH_xtl(i,z,r); # [Mxtl/L.min] =
[m/min]*[Mxtl/L.m] + [Mxtl/L.min]
      END
      rate_g(z,r) = SIGMA(NDASH_xtl(,z,r)*1/number_scaling*v)*1E-18*1E3*1710/245.41; #
[Molar/min] = [Mxtl/L.mim]*[1E6xtl/Mxtl]*[micron^3/xtl.L]*[1E-
18m^3/micron^3]*[1000L/m^3]*[1710g/L]*[1mol/245.41g]
      # Molar rate of MAP production:
      rate(z,r) = rate_g(z,r); # + rate_d(z,r); # [Molar/min]
      # NDASH
      $N(,z,r) = NDASH_tot(,z,r); # [Mxtl/L.min];    combination of number change due to
crystallisation and advection
    END #FOR
  END #FOR

#-------------------          PSD PROPERTIES          -------------------
# Distribution descriptions can occur over whole reactor.
  FOR z := 0 TO ReactorLength DO
    FOR r := 0 TO ReactorRadius DO
      # Number/ number density relation for all cells
```

```
         FOR i := 1 TO NEQ DO
            #n_density(i) = N(i)/(LOWER(i+1)-LOWER(i));
            n_density(i,z,r) = N(i,z,r)/W(i); # [1/um^3.L] = [1/L]/[um^3]
            # Number density Length-Volume relationship
            n_density_length(i,z,r) = n_density(i,z,r)*pi/2*L(i)^2; # [1/um.L] = [1/um^3.L]*[um^2]
         END #FOR

         # Numerical zeroth and first moments
         MOM(1,z,r) = SIGMA(N(,z,r)/number_scaling);  #ZEROTH MOMENT - total particle number
         MOM(2,z,r) = SIGMA(v*N(,z,r)/number_scaling);  #FIRST MOMENT - total volume [micron^3/L]
         # Volume weighted mean diameter:
         D_4_3(z,r) = SIGMA(N(,z,r)*L^4)/SIGMA(N(,z,r)*L^3);
         #will sigma operator work or do i need to define N(,z,r)?
         # when referring to a 3D array i think you need to refer to the whole row - check
         # Number volume mean diameter:
         D_3_0(z,r) = (SIGMA(N(,z,r)*L^3)/SIGMA(N(,z,r)))^(1/3);
      END #FOR
   END #FOR

# VOLUME % @ OUTLET
   FOR i := 1 TO NEQ DO
   # for every size range, volume% [%] * total crystal volume at reactor exit [um^3/L] = volume of the
size range [um^3] * total number of particles in that range exiting the reactor [1/L]
      VP_out(i)*SIGMA(MOM(2,ReactorLength,)) =
v(i)*SIGMA(N(i,ReactorLength,)/number_scaling)*100; # has to be written this way to avoid div0 at
t=0
      N_out(i) = SIGMA(N(i,ReactorLength,));
   END

# CUMULATIVE VOLUME % @ OUTLET
   VPC_out(1) = VP_out(1);
   FOR i := 2 TO NEQ DO
      VPC_out(i) = VPC_out(i-1) + VP_out(i);
   END #FOR

# D[10], D[90] & VOLUME MEDIAN DIAMETER @ OUTLET
   FOR i := 1 TO NEQ-1 DO
      VMD_cell_out(i) = MAX( 0,SGN(VPC_out(i+1) - 50) ) * MAX(0,SGN(50 - VPC_out(i)) ) * ( (50-
VPC_out(i))/((VPC_out(i+1) - VPC_out(i))/(L(i+1) - L(i))) + L(i) ) ;
      D10_cell_out(i) = MAX( 0,SGN(VPC_out(i+1) - 10) ) * MAX(0,SGN(10 - VPC_out(i)) ) * ( (10-
VPC_out(i))/((VPC_out(i+1) - VPC_out(i))/(L(i+1) - L(i))) + L(i) ) ;
      D90_cell_out(i) = MAX( 0,SGN(VPC_out(i+1) - 90) ) * MAX(0,SGN(90 - VPC_out(i)) ) * ( (90-
VPC_out(i))/((VPC_out(i+1) - VPC_out(i))/(L(i+1) - L(i))) + L(i) ) ;
   END
   VMD_out = SIGMA(VMD_cell_out);
   PSD_width_out = SIGMA(D90_cell_out) - SIGMA(D10_cell_out);
```

E.2.3. CAT explicit nucleation, growth and aggregation kinetics

```
{ This model uses the implicit numerical NCG model only.

Solution description:
 - Within the reactor:
```

```
   - particle number changes are described by an advection and reaction (DPB) model
   - molar rate of MAP production/ species consumption is the sum of particle number changes
   - liquid species concentrations are described by an advection and reaction model
 - At the boundaries (as advised by all texts including Rice & Do):
   - inlets are defined using type 1/ dirichlet boundary conditions i.e. the feeds
   - others are defined using type 2/ Neumann boundary condition (dC/dz=0), which gives
homogeneous problem definition (only one solution)
   - symetry condition is applied to the centreline dC/dr=0
      - From what i can tell from Rice & Do, dC/dr @ R is linked to this symetry condition
         Nick also said that this is physically correct due to no slip condition
   - outlet boundary dC/dz=0 stops numerical accumulation upstream (especially relevant when
diffusion is included)
   - rate terms defined within the model are set to zero at all boundaries as they are not used in the
problem description
      and N & C are defined by the boundary conditions. This is confirmed by running the boundary
rate at different values.

SCALING:
 - scale to have units of N be [million crystals]
   - scale: B_nuc; N; n_density; n_density_length; MOM(1)
      -> NDASH_xtl and NDASH_tot will be reduced accordingly
   - reverse scale: rate_g; rate
}

UNIT
   # Insert an instance of the thermo model into this one to refer to the Sa variable
   Thermo AS Thermodynamics_dist

PARAMETER
   PI               AS  REAL DEFAULT 3.14159265  #Pi
   NEQ              AS  INTEGER #The number of discrete size domains. Selected such that particles do
not grow to the last cell size
   rho_struvite       AS  REAL    # kg/m^3
   rho_water          AS  REAL    # kg/m^3
   mu_water           AS  REAL    # Pa.s
   ReactorLength      AS  REAL    # [m]
   ReactorRadius      AS  REAL    # [m]
   number_scaling     AS  REAL
   k_H     AS REAL DEFAULT 1E30 #1E7 # see analytic H-step function for explanation


DISTRIBUTION_DOMAIN
Axial      AS  [ 0 : ReactorLength ]
Radial     AS  [ 0 : ReactorRadius ]


VARIABLE
# PSD properties
   N_out            AS  Distribution(NEQ)                OF NDENSITY
   N                AS  Distribution(NEQ,Axial,Radial)      OF NDENSITY # [1E6 xtl/L];       Total number of
particles at each node. Use NDENSITY variable type - same bounds
```

```
    n_density          AS  Distribution(NEQ,Axial,Radial)      OF NDENSITY # [1E6 xtl/um^3.L];   Number
density of particles for each node
    n_density_length    AS  Distribution(NEQ,Axial,Radial)      OF NDENSITY # [1E6 xtl/um.L];     length
based discretisation number density
    MOM                AS  Distribution(2,Axial,Radial)       OF NOTYPE   # [1E6 xtl/L]; [um^3/L]; Moments
of the particle size distribution
    D_4_3              AS  Distribution(Axial,Radial)         OF Length   # [um]         Volume weighted median
diameter
    D_3_0              AS  Distribution(Axial,Radial)         OF Length   # [um]         Number weighted
median diameter
    VP_out             AS ARRAY(NEQ)                  OF Dimensionless    # [%];         volume % exiting the
reactor
    VPC_out            AS ARRAY(NEQ)                  OF Dimensionless    # [%];         cumulative volume %
exiting the reactor
    VMD_out            AS                             Length          # [um];        the VMD exiting the reactor =
SIGMA(VMD_out)
    VMD_cell_out       AS ARRAY(NEQ-1)                OF Length          # [um];        an array of particle sizes
where all elements are zero accept that where the VMD lies
    D10_cell_out       AS ARRAY(NEQ-1)                OF Length          # [um];        an array of particle sizes
where all elements are zero accept that where the D10 lies
    D90_cell_out       AS ARRAY(NEQ-1)                OF Length          # [um];        an array of particle sizes
where all elements are zero accept that where the D90 lies
    PSD_width_out      AS                             Length          # [um];        the PSD width exiting the reactor
    particulate_num    AS  NOTYPE

# PSD discretisation:
    v                  AS  Distribution(NEQ)          OF Volume   # [um^3];      representative volume of
each node
    L                  AS  Distribution(NEQ)          OF Length   # [um];        representative length of each
node
    W                  AS  Distribution(NEQ+1)        OF NOTYPE   # [um^3];      width of volume
distributed cells
    W_L                AS  Distribution(NEQ+1)        OF NOTYPE   # [um];        width of length
distributed cells
    LOWER              AS  Distribution(NEQ+2)        OF NOTYPE   # [um^3];      Lower bound on cell i.
    LOWER_L            AS  Distribution(NEQ+2)        OF NOTYPE   # [um];        Lower length bound
on cell i.
    q                  AS  NOTYPE                                #              geometric progression coarseness factor

# Nucleaiton kinetics:
    B_nuc              AS  Distribution(Axial,Radial)         OF NOTYPE   # [1E6 xtl/L.min];    Nucleation rate
varies through reactor but only exists in the first size range.
    V_nuc              AS  Distribution(Axial,Radial)         OF NOTYPE   # [1E6 xtl/L.min];    Nucleation rate
varies through reactor but only exists in the first size range.
    induction_fcn      AS  Distribution(Axial,Radial)  OF  NOTYPE
    t_ind              AS  NOTYPE

# Growth kinetics:
    G_v                AS Distribution(NEQ,Axial,Radial)      OF NOTYPE   # [um^3/min];   constant volume
growth rate
```

```
   G_L              AS Distribution(Axial,Radial)        OF NOTYPE   # [um/min];     constant length based
growth rate - size independent growth
   B_growth          AS Distribution(NEQ,Axial,Radial)   OF NumRate # [particles/min] {0 to 1E25} Total
birth rate of particles due to growth at each node
   D_growth          AS Distribution(NEQ,Axial,Radial)   OF NumRate # [particles/min] {0 to 1E25} Total
birth rate of particles due to growth at each node
   V_growth          AS Distribution(NEQ,Axial,Radial)   OF VolRate # [um^3/min] {0 to 1E25} Volume
contribution due to growth in each cell
   v_0_g            AS Volume # [um^3] Volume of small particles agglomerating to represent growth.

# Aggregation kinetics:
   agg_size                    AS ARRAY(NEQ,NEQ)      OF VOLUME # agg volume due to collisions
between
   AGG_INDEX                    AS ARRAY(NEQ,NEQ,NEQ)   OF ARGUMENT # binary multiplier indicating
whether aggregation between cells j and k result in an aggregate in cell i.
   MODIFIER                    AS ARRAY(NEQ,NEQ)      OF ARGUMENT # modify aggregation for i=j so
collisions aren't counted twice
   # Distributed:
   Beta_agg                    AS Distribution(Axial,Radial)            OF NOTYPE
   agg_rate                    AS Distribution(NEQ,NEQ,NEQ,Axial,Radial)   OF RATE # rate of births in i
due to collisions between j and k
   agg_vol_i                   AS Distribution(NEQ,NEQ,NEQ,Axial,Radial)   OF VOLUME # volume of births
in i due to collisions between j and k
   B_agg                      AS Distribution(NEQ,Axial,Radial)         OF RATE # total birth rate in cell i
   D_agg                      AS Distribution(NEQ,Axial,Radial)         OF RATE # total death rate in cell i
   V_agg                      AS Distribution(NEQ,Axial,Radial)         OF VOLUME # total volume of
particles born into cell i


# Combined kinetics:
   v_z              AS  Distribution(Radial)             OF Velocity # [m/min];      discrete fluid velocity at a
given radius
   v_set             AS  Distribution(NEQ)               OF Velocity # [m/min];       representative volume of
each node
   rate              AS  Distribution(Axial,Radial)        OF rate     # [Molar/min];  refers to the molar
production rate of struvite
   rate_g            AS  Distribution(Axial,Radial)        OF rate     # [Molar/min];
#    rate_d            AS  Distribution(Axial,Radial)        OF rate     # [Molar/min];
   NDASH_xtl         AS  Distribution(NEQ,Axial,Radial)     OF rate     # [1E6 xtl/L.min];    change in
particle number in a size due to crystallisation
   NDASH_tot         AS  Distribution(NEQ,Axial,Radial)     OF rate     # [1E6 xtl/L.min];    total change
in particle number including advection

# Cell Average reassignment:
   v_bar             AS Distribution(NEQ,Axial,Radial)   OF VOLUME # average volume of particles born
into cell i
   V_TOT             AS Distribution(NEQ,Axial,Radial)   OF VolRate # [um^3/min] {0 to 1E25} Total
volume added to each cell
   B_TOT             AS Distribution(NEQ,Axial,Radial)   OF NumRate # [particles/min] {0 to 1E25} Total
number of particles added to each cell
```

```
   D_TOT              AS Distribution(NEQ,Axial,Radial)   OF NumRate # [particles/min] {0 to 1E25} Total
death rate due to all mechanisms
   v_h                        AS Distribution(NEQ,4,Axial,Radial)        OF ARGUMENT # four different
arguments to be used in
   H                          AS Distribution(NEQ,4,Axial,Radial)        OF HYPERBOLIC # result of argument
after being assessed using the heaviside step function
   LAMBDA_1, LAMBDA_4             AS Distribution(NEQ,Axial,Radial)         OF LAMBDA_1_4 #(Defined
differently due to different parameter constraints)
   LAMBDA_2, LAMBDA_3             AS Distribution(NEQ,Axial,Radial)         OF LAMBDA_2_3 # lambda
function to be combined with result of
   Lambda_scaling                 AS Distribution(NEQ,Axial,Radial)         OF NOTYPE
   Lambda_offset                  AS Distribution(NEQ,Axial,Radial)         OF NOTYPE
   Term_1, Term_2, Term_3, Term_4  AS Distribution(NEQ,Axial,Radial)          OF TOT_RATE     # each
heaviside step function in the final cell average equation
   d_N_dt                     AS Distribution(NEQ,Axial,Radial)         OF TOT_RATE # [particles/min] {-
1E25 to 1E25} combined total particle number change per cell


# PARAMETERS TO BE ESTIMATED
   k_g              AS  NOTYPE
   n_g              AS  NOTYPE
   k_nuc             AS  NOTYPE
   n_nuc             AS  NOTYPE
   k_agg             AS  NOTYPE
   n_agg             AS  NOTYPE

   # ALTERNATIVE GROWTH KINETICS
   k_g_avg           AS  NOTYPE
   n_g_avg           AS  NOTYPE
   S_r              AS  Distribution(Axial,Radial) OF Dimensionless
   # ALTERNATIVE NUCLEATION KINETICS
   tension           AS  NOTYPE
   A_factor          AS  NOTYPE
   omega             AS  Distribution(Axial,Radial) OF Dimensionless
   G_L_2             AS  Distribution(Axial,Radial)        OF NOTYPE   # [um/min];     constant length based
growth rate - size independent growth
   B_nuc_2           AS  Distribution(Axial,Radial)        OF NOTYPE   # [1E6 xtl/L.min];    Nucleation rate
varies through reactor but only exists in the first size range.
   Null_Sat          AS                       NOTYPE

SET
   rho_struvite       :=  1740; #kg/m^3
   rho_water          :=  998; #kg/m^3
   mu_water           :=  0.001002; #Pa.s
#    k_d              :=  0; #12.49; # set as the same as growth rate via galbraith model
#    n_d              :=  5.06; # set as the same as growth rate via galbraith model
   NEQ              :=  3; #87; #101; #35 was previously 35 but PFC only achieves 24, simulation will fail
if bound is hit
#    number_scaling     :=  1E-6; # [Mxtl/1E6xtl] - scale particle number to avoid integration errors

BOUNDARY
```

```
# ONLY R BOUNDARY - arbitrary and doesn't affect the final solution
   # rate_g @ r=R for 0|+ - L|-
FOR z := 0|+ TO ReactorLength|- DO
   rate_g(z,ReactorRadius) = 1;
   # rate_g @ r=0 for 0|+ - L|-
   rate_g(z,0) = 1;
END #FOR
   # rate_g @ z=0 for 0 - R
   rate_g(0,) = 1;
   # rate_g @ z=L for 0 - R
   rate_g(ReactorLength,) = 1;

FOR z := 0|+ TO ReactorLength|- DO
   # rate @ r for 0|+ - L|-
   rate(z,ReactorRadius) = 0;
   # rate @ r=0 for 0|+ - L|-
   rate(z,0) = 0;
END #FOR
   # rate @ z=0 for 0 - R
   rate(0,) = 0;
   # rate @ z=L for 0 - R
   rate(ReactorLength,) = 0;

# NDASH can be defined at the boundary as it's not used here
# Give the same definitions for total and crystallisation NDASH
FOR z := 0|+ TO ReactorLength|- DO
   # NDASH_tot @ r for 0|+ - L|-
   NDASH_tot(,z,ReactorRadius) = 0;
   # NDASH_tot @ r=0 for 0|+ - L|-
   NDASH_tot(,z,0) = 0;
   # NDASH_xtl @ r for 0|+ - L|-
   NDASH_xtl(,z,ReactorRadius) = 0;
   # NDASH_xtl @ r=0 for 0|+ - L|-
   NDASH_xtl(,z,0) = 0;
END #FOR
   # NDASH_tot @ z=0 for 0 - R
   NDASH_tot(,0,) = 0;
   # NDASH_tot @ z=L for 0 - R
   NDASH_tot(,ReactorLength,) = 0;
   # NDASH_xtl @ z=0 for 0 - R
   NDASH_xtl(,0,) = 0;
   # NDASH_xtl @ z=L for 0 - R
   NDASH_xtl(,ReactorLength,) = 0;

   # PARTICLE NUMBER BOUNDARY CONDITIONS:
   # @ z=0, for all r, @ NEQ = 1, N = 1 - one particle of the smallest size enters the reactor at all radii
   # INLET
   # @ z=0, for all r:
      FOR r := 0 TO ReactorRadius DO
         N(1,0,r) = number_scaling*particulate_num; # always 1E6 particles coming in in the first size
bracket - avoids div0 errors
```

```
         N(2:NEQ,0,r) = 0;
      END

   # OUTLET
   # @ z = ReactorLength, for all r, for all NEQ, dN/dz = 0 - number of particles does not change
axially at the exit
      #does this need an iterator? Unlikely - others boundaries are just explicitly defined over all r.
      FOR r := 0 TO ReactorRadius DO
         PARTIAL(N(,ReactorLength,r),Axial)   =    0;
      END

   # CENTRELINE
   # @ r = 0, for all z (except the ends), for all NEQ, dN/dr = 0 - number of particles does not vary
radially at the centreline
      FOR z := 0|+ TO ReactorLength|- DO
         PARTIAL(N(,z,0),Radial)        =   0;
      END #FOR
   # WALL
   # @ r = ReactorRadius, for all z (except the ends), for all NEQ, dN/dr = 0 - number of particles does
not vary radially at the boundary
      FOR z := 0|+ TO ReactorLength|- DO
         PARTIAL(N(,z,ReactorRadius),Radial)        =   0;
      END #FOR

EQUATION
#--------------          PSD DISCRETISATION (Malvern)          ---------------
   # Discretisation factor - define just to make the model work:
   q = 4;
   # Length-Volume relationship
   v = pi/6*L^3;

   # Lower bounds:
   LOWER(1) = 0;
   LOWER_L(1) = 0;
   # lower bound of 2nd to NEQ+1 cell (determined by width discretisation)
   FOR i := 2 TO NEQ+2 DO
   # Both of these can be defined at the same time as they are independent
      LOWER(i) = LOWER(i-1) + W(i-1); # (4)
      LOWER_L(i) = LOWER_L(i-1) + W_L(i-1); # (2)
   END
   # Widths:
   W(1) = 2*v(1);
   W_L(1) = 2*L(1); #know L(1) from the v/L relationship above
   # Width of 2nd to NEQ cell determined by geo discretisation
   FOR i := 2 TO NEQ+1 DO
      W_L(i) = LOWER_L(i+1) - LOWER_L(i); # (1)
      W(i) = LOWER(i+1) - LOWER(i); # (3)
   END

   # Malvern cell sizes (Particle diameter)
   L(1)= 0.01      ;
```

```
   L(2)= 0.0114  ;
   L(3)= 0.0129  ;
#   L(4)=          0.0147  ;
#   L(5)=          0.0167  ;
#   L(6)=          0.0189  ;
#   L(7)=          0.0215  ;
#   L(8)=          0.0244  ;
#   L(9)=          0.0278  ;
#   L(10)=         0.0315  ;
#   L(11)=         0.0358  ;
#   L(12)=         0.0407  ;
#   L(13)=         0.0463  ;
#   L(14)=         0.0526  ;
#   L(15)=         0.0597  ;
#   L(16)=         0.0679  ;
#   L(17)=         0.0771  ;
#   L(18)=         0.0876  ;
#   L(19)=         0.0995  ;
#   L(20)=         0.113   ;
#   L(21)=         0.128   ;
#   L(22)=         0.146   ;
#   L(23)=         0.166   ;
#   L(24)=         0.188   ;
#   L(25)=         0.214   ;
#   L(26)=         0.243   ;
#   L(27)=         0.276   ;
#   L(28)=         0.314   ;
#   L(29)=         0.357   ;
#   L(30)=         0.405   ;
#   L(31)=         0.46    ;
#   L(32)=         0.523   ;
#   L(33)=         0.594   ;
#   L(34)=         0.675   ;
#   L(35)=         0.767   ;
#   L(36)=         0.872   ;
#   L(37)=         0.991   ;
#   L(38)=         1.13    ;
#   L(39)=         1.28    ;
#   L(40)=         1.45    ;
#   L(41)=         1.65    ;
#   L(42)=         1.88    ;
#   L(43)=         2.13    ;
#   L(44)=         2.42    ;
#   L(45)=         2.75    ;
#   L(46)=         3.12    ;
#   L(47)=         3.55    ;
#   L(48)=         4.03    ;
#   L(49)=         4.58    ;
#   L(50)=         5.21    ;
#   L(51)=         5.92    ;
#   L(52)=         6.72    ;
```

```
#    L(53)=          7.64      ;
#    L(54)=          8.68      ;
#    L(55)=          9.86      ;
#    L(56)=          11.2      ;
#    L(57)=          12.7      ;
#    L(58)=          14.5      ;
#    L(59)=          16.4      ;
#    L(60)=          18.7      ;
#    L(61)=          21.2      ;
#    L(62)=          24.1      ;
#    L(63)=          27.4      ;
#    L(64)=          31.1      ;
#    L(65)=          35.3      ;
#    L(66)=          40.1      ;
#    L(67)=          45.6      ;
#    L(68)=          51.8      ;
#    L(69)=          58.9      ;
#    L(70)=          66.9      ;
#    L(71)=          76        ;
#    L(72)=          86.4      ;
#    L(73)=          98.1      ;
#    L(74)=          111       ;
#    L(75)=          127       ;
#    L(76)=          144       ;
#    L(77)=          163       ;
#    L(78)=          186       ;
#    L(79)=          211       ;
#    L(80)=          240       ;
#    L(81)=          272       ;
#    L(82)=          310       ;
#    L(83)=          352       ;
#    L(84)=          400       ;
#    L(85)=          454       ;
#    L(86)=          516       ;
#    L(87)=          586       ;

#-------------------              KINETICS              -------------------
   # NOTE: Kinetics can be defined over the whole reactor and not used at the boundaries

   # Induction time:
   FOR z := 0 TO ReactorLength DO
      FOR r := 0 TO ReactorRadius DO
         induction_fcn(z,r) = (tanh(1E10*(z - v_z(r)*t_ind))+1)/2; # zero when length is less than
induction length
      END
   END

   # NUCLEATION RATE:
   B_nuc = number_scaling*induction_fcn*(k_nuc*(Thermo.SI* ( (tanh(1E20*Thermo.SI)+1) / 2)
)^n_nuc); # [Mxtl/L/min]=[Mxtl/1E6 xtl][xtl/L.min]
```

```
   # AGGREGATION RATE:
   Beta_agg = induction_fcn*k_agg*(Thermo.SI*(tanh(1E20*Thermo.SI)+1)/2)^n_agg; # [um/min]

   # GROWTH RATE:
   # size of a very small particle considered in CAT growth
   v_0_g = v(1)*0.01; # As this value becomes progressively smaller than the first cell, the number of
nuclei (appearing in the first cell) which remain in the first cell diminishes
   # Growth rate:
   G_L = induction_fcn*k_g*(Thermo.SI*(tanh(1E20*Thermo.SI)+1)/2)^n_g; # [um/min]

   # Alternative growth kinetics: (comment in and change to G_L as required):
      # Screw dislocation model:
      omega = 10^Thermo.SI ;
      S_r = (omega)^(1/3)-1;
   #    G_L_2 = induction_fcn*k_g_avg*(S_r*(tanh(1E20*Thermo.SI)+1)/2)^n_g_avg;

      # Birth and spread model:
      G_L_2 = induction_fcn*k_g_avg*(S_r*(tanh(1E20*Thermo.SI)+1)/2)^2 * exp(-
((10^Null_Sat)^(1/3)-1)/(S_r*(tanh(1E20*Thermo.SI)+1)/2));
      Null_Sat = 0.3;

      # Theoretical nucleation rate - should be in the range of 1E7 at inlet to 1E-4 at outlet
      B_nuc_2 = induction_fcn*number_scaling*A_factor*exp(-16.75*(tension/1000)^3*(7.94655E-
23/1E6)^2/(1.38E-23^3*298^3*(log(omega))^2));

   # Converting to volumetric growth rate:
   FOR z := 0 TO ReactorLength DO
      FOR r := 0 TO ReactorRadius DO
         # Number/ number density relation for all cells
         FOR i := 1 TO NEQ DO
            # GROWTH RATE - Define the growth rate in the DPB in terms of the SI
            # ignore rate constants for purposes of model validation
            G_v(i,z,r) = pi/2*(6*v(i)/pi)^(2/3)*G_L(z,r); # [um^3/min] = [um^3]^(2/3) * [um/min]
         END #FOR
      END #FOR
   END #FOR


#-------------------            SETTLING            -------------------

# Stokes Settling velocity (<40microns)
   FOR i := 1 TO 17 DO
      v_set(i) = 2/9*(1740-998)/0.001002*9.81*(L(i)/2/1E6)^2*60; # [m/min] =
[2/9]*[kg/m^3]/[kg.m/s]*[m/s^2]*[m^2]
   END
# Settling velocity (>40 microns)
   FOR i := 18 TO NEQ DO
      v_set(i) = 8*(1740-998)*9.81*(L(i)/2/1E6)/(3*998*0.44)*60; # [m/min] =
[2/9]*[kg/m^3]/[kg.m/s]*[m/s^2]*[m^2]
      # where an iterative solution is avoided by using C_D = 0.44:
      #C_D = 0.44; #(24/Re_p)*(1+0.14*Re_p^0.7);
```

```
      #Re_p = L(i)*v_set(i)*998/0.001002;
   END

#-------------------          NCGA DPB          -------------------
# DPB exists to give rate

# AGGREGATION:
   {AGGREGATE SIZES}
   # Set up array of all possible aggregate sizes due to collisions between particles
   # for two particles (j and k) aggregating to form a particle in the range i-1/2 and i+1/2 i.e. v_i-1/2
<= (v_j + v_k) < v_i+1/2 where j>=k
   FOR j := 1 TO NEQ DO
      FOR k := 1 TO NEQ DO
         agg_size(j,k) = v(j)+v(k); # vector of all sizes produced by v_j + v_k
         MODIFIER(j,k) = 1-((0.5+0.5*tanh(1E3*(j-k))) * (0.5+0.5*tanh(1E3*(k-j))))/0.5;
      END #FOR
   END #FOR

   {AGGREGATION INDEX}
   # Matrix indicating whether the combination of particles j and k results in a birth
   # in cell i. This remains constant through time.
   FOR i := 1 TO NEQ DO
      FOR j := 1 TO NEQ DO
         FOR k := 1 TO NEQ DO
            # checked - works. Halves solution time.
            AGG_INDEX(i,j,k) = (0.5+0.5*tanh((LOWER(i+1)-(agg_size(j,k)+1E-
10))*1E10))*(0.5+0.5*tanh(((agg_size(j,k)+1E-10)-LOWER(i))*1E10));
         END #FOR
      END #FOR
   END #FOR

# WITHIN THE WHOLE REACTOR:
   FOR z := 0|+ TO ReactorLength|- DO
      FOR r := 0|+ TO ReactorRadius|- DO
         #---------------- NUCLEATION KINETICS ------------------------------------------
         V_nuc(z,r) = B_nuc(z,r)*v(1); # [um^3/min] {0 to 1E25}

         #---------------- GROWTH KINETICS ---------------------------------------------

         ## Birth rate due to growth
         # Assuming that G=Beta*n(v_0_g)*v_0_g gives the first order upwind discretisation of growth.
         FOR i := 1 TO NEQ DO
            B_growth(i,z,r) = G_v(i,z,r)*N(i,z,r)/v_0_g; # [particles/min] {0 to 1E25} v_0_g is the volume
of the discrete nuclei contributing to the growth process

            ## Death rates due to growth (none due to nucleation)
            D_growth(i,z,r) = G_v(i,z,r)*N(i,z,r)/v_0_g; # [particles/min] {0 to 1E25}

            # Volume change of a particle size range due to growth
            V_growth(i,z,r) = B_growth(i,z,r)*(v(i)+v_0_g); # [um^3/min] {0 to 1E25}
         END
```

```
    # AGGREGATION BIRTH RATE - Number & Volume - NO LOGIC
    FOR i := 1 TO NEQ DO
       FOR j := 1 TO NEQ DO
          FOR k := 1 TO NEQ DO
             # NUMBER RATE - dN(i)/dt - using aggregation index to calculate the aggregation rate for every co-ordinate - most will be 0
             agg_rate(i,j,k,z,r) = AGG_INDEX(i,j,k) * MODIFIER(j,k) * Beta_agg(z,r) * N(j,z,r) * N(k,z,r); #SGN(N(i)) *
             # VOLUME RATE -#dV(i)/dt
             agg_vol_i(i,j,k,z,r) = agg_rate(i,j,k,z,r) * agg_size(j,k); # Don't need to include AGG_INDEX because it's part of agg_rate
          END #FOR
       END #FOR
    END #FOR

    FOR i := 1 TO NEQ DO
       B_agg(i,z,r) = SIGMA(agg_rate(i, 1:NEQ, 1:NEQ, z, r));  # Total number rate of aggregates formed in i = sum of all aggregation rates associated with cell i. Many are zero.
       V_agg(i,z,r) = SIGMA(agg_vol_i(i, 1:NEQ, 1:NEQ, z, r));  # Total volume rate of aggregates formed in i = sum of all volume rates of aggregation contributing to cell i.
    END #FOR

    FOR i := 1 TO NEQ DO
       D_agg(i,z,r) = N(i,z,r)*SIGMA(Beta_agg(z,r)*N(1:NEQ,z,r));
    END #FOR

    #---------------- COMBINED KINETICS -------------------------------------------
    {TOTAL VOLUME AND NUMBER RATES}
    B_TOT(,z,r) = B_nuc(z,r) + B_agg(,z,r)  + B_growth(,z,r) ; # can B_growth be negative irl? Add offset or adjust limits.
    D_TOT(,z,r) = D_agg(,z,r)  + D_growth(,z,r) ;
    V_TOT(,z,r) = V_nuc(z,r) + V_agg(,z,r)  + V_growth(,z,r) ;
    # NOTE: The death rate due to agglomeration is lower when growth is occurring.

    {AVERAGE AGGREGATE VOLUME - v_bar}
    # Using below formulation with offset to avoid div-0 works ok but can cause numerical problems - a better solution should be implemented in future.
    v_bar(,z,r) = (V_TOT(,z,r)+1E-12)/(B_TOT(,z,r) + 1E-12); # IF B_TOT becomes slightly negative, so does V_TOT. This offsets this. Try remove once all scaling is complete

    #---------------- CELL AVERAGE REASSIGNMENT ------------------------------------
    {HEAVISIDE STEP FUNCITON:}
    # NOTE:
    # We can't evaluate the input to the heaviside step function at the first term in the first cell or the last term in the last cell - these are adjusted manually.
    # During Manual adjustment, let the input v_h(i,j) be less than 1 (-1) so that the heaviside output is 0. This is ok because this contributes to the birth rate in the (i-1)th and (i+1)th cell which are 0 at the boundaries.

    # First Cell
```

```
# H function input arguments:
v_h(1,1,z,r) = -1; # see above for justification
v_h(1,2,z,r) = v(1) - v_bar(1,z,r);
v_h(1,3,z,r) = v_bar(1,z,r) - v(1);
v_h(1,4,z,r) = v(1+1) - v_bar(1+1,z,r);
# Mid Cells
FOR i := 2 TO NEQ-1 DO # do we need to define v_h at the boundaries?
  v_h(i,1,z,r) = v_bar(i-1,z,r) - v(i-1); # how do we address the first cell?
  v_h(i,2,z,r) = v(i) - v_bar(i,z,r);
  v_h(i,3,z,r) = v_bar(i,z,r) - v(i);
  v_h(i,4,z,r) = v(i+1) - v_bar(i+1,z,r); # how do we address the last cell?
END #FOR
# Last Cell
v_h(NEQ,1,z,r) = v_bar(NEQ-1,z,r) - v(NEQ-1);
v_h(NEQ,2,z,r) = v(NEQ) - v_bar(NEQ,z,r);
v_h(NEQ,3,z,r) = v_bar(NEQ,z,r) - v(NEQ);
v_h(NEQ,4,z,r) = -1;

# H function continuous approximation:
FOR i := 1 TO NEQ DO # for all cell sizes:
  FOR a := 1 TO 4 DO # for all four possible H-step input arguments:
    H(i,a,z,r) = 0.5+0.5*tanh(k_H*(v_h(i,a,z,r)));
  END # FOR
END # FOR

{LAMBDA FUNCTION}
# First Cell
LAMBDA_1(1,z,r) = 0; # combines to make a birth multiplier for the (i-1)th cell. There is no birth in the (i-1)th cell so let this term equal zero
LAMBDA_2(1,z,r) = v_bar(1,z,r)/v(1); # if v_bar=v(1) i.e. first nucleation, the 2nd term Heaviside step function output is 0.5 and combines with this term to assign hlaf the nuclei at this point. If v_bar(1)>v(1), H-step=0.
LAMBDA_3(1,z,r) = (v_bar(1,z,r) -   v(1+1))/(v(1)-v(1+1)); # same
LAMBDA_4(1,z,r) = (v_bar(1+1,z,r) - v(1+1))/(v(1)-v(1+1)); # same
# Middle Cells
FOR i := 2 TO NEQ-1 DO
    LAMBDA_1(i,z,r) = (v_bar(i-1,z,r) - v(i-1))/(v(i)-v(i-1)); # H=v_bar(i-1) - v(i-1)
    LAMBDA_2(i,z,r) = (v_bar(i,z,r) -   v(i-1))/(v(i)-v(i-1)); # H=v(i) - v_bar(i)
    LAMBDA_3(i,z,r) = (v_bar(i,z,r) -   v(i+1))/(v(i)-v(i+1)); # H=v_bar(i) - v(i)
    LAMBDA_4(i,z,r) = (v_bar(i+1,z,r) - v(i+1))/(v(i)-v(i+1)); # H=v(i+1) - v_bar(i+1)
END #FOR
# Last Cell
LAMBDA_1(NEQ,z,r) = (v_bar(NEQ-1,z,r) - v(NEQ-1))/(v(NEQ)-v(NEQ-1)); # same
LAMBDA_2(NEQ,z,r) = (v_bar(NEQ,z,r) -   v(NEQ-1))/(v(NEQ)-v(NEQ-1)); # same
LAMBDA_3(NEQ,z,r) = 0;
LAMBDA_4(NEQ,z,r) = 0;


#---------- ODE FOR AGGREGATION USING CELL AVERAGE TECHNIQUE -------------------
# Term_1 - birth into cell i from lower cell
# Term_2 - birth in cell i when v_bar is lower than v
```

```
      # Term_3 - birth in cell i when v_bar is greater than v - this is becoming negative - why? not B_TOT.
      # Term_4 - birth in cell i from upper cell
        # First Cell
        Term_1(1,z,r) = 0; #remove first term because for i=1, birth in B_TOT(i-1) = 0
        Term_2(1,z,r) = B_TOT(1,z,r)*LAMBDA_2(1,z,r)*H(1,2,z,r);
        Term_3(1,z,r) = B_TOT(1,z,r)*LAMBDA_3(1,z,r)*H(1,3,z,r);
        Term_4(1,z,r) = B_TOT(2,z,r)*LAMBDA_4(1,z,r)*H(1,4,z,r);
        NDASH_xtl(1,z,r) = Term_1(1,z,r) + Term_2(1,z,r) + Term_3(1,z,r) + Term_4(1,z,r) - D_TOT(1,z,r);
        #$N(1) = B_TOT(1)*LAMBDA(1,2)*H(1,2) + B_TOT(1)*LAMBDA(1,3)*H(1,3) + B_TOT(1+1)*LAMBDA(1,4)*H(1,4) - D_agg(1);

        # Middle Cells
        FOR i := 2 TO NEQ-1 DO
          Term_1(i,z,r) = B_TOT(i-1,z,r)*LAMBDA_1(i,z,r)*H(i,1,z,r);
          Term_2(i,z,r) = B_TOT(i,z,r)*LAMBDA_2(i,z,r)*H(i,2,z,r);
          Term_3(i,z,r) = B_TOT(i,z,r)*LAMBDA_3(i,z,r)*H(i,3,z,r);
          Term_4(i,z,r) = B_TOT(i+1,z,r)*LAMBDA_4(i,z,r)*H(i,4,z,r);
          NDASH_xtl(i,z,r) = Term_1(i,z,r) + Term_2(i,z,r) + Term_3(i,z,r) + Term_4(i,z,r) - D_TOT(i,z,r);
          #$N(i) = B_TOT(i-1)*LAMBDA(i,1)*H(i,1) + B_TOT(i)*LAMBDA(i,2)*H(i,2) + B_TOT(i)*LAMBDA(i,3)*H(i,3) + B_TOT(i+1)*LAMBDA(i,4)*H(i,4) - D_agg(i);
        END

        # Last Cell
        Term_1(NEQ,z,r) = B_TOT(NEQ-1,z,r)*LAMBDA_1(NEQ,z,r)*H(NEQ,1,z,r);
        Term_2(NEQ,z,r) = B_TOT(NEQ,z,r)*LAMBDA_2(NEQ,z,r)*H(NEQ,2,z,r);
        Term_3(NEQ,z,r) = B_TOT(NEQ,z,r)*LAMBDA_3(NEQ,z,r)*H(NEQ,3,z,r);
        Term_4(NEQ,z,r) = 0; #remove last term because birth in B_TOT(i+1) = 0
        NDASH_xtl(NEQ,z,r) = Term_1(NEQ,z,r) + Term_2(NEQ,z,r) + Term_3(NEQ,z,r) + Term_4(NEQ,z,r) - D_TOT(NEQ,z,r);
        #$N(NEQ) = B_TOT(NEQ-1)*LAMBDA(NEQ,1)*H(NEQ,1) + B_TOT(NEQ)*LAMBDA(NEQ,2)*H(NEQ,2) + B_TOT(NEQ)*LAMBDA(NEQ,3)*H(NEQ,3);

      #ADVECTION TERM

      FOR i := 1 TO NEQ DO
        NDASH_tot(i,z,r) = -(v_z(r)+v_set(i))*PARTIAL(N(i,z,r),Axial) + NDASH_xtl(i,z,r); # [Mxtl/L.min] = [m/min]*[Mxtl/L.m] + [Mxtl/L.min]
      END

      # REAGENT CONSUMPTION RATE
      rate(z,r) = SIGMA(NDASH_xtl(,z,r)*1/number_scaling*v)*1E-18*1E3*1710/245.41; # [Molar/min] = [Mxtl/L.mim]*[1E6xtl/Mxtl]*[micron^3/xtl.L]*[1E-18m^3/micron^3]*[1000L/m^3]*[1710g/L]*[1mol/245.41g]
      # NDASH Differential
      $N(,z,r) = NDASH_tot(,z,r); # [Mxtl/L.min];    combination of number change due to crystallisation and advection
    END #FOR
  END #FOR
```

```
#-------------------          PSD PROPERTIES          -------------------
#Distribution descriptions can occur over whole reactor. Is rate also defined over whole reactor? It
can't be because it depends on NDASH
   FOR z := 0 TO ReactorLength DO
      FOR r := 0 TO ReactorRadius DO
         # Number/ number density relation for all cells
         FOR i := 1 TO NEQ DO
            #n_density(i) = N(i)/(LOWER(i+1)-LOWER(i));
            n_density(i,z,r) = N(i,z,r)/W(i); # [1/um^3.L] = [1/L]/[um^3]
            # Number density Length-Volume relationship
            n_density_length(i,z,r) = n_density(i,z,r)*pi/2*L(i)^2; # [1/um.L] = [1/um^3.L]*[um^2]
         END #FOR

         # Numerical zeroth and first moments
         MOM(1,z,r) = SIGMA(N(,z,r)/number_scaling);  #ZEROTH MOMENT - total particle number
         MOM(2,z,r) = SIGMA(v*N(,z,r)/number_scaling);  #FIRST MOMENT - total volume
[micron^3/L]
         # Volume weighted mean diameter:
         D_4_3(z,r) = SIGMA(N(,z,r)*L^4)/SIGMA(N(,z,r)*L^3);
         #will sigma operator work or do i need to define N(,z,r)?
         # when referring to a 3D array i think you need to refer to the whole row - check
         # Number volume mean diameter:
         D_3_0(z,r) = (SIGMA(N(,z,r)*L^3)/SIGMA(N(,z,r)))^(1/3);
      END #FOR
   END #FOR

# VOLUME % @ OUTLET
# split terms to see which one causes a an integration failure in the VP_out calc below. same failure,
both new variables involved. Log scale doesn't work because of zero particles in cells.
FOR i := 1 TO NEQ DO
# for every size range, volume% [%] * total crystal volume at reactor exit [um^3/L] = volume of the
size range [um^3] * total number of particles in that range exiting the reactor [1/L]
   VP_out(i)*SIGMA(MOM(2,ReactorLength,)) =
v(i)*SIGMA(N(i,ReactorLength,)/number_scaling)*100; # has to be written this way to avoid div0 at
t=0
   N_out(i) = SIGMA(N(i,ReactorLength,));
END

# CUMULATIVE VOLUME % @ OUTLET
VPC_out(1) = VP_out(1);
FOR i := 2 TO NEQ DO
   VPC_out(i) = VPC_out(i-1) + VP_out(i);
END #FOR

# D[10], D[90] & VOLUME MEDIAN DIAMETER @ OUTLET
FOR i := 1 TO NEQ-1 DO
   VMD_cell_out(i) = MAX( 0,SGN(VPC_out(i+1) - 50) ) * MAX(0,SGN(50 - VPC_out(i)) ) * ( (50-
VPC_out(i))/((VPC_out(i+1) - VPC_out(i))/(L(i+1) - L(i))) + L(i) ) ;
   D10_cell_out(i) = MAX( 0,SGN(VPC_out(i+1) - 10) ) * MAX(0,SGN(10 - VPC_out(i)) ) * ( (10-
VPC_out(i))/((VPC_out(i+1) - VPC_out(i))/(L(i+1) - L(i))) + L(i) ) ;
```

```
   D90_cell_out(i) = MAX( 0,SGN(VPC_out(i+1) - 90) ) * MAX(0,SGN(90 - VPC_out(i)) ) * ( (90-VPC_out(i))/((VPC_out(i+1) - VPC_out(i))/(L(i+1) - L(i))) + L(i) ) ;
#    VMD_cell_out(i) = 0 ;
#    D10_cell_out(i) = 0 ;
#    D90_cell_out(i) = 0 ;
END
VMD_out = SIGMA(VMD_cell_out);
PSD_width_out = SIGMA(D90_cell_out) - SIGMA(D10_cell_out);
```

E.2.4. GMH nucleation, growth and aggregation kinetics

A basic version of this model can be found in the PhD thesis of Galbraith (Galbraith, 2011)

E.2.5. Thermodynamics

```
{ This model describes non-ideal thermodynamics over the radial and axial domains
of the PFR. It includes various species formed by the aqueous combination of
magnesium, ammonium, phosphorus and chlorine. A charge balance is used so that pH
is predicted.
}

PARAMETER
   # Distribution domains
   ReactorLength       AS REAL
   ReactorRadius       AS  REAL

   {log equilibrium constants}
   log_K_NH4          AS REAL
   log_K_HPO4         AS REAL
   log_K_H2PO4        AS REAL
   log_K_MgOH         AS REAL
   log_K_MgH2PO4      AS REAL
   log_K_MgHPO4       AS REAL
   log_K_MgPO4        AS REAL
   log_K_so           AS REAL
   log_K_w            AS REAL

   {DeBye Huckle eqn with Davies modification - DeBye Huckle constant A}
   A             AS REAL

   {ionic charges for calculating ionic strength}
   Z1            AS REAL
   Z2            AS REAL
   Z3            AS REAL

   {activity coefficient for neutrally charged compounds}
   log_Gamma0      AS REAL

   {charge balance}
   CB            AS REAL


DISTRIBUTION_DOMAIN
   Axial   AS [ 0 : ReactorLength ]
   Radial  AS  [ 0 : ReactorRadius ]

VARIABLE
   {total concentrations in solution}
   C_T_Mg         AS Distribution(Axial,Radial) OF Concentration
   C_T_NH4        AS Distribution(Axial,Radial) OF Concentration
```

```
C_T_PO4        AS Distribution(Axial,Radial) OF Concentration

{free ion concentrations}
C_Mg          AS Distribution(Axial,Radial) OF Concentration
C_MgOH         AS Distribution(Axial,Radial) OF Concentration
C_MgPO4        AS Distribution(Axial,Radial) OF Concentration
C_MgHPO4       AS Distribution(Axial,Radial) OF Concentration
C_MgH2PO4      AS Distribution(Axial,Radial) OF Concentration
C_NH4          AS Distribution(Axial,Radial) OF Concentration
C_NH3          AS Distribution(Axial,Radial) OF Concentration
C_PO4          AS Distribution(Axial,Radial) OF Concentration
C_HPO4         AS Distribution(Axial,Radial) OF Concentration
C_H2PO4        AS Distribution(Axial,Radial) OF Concentration
C_H           AS Distribution(Axial,Radial) OF Concentration
C_OH          AS Distribution(Axial,Radial) OF Concentration
C_Cl             AS Distribution(Axial,Radial) OF Concentration
C_Na          AS Distribution(Axial,Radial) OF Concentration

{log free ion concentrations}
log_C_Mg          AS Distribution(Axial,Radial) OF LogConcentration
log_C_MgOH         AS Distribution(Axial,Radial) OF LogConcentration
log_C_MgPO4        AS Distribution(Axial,Radial) OF LogConcentration
log_C_MgHPO4       AS Distribution(Axial,Radial) OF LogConcentration
log_C_MgH2PO4      AS Distribution(Axial,Radial) OF LogConcentration
log_C_NH4          AS Distribution(Axial,Radial) OF LogConcentration
log_C_NH3          AS Distribution(Axial,Radial) OF LogConcentration
log_C_PO4          AS Distribution(Axial,Radial) OF LogConcentration
log_C_HPO4         AS Distribution(Axial,Radial) OF LogConcentration
log_C_H2PO4        AS Distribution(Axial,Radial) OF LogConcentration
log_C_H           AS Distribution(Axial,Radial) OF LogConcentration
log_C_OH          AS Distribution(Axial,Radial) OF LogConcentration
log_C_Cl          AS Distribution(Axial,Radial) OF LogConcentration
log_C_Na          AS Distribution(Axial,Radial) OF LogConcentration

{ion activities}
A_Mg          AS Distribution(Axial,Radial) OF Activity
A_MgOH         AS Distribution(Axial,Radial) OF Activity
A_MgPO4        AS Distribution(Axial,Radial) OF Activity
A_MgHPO4       AS Distribution(Axial,Radial) OF Activity
A_MgH2PO4      AS Distribution(Axial,Radial) OF Activity
A_NH4          AS Distribution(Axial,Radial) OF Activity
A_NH3          AS Distribution(Axial,Radial) OF Activity
A_PO4          AS Distribution(Axial,Radial) OF Activity
A_HPO4         AS Distribution(Axial,Radial) OF Activity
A_H2PO4        AS Distribution(Axial,Radial) OF Activity
A_H           AS Distribution(Axial,Radial) OF Activity
A_OH          AS Distribution(Axial,Radial) OF Activity
A_Cl             AS Distribution(Axial,Radial) OF Activity
A_Na          As Distribution(Axial,Radial) OF Activity

{log ion activities}
```

```
    log_A_Mg          AS Distribution(Axial,Radial) OF LogActivity
    log_A_MgOH        AS Distribution(Axial,Radial) OF LogActivity
    log_A_MgPO4       AS Distribution(Axial,Radial) OF LogActivity
    log_A_MgHPO4      AS Distribution(Axial,Radial) OF LogActivity
    log_A_MgH2PO4     AS Distribution(Axial,Radial) OF LogActivity
    log_A_NH4         AS Distribution(Axial,Radial) OF LogActivity
    log_A_NH3         AS Distribution(Axial,Radial) OF LogActivity
    log_A_PO4         AS Distribution(Axial,Radial) OF LogActivity
    log_A_HPO4        AS Distribution(Axial,Radial) OF LogActivity
    log_A_H2PO4       AS Distribution(Axial,Radial) OF LogActivity
    log_A_H           AS Distribution(Axial,Radial) OF LogActivity
    log_A_OH          AS Distribution(Axial,Radial) OF LogActivity
    log_A_Cl          AS Distribution(Axial,Radial) OF LogActivity
    log_A_Na          AS Distribution(Axial,Radial) OF LogActivity

    {Activity coefficients}
    log_Gamma1        AS Distribution(Axial,Radial) OF LogActivityCoeff
    log_Gamma2        AS Distribution(Axial,Radial) OF LogActivityCoeff
    log_Gamma3        AS Distribution(Axial,Radial) OF LogActivityCoeff

    Gamma1        AS Distribution(Axial,Radial) OF ActivityCoeff
    Gamma2        AS Distribution(Axial,Radial) OF ActivityCoeff
    Gamma3        AS Distribution(Axial,Radial) OF ActivityCoeff

    {Ionic Strength}
    I             AS Distribution(Axial,Radial) OF IonicStrength

    {saturation index}
    SI            AS Distribution(Axial,Radial) OF Dimensionless
    Sa            AS Distribution(Axial,Radial) OF Dimensionless

    {pH}
    pH            AS Distribution(Axial,Radial) OF pH

    {Ion Activity Product}
    log_IAP          AS Distribution(Axial,Radial) OF Dimensionless

  SET
    {log equilibrium constants}
    log_K_NH4         :=  -9.25;
    log_K_HPO4        :=  -12.35;
    log_K_H2PO4       :=  -7.20;
    log_K_MgOH        :=  -2.56;
    log_K_MgH2PO4     :=  -0.45;
    log_K_MgHPO4      :=  -2.91;
    log_K_MgPO4       :=  -4.80;
    log_K_so          :=  -13.26;
    log_K_w           :=  -14;

    {Davies equation with DeBye Huckle modification}
    A             :=   0.509;
```

```
  {ionic charges for calculating ionic strength}
  Z1          :=  1;
  Z2          :=  2;
  Z3          :=  3;

  {charge balance}
  CB          :=  0;

  {activity coefficient for neutrally charged compounds}
  log_Gamma0        :=  0;


  # BOUNDARY
  # Boundary condition equations


EQUATION
  {mass balances - the total amount of each element of interest is the amount
  added or measured in solution}
  {Define in process}
  {how do you write the mass balances for dynamic situations}
  C_T_Mg        =   C_Mg + C_MgOH + C_MgPO4 + C_MgHPO4 + C_MgH2PO4; # [moles/L]
  C_T_NH4    =   C_NH4 + C_NH3; # [moles/L]
  C_T_PO4    =   C_PO4 + C_HPO4 + C_H2PO4 + C_MgPO4 + C_MgHPO4 + C_MgH2PO4; # [moles/L]

  # Model equations
  {free ion concentrations}
  C_Mg          =  10^log_C_Mg; # [moles/L]
  C_MgOH        =  10^log_C_MgOH; # [moles/L]
  C_MgPO4       =  10^log_C_MgPO4; # [moles/L]
  C_MgHPO4      =  10^log_C_MgHPO4; # [moles/L]
  C_MgH2PO4     =  10^log_C_MgH2PO4; # [moles/L]
  C_NH4         =  10^log_C_NH4; # [moles/L]
  C_NH3         =  10^log_C_NH3; # [moles/L]
  C_PO4         =  10^log_C_PO4; # [moles/L]
  C_HPO4        =  10^log_C_HPO4; # [moles/L]
  C_H2PO4       =  10^log_C_H2PO4; # [moles/L]
  C_H           =  10^log_C_H; # [moles/L]
  C_OH          =  10^log_C_OH; # [moles/L]
  C_Cl          =  10^log_C_Cl; # [moles/L]
  C_Na          =  10^log_C_Na; # [moles/L]

  {ion activities}
  A_Mg          =  10^log_A_Mg; # [moles/L]
  A_MgOH        =  10^log_A_MgOH; # [moles/L]
  A_MgPO4       =  10^log_A_MgPO4; # [moles/L]
  A_MgHPO4      =  10^log_A_MgHPO4; # [moles/L]
  A_MgH2PO4     =  10^log_A_MgH2PO4; # [moles/L]
  A_NH4         =  10^log_A_NH4; # [moles/L]
  A_NH3         =  10^log_A_NH3; # [moles/L]
```

```
A_PO4          =  10^log_A_PO4; # [moles/L]
A_HPO4         =  10^log_A_HPO4; # [moles/L]
A_H2PO4        =  10^log_A_H2PO4; # [moles/L]
A_H            =  10^log_A_H; # [moles/L]
A_OH           =  10^log_A_OH; # [moles/L]
A_Cl           =  10^log_A_Cl; # [moles/L]
A_Na           =  10^log_A_Na; # [moles/L]

{Log Equilibrium Equations}
log_A_NH4 + log_K_NH4           =  log_A_NH3   + log_A_H;
log_A_HPO4 + log_K_HPO4         =  log_A_H     + log_A_PO4;
log_A_H2PO4 + log_K_H2PO4       =  log_A_H     + log_A_HPO4;
log_A_MgOH + log_K_MgOH         =  log_A_Mg    + log_A_OH;
log_A_MgH2PO4 + log_K_MgH2PO4   =  log_A_Mg    + log_A_H2PO4;
log_A_MgHPO4 + log_K_MgHPO4     =  log_A_Mg    + log_A_HPO4;
log_A_MgPO4 + log_K_MgPO4       =  log_A_Mg    + log_A_PO4;

{log activities}
log_A_Mg          =   log_C_Mg       + log_Gamma2;
log_A_MgOH        =   log_C_MgOH     + log_Gamma1;
log_A_MgPO4       =   log_C_MgPO4    + log_Gamma1;
log_A_MgHPO4      =   log_C_MgHPO4   + log_Gamma0;
log_A_MgH2PO4     =   log_C_MgH2PO4  + log_Gamma1;
log_A_NH4         =   log_C_NH4      + log_Gamma1;
log_A_NH3         =   log_C_NH3      + log_Gamma0;
log_A_PO4         =   log_C_PO4      + log_Gamma3;
log_A_HPO4        =   log_C_HPO4     + log_Gamma2;
log_A_H2PO4       =   log_C_H2PO4    + log_Gamma1;
log_A_H           =   log_C_H        + log_Gamma1;
log_A_OH          =   log_C_OH       + log_Gamma1;
log_A_Cl          =   log_C_Cl       + log_Gamma1;
log_A_Na          =   log_C_Na       + log_Gamma1;

{Activity Co-efficients - Davies eqn with DeBye Huckle approximation}
log_Gamma1 =    -A*(Z1^2)*((I^0.5)/(1+(I^0.5))-0.3*I);
Gamma1 = 10^log_Gamma1;

log_Gamma2 =    -A*(Z2^2)*((I^0.5)/(1+(I^0.5))-0.3*I);
Gamma2 = 10^log_Gamma2;

log_Gamma3 =    -A*(Z3^2)*((I^0.5)/(1+(I^0.5))-0.3*I);
Gamma3 = 10^log_Gamma3;

{Ionic Strength}
I   =   0.5*(
C_Mg*(Z2^2) +
C_MgOH*(Z1^2) +
C_MgPO4*(Z1^2) +
C_MgH2PO4*(Z1^2) +
C_NH4*(Z1^2) +
C_PO4*(Z3^2) +
```

```
   C_HPO4*(Z2^2) +
   C_H2PO4*(Z1^2) +
   C_H*(Z1^2) +
   C_OH*(Z1^2) +
   C_Cl*(Z1^2) +
   C_Na*(Z1^2));

   {Charge Balance}
   CB   =
   C_Mg * Z2 +
   C_MgOH * Z1 +
   C_MgPO4 * (-Z1) +
   C_MgH2PO4 * Z1 +
   C_NH4 * Z1 +
   C_PO4 * (-Z3) +
   C_HPO4 * (-Z2) +
   C_H2PO4 * (-Z1) +
   C_H * Z1 +
   C_OH * (-Z1) +
   C_Cl * (-Z1) +
   C_Na * Z1;

   {pH}
   pH = -log_A_H;
   log_K_W = log_A_H + log_A_OH;

   {Solubility Index}
   log_IAP = log_A_Mg + log_A_NH4 + log_A_PO4;
   SI = log_IAP - log_K_so;
   Sa = (10^(log_IAP - log_K_so))^(1/3) - 1;
```

E.2.6. Stochastic simulation

```
{ --------- STOCHASTIC UNCERTAINTY PROPAGATION -----------------
Stochastic simulations assess the uncertainty of key process
variables as a result of distributed uncertainties in selected variables.

This model is called by the process 'StochasticSimulation', which feeds required
variables to run the simulation.

The following variables will be analysed by stochastic uncertainty analysis:

Output variables of interest:
 - VMD - volume median diameter/ D[50]
 - SI - saturation index
 - Thermo_Yield - thermodynamic yield

Input variables of interest (measured variables most likely to change during
experiments) - feed concentrations, feed flows, reactor total flow
}

PARAMETER
   # Number of scenarios in the stochastic simulation
```

```
    NoScenarios         AS  INTEGER


UNIT
  # An array of the mass balance model (which calls necessary sub-models) to
  # simultaneously obtain a solution for each scenario
  ScenarioMB     AS  ARRAY(NoScenarios)    OF  PFR_Mass_Balance_industrial


VARIABLE
  # INPUTS:
  # Whatever inputs are included here, they must be removed from the assigned
  # variables list in the deterministic process model.
    Flow_NaOH_Batch     AS  ARRAY(NoScenarios)  OF  FlowRate # [L/h] flow rate of NaOH entering
the reactor
    Flow_Reagent_Batch  AS  ARRAY(NoScenarios)  OF  FlowRate # [L/h]
    C_NaOH_batch        AS  ARRAY(NoScenarios)  OF  Concentration # [mol/L]
    C_NH4_batch         AS  ARRAY(NoScenarios)  OF  Concentration # [mol/L]
    C_PO4_batch         AS  ARRAY(NoScenarios)  OF  Concentration # [mol/L]
    C_MgCl26H2O_batch   AS  ARRAY(NoScenarios)  OF  Concentration # [mol/L]
    Flow_T              AS  ARRAY(NoScenarios)  OF  FlowRate
    # GROWTH KINETICS
    k_g          AS  ARRAY(NoScenarios)  OF  NOTYPE
    n_g          AS  ARRAY(NoScenarios)  OF  NOTYPE
    # NUCLEATION KINETICS
    k_nuc        AS  ARRAY(NoScenarios)  OF  NOTYPE
    n_nuc        AS  ARRAY(NoScenarios)  OF  NOTYPE

  # OUTPUTS:
    VMD_out        AS  ARRAY(NoScenarios)  OF  Length # volume median diameter exiting the reactor
    PSD_width_out  AS  ARRAY(NoScenarios)  OF  Length
    SI_out         AS  ARRAY(NoScenarios)  OF  Dimensionless
    Yield_thermo   AS  ARRAY(NoScenarios)  OF  Notype
    pH_out         AS  ARRAY(NoScenarios)  OF  Notype

EQUATION
#-------------- Assigning variables in this simulation to values from each scenario -------------#
  FOR i := 1 TO NoScenarios DO
    # INPUTS (which will be varied):
    Flow_NaOH_Batch(i)        = ScenarioMB(i).Flow_NaOH_Batch ; # Flow_NaOH_Batch in each
scenario is set based on the corresponding value defined by the normal distribution function in the
process.
    Flow_Reagent_Batch(i)   = ScenarioMB(i).Flow_Reagent_Batch ;
    Flow_T(i)               = ScenarioMB(i).Flow_T;

    C_NaOH_batch(i)         = ScenarioMB(i).C_NaOH_batch ;
    C_PO4_batch(i)          = ScenarioMB(i).C_PO4_batch ; # RHS assigned by process
    C_MgCl26H2O_batch(i)    = ScenarioMB(i).C_MgCl26H2O_batch ;
    C_NH4_batch(i)          = ScenarioMB(i).C_NH4_batch ; # Assigning C_NH4_batch(i) in this model to
that in the scenario model
```

```
    k_g(i)              = ScenarioMB(i).Kinetics.k_g_avg;
    n_g(i)              = ScenarioMB(i).Kinetics.n_g_avg;
    k_nuc(i)              = ScenarioMB(i).Kinetics.tension;
    n_nuc(i)              = ScenarioMB(i).Kinetics.A_factor;

    # OUTPUTS:
    VMD_out(i)        =   ScenarioMB(i).Kinetics.VMD_out ; # The VMD_out in the stochastic model is
equated to that calculated by the lower models
    PSD_width_out(i)    =   ScenarioMB(i).Kinetics.PSD_width_out;
    SI_out(i)         =   ScenarioMB(i).SI_out ;
    Yield_thermo(i)     =   ScenarioMB(i).Yield_thermo ;
    pH_out(i)         =   ScenarioMB(i).pH_out ;
  END
```

Appendix F Grid convergence methods

F.1. Grid convergence order

Grid fineness was increased using methods taken from (Roache, 1998), described below. The convergence order was calculated to identify which grids converge faster and to identify the approximate number of grid elements in which convergence is likely to occur. A power law model (equation 0.97) was used to model the relationship between the error in a selected variable f, termed E_f,and the grid spacing, h (defined by equation 0.99). The order of this power law model indicates the rate at which a variable will converge with increasing grid fineness, indicating the sensitivity of the selected variable to the grid.

$$E_f = f(h_j) - f_{exact} = Ch^p + H.O.T. \qquad 0.97$$

Where $f(h)$ is the numerical solution, f_{exact} is the exact solution, p and C are the grid convergence rate constant and order, respectively, and $H.O.T$ denotes possible higher order terms which are not considered here (a common practice). When f_{exact} is unknown (*i.e.* for output concentration), it is assumed as the numerical solution to E at which a decrease in h yields no further change in $f(h)$. The value of p can then be determined by fitting to a log-log chart using equation 0.98

$$\log(E_f) = \log(C) + p\log(h) \qquad 0.98$$

The selection of variable f used to determine the grid dependence is important. This variable should have the following characteristics: (1) Its value and uncertainty can be measured, (2) it is sensitive to the grid coarseness, and (3) it is a key indicator of process performance. Key process variables identified were: (1) flow rate exiting the reactor and (2) total phosphate concentration near the beginning, middle and end of the reactor. Conservation of phosphorus mass over the reactor was also used as an indication of grid independence. The variation of grid spacing (h) is determined by equation 0.99 via the number of elements, N, in each dimension for the n^{th} simulation.

$$N = 2^n m + 1 \tag{0.99}$$

where m is an integer which can vary for each dimension (assumed to be 1 here). The axial and radial grid spacing are related to the number of elements by $h_z = Z/N$ and $h_r = R/N$, respectively, where Z and R are the total reactor length and radius, respectivley. For this work, h_z and h_r each remain constant.

Appendix G Supplementary batch experiment procedure

Batch experiments were conducted with 5-L batches of nutrient solution with an elemental phosphorus concentration of 0.02 M and elemental Mg:N:P molar ratios of 1.5:1:1. Stock nutrient solutions were made using $NH_4H_2PO_4$ and $MgCl_2 \cdot 6H_2O$ and SI values of 0.8, 1.0 and 1.4 were achieved by the addition of 16.5, 17.6 and 19.3 mM caustic ($NaOH$) solution, achieving predicted non-equilibrium pH values of 7.172, 7.351 and 7.727 respectively. Solutions were made with Sigma-Aldrich analytical grade reagents and RO filtered water, subsequently filtered through 0.2-μm cellulose nitrate membrane filter. All solutions were stored in sealed vessels to minimise CO_2 intrusion, which can impact solution thermodynamics through carbonate chemistry. Experiments ran for an equivalent residence time to the PFR (23.26 min) in an 0.5 L beaker, with no sonication, mixed with a 20mm diameter propeller at 1200 rpm (the minimum stirring rate to ensure particle suspension during PSD measurements). For ease of PSD measurements, experiments were conducted using the sample mixing device of the Malvern Mastersizer3000, as shown in Figure 0.1.

Figure 0.1 – Apparatus used for batch experiments

18 PSD samples and 6 phosphorus concentration samples were taken. Sample residence times were selected to equal average residence times of axial elements in the Poiseuille flow reactor for comparative purposes. Phosphate concentration was determined with an Agilent 8453 UV-Vis spectro-photometer using the molybdo-vanado-phosphoric acid method (APHA et al., 1999). PSD analysis was performed by laser diffraction (LD) using a Malvern Mastersizer3000. Samples were sonicated at 40 W and 40 kHz for 5 min at the conclusion of each experiment to separate nucleation and crystal growth from aggregation mechanisms – aggregation was found to play an insignificant role.